DOCTOR OF SCIENCES

Probing the physics of magnetron sputtering for thin-film deposition by Virtual Coater application to TiO2

Tonneau, Romain

Award date:
2021

Awarding institution:
University of Namur

University of Namur – Faculty of Sciences

Namur Institute of Structured matter (NISM)

Probing the physics of magnetron sputtering for thin-film deposition by Virtual Coater: application to TiO_2

Dissertation presented by
Tonneau Romain
for the degree of doctor of sciences

Jury members:

Prof. Stéphane LUCAS (Supervisor)
Laboratoire d'Analyse par Réactions Nucléaires (LARN - NISM)
UNamur, Namur, Belgium

Dr. Andreas PFLUG (Co-supervisor)
Fraunhofer Institute for Surface Engineering and Thin Films IST
Braunschweig, Germany

Dr. Pavel MOSKOVKIN
Laboratoire d'Analyse par Réactions Nucléaires (LARN - NISM)
UNamur, Namur, Belgium

Dr. Wilmert De BOSSCHER
Chief Technology Officer - SOLERAS Advanced Coatings
Deinze, Belgium

Prof. Stéphanos KONSTANTINIDIS
Laboratoire de Chimie des Interactions Plasma-Surface (ChiPS)
UMons, Mons, Belgium

Prof. Achim von KEUDELL
Chair Experimental Physics II – Reactive Plasmas
RUB, Bochum, Germany

Prof. Luc HENRARD (Chairman)
Laboratoire de physique du solide (LPS – NISM)
UNamur, Namur, Belgium

UNamur - 2021

The most worth-while thing is to try to put happiness into the lives of others

Robert Baden-Powell

Remerciements

À l'heure d'écrire ces dernières lignes, le monde est toujours occupé à combattre la pandémie de COVID-19. C'est donc dans un contexte tout-à-fait particulier que ce travail fut écrit. Un contexte aseptisé de contact physique, où nous avons tous dû apprendre à vivre dans nos bulles respectives, nous privant des relations sociales si chères à notre bonne santé psychologique. Un contexte favorisant la prise de distance, la proscription de tout événement récréatif… En somme : le repli sur soi-même. C'est ainsi que l'importance cruciale des relations humaines et des personnes qui nous entourent nous a été rappelé de façon assez violente. J'espère que nous sortirons (rapidement) grandi et plus fort de cette crise sanitaire. En attendant, cette situation me fait voir l'impact très positif de mon entourage sur ma vie et mon travail, et donc cette thèse. Et du plus profond de mon cœur je tiens à remercier toutes les personnes impliquées de près ou de loin dans ce travail. Sachez que même si je ne nomme pas tout le monde, j'aurai eu une pensée spéciale pour vous tous.

Pour commencer, je remercie tout particulièrement mes promoteurs, Stéphane Lucas et Andreas Pflug pour leur accueil, leur patience et sans qui ce travail n'aurait pas vu le jour. Merci d'avoir cru en moi, même lorsque j'en doutais moi-même. L'un expérimentateur jusqu'au bout des doigts, l'autre mariant à merveille physique et numérique, quel duo de choc vous avez été pour moi ! Mille merci.

Je remercie également les docteurs Pavel Moskovkin et Wilmert De Bosscher, ainsi que les professeurs Stéphanos Konstantinidis, Achim von Keudell et Luc Henrard d'avoir accepté de faire partie de ce jury de thèse et pour les discussions très constructives qui m'ont permis d'améliorer ce travail.

La partie simulation de cette thèse a été grandement rendue possible grâce à l'aide de l'équipe de simulation de l'IST ainsi qu'aux interventions récurrentes d'Isabelle Derycke, Jérôme Muller, Frédéric Wautelet et l'équipe du super calculateur Zenobe de Cenaero. À vous tous, merci.

La partie expérimentale quant à elle a été largement tributaire des interventions de Julien Colaux, Francesca Cecchet, Tijani Tabarrant, Rémy Wauters et Alexia Petit. Merci pour votre précieux temps et votre patience avec moi.

Cette thèse a été réalisée au Laboratoire, d'Analyse par Réactions Nucléaires de l'UNamur, le « LARN » pour les intimes. Elle est le fruit de 7 années de labeur parsemé d'innombrables bons moments prodigués par l'incroyable équipe du LARN. Merci à toutes et tous pour cette bonne humeur, ces kilos de tartes, week-end LARN, repas de Noël, pauses café, bières du vendredi, … Je n'aurais voulu réaliser cette thèse dans aucun autre environnement tant vous avez été extraordinaires. Mon

Patachon, on en a fait du chemin depuis ces journées passées à aligner les petits capillaires de ce bon Tokihiro… Je suis heureux d'avoir pu t'accompagner jusqu'au bout et te remercie pour ton éternel soutient.

Tout de même, une thèse ce n'est pas une vie. Il y a tant d'autres choses à (re)chercher en dehors des murs du laboratoire. J'estime avoir déjà trouvé beaucoup de ces petites choses, qui, mises bout-à-bout forment une vie heureuse et nous font rêver en couleur. Tout cela a eu un impact titanesque sur la personne que je suis aujourd'hui et donc sur ce travail. Dès lors, **V**ous aussi êtes acteurs de ce manuscrit :

- Cécé, Polo et Louis, les meilleurs compagnons possibles sur les bancs de l'université ainsi que co-assistants et collègues. Aurais-je fait tout ce chemin en science sans vous ?

- Tous les compagnons des « jeudredis » trop arrosés. Savez-vous quel est votre problème ?

- Adrien, Mathieu, Sylvain, Mathilde, Mika, Mirko, Ben, Bruno et tous les assistants avec qui j'ai eu la chance de travailler. Avec une pensée toute particulière pour Fernande et Laurent, vous avez réellement été aux petits soins pour nous. En fin de compte, être assistant n'est-ce pas apprendre à se couper en mille morceaux tout en restant entier avec tout un chacun, soi-même compris ?

- Marting, Eve, Floflo, Adrien, Sébastien, Boulbi, Bruno et Nathalie/Enhydra, 7 années de colocation tellement riches en émotions et souvenirs grâce à vous. Me pardonnerez-vous ces moments d'égarement où je ne paraissais certainement pas toujours sain d'esprit ?

- Lucie, Cécile et Pauline, vous ai-je déjà dit tout le bien que vous m'avez apporté pendant ces années ?

- L'entièreté de la NO26, unité scoute de Boninne. Vous m'avez apporté tellement, de temps, de talent et de coeur. Tout particulièrement Daguet et Suricate, infatigables chefs d'U ; Harfang et Wombat, la dream team d'animation (dans le doute, désolé de nous avoir parfois perdu avec nos jeunes au fin fond d'un pays étrangé) ; Mara, Isatis, Saluki, Chipmunk et Sitatunga, des pilliers de vie et ami(es)natrices en or. Que/Qui serais-je sans vous ?

- JP, Loïc, Amaury et Sisi, probablement parmi mes plus anciens compagnons de vie. Ces amitiés inconditionnelles traversant les âges… Quelle plus belle richesse ?

Je ne vous remercierai jamais assez =)

Finalement, merci à ma famille, ma tribu, mon refuge pour leur soutient de tous les instants et plus encore.

Table of content

List of publications

1. Félicien Hespeels ; **Romain Tonneau** ; T Ikeda ; Stéphane Lucas
   ⇨ "Comparison of experimental and Monte-Carlo simulation of MeV particle transport through tapered/straight glass capillaries and circular collimators"
   Nuclear Instruments and Methods in Physics Research Section B: Beam Interactions with Materials and Atoms
   DOI: 10.1016/j.nimb.2015.09.030
   Status: Published November **2015**; 3 citations.

2. **R Tonneau**, P Moskovkin, A Pflug and S Lucas
   ⇨ "TiOx deposited by magnetron sputtering: a joint modelling and experimental study" *Journal of Physics D: Applied Physics*
   DOI: 10.1088/1361-6463/aabb72
   Status: Published April **2018**; 12 citations.

3. Holger Badorreck, Morten Steinecke, Lars Jensen, Detlev Ristau, Marco Jupé, Jérôme Müller, **Romain Tonneau**, Pavel Moskovkin, Stephane Lucas, Andreas Pflug, Lina Grinevičiūtė, Algirdas Selskis, and Tomas Tolenis
   ⇨ "Correlation of structural and optical properties using virtual materials analysis" *Journal of Physics D: Applied Physics*
   DOI: 10.1364/OE.27.022209
   Status: Published July **2019**; 5 citations.

4. Stella Mathioudaki, Cédric Vandenabeele, **Romain Tonneau**, Andreas Pflug, and Stéphane Lucas
   ⇨ "Characterization of a pulsed low pressure argon discharge in a cylindrical magnetron reactor by plasma diagnostic and 3D plasma modeling"
   Journal of Vacuum Science & Technology A
   DOI: 10.1116/1.5064690
   Status: Published February **2019**; 4 citations.

5. Stella Mathioudaki, Cédric Vandenabeele, **Romain Tonneau**, Andreas Pflug, Jonathan Tennyson, and Stéphane Lucas
   ⇨ "Plasma polymerization of cyclopropylamine in a low-pressure cylindrical magnetron reactor: A PIC-MC study of the roles of ions and radicals"
   Journal of Vacuum Science & Technology A
   DOI: 10.1116/1.5142913
   Status: Published March **2020**

6. **R Tonneau**, A Pflug and S Lucas
   ⇨ "Magnetron sputtering: determining scaling relations towards real power discharges using 3D particle-in-cell Monte Carlo models"
   Plasma Sources Science and Technology
   DOI: 10.1088/1361-6595/abb3a0
   Status: Published November **2020**

7. **R. Tonneau**, P. Moskovkin, J. Muller, T. Melzig, E. Haye, S. Konstantinidis, A. Pflug, S. Lucas
   ⇨ "Understanding the role of energetic particles during the growth of TiO2 thin films by reactive magnetron sputtering through multi-scale Monte Carlo simulations and experimental deposition"
   Journal of Physics D: Applied Physics
   DOI: 10.1088/1361-6463/abd72a
   Status: Published December **2020**

List of figures

Abbreviation list

PVD: Physical vapor deposition

CVD: Chemical vapor deposition

MS: Magnetron Sputtering

RMS: Reactive magnetron sputtering

U_0: Surface binding energy

HPC: High-performance computer

MD: Molecular dynamic

VC: Virtual coater

***s*:** Sticking coefficient

DFT: Density functional theory

PICMC: Particle-in-cell Monte Carlo

DSMC: Direct simulation Monte Carlo

kMC: kinetic Monte Carlo

IPVD: Ionized physical vapor deposition

OES: Optical emission spectroscopy

EEDF: Electron energy distribution function

ATP: Active thermal probe

NEF: Normalized energy flux

RBS: Rutherford backscattering spectroscopy

SEM: Scanning electron microscopy

AFM: Atomic force spectroscopy

XRD: X-ray diffraction

BCA: Binary collision approximation

VSS: Variable soft sphere

SE: Secondary electron

SEEY: Secondary electron emission yield

L_D: Diffusion length

γ_{sput}: Sputtering yield

β: Column tilting angle

V_{disch}: Discharge potential

I_{disch}: Discharge current

Units:

Å: Angström

K: Kelvin

eV: electron volt

sccm: standard cubic centimetre per minute

Pa: Pascal

Université de Namur

Faculté des sciences

61, rue de Bruxelles, B-5000 Namur, Belgique

Sonder la physique de la pulvérisation magnétron pour le dépôt de couches minces par Virtual Coater : application au TiO_2

Résumé

L'objet de cette thèse de doctorat a porté sur le développement d'une nouvelle génération d'outils de prédiction dédiés au dépôt de couches minces par des procédés sous vide. Même si ces processus forment l'un des principaux piliers de notre société technologique, leur compréhension et leur maitrise ne sont pas encore totales. Il reste toujours des zones grises que les connaissances scientifiques actuelles ne peuvent décrire ou expliquer. Cependant, l'avènement de l'informatique a ouvert la porte d'un nouveau type d'approche, permettant aux scientifiques de simuler des procédés complexes afin d'élucider leur compréhension. Avec l'évolution des moyens de calcul haute performance, la complexité des modèles numériques ne cesse de croître. Les anciens modèles 1D ou 2D peuvent désormais céder la place à des modèles 3D réalistes implémentant une physique très détaillée et offrant aux scientifiques de nouvelles façons d'observer et de voir les processus régissant l'Univers. Au lieu d'essayer d'expliquer l'Univers tout entier, cette thèse de doctorat se concentre sur la technique dite de pulvérisation magnétron réactive qui est une méthode largement utilisée pour le dépôt de couches mince de composés tant en laboratoire qu'en industrie. Par conséquent, sa compréhension est d'une grande importance pour maîtriser la qualité et les propriétés des produits. Les processus physiques impliqués étant de nature complexe et non linéaire, ils nécessitent l'utilisation d'un large éventail de techniques et de modèles de simulation. Ce travail de doctorat a établi une chaîne de simulation multi-échelle 3D du procédé de dépôt par plasma (Virtual Coater^{TM}). Celle-ci est basée sur la combinaison d'algorithmes de type « Particle-in-cell Monte Carlo » pour la simulation de la phase plasma et de « kinetic Monte Carlo » pour la croissance de film.

La première étape de ce travail explique les liens et interfaces entre les différents algorithmes utilisés pour obtenir une vision globale du procédé de dépôt. Dans un deuxième temps, l'attention est portée sur le rôle des particules neutres pendant le dépôt. La caractérisation expérimentale des propriétés plasma et des couches minces est effectuée et comparée avec les simulations réalisées. Pour une géométrie donnée, l'hystérésis de la phase plasma, la composition du film et sa morphologie sont prédits et expliqués.

Dans un troisième temps, les défis surgissant lors de la modélisation de particules chargées sont mis en évidences et expliqués. Lors d'un dépôt plasma se produisant à une densité de puissance réaliste, les flux de particules s'écoulant vers le substrat sont démontrés prédictibles sur base de simulations 3D fonctionnant à des densités de puissance inférieures. Il a été également démontré que ces simulations prédisent l'existence des instabilités propagatrices du plasma appelées, spokes. Finalement, à la lumière des contraintes du modèle, le domaine de validité de cette stratégie de prédiction des flux est établi et clairement défini.

La dernière étape de ce manuscrit applique avec succès la chaîne de simulation multi-échelle 3D établie pour la croissance de films minces de TiO_2 par pulvérisation magnétron réactive. Le modèle prédit efficacement les densités et les flux de particules chargées et neutres vers le substrat et permet d'expliquer les changements de propriétés des films déposés tout au long de la transition plasma du mode de dépôt métallique au mode de dépôt stœchiométrique (TiO_2). De plus, les ions négatifs très énergétiques d'oxygène monoatomique provenant des cibles sont identifiés comme étant à l'origine de l'inclinaison anormalement faible de la structure en colonnes expérimentalement observée sur les revêtements obtenus en mode oxydé. En outre, le changement, lors de la transition plasma, de la structure cristallographique des couches minces depuis une phase amorphe vers une phase anatase, est observé par une analyse par diffraction des rayons X des couches produites. Cette modification est attribuée à l'augmentation du flux d'énergie normalisé (NEF) à l'emplacement du substrat.

Au final, le développement de Virtual Coater à travers ce travail a permis d'améliorer la connaissance de l'interaction entre les propriétés du plasma et la qualité des couches minces obtenues. Cette nouvelle procédure de simulation ouvre la voie à de nouvelles méthodes d'étude de l'état plasma en tant que procédé de dépôt.

University of Namur

Faculty of Sciences

61, rue de Bruxelles, B-5000 Namur, Belgium

Probing the physics of magnetron sputtering for thin-film deposition by Virtual Coater: application to TiO_2

Abstract

The purpose of this Ph.D. thesis is the development of a new generation of predictive tools dedicated to thin film deposition by vacuum-based techniques. Even though these processes are one of the main pillars of our technological society, the understanding of these techniques has not yet come to an end. There are still grey areas that today's scientific knowledge cannot describe or explain. However, the advent of computer science opens up the door to a brand-new kind of approaches, allowing scientists to simulate complex processes in order to unravel their understanding. With the evolution of High-Performance Computing resources, the complexity of the numerical models is continuously growing. The former basic 1D or 2D models can now give way to realistic 3D models including a very detailed physics and providing scientist new ways to observe and see the processes governing the universe. Rather to aim to explain the whole universe, this PhD thesis focuses on the reactive magnetron sputtering technique which is a widely used method for the deposition of various compound layers both in laboratories and in industries. Therefore, its understanding is of great importance to master the quality and the properties of the products. The involved physical processes have complex and non-linear nature requiring the use of a wide range of simulation techniques and models. This PhD work established a 3D multi-scale simulation chain of plasma deposition process (a.k.a. Virtual Coater^{TM}), based on a combination of Particle-In-Cell Monte Carlo (plasma phase) algorithms and a kinetic Monte Carlo (film growth) code.

The first step of this work demonstrates the connections between the several codes in order to provide a global picture of the deposition process. In a second time,

attention is focused on the role of neutral particles during the deposition process. Experimental characterization of both the plasma phase and the film properties are performed and compared together with simulation results. The experimental results are in agreement with the simulated ones. For a given coater, the plasma phase hysteresis behaviour, film composition and film morphology are predicted and explained.

In a third time, the challenges arisen when modelling charged particles are highlighted and addressed in a dedicated section. The various fluxes of particles flowing towards the substrate during a plasma deposition process occurring at realistic power density are proved to be scalable from 3D PICMC simulations operating at lower power density. The simulations also feature propagating plasma instabilities, so-called spokes. The validity domain of the scaling strategy is discussed in the light of the model constraints.

The last step successfully applies the established 3D multi-scale simulation chain to the growth of TiO_2 thin films by means of reactive magnetron sputtering. The model efficiently predicts the densities and fluxes of both charged and neutral particles towards the substrate. It also enables to explain the changes of properties of the deposited films throughout the transition from metallic deposition to stoichiometric TiO_2. Moreover, the high energy negative atomic oxygen ions originating from the targets are identified as origin of the abnormally low inclination of the columnar structure experimentally observed for the oxide mode coatings. Also, the change of the crystallographic arrangement of the coatings during the plasma transition from amorphous to anatase is observed by x-ray diffraction. This modification is explained by an increase of the normalized energy flux (NEF) at the substrate location.

Altogether, the development of Virtual Coater through this work enable the improvement of our knowledge of the interaction between plasma properties and thin films quality. This proposed new simulation procedure paved the way to new methods of studying the plasma state as a deposition process.

1 Introduction

Materials science is a broad interdisciplinary field, which gathers the study of the structure and properties of material, the creation of new types of materials, and the tuning of materials properties to suit the needs of specific applications. One of the foundations of material science is to tailor the performance of a material to fit with the desired properties and relative performance for a given application. The physical properties of materials usually play an important role in the selection of materials for a particular application. This involves many factors such as material composition and structure, fracture and stress analysis, conductivity, optical, and thermal properties, to name a few. It also involves design, modelling, simulation, processing, and production methods. Nowadays, one of the current pillars towards the creation of new materials are thin films. Thin film technology has become a sophisticated and advanced technology used in various fields. Surface engineering using thin film technology generates a new class of materials at the nanoscale, which exhibit functional alteration of the material bulk properties. By definition, thin films are material layers with thickness ranging from a few nanometres (10^{-9} m) to a few micrometres (10^{-6} m). They are already used in a wide range of applications in today's world. Indeed, coated materials enable to combine the benefits of two or more materials involved, i.e., the substrate and one or more coating layers. These composite materials have characteristics which are not available in bulk materials. In this way, the surface properties of bulk materials are usefully altered by the deposited coatings according to the requirements such as wear, corrosion and fatigue resistance, biocompatibility, self-cleaning and anti-bacterial properties, solar cell applications, decorative coatings, … The properties of the deposited coatings depend on the substrate, the deposition process and the material(s) used. To get the best success in designing coatings for special applications, it is then necessary to know which parameters predominantly influence their properties. It is thus of great interest to study the relationships between processing, structure and material properties.

Film deposition can be carried out by several deposition techniques. They are usually sorted out in two major families of processes, namely chemical deposition and physical

deposition. However, for the present work, it is more convenient to use two different major families i.e., wet and dry deposition techniques (see Figure 1).

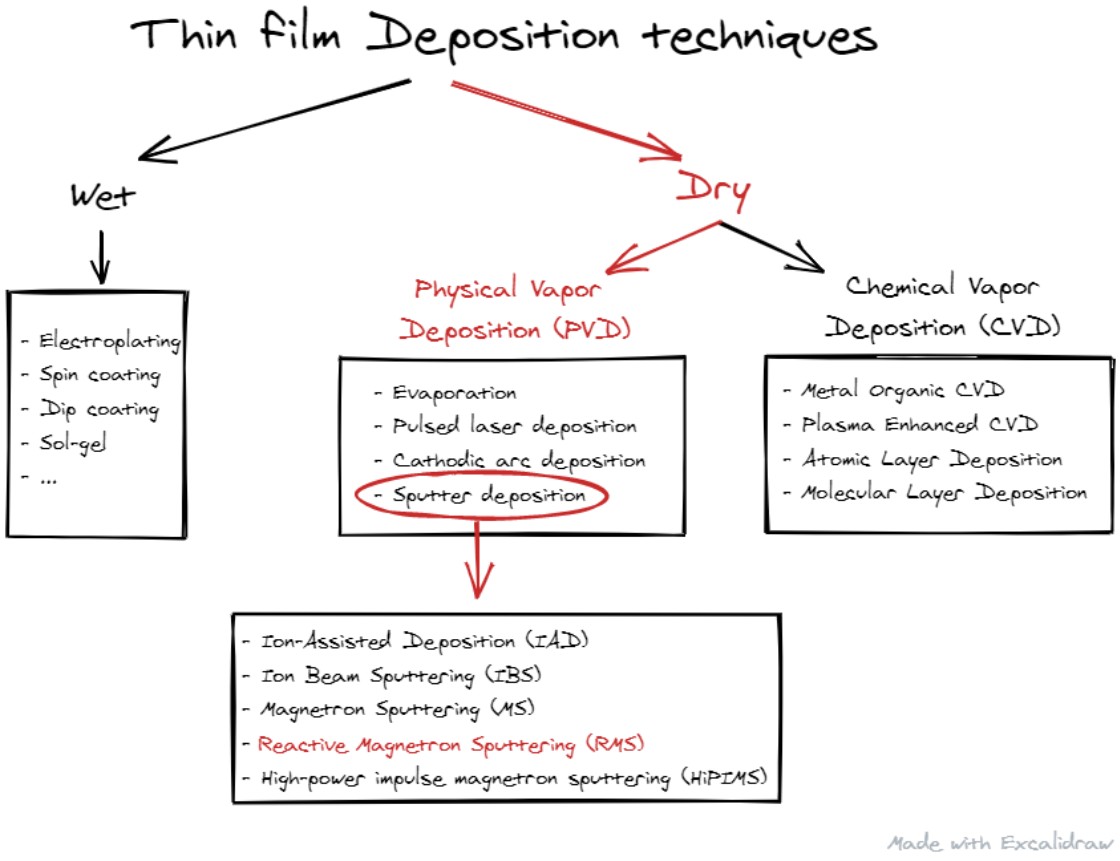

Figure 1 *Classification of the main thin film deposition techniques*

The wet family groups all the techniques where the surface to be coated is in contact with a fluid precursor undergoing chemical reactions at the substrate's surface and generating a solid layer. These techniques comprise plating, chemical solution deposition, spin coating, dip coating, sol-gel... to name a few. As opposed to wet deposition, the dry deposition family groups techniques in which the coating material is used in a vapor phase. These techniques enable a better control on the coating composition, as it can operate under vacuum, which limits the amount of impurity. Dry deposition techniques can be sub-categorized in two main groups. On the one hand, the chemical vapor deposition (CVD) techniques group processes in which the precursor gases containing the source material are introduced in a reactor and come into contact with the substrate. Near or at the surface, many heterogeneous chemical reactions take place (decomposition, reduction, desorption, polymerization, etc.) induced by heat, plasma or ultraviolet light, and their products progressively form a

stable solid film [1–3] . On the other hand, the physical vapor deposition (PVD) processes can be defined as “atomistic deposition processes in which the material is vaporized from a solid or liquid source in the form of atoms or molecules, transported in the form of a vapor through a vacuum or low-pressure gaseous environment to the substrate where it condenses” [4]. Depending on the vaporization procedure, PVD’s are also subcategorized by heating (evaporation) or ion bombardment (sputtering) of a liquid or solid source material. Both the vapor transport from the source material to the substrate and the deposition process (vapor condensation) take place by physical means, no or few chemical reactions are involved. Basic conceptual drawings are pictured in Figure 2:

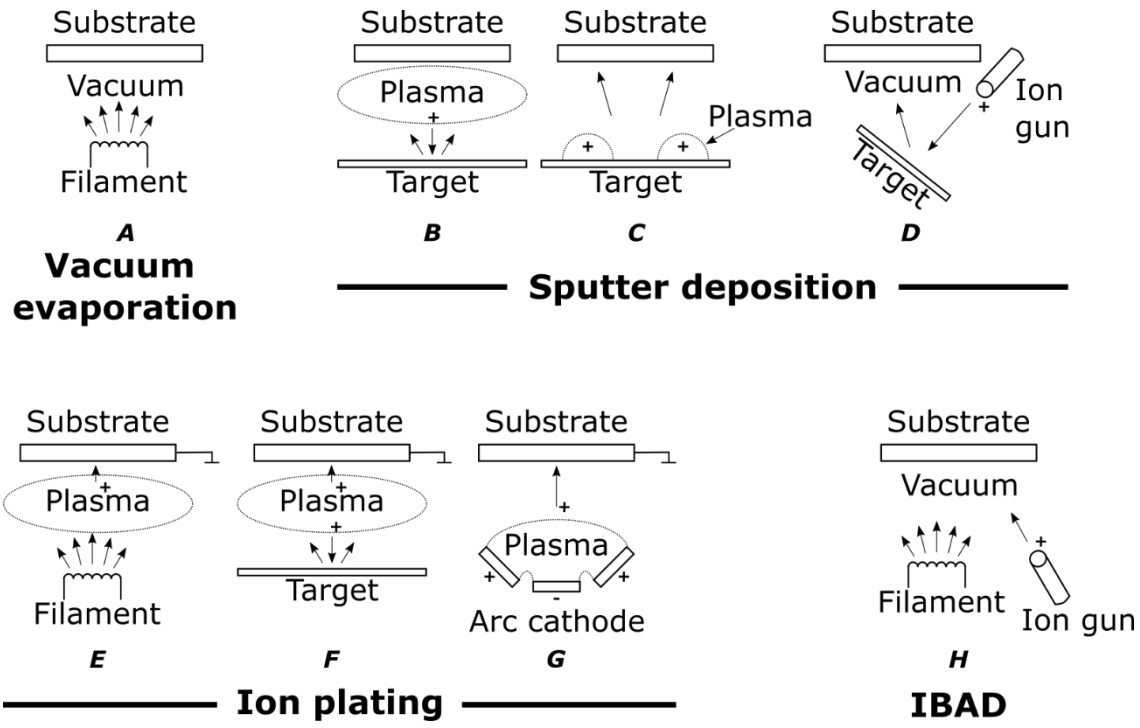

Figure 2 *A vacuum evaporation, B plasma sputter deposition, C magnetron sputtering, D ion beam sputtering, E ion plating with evaporation source in plasma environment, F ion plating with sputter source, G ion plating with arc vaporization source, H Ion Beam Assisted Deposition (IBAD) with evaporation source [4]*

In the particular case of reactive PVD, widely used to deposit compounds, there is a combination of both chemical and physical deposition. The precursors originate from a metallic target and decompose a reactive gas (using thermal decomposition, pyrolysis, plasma, etc.). PVD processes (and CVD in some cases) are carried out at low pressure (below atmospheric pressure) and even in vacuum, offering an efficient use of high-performance source materials and a reduction of contaminants and power consumption. Magnetically assisted PVD techniques arise from the need to reduce the

working pressure in order to produce coatings with as low as possible contaminants. Due to physical limitations to ignite and sustain the plasma, a minimal pressure is required (several tens of mTorr). These limitations can be overcome by using an additional magnetic field near the target, enabling the sputtering system to work at a lower pressure.

Generally speaking, PVD's are extremely versatile processes, enabling deposition of any metal, alloy or compound or their mixtures as well as some organic materials. In this regard, the PVD processes are superior to any other deposition process. Additional benefits against CVD and wet processes arise from the possibility to vary the substrate orientation and substrate temperature within very wide limits, from sub-zero to high temperatures. Thus, knowing the interrelations between processing, structure and properties of materials is of paramount importance. Predominant deposition parameters, which affect the properties of PVD coatings are:

- Background pressure.
- Background gas composition.
- Mass, energy, direction and relative flux of each species bombarding the growing film.
- Deposition rate and composition of the coating
- Substrate material (composition, surface roughness, cleanliness, crystallographic. structure…).
- Substrate temperature.
- Substrate orientation and/or substrate relative motion to target(s).
- Substrate electric potential (grounded, floating, positively/negatively charged).

Amongst PVD processes, magnetron sputtering (MS) is one of the most common technique used to deposit high quality and uniform thin films. The sputtering process involves the bombardment of high energy plasma ions on the surface of sputtering metal, which cause to dislodge a physical target atom to vaporize and then condense into a thin film of the target material [5]. The sputtering process is schematized in Figure 3.

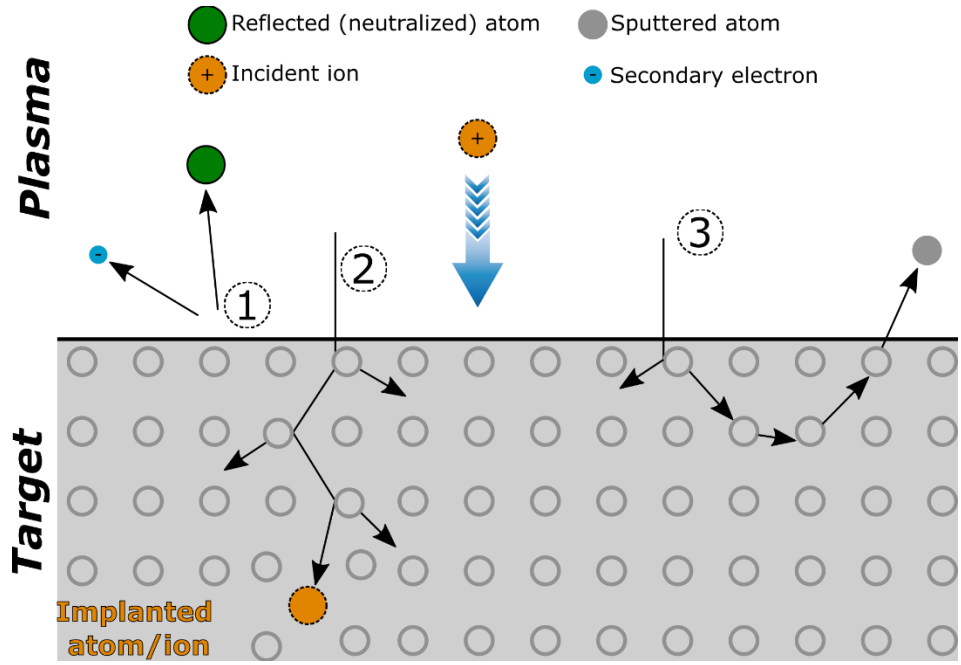

Figure 3 *Schematic drawing of the sputtering process, adapted from [6]. The three numbered processes which may happens, depending on the ion's energy, 1: ion reflection and neutralization, 2: implantation, 3: sputtering. Secondary electron emission may occur during in any of these 3 processes.*

Incident gas ions (such as Ar^+) impinging the target produce sputtered species and can be reflected from the surface as neutrals through elastic collision effects. In addition, secondary electron emission, photon emission and the heating of the target surface may result from inelastic processes. Since the incident ions lead to collision cascades in the target, the energy transferred to the target atoms can be high enough to overcome the potential binding (U_0) of the surface, and if the momentum is directed outward from the surface, they will escape into the gas phase. The sputtering process is only possible when the energy of the arriving particles is much higher than the surface binding potential. More information about the sputtering process can be found in Chapter 5 of this thesis.

Nowadays, magnetron sputter deposition has become the established technique of choice for the deposition of a large variety of industrially important thin films. Coatings based on metals, oxides, nitrides, carbides or composites with unique mechanical, electrical, optical and other properties can be prepared by magnetron sputtering. This deposition technique has many other advantages [7] such as:

- High deposition rate
- High purity films
- Extremely high adhesion of films
- Excellent coverage of steps and small surface features
- Ability to coat heat-sensitive substrates
- Ease of automation
- Possibility of good process control and long-term stability.
- Excellent uniformity on large-area substrates
- Relatively cheap deposition process.

For all these reasons, MS processes have been widely investigated over the years. However, several experimental techniques can only be carried out at limited locations in the discharge, and certain characteristics are difficult to measure, or cannot be measured at all. Usual investigation techniques, such as Langmuir probe measurements, disturb the discharge. Although MS can be easily applied at an industrial scale, adapting experimental procedures developed in a research-size coater to production usually requires several more months of work, through tedious trial and error, to reproduce the same coating properties. It is because the relationships between the experimental parameters and the internal parameters of the process are not straightforward. It is generally difficult to predict the film properties or the thickness profile from experimental parameters, and many repetitions of the experiments are necessary to optimize such conditions.

2 Aims of the thesis

The subject of this PhD thesis is to design and validate *Virtual Coater*[TM1]. The concept of *Virtual Coater* is to provide an efficient and versatile suite of tools able to predict the properties of thin films depending on the deposition techniques and the deposition conditions. Therefore, the *Virtual Coater* would not only enable to simulate the entire deposition process, but it would also help to deeper understand the interplay between the deposition parameters and the film properties. The schematic illustration of the concept is displayed in Figure 4.

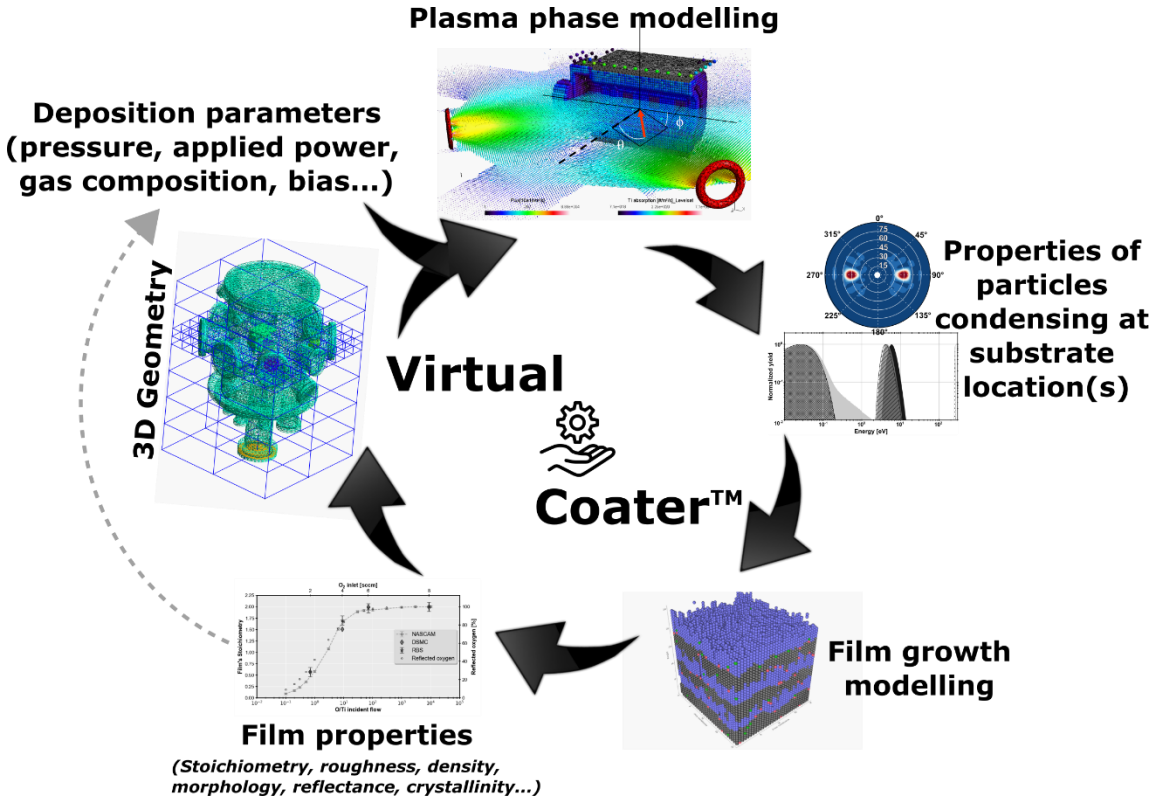

Figure 4 *Schematic representation of the Virtual Coater concept*

Today's scientific literature contains many examples of simulation tools dedicated to the various steps of a deposition process but none of them is able to close the loop of

[1] Trademark of the University of Namur

the 3D process. The main reasons are the time and space scales involved, see Figure 5.

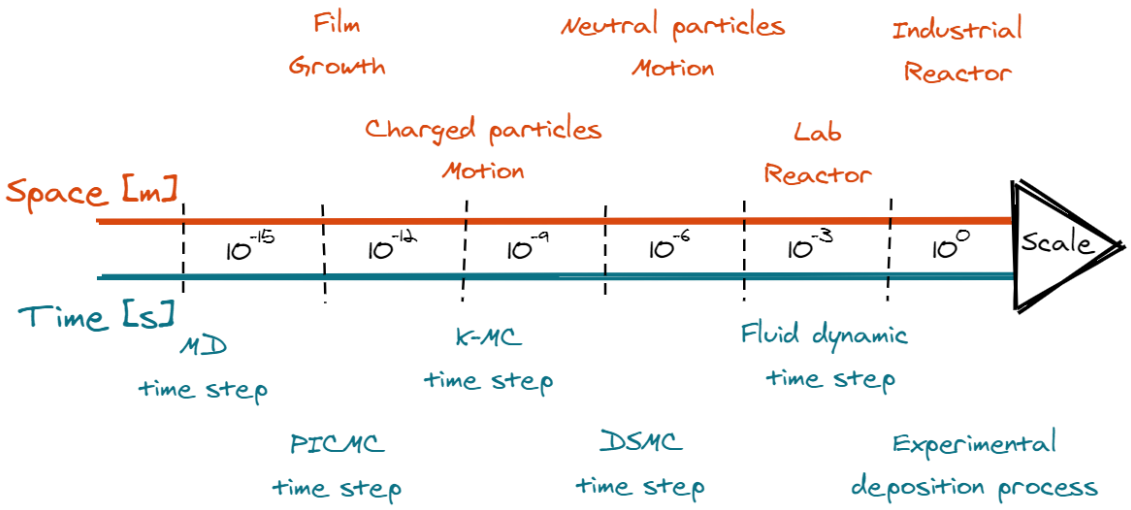

Figure 5 *Typical space and time scales of processes involved in a Virtual Coater*

On the one hand, the gas phase and particles transport of PVD's processes can be accurately simulated using either the binary collision Monte Carlo, direct simulation Monte-Carlo (DSMC), fluid dynamic or particle-in-cell Monte Carlo (PICMC) algorithms. The timescale of the involved physical phenomena is the order of magnitude of 1 s, while the space scale is the order of 10^{-2} m for a lab-scale coater. Some difficulties already arise at this step because when charged particles are involved, the time resolution needed to correctly compute their trajectories is in the order of a pico-second (10^{-12} s). On the second hand, once the production and the transport of coating material through the gas phase is computed, the film growth can be handled. Several modelling strategies already exist to simulate this last step. The main ones are the molecular dynamic (MD) and the kinetic Monte Carlo (kMC) approaches. Either way, the algorithm has to deal with atom deposition. The space scale is therefore the atomic size i.e., 10^{-9} m and the involved time scale varies depending on the algorithm: for MD and kMC the time resolutions are respectively in the range of 10^{-15} s and 10^{-8} s. Hence, there is no single simulation technique able to simulate the full coating process from coating material generation to film properties. Consequently, several simulation techniques have to be combined into a multiple scale model, whereby each method within the simulation chain is dedicated to a specific problem.

This PhD thesis aims to demonstrate how one can combine multiscale approaches by using DSMC/PICMC techniques and the kMC algorithm in a Virtual Coater (VC). The VC is applied to the growth of TiO_2 by a reactive dual-magnetron sputtering process. In order to validate the VC, experimental characterization of both the plasma phase and the deposited coating is performed and compared to the predictions of the VC. The reason of the selected case study, i.e., TiO_2, is threefold. First, TiO_2 coatings are still scientifically and industrially very interesting due to the many applications of the material and the relatively high abundance of titanium on Earth. Second, the growth of titanium dioxide is already very well documented, providing a well-established scientific background to rely on. Third, even though it is well documented, the growth of TiO_2 by magnetron sputtering techniques still offers challenges. For example, it is now admitted for 20 years that during the growth of TiO_2 by reactive magnetron sputtering, a flux of negative ions, O^-, is generated at the target surface and then bombards the growing film at sufficiently high energy to induce damages. This flux of negative oxygen ions, was experimentally evidenced for the growth of oxide by RMS but there is a lack of modelling work regarding the impact of this flux on both the plasma phase and the coating properties.

The present dissertation is divided in five sections:

(1) Current state of the art

Brief introduction and explanation of the main theoretical scientific knowledge involved in this study i.e., TiO_2 as a material, plasma physics, magnetron sputtering, growth of thin film and the existing approaches to model these phenomena.

(2) Designing the Virtual Coater

The aim of this section is to introduce the Virtual Coater concept with more details i.e., which algorithms are involved in its design and how they are nested together in order to produce a coherent simulation workflow.

(3) The role of neutral particles

First iteration over the Virtual Coater loop by considering only neutral particles. This section is the demonstration of the feasibility of the Virtual Coater concept.

The hysteresis behaviour and gas phase composition evolution are compared as experimentally measured and predicted by the Virtual Coater. Also, $TiO_{x\leq 2}$ coatings are experimentally produced and characterized. The morphology and the stoichiometry of the films are reproduced and explained by the multiscale simulation chain.

(4) The challenges of charged particles modelling

In order to simulate a plasma process, it is paramount to include charged particles in the *Virtual Coater* loop. This section explains the challenges and the compromises one has to make by adding charged particles into the plasma phase modelling part of the simulation chain. Solutions about the possibility to overcome some of the constraints imposed by charged particles simulation are proposed and discussed.

(5) The role of charged particles

Second and last iteration over the *Virtual Coater* loop. The same conditions as the first iteration are used and charged particles are added to the process. Their role during the film growth is therefore highlighted with both experimental characterization of the plasma phase and the deposited coatings.

3 Current state of the art

3.1. Plasmas

Plasma is the fourth state of matter. It consists of a mixture of ions, electrons and neutrals species, which is characterized by a common charged particle density of electrons (η_e) and ions (η_i), $\eta_e \approx \eta_i$ particles per m^3. They are obtained by adding sufficient energy into a gas, enabling it to become partly or fully ionized. Several processes can be used to supply energy and the most common ones are the use of electrical fields, chemical reactions or heat. The supplied energy is converted into kinetic energy or as internal energy excitation of the plasma species. The plasma state is considered as the fourth state of matter and is the most common state of matter in the Universe. Stars and stellar winds are the most famous examples. Plasmas are also abundant on Earth e.g., lightning, neon signs, aurora borealis and flames. Dr. Irving Langmuir was the first to use the term plasma to define this state of matter [8] in 1928. Since then, plasma science has seen a rapid development and became the core of numerous technologies in industry, which led to applications in a wide field of applications such as automotive, decontamination, microelectronics, medicine, glass industry, jewellery and gas conversion to cite a few. The major property of plasmas is their non-equilibrium nature with various temperatures for the species composing it. As the temperature is the manifestation of thermal energy, which, in the case of gas, can be assumed proportional to the kinetic energy of particles, different temperatures mean a different kinetic energy for different species. It opens up a multitude of reaction pathways, which are inaccessible to conventional methods in chemistry.

Usually, plasmas are subcategorized in two groups, low and high temperature plasmas, where the notion of temperature is related to the electrons. High temperature plasmas are used for nuclear fusion of hydrogen isotopes to generate energy with temperatures reaching millions of Kelvin (>100 eV). The natural appearance of theses plasmas are the stars. In this dissertation, only low temperature plasmas are considered i.e., with electron temperatures in the range of a few electron volts. Even if such temperature is classified as low temperature, it is sufficient to trigger the dissociation of molecules, or the excitation and ionization of species by electron impact. The heavy species temperature is often close to room temperature (26 meV). A low temperature plasma is often generated by applying an electric field to a gas

between two or more electrodes. A gas always has some free electrons (due, for example, to cosmic radiation), which will be accelerated when applying a voltage. When a certain threshold voltage (called the breakdown voltage) is reached, the plasma ignites. The breakdown voltage depends on the gas pressure and the distance between the two electrodes, which is a rule known as Paschen's law. The ignition occurs in the following stages: the accelerated electrons in the gap between the electrodes cause a sharp increase in the current flow. They collide with the gas atoms/molecules and cause them to excite, dissociate, ionize… The main and typical processes that occur in a plasma, starting from the ignition, are shown in Table 1.

Table 1*Typical processes occurring in low temperature plasmas.*

Reactions with electrons as reactant			
Momentum transfer	$e^- + A$	$\rightarrow$	$e^- + A$
Excitation	$e^- + A$	$\rightarrow$	$A^* + e^-$
Dissociation	$e^- + A_2$	$\rightarrow$	$2A + e^-$
Attachment	$e^- + A$	$\rightarrow$	A^-
Dissociative attachment	$e^- + A_2$	$\rightarrow$	$A^- + A$
Ionization	$e^- + A$	$\rightarrow$	$A^+ + 2e^-$
Dissociative ionization	$e^- + A_2$	$\rightarrow$	$A^+ + A + 2e^-$
Dissociative recombination	$e^- + A_2^+$	$\rightarrow$	$A + A$
Detachment	$e^- + A_2^-$	$\rightarrow$	$A_2 + 2e^-$
Reactions between atoms or molecules			
Momentum transfer	$A + B$	$\rightarrow$	$A + B$
Penning dissociation	$A_2 + B^*$	$\rightarrow$	$2A + B$
Penning ionization	$A + B^*$	$\rightarrow$	$A^+ + B + e^-$
Charge transfer	$A + B^-$	$\rightarrow$	$A^- + B$

Besides the species shown in this table, photons are also present in the plasma. The photons are generated by the de-excitation of excited molecules or atoms. For electronically excited species, an electron is excited and can thus be found in a high energy orbital, further away from the nucleus, leaving a hole in the lower orbital. Since this state is metastable, the molecule or atom can spontaneously return to the ground state, releasing the excess energy as a photon. Since many excited species exist in

the plasma, many photons can be formed, therefore giving plasmas a visible glow, depending on the energy level of the excited species. The number of ions produced in a plasma is defined by the degree of ionization, which indicates the ratio of the density of charged particles to the density of neutral species. For most thin film deposition applications, the ionization degree is rather low, and lies typically below 1%. Not only ions and photons have their typical role in the plasma, other species also contribute in their own way. Electrons pass their initial energy on to the gas, creating reactive species through collisions. Gas heating takes place via vibrational excitation and subsequent vibrational-translational relaxation. The enhanced gas temperature may also contribute to accelerating chemical reactions. Synthesis of components often proceeds via ions and radicals, and they can react at temperatures lower than required for thermal processes. Hence, a plasma is a very reactive, complex mixture, which makes controlled and selective conversion very challenging and dependent on many different parameters. Depending on the intended outcome and application, different types of plasma can be applied, which differ according to the type of applied electric field, discharge type and the design of the reactor and will thus lead to different temperature profiles and different distributions of species.

3.2. Magnetron sputtering

The type of the most suitable plasma depends on the particular application and the required pressure range. Most commonly, the plasma is generated by applying an electrical field via 2 electrodes. Depending on the frequency of the electric fields, the plasma is correspondingly different due to the different inertia of electrons and ions. In addition, the charged particles can be manipulated/confined by using magnetic fields since they mainly follow the magnetic field lines. One may distinguish four different plasma types depending on the frequency of the applied electric fields used for plasma generation:

- *DC plasmas*: The plasma is ignited between two electrodes and a direct current flows through the system. The plasma density can be enhanced by combining a magnetic field as for example in magnetron plasmas.
- *AC plasmas (kHz)*: Those plasmas often have the same geometrical configuration as DC plasmas. However, in this case, the frequency of the electric field is low enough to enable electrons and ions to follow the oscillations. These plasmas are frequently used for high power and large-scale applications.
- *RF plasmas (MHz)*: In an RF plasma, the frequency of the electric field is in the range of radio waves. Only electrons can follow the oscillations of the electric field; the ions remain almost at rest. The advantage of these plasmas is that the current is dominated by displacement current rather than by conduction current. Therefore, non-conducting layers on the electrodes are possible, which is essential for plasma treatment of insulators.
- *Wave heated plasmas (GHz)*: In this case, the frequency of the electric field is so high that electrons can just follow the oscillations. At such frequency, the electromagnetic wave cannot penetrate completely into the plasma. However, by applying an additional magnetic field, resonant heating of the electrons becomes possible.

As the starting point of the use of *Virtual Coater*, this study is focused on the use of low temperature plasma as sputter deposition technology. Dual magnetron plasmas operating in DC mode are used.

Magnetron sputtering was invented and continuously improved in order to overcome low ionization efficiencies in the plasma, low deposition rates and high substrate heating effects in the sputtering process. Magnetron sputtering is based on the plasma confinement in front of the target in contact with the cathode, while the substrate works as an anode. The confinement is obtained by combining the electrical and magnetic fields in a high vacuum process. The magnetic fields, which are used in common sputtering systems, only affect the motion of electrons, whereas the ions are too massive and thus remain nearly unaffected [9]. The primary interaction between a moving charged particle and a magnetic field is to produce a force on the particle. The direction of the force is perpendicular to both the magnetic field and the moving direction. The purpose of using a magnetic field in a sputtering system is to use the electrons in a more efficient way, and cause them to produce more ionization. In a conventional glow discharge, electrons are soon lost by recombination at the walls [10]. The schematic view of standard magnetron process is illustrated in Figure 6.

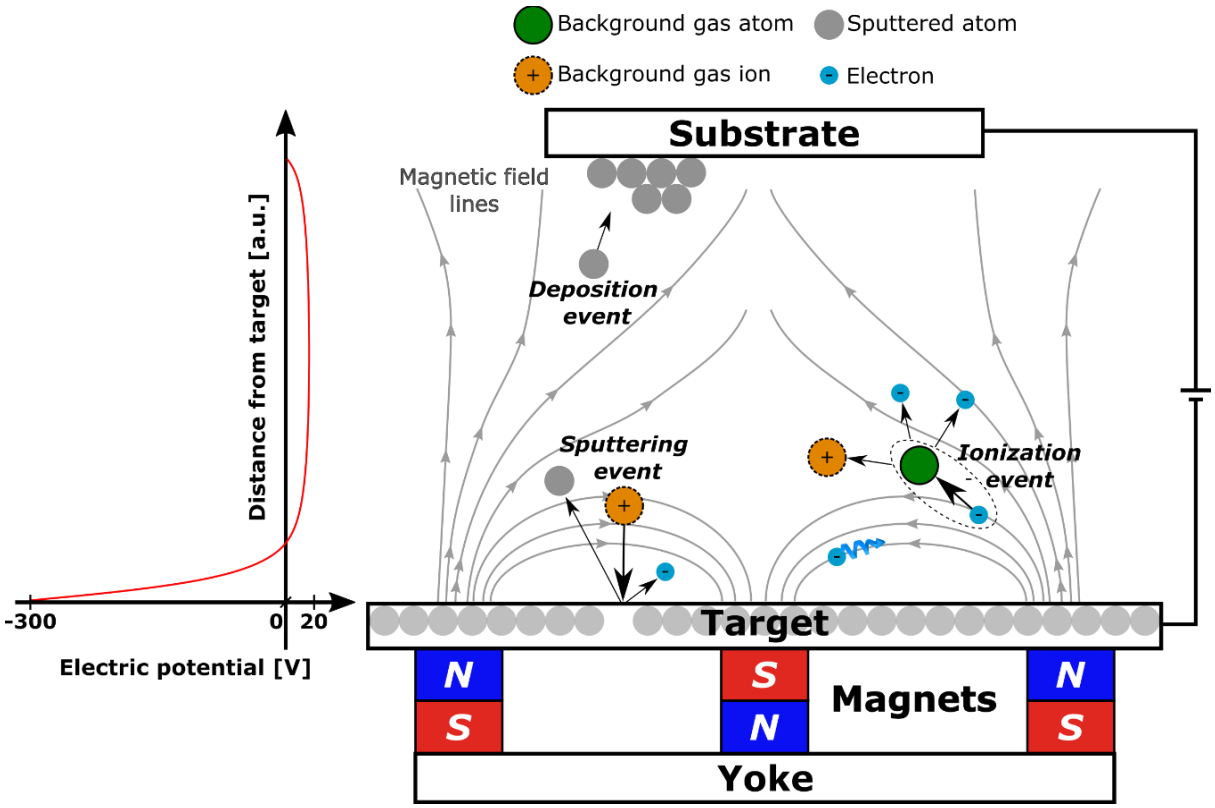

Figure 6 *Schematic drawing of a magnetron sputtering configuration. The typical evolution of the electric potential (red line) is drawn on the left-hand side. The target is supposed at -300 V and the substrate grounded.*

Due to the high energy transferring from impinging ions (such as Ar^+), the neutral atoms from the target are sputtered and escape into the gas phase to condense afterward to a thin film on the substrate. At the same time, emitted secondary electrons are trapped near the target surface due to the magnetic field generated by the magnets located behind the target. Therefore, the bombardment of the substrate with electrons, which induces the main cause of defects of deposited film, is strongly reduced. Moreover, ion density near the target surface is also enhanced as ionization occurs by electron impact collisions. Consequently, the target bombardment and film deposition efficiencies are improved. The potential distribution in the discharge determines the energies of the charged species involved in the deposition process. In DC magnetron sputtering (dcMS), only a small fraction of the sputtered atoms is ionized (~ 1%). When the sputtered flux consists of more ions than neutrals, $\Gamma_{M^+} > \Gamma_M$, the process is referred to as ionized physical vapor deposition (IPVD). For some applications, it is desirable to have a high ionization fraction of the sputtered flux, in particular for depositions of metal layers and diffusion barriers into trenches in integrated circuits (ICs) manufacturing. The sputtered flux is ionized and a substrate bias voltage can control the ion bombardment energy.

A conventional dcMS discharge operates at a pressure of 1-10 mTorr with a magnetic field strength of 10-50 mT and cathode potentials 300-700 V. At the target, the dissipated power by the large ion currents involved causes an increased heating of the target itself. Therefore, they are usually directly water-cooled.

Two single magnetrons can be combined into a dual configuration. Different reasons can be found for using this configuration. The most important application of a dual-magnetron configuration is related to materials research of complex materials. Indeed, to modify the stoichiometry in a flexible way, a dual-magnetron configuration is often chosen. By changing the target–substrate distance and/or the target power for both cathodes independently, a large range of compositions can be investigated [11–14]. This flexibility comes at a cost, especially in reactive magnetron sputtering. Indeed, both cathodes will react independently upon the addition of the reactive gas, resulting in possible target poisoning differences. An important issue in a dual-magnetron configuration is the magnetic field design. Two designs are possible, i.e., closed field and mirror field, see Figure 7.

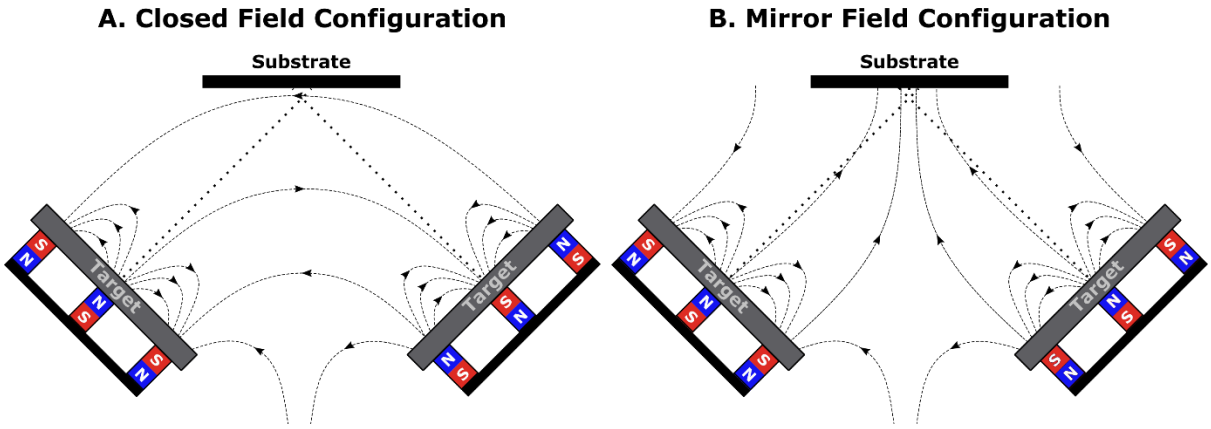

Figure 7 *Schematic view of the two possible configurations of a dual magnetron system. A: in closed field configuration, the two involved magnetrons have opposite magnetic configuration. B: in mirror field configuration, both magnetrons have the same magnetic configuration.*

In the mirror-field configuration, the magnets of both magnetrons are mounted in the same way. On the other hand, in the closed-field configuration, the magnets of both magnetrons are mounted in the opposite way, so that the field lines close in across the chamber. Electrons following these field lines can give rise to ionizing collisions and maintain a high plasma density near the substrate. In the mirror field, the electrons are directed towards the chamber walls, resulting in a lower plasma density. This was demonstrated by Musil and Baroch [15,16]. Therefore, the choice of the magnetic field design can have a strong influence on the thin film growth. The scientific literature contains a certain amount of experimental work on the plasma characterization of these configurations, but there is still a lack of a detailed description. As dual-magnetron configurations are becoming more popular in materials research of complex materials, there is a need to deeply investigate this configuration. Modelling can assist in understanding this configuration. However, almost no modelling on dual-magnetron configurations has been performed so far. Yusupov *et al.* [17,18] use a Monte Carlo model to simulate the motion of electrons in a dual magnetron configuration. In both magnetic configurations, they showed that electrons are created and then absorbed again at the target after one or several circulations around the magnetic field lines. For the closed field configuration, they showed that 12% of the generated electrons could travel from one magnetron region to the other at least one time. In the mirror field configuration, no crossing electron from one target to the other occurred because of the magnetic field. Melzig *et al.* [19] also studied the dual magnetron configuration with a 3D particle-in-cell Monte Carlo algorithm. However, they were only interested in the phenomenon occurring near the targets. Indeed, their

goal was to elucidate electron current constriction to the anode of the set-up and provide solutions to avoid them. Therefore, the scientific literature does not contain any modelling work involving both dual magnetron configuration and film growth. Moreover, none of the cited previous modelling work ever include the deposition of compound material by the introduction of reactive gas in the gas phase, e.g., O_2, C_2H_2 or N_2.

3.3. Reactive magnetron sputtering

The chemical composition of a sputtered film in an inert atmosphere is very close to the one of the target from which it was sputtered. Sputter deposition of compounds, like nitrides or oxides, can also be produced by various chemical reactions between the sputtered metallic target atoms (e.g., Ti, Cr) and a reactive gas introduced into the deposition chamber. The reactions to form the compound may occur either in the gas phase or on the solid surfaces, e.g., the target and substrate as well as the chamber walls. However, reaction probability between sputtered atoms and reactive gas atoms in the gas phase is very small because the collision cross-sections are small at the low gas pressures commonly used in magnetron sputtering. More over oxidation is an exothermic process and thus requires a three-body collision to occur in gas phase. In a low-pressure chamber, the probability of such reaction is very small and therefore solid surfaces play a major role in reactive deposition processes. Usually, the deposition rate decreases if the flow rate increases, and consequently the partial pressure of the reactive gas is increased. This is caused by the formation of a compound, which can fully cover the sputtering area at a certain reactive flow rate. The effect of this target poisoning on the reactive sputtering process depends on the specific combination between the metal and the reactive gas and the properties of the cathode surface of the formed compound layer. Thus, the compound is sputtered instead of the original target material. This will significantly change the discharge conditions and hence also the deposition process. The main reasons for this behaviour is the typically different sputtering as well as secondary electron emission yields of compounds compared to their pure targets [20]. A pronounced poisoning effect occurs for reactive sputtering in oxygen of materials such as Al, Cr, Ti, Ta, which form tenacious oxides. It is generally less for other reactive gases such as N_2 and C_2H_2 [21].

The addition of the reactive gas to the discharge influences the deposition process in several ways while increasing the complexity of the overall process. The addition or removal of a reactive gas from the discharge is generally achieved with a gas flow controller. A typical experiment, as shown in Figure 8, is to stepwise increase the reactive gas flow over a given interval, and wait between the steps until the process is stable, at what time some process parameters (pressure…) are recorded. After reaching a maximum flow, the reactive gas flow is decreased stepwise, and again one gives the system sufficient time to stabilize after each step. At a given reactive gas flow of 5.5 sccm (first critical point), there is an abrupt change in the total pressure.

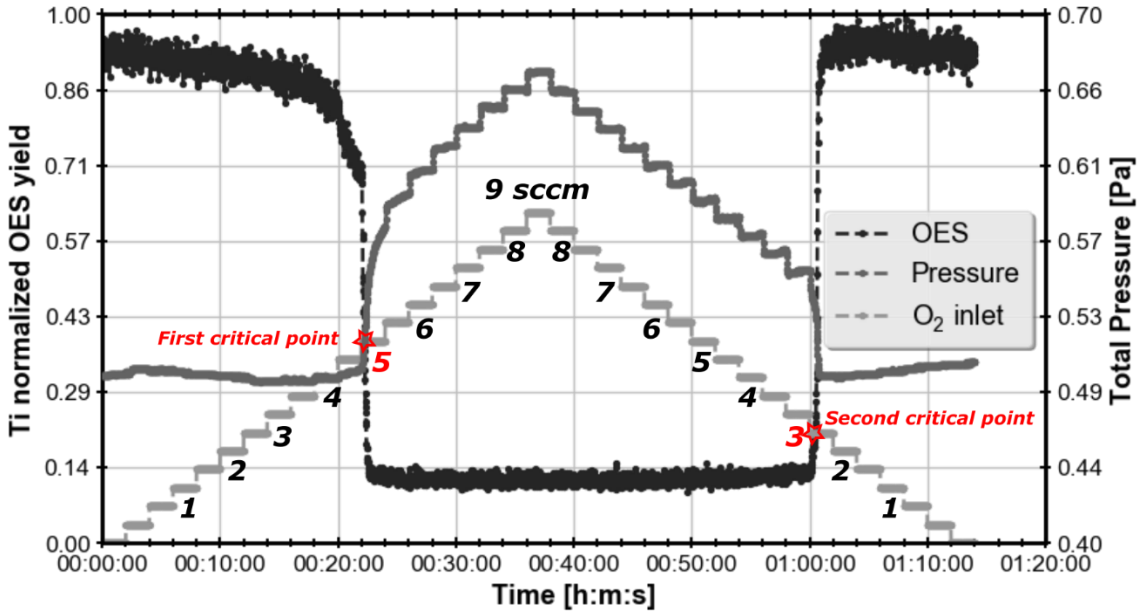

Figure 8 *Stepwise experiment of increasing and decreasing oxygen inlet in a dual magnetron system operating in DC mode with Ti targets. The black curve records the evolution of the Optical Emission Spectroscopy yield related to metallic Ti within the gas phase. The dark grey curve is the evolution of the total pressure as measured by a baratron gauge. The light grey curve is the oxygen inlet flow rate, corresponding values are written directly on the graph. For each oxygen inlet step, the discharge is kept constant for 2 minutes.*

One also notices that the reactive gas flow must be decreased to a much lower value than the first critical point detected to reach the second critical point, i.e., when the pressure abruptly decreases (3 sccm). Stated differently, there is a hysteresis in the total pressure due to reactive gas injection. The low oxygen flow region is defined as “metal mode”, and is characterized by a low reactive gas partial pressure and a high deposition rate. The high oxygen flow region is defined as the “compound mode”, or “poisoned mode”, with a high partial pressure and a low deposition rate. The deposited film is essentially a pure compound.

3.4. Film growth structure

Now that the basics of the plasma environment and magnetron configuration for reactive sputter deposition have been provided, the details of processes occurring during film growth can be elaborated upon.

When a flux of vapor atoms impinges onto a substrate, the angular and energy distributions of the flux plays a significant role in shaping the surface. The film growth can be divided into several stages: condensation of the vapor on the growing surface (adsorption), desorption (re-evaporation or reemission) from the surface, diffusion of the atoms, form atoms of stable nuclei, followed by the coalescence of the reacted material into islands, and then the formation of a continuous film. Those processes are illustrated in Figure 9.

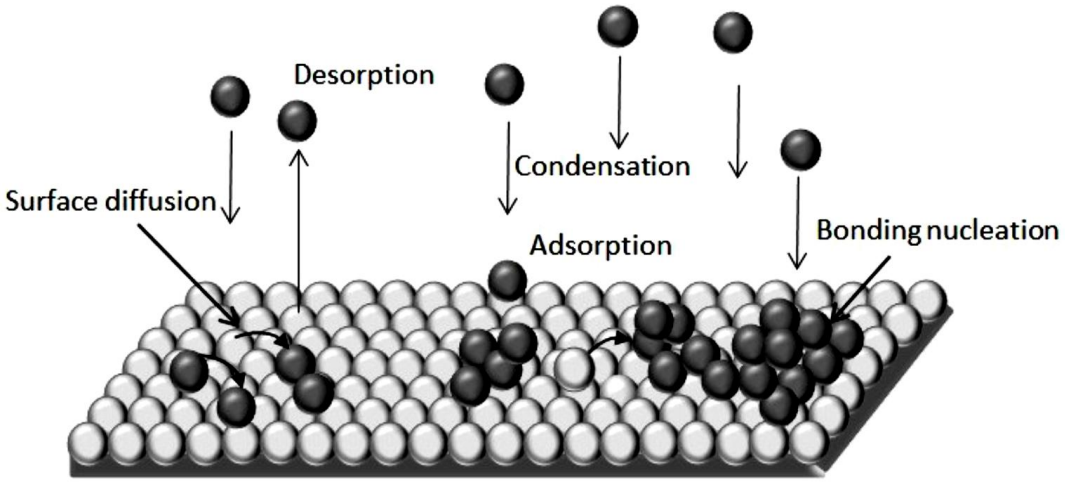

Figure 9 *Events occurring in a typical vapor-phase thin film growth process, reproduced from* [22].

The condensed atoms interact with the substrate surface either by van der Waals forces (physisorption, ≈ 0.25 eV), or by chemical bonding (chemisorption, ≈ 1~10 eV) either through ionic or covalent bonding [22]. Due to their own initial energy or by substrate-supplied energy or the energy they receive from the impinging particles, they might immediately desorb or diffuse over the surface. Obviously, the desorption barrier in the physisorption state is much lower than that of the chemisorption state. To describe the desorption process, a sticking coefficient, s, is defined. It is the probability for a particle to remain adsorbed and is the ratio between the particles that stick to the surface to the number of total impinging atoms upon that surface ($s \in [0,1]$). For very low temperature deposition, the sticking coefficient is usually very close to 1, indicating

no desorption. Through the thermal effects or the knock-on event of an energetic impinging particle, *s* will decrease. For the adatoms moving over the surface, atoms move between energy minima on the substrate surface and diffuse to a position with the lowest potential. The diffusion process might lead to adsorption, particularly at special sites like edges or other defects, or the diffusing particle may re-evaporate if the characteristic activation barrier is overcome. Both, diffusion and desorption, are local processes since both are thermally activated and determined by bonds to the nearest neighbours. In addition, due to the nature of some deposition process, the impinging atoms approach to substrate surface from different directions, e.g., because of scattering with background gases or oblique incidence. If the surface already has some degree of roughness, due to the geometrical shadowing, some of the incident atoms will be captured at high positions and may not reach the lower valleys of the surface. Then lower positions will be shadowed from the impinging flux by sites far from it, making the shadowing mechanism non-local. This process will result in an enhancement of the growth roughness.

The morphology of films and the primary factors that affect film morphology are illustrated in the structure zone model for sputter deposited films. It is also known as the Thornton model (Figure 10).

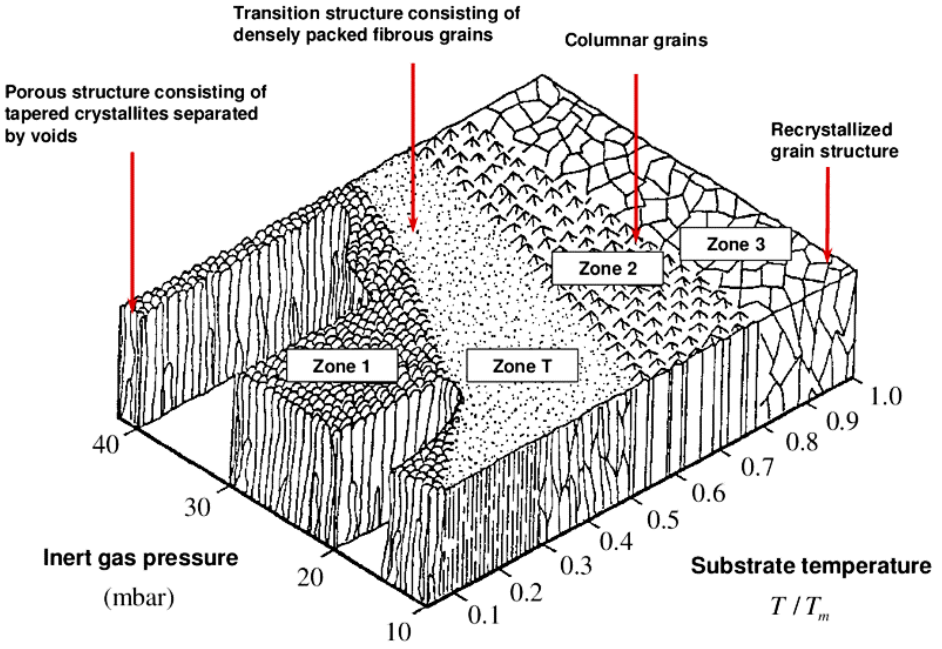

Figure 10 *Structure zone model or Thornton model for sputter deposition of material* [23]

Film morphology can be categorized in one of four growth regimes or modes. These growth modes are most heavily dependent on the working gas pressure and the ratio of substrate temperature to the melting temperature of the sputtered material. The four growth modes are named: Zone 1, Zone T, Zone 2, and Zone 3. These zones are each associated with conditions where the physics of coating growth is dominated by a particular mechanism [24]. The mechanisms for the respective zones are: (1) atomic shadowing during deposition, (2) surface diffusion and (3) bulk diffusion

Zone 1 structures (T_S/T_M <0.3 for metals and T_S/T_M <0.26 for oxides) are voided columns with domed tops due to self-shadowing effects and very limited adatom mobility at low temperature. The columns generally consist of amorphous-like structures. **Zone 2** structures (0.3<T_S/T_M <0.45 for metals and 0.26<T_S/T_M <0.45 for oxides) exhibit a dense columnar structure separated by grain boundaries. Surface and grain-boundary diffusion apparently becomes more important in the evolution of this structure, because the columnar grain size increases with T_S/T_M in accordance with the activation energies for these mass-transport mechanisms. In z**one 3**, (T_S/T_M>0.45 for metals and oxides) high recrystallization occurs, which is characterized by high, well-defined crystals of sputtered material. The thin film can switch from a columnar structure to a highly crystalline one, where the width of the crystals is higher than film thickness. **Zone T** is a transition zone between zones 1 and 2 characterized by a densified crystalline structure with small grains achieved by bombardment of the surface by high-energy neutral particles at low total pressure.

Generally, the boundaries between these three zones are diffuse and the transition from one zone to another occurs gradually over a relatively wide range in T_S/T_M. This simple model enables to predict the microstructure of the deposited films in dependence on two deposition parameters. An extended structure zone diagram, suggested by Anders, includes energetic deposition, characterized by a larger flux of ions [25], see Figure 11.

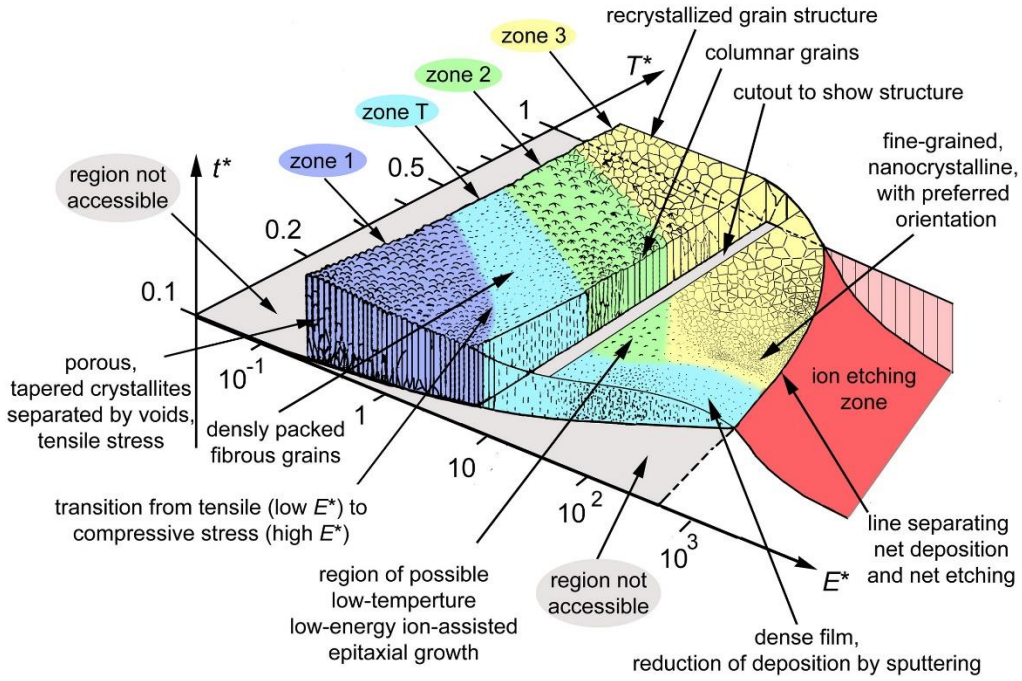

Figure 11 Extended structure zone diagram, reproduced from [25], applicable to thin film deposition in the presence of energetic particles fluxes.

The diagram shows the dependence of the film microstructure with (1) T^*, the generalized temperature, which is the temperature of the substrate plus a temperature shift caused by the potential energy of particles arriving on the surface; (2) E^*, the normalized kinetic energy of bombarding particles, replacing the linear pressure axis; the axis describes the displacement and heating effects caused by kinetic energy of bombarding particles; (3) t^*, the net film thickness, enabling the qualitative illustration of the film structure while indicating thickness reduction by densification and sputtering. It also allows to include a “negative thickness” zone related to ion etching. In addition to the 4 zones the Thornton’s diagram predicts other structures of growing films such as the fine-grained nanocrystalline structure or a possible zone of low-energy epitaxial growth.

3.5. Plasma modelling

In this section, methods for plasma deposition process modelling will be presented in order (1) to locate the present study amongst the scientific literature and (2) introduce and justify the modelling methods selected to build the *Virtual Coater*. At first, the discussion will be oriented towards the plasma/gas phase modelling possibilities. Secondly, the main methods for film growth modelling will be presented.

3.5.1. Gas phase modelling

Today's scientific literature contains several approaches for processing plasmas. Each of these approaches has its strengths, limitations and dedicated field of application.

Analytical models: analytical formulas describing the dependency of certain plasmas quantities from macroscopic parameters (voltage, current, pressure…). This method [26–30] can predict plasma properties very quickly. However, the results are only valid for a limited range of conditions and usually do not account for the involved geometry.

Fluid models: such models are based on the continuity equations of particle density, momentum and energy. These equations are coupled to Poisson's equation to calculate a self-consistent electric field distribution. Such a method is simple, fast and allows the use of complex 3D geometry, but has the major drawback to assumes that the plasma species are more or less in equilibrium with the electric field. Even though such assumption can be valid for high pressure process. At sufficiently low pressure, when the gas flow switches from laminar to molecular regime, fluid models are not valid anymore to describe the physics of the gas kinetics. It is the reason why modelling magnetron discharges with a fluid model is not so common, since they cannot simply be considered as a fluid. Furthermore, the complexity of the magnetic field makes a fluid model for magnetron discharges very inefficient [31].

Boltzmann transport equation: by solving this equation, the non-equilibrium behaviour of the plasma species is fully accounted for. Simulation models based on the solution of the Boltzmann kinetic equation are capable to calculate the electron energy distribution function and therefore give a self-consistent electric field distribution. However, the models become computationally too expensive, especially for calculations lasting for a longer time than a few collisions. Moreover, the coupling of Boltzmann equation to the Poisson's equation is a difficult numerical problem.

Direct Simulation Monte Carlo (DSMC): these kind of simulations [32], have the major advantage to be mathematically easy to implement and, as fluid modelling, can account for complex 3D geometries. They can also account for the non-equilibrium nature of the plasma. The Newton laws are used to compute the trajectories of the various species. The name, Monte Carlo, comes from the way the gas phase collisions are handled, by using a random number generator. In order to be statistically valid, a large number of individual particles need to be simulated. Therefore, DSMC simulations can be very time-consuming, especially when it comes to very short time steps to resolve fast moving particles mixed in with slow-moving particles. Unlike the fluid modelling approach, DSMC simulations are not self-consistent as the electric field distribution is required as input.

The DSMC method is the first of the two simulation techniques selected to deal with the plasma phase in the Virtual Coater. The low-pressure involved in the PVD processes does not enable the use of fluid modelling approach. DSMC's enabled the simulation of vacuum-based processes and also includes complex 3D geometry, which is essential for reactive deposition processes.

Particle-in-Cell Monte Carlo (PICMC): this method [19,33–35] is the evolution of the previous DSMC simulation. It couples the Poisson equation with DSMC simulation in order to include a self-consistent electric field distribution. For this purpose, the positions of the species are projected onto a grid, to obtain a charge density distribution, from which the electric field distribution can be calculated with the Poisson equation. This method is particularly well suited for low pressure processes where, in the case of plasma processes, high energy species are not in equilibrium with the electric field or when the plasma dynamics need to be detailed. The method is able to produce a wealth of data, such as cathode voltage and current, species densities, fluxes and energies, potential distribution, and information on the individual collisions in the plasma. This method shares the same drawback as DSMC simulations, as they can be very time consuming, limiting the simulation to short-term plasma chemistry evolution. In order to reduce the computational time, a number of so-called super-particles replace the real particles, with a weight corresponding to the number of real particles they represent. Nevertheless, calculation times can still rise to several weeks for describing magnetron discharges, certainly when attempts are made to include plasma chemistry description, such as for reactive sputter- deposition applications.

However, permanently evolving computational devices (fast computers) and methods (code parallelization) make these methods very attractive nowadays. Therefore, the PICMC method is the second brick composing the plasma phase part of the Virtual Coater. Indeed, PICMC appears as the legitimate partner of the DSMC method. It enables self-consistent electric field distribution coupled with a complex 3D geometry, which is crucial for the charged particles motion.

Hybrid models: by combining two or more of the presented modelling approaches, one can efficiently benefit from the many advantages of several models, while overcoming the limitations of the single model approach [36]. For instance, the MC and fluid models can be combined together. The MC model for energetic plasma species and the fluid model for slow species assumed to be in thermal equilibrium.

3.5.2. Film growth modelling

Film growth modelling is the dedicated simulation of the plasma-wall interactions at substrate location i.e., the simulation of the processes taking place during thin film deposition. Clearly, the choice of the method depends on the desired outcome. According to the current scientific literature, there are three major simulation techniques suitable for simulation.

Quantum-based simulations: including the *ab-initio* density functional theory (DFT) and tight-binding methodologies. It is the most accurate type of simulation. The calculations are based on quantum-mechanical ideas and theoretical considerations instead of empirical fits like in classical molecular dynamic. The advantage of *ab-initio* calculations is their accuracy, and the possibility to calculate electronic quantities, such as density of states. Their main disadvantage is the computational cost. The most efficient DFT codes can usually only handle a few hundreds of atoms.

Molecular dynamics (MD): In a molecular dynamic simulation, atoms are treated classically (Newton's laws), using empirical potential energy functions to determine the forces between the atoms. Molecular dynamic simulations are less accurate compared to *ab-initio* simulations, but enables the simulation of thousands of atoms. However, an important drawback of MD simulations is the limited physical time and length scales that can be simulated.

Kinetic Monte Carlo (kMC): This is another important technique to simulate thin films and thin film growth on longer time and length scales. In this technique, atoms are moved according to some probability over a lattice, according to the energy calculated from a specified interatomic potential. Usually, a list of all the possible transitions (atomic moves) needs to be available in advance. Because kMC does not take into account the atoms vibration movement, it is possible to use kMC to model the evolution of the system for a longer period of time. This last argument is the main reason why this technique is selected to be part of the Virtual Coater. Indeed, if one wants to be able to compute the major properties of a coating based on simulation results, it is crucial to simulate the deposition of a large enough number of atoms.

3.6. Experimental characterization techniques

This section presents the main characterization techniques used during the thesis. The purpose is to refresh the reader with the main operating principles and measurements outputs. Literature contains very detailed references for each, to which the reader can refer to, should he wish to have more details. The followings techniques are sorted in two categories: *in situ* (i.e., in the plasma chamber) and *ex situ* (i.e., measurement performed outside of the plasma chamber).

3.6.1. *In Situ* techniques

❖ Mass spectrometry (MS)

Mass spectrometry is a diagnostic technique capable of measuring neutral species as well as positive and negative ions. A mass spectrometer is a multi-species ion beam detector able to separate and quantitatively detect the various charge and mass of the primary beam. Separation is achieved based on different trajectories of moving ions with different mass/charge (m/z) ratios in electrical and/or magnetic fields. For neutral species measurement, the mass spectrometer uses an ionization chamber in which an energetic electron beam is used to ionize the neutral gaseous species and feed the mass spectrometer with the produced ions.

Mass spectrometry is a very wide and complex field; many books and PhD theses are dedicated to this technique [37,38]. A Hiden Analytical HAL 301 mass spectrometer was used for this thesis.

❖ Optical emission spectroscopy (OES)

Spectroscopic optical methods for plasma diagnostics are the least intrusive methods, and they record the emitted, absorbed or dispersed radiation [39]. This technique is non-invasive, easy to implement and measurements are fast. The OES method used in this thesis is passive and based on recording the light emitted from the plasma. Through collisions of plasma particles with electrons, the plasma particles are excited to higher electronic states. The relaxation of excited particles, which are present in the chamber to lower energy states, is the origin of the emitted photons. Since the energy of a transition is a characteristic of the particle species, the analysis of the photon energy can reveal the composition of the plasma, which can in turn be correlated with the physico-chemical characteristics of the deposited coating. Time and spatial monitoring of the plasma can also be performed with this technique, as well as the determination of the electron temperature and energy distribution. Furthermore, OES can also be used as a control tool to regulate a process. In the present work, the used OES is embedded in a regulation system, FloTron^{TM} from Nova Fabrica Ltd, controlling the oxygen mass flow, enabling feedback regulation control based on the optical emission signal of Ti.

❖ Langmuir probe

The Langmuir probe method is one of the oldest and still one of the most useful tools for diagnosing a plasma. Langmuir (1926) and Druyvesteyn (1930) were the first to study the relation between the second derivative of the electron current collected by a biased probe and the electron energy distribution function (EEDF). The Langmuir probe, usually in the form of a tip, is placed inside the discharge and biased positively or negatively to draw electron or ion current, respectively. The relationship between the voltage applied to the Langmuir probe and the collected current is referred to as the I-V characteristic. From the Langmuir probe I-V characteristic, the parameters describing the energy of the electrons in the plasma can be found among other plasma parameters such as the plasma potential and the floating potential. For a negative voltage on the probe below the floating potential V_F, ions are drawn to the probe. For

applied voltages higher than the plasma potential V_P, only electrons are drawn to the probe. In this work, an EPSION Langmuir probe from Hiden Analytical was used. The probe is biased to a voltage V_{probe}, which is in the range from -30 to 15 V, with respect to ground (chamber wall). The plasma is at a potential V_P with respect to ground. For $V_{probe} < V_P$ the electrons are repelled according to the Boltzmann relation, until V_F where the probe is sufficiently negative with respect to the plasma, that the electron and ion current are equal. For $V_P < V_{probe} \leq V_F$, the ion contribution of the current increases, tending to an ion saturation current that may also vary with voltage due to the change of the effective collection area around the probe. The magnitude of the ion saturation current is much smaller than the electron saturation current due to the much greater mass of the ions. The ions will move much slower than the electrons, meaning that fewer ions will reach the Langmuir probe at a given time resulting in a lower ion saturation current, while electrons are faster and more charge reaches the probes and gives a higher electron saturation current. The floating potential V_F is defined as the potential where the ion and electron currents to the probe are equal, in other words when the total current is zero. Therefore, the floating potential is the potential at which an insulated probe, which cannot draw current, will charge. More details about the various probe setups and the data analysis can be found in [40–42].

❖ Active thermal probe (ATP)

Almost all plasma-technological applications are based on plasma/surfaces interactions. An excellent tool for process diagnosis is the thermal probe, which measures the energy input from the plasma into the substrate. Usually, passive probes are used for this kind of measurement [43,44] but their disadvantage is the thermal inertia which requires to interrupt the energy influx by shutting down the energy source or by using suited apertures. Hence, these probes are not suitable for a continuous process control. The present work uses a continuously working active probe [45], from Neoplas Control GmbH, which does not need to be calibrated and compensates the environmental effects as well as the heat conduction by the probe holder. The probe is set to a working temperature and then the energy supply supporting the working temperature is measured. The energy influx by external sources is compensated by decreasing the heating power. A typical measurement is shown in Figure 12.

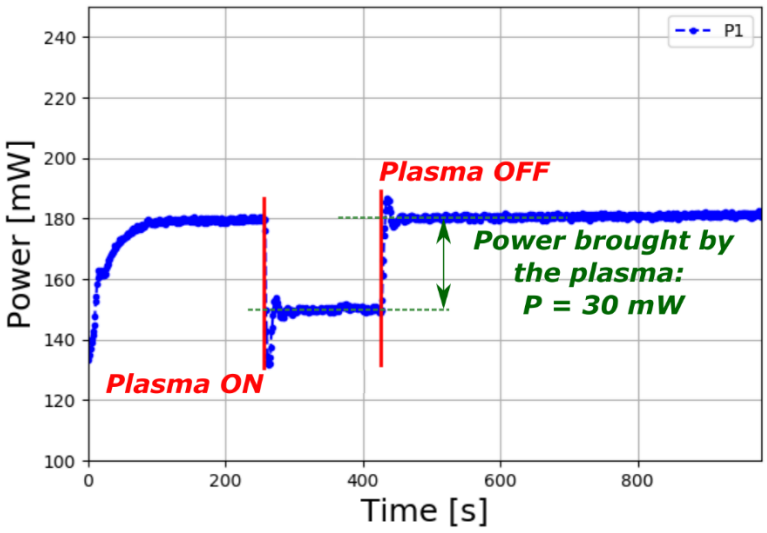

Figure 12 *Typical ATP measurement. The curve is the needed power to maintain the probe at 250 °C. The first drop corresponds to plasma ignition (250 s). The plasma is kept alive for 3 minutes and then turned off (430 s).*

This kind of investigation enables to probe the total energy influx towards the substrate location of a PVD system i.e., the probe sums up all types of energy components (radiations, surface chemical reactions, particles deposition…). It also opens up the opportunity to evaluate the normalized energy flux (NEF), i.e., the energy per deposited atom. This last quantity requires measuring the number of atoms deposited during a deposition process. The next presented characterization technique, Rutherford backscattering spectroscopy, enables such measurements.

3.6.2. *Ex Situ* techniques

❖ Rutherford backscattering spectroscopy (RBS)

RBS is a very powerful technique for quantitative analysis of the composition, thickness and depth distribution of elements in thin solid films or solid samples near the surface region with film thickness up to a few hundred nanometres. In RBS, a beam of monoenergetic ions, usually He of a few MeV, is directed at a target sample, and the energies of the ions which are scattered backwards by nuclei in the sample are measured and analysed. The higher the mass of an atom hit by an ion, the higher the energy of the ion will be after backscattering, which results in mass analysis. By counting the backscattered ions as a function of energy, the number of atoms of each element present can be determined. Besides mass information, depth information is gained via the energy loss of the projectile on its inward and outward paths through the sample. More info can be found in [46].

❖ Scanning electron microscopy (SEM)

SEM is a versatile and widely used tool as it enables the study of both morphology and composition of materials. A monochromatic electron beam is focused onto a fine probe scanned over a rectangular area of the sample. As the electrons collide with the surface, a number of interactions occur resulting in the emission of electrons and photons from the surface. The intensity of the secondary electrons is point-to-point mapped onto a detector which is synchronized with the electron beam scanning the sample. High-resolution images of the morphology or topography of a sample at very high magnifications can be obtained. In this work, a Hitachi S4800 SEM-FEG microscope from the Instituto de Ciencia de Materiales de Sevilla, Spain and a Jeol 7500F from the University of Namur were used. More details about the SEM can be found in [47].

❖ Atomic Force Microscopy (AFM)

AFM, also known as scanning force microscopy, is a technique with minimal sample preparation requirements. It is based on detection of the force interaction between a sample surface and a sharp tip mounted on a flexible cantilever, and produces, in such a way, topographic images of a surface with atomic resolution in all three dimensions. When the tip is brought to a close proximity (a few Å) of a sample's surface, repulsive Van der Waals forces between the atoms of the tip and those of the sample cause the cantilever to deflect. The deflection magnitude depends on the distance between the tip and the sample. For the present thesis, AFM images were recorded in air, in tapping mode with a Nanoscope III from Veeco Instruments (Santa Barbara, CA, USA). The cantilevers (Tap300Al-G from Budget Sensors) were silicon cantilevers with a resonance frequency around 300 kHz and a typical spring constant of around 40 N/m, and an integrated silicon tip with a nominal apex radius of curvature <10 nm. More information on the AFM technique can be found in [48].

❖ X-Ray diffraction (XRD)

X-ray diffraction (XRD) is the most common technique to identify the crystalline phases present in materials, and also to measure the structural properties such as the phases preferred orientation, crystallite size and defect structure. X-rays have wavelengths in the order of a few angstroms, the same as typical interatomic distances in crystalline solids. When certain geometric requirements are met, X-rays scattered from a crystalline solid can constructively interfere, producing a diffracted beam. The Bragg law gives the condition for constructive interference:

$$n\,\lambda = 2\,d\,sin(\theta)$$

where n is an integer, λ is the wavelength, d is described as the distance between planes of atoms that give rise to diffraction peaks , and θ is the diffraction angle. The diffracted beam intensity depends on several factors such as the chemical composition of the film and the local arrangement of the atoms. More information can be found in [49]. In this work a PANalytical X'Pert PRO diffractometer, Cu Kα 1.5406 Å, θ/2θ configuration was used.

3.7. The titanium dioxide as material

TiO_2 (titania) belongs to the group of transition metal oxides, and exists in both crystalline and amorphous forms. Titanium is the most abundant element on the earth's crust, with an estimated 0.62% [50]. TiO_2 is the only natural occurring oxide of titanium and crystallizes in three major different structures: rutile, anatase and brookite [51,52]. Anatase and brookite are the metastable phases whereas rutile is the most stable phase of TiO_2. Only anatase and rutile phases play an important role in most TiO_2applications because of the low stability of the brookite phase. The main properties of titania are [52]:

- High melting point T_m > 1850 °C
- Corrosion resistance
- Chemical stability
- Bio/Hemocompatibility

- High refractive index: 2.5 for anatase and up to 2.9 for the rutile
- High transparency for the visible spectrum
- Absorption of the UV spectrum
- Photoactivity induced by the UV irradiation – superhydrophilicity and photo catalytical decomposition

Titanium dioxide is therefore an industrially and technologically important material, as evidenced by its wide variety of applications. It is used in such fields as pigments, cosmetics, photocatalysis, solar cells, biomaterials and sensors. These diverse applications have derived from the unique properties exhibited by TiO_2 polymorphs. In particular, the anatase and rutile crystalline phases have been the subject of many studies aimed at improving the performance of titania in existing products or exploring the development of new applications. Because titania has the highest index of refraction of all oxides, the amorphous form is also technologically useful, especially in the manufacture of optical and photonic components.

Rutile

The rutile phase of TiO_2 is the most stable; it shows stability at all the temperatures and pressure up to 60 kBar. This phase shows small free energy as compared with anatase. TiO_2 rutile has a tetragonal structure. Each Ti atom is bounded to six O atoms with equatorial Ti-O bond length 1.946 Å. The lattice parameters for the rutile phase are a=b=4.583 Å, c=2.958 Å. Due to its stability at high temperatures, rutile is used as a protective coating or in microelectronics.

Anatase

The anatase phase of TiO_2 has the same tetragonal crystalline structure as the rutile, but it shows slightly more distortion of the TiO_6 octahedron. The lattice parameter for anatase TiO_2 are a=b=3.784 Å, c=9.502 Å with equatorial and apical bond length of respectively, 1.934 Å and 1.980 Å. The anatase structure is the one phase getting the greatest attention. It is a low temperature phase and exhibits the UV induced photoactivity, firstly reported by Fujishima [53].

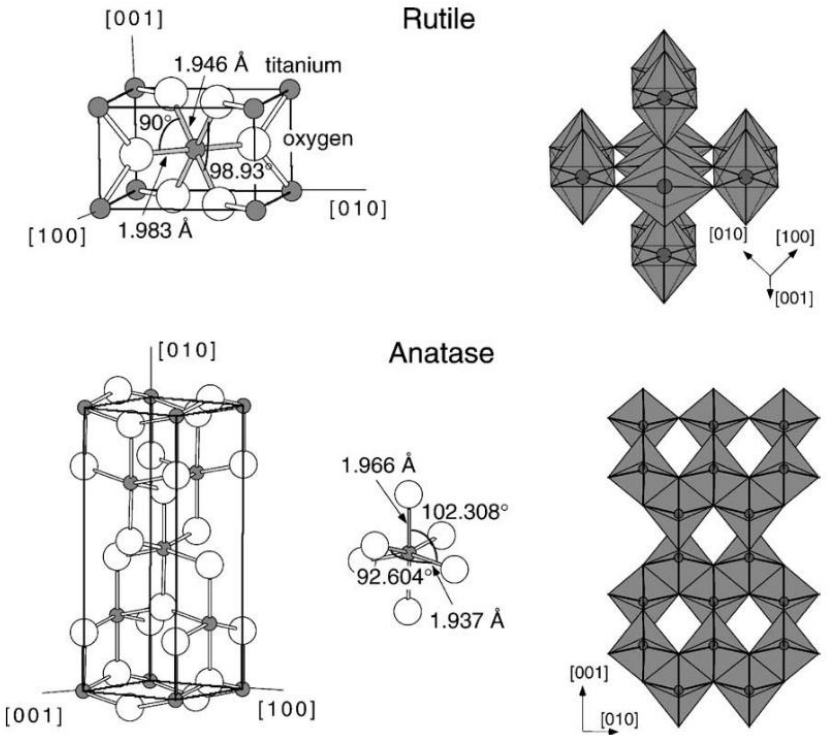

Figure 13 *Bulk structures of rutile and anatase. In both structures, slightly distorted octahedra are the basic building units. The bond lengths and angles of the octahedrally coordinated Ti atoms are indicated and the stacking of the octahedra in both structures is shown on the right side* [54].

Due to its broad range of interesting properties, the scientific literature already contains a lot of work dealing with the deposition of TiO_2 by PVD processes. However, only few groups have elaborated relevant numerical models enabling deeper understanding of the intrinsic physics governing the deposition of TiO_2. Amongst them, the group of Depla *et al.* [55] have developed one of the most advanced model dedicated to the reactive sputter deposition technique. Their model is based on the well-known, 30 years old, Berg model [56] which gives a good understanding of the origin of the hysteresis in reactive sputtering. The original model describes the hysteresis under steady state conditions, and is based on differential equations. For a given flow of reactive species, the target and substrate state and the different gas consumptions can be computed. As such the hysteresis is simulated in a pressure-controlled way which enables modelling the various working regimes of the discharge. The major drawback of the Berg model is that it only accounts for the process of chemisorption for the compound forming on the surfaces. Therefore, Depla and his co-workers have upgraded the Berg model by including:

- Re-deposition process on the target [57]
- Implantation of the target by reactive ions participating to sputtering [58]
- Implantation of the target by knocked-on chemisorbed atoms [59]
- Addition of a spatially resolved current profile on the target
- Addition of a spatially resolved deposition profile on the substrate

Quoting the authors of [55], this time dependant model from 2014 is *"a big step forward in the direction of a genuine model of the process".*

In order to move one step further in the same direction, it is necessary to include more features in this model. For example, this previous model doesn't account for the geometry of the coater, nor the locations of the gas inlets or the pumps. The reason is because the model does not include particles motion i.e., the plasma phase is not modelled. However, the same team also proposed a workaround to this limitation by enabling the model to work together with the SiMTra code described in [60]. This model implements a Monte Carlo algorithm which simulates the transport of the metal flux sputtered from a magnetron target through a background inert gas. The main output of this model is the deposition profile on the substrate. Despite the improvement of the calculations by the addition of a particle-based algorithm, the approach still suffers from several drawbacks. The first one is the absence of reactive species in the gas phase. The second one is the limitation of the model to elastic collisions i.e., no excitation or ionization. The third one is that no charged particles are included in the framework. From a coating quality point of view, it is a major issue. For example, RMS processes are known to generate high-energy negative oxygen ions which can drastically impact the properties of the growing film. In the literature most of the related articles are focussed on experiments to reveal their existence [61–64] and to elaborate about their impacts on the film growth [65–67]. Unfortunately, this literature is not as extensive regarding the modelling of their production yield. One of the best approach is performed by Mahieu *et al* [68] who included negative oxygen ion emission from an Al_2O_3 target in the SiMTRA [60] model. Simulation results were compared to experimental measurements obtained from energy resolved mass spectrometry. They demonstrated that the energy and spatial distributions of the high-energy O^- ions can be reproduced by creating those ions at the target surface and computing their transport through the neutral gas. However, these are treated as neutral species, i.e.,

no electric potential effect is computed (acceleration in the sheath...) and their initial energy distribution is assumed.

From another point of view, pure particle-based algorithms already exist in the literature. The first one implementing 2D geometry together with a mixture of Ar and reactive species in the gas phase is attributed to Vahedi and Surendra [69] in 1995. Their model arises from the considerable effort to develop self-consistent kinetic models with no assumptions about the distribution functions in order to master the inherently complex discharges where particle velocity distributions can be non-Maxwellian. This model only includes few inelastic collisions and wall chemistry was neglected. It acts as proof of principles of such method for the simulation of reactive sputter deposition processes and paved the way to more complex algorithm.

In the late 90's, Kondo *et al.* [70] and Nanbu *et al.* [71] have modelled a magnetron discharge using a 3D PICMC model. However, these particle models only describe the case of low magnetic fields and do not cover the case of reactive deposition. Another PICMC model was developed by Bultinck and Bogaerts [72,73] during a Ph.D. thesis presented in 2009. In this work, E. Bultinck developed a 2d3v PICMC model to investigate the physical processes in a magnetron discharge during the reactive sputter deposition of TiO_x coatings. The model includes both neutral and charged species generation, simple 2D geometry and the effect of target poisoning was added by modification of the sputtering yield and the secondary emission electron yield (no wall chemistry was implemented). Using this code, the author was able to conclude that the deposited O in the TiO_x film originates almost entirely from the O_2 gas. Even though the complexity of the existing models keeps increasing, none of them includes a dynamic wall chemistry or closed the loop of the deposition process by modelling the film growth based on the particles flux results.

4 Designing Virtual Coater

In order to support the experimental endeavours of linking the macro-parameters of a PVD process to the micro-properties of thin films, three different pieces of software were used. The plasma phase is handled by two algorithms developed at the Fraunhofer Institute of Braunschweig [19,74,75], neutral particles and wall chemistry are managed by a DSMC algorithm while a PICMC algorithm deals with charged particles. Both algorithms move particles through a discretized computational space-time domain. After each time step, particles are paired up with the other particles located in the same computational vicinity and collision probability (according to collision cross section) is computed for these pairs. In the DSMC method, one of the fundamental assumptions is that particle movement can be decoupled from collisional behaviour and that particles move along straight-line paths with discrete changes in their velocity and energy caused by collisions. The simulation is divided into time steps that have to be small enough compared to the average time between collisions. Moreover, the volume wherein collisions take place (the cell) should be defined so that the collision probability is less than 1 at each time step. Therefore, its dimensions should be less than the mean free path. Fortunately, this constraint still enables to run a DSMC's over several seconds of simulation time. More details about the mechanisms of the DSMC algorithm are presented in Chapter 5. In the PICMC method, a discretized simulation volume is also used. In this case, the magnetic field is pre-computed from the magnet geometry and material, and is superimposed to the simulation grid. The magnetic field is assumed constant throughout the simulation. In contrast, the electric field is computed at each time step as it evolves with the charged particles motion. As in the DSMC method, the cell dimension has also to meet constraints imposed by the physics, limiting the simulation to run over a time-scale of the order of few hundreds of microseconds in a reasonable computational time. The main features of the PICMC method are described in Chapter 6 of the present manuscript. Figure 14 summarizes the different software packages included in the *Virtual Coater* design.

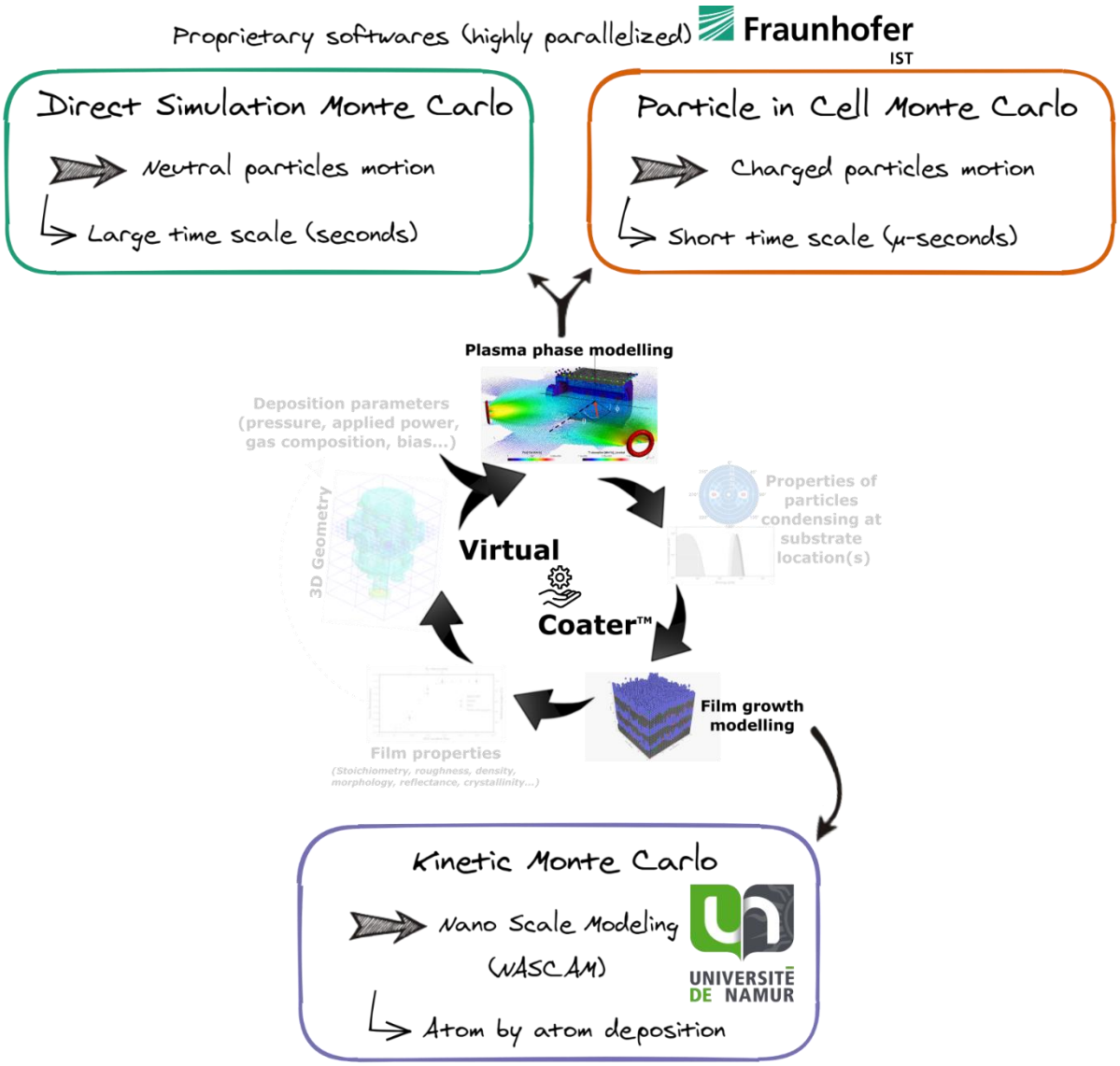

Figure 14 *Simulation tools included in the Virtual Coater design*

Finally, the film growth is managed by a kMC code called Nascam and developed at the University of Namur. Nascam (NanoSCAle Modelling) is dedicated to the modelling, at the atomic scale, of a system under deposition by using the kinetic Monte Carlo method to simulate the diffusion, nucleation and growth of a film on a substrate. The current distributed version of the software is Nascam 4[2] [76] enabling to simulate complex incident gas flow (up to 2 metal, 2 reactive and 1 neutral species) and PVD deposition according to hard-coded rules based on physical principles restricted to

[2] https://www.unamur.be/sciences/physique/ur/larn/logiciels/nascam

"common" experimental situations. The software uses an approach where a list of possible events is created and activation energies for these events are used as an input. The computational domain is discretized in a way that predefines the positions possibly occupied by a moving atom during the simulation process. This does not enable the crystallinity of the coating to evolve during the simulation. To overcome these restrictions, a new version of Nascam was implemented. The version 5 of Nascam is built as a sandbox, which is editable at will by the user. Then the main goal of Nascam 5 consists in giving the user the possibility to build his own simulation environment, enabling the modelling of complex crystallographic structures, or "uncommon" physical rules specific to a given deposition process.

Now that the selected software package designing *Virtual Coater* are introduced, Figure 15 presents the flowchart of the *VC* concept i.e., how the simulation tools interact together to provide a full description of the thin film deposition process.

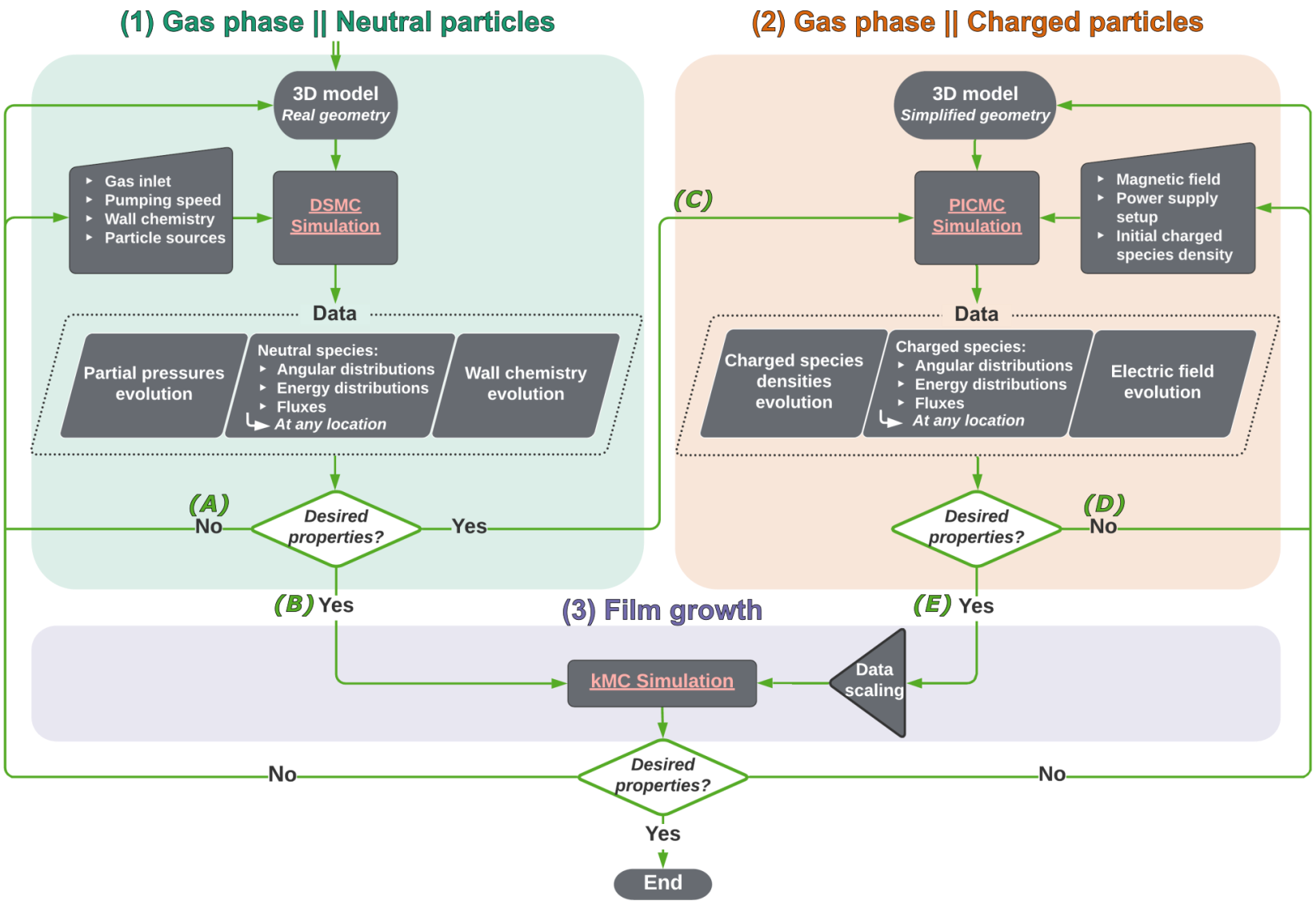

Figure 15 *Flowchart of the Virtual Coater concept*

The three software programs act as building blocks. First, the DSMC algorithm is used with a complete 3D representation of the deposition chamber. Three outcomes are possible, (A) the DSMC results do not match with experimental characterization meaning the model has to be improved; (B) based on the neutral particles distributions and fluxes, film growth modelling is started. The film properties obtained can then be used as a feedback to adjust initial DSMC simulation parameters; (C) neutral gas distributions as computed by the DSMC method are interfaced and used as an input to ignite a plasma with the PICMC algorithm. Based on this simulation, (D) the results do not match with experimental plasma characterization, meaning either the PICMC parameters or the DSMC parameters have to be adjusted; (E) a subsequent film growth simulation, including charged species, can be started. It will then act as a feedback either on the DSMC inputs or on the PICMC inputs. Due to restrictions imposed by the PICMC method (see Chapter 6), the results obtained need to be scaled in order to fit with real experimental deposition conditions. This step is the “Species flux scaling” triangle box in the flowchart.

In the following:

- Chapter 5 will cover the combination of the blocks (1) and (3).
- Chapter 6 will describe and discuss the interface (C), as well as the “Data Scaling”
- Chapter 7 will cover the combination of all three blocks together.

Throughout the construction of *Virtual Coater*, the computed results are compared along with experimental measurements performed on the dual-magnetron coater “Mantis” located at laboratories LARN (Laboratoire d’Analyse par Réactions Nucléaires) of the University of Namur. The main experimental measurements involve characterization techniques of the gas phase such as:

- Total pressure evolution via baratron gauge measurements record.
- The target current-voltage curve (I-V) evolution analysis.
- Mass Spectrometry (MS) analysis to investigate the gas composition evolution during hysteresis experiments.

- Optical Emission Spectroscopy (OES) embedded in the FloTron™ system to track the relative gas composition on sputtered species to allow the use of a feedback control loop on the O_2 gas inlet.
- Use of an Active Thermal Probe (ATP) to evaluate the energy flux towards the substrate holder.
- Langmuir probe measurements to evaluate the electron density.

In addition, deposited thin films are also characterized with various techniques:

- Rutherford Backscattering Spectroscopy (RBS) with the Altaïs particles accelerator of the LARN lab to probe the stoichiometry.
- Scanning Electron Microscopy (SEM) to capture the morphology of both the top surface and side cross section of the coatings.
- Atomic Force Spectroscopy (AFM) to measure the coating roughness.
- X-ray diffraction (XRD) to evaluate the crystallinity the deposited thin films.

Before to dive in the step-by-step process of elaborating Virtual Coater, it has to be mentioned that a fourth code was added to the framework. The need of this last one comes from the necessity to pipe data from one code to another and especially to handle the large datasets. Indeed, the data generated by DSMC and PICMC are challenging both for their storage and their manipulation. A quick glimpse at the data generated by Virtual Coater is the following: data can either be density, velocity, absorption, desorption, number or particles, … For each species and each time, a new file containing the corresponding data is created. A typical file produced by either of these algorithms is organized as the following:

x	**y**	**z**	**Value**
…	…	…	…
…	…	…	…

With the column *value* containing either one value in the case of scalar output (density, number…) or three for vector (velocity, flux…) output. At each cells of the simulation geometry correspond one line in the file. The involved 3D geometries are composed of at least 3 000 000 cells, easily producing a total of 300 GB/simulation. Therefore, it was necessary to develop a strategy to manage the amount of data to avoid the multiplication of storage devices. A Python3 module, PyCMC, was developed to

achieve this goal. The module combines the use of SQLite[3] database and Hierarchical Data Formats (HDF5)[4] to provide versatile, scalable and on the fly storage of the data, i.e., the data can be compiled as soon as they are outputted. Moreover, the HDF5 solution enables data compression and partial load of the data in the RAM. Figure 16 shows the entity relationship diagram of the implemented database.

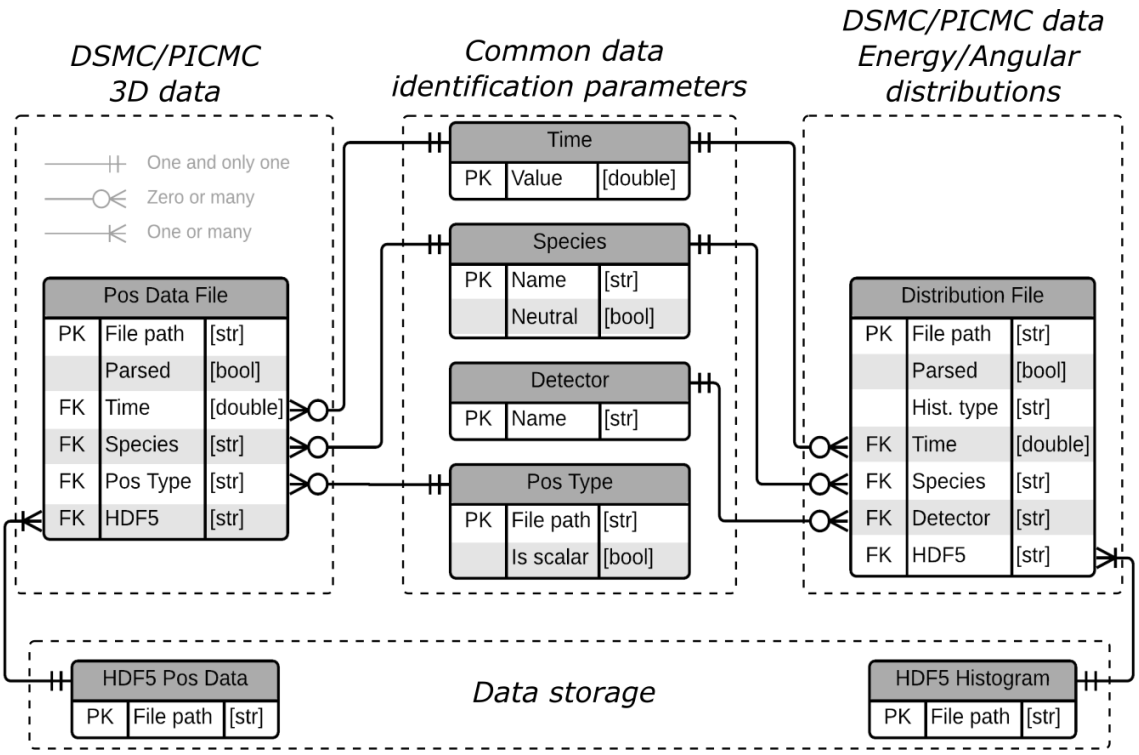

Figure 16 Entity Relationship Diagram of the SQLite database embedded in PyCMC.

The PyCMC module scans the simulation folder for new 3D data file (Pos files) or for energy or angular distribution files. When a new file is detected, the species, time and data type (density, pressure, temperature, velocity, absorption…) are determined by using regular expressions on the file name. If the corresponding HDF5 file compiling all these data is already existing, the data file is read and a new array is added to the HDF5 file (see Figure 17). If the corresponding HDF5 file does not exists, it is created prior to include data. At the end of the simulation, when all raw data have been compiled, the simulation data are composed of one database file and several HDF5

[3] https://www.sqlite.org/index.html
[4] https://www.hdfgroup.org/solutions/hdf5/

files, one for each entity *species-data type*. One HDF5 file contains the time evolution data for one data type of one species. The total size of the compiled data can be as heavy as 15 GB, reducing by a factor 20 the size of the simulation and without data loss.

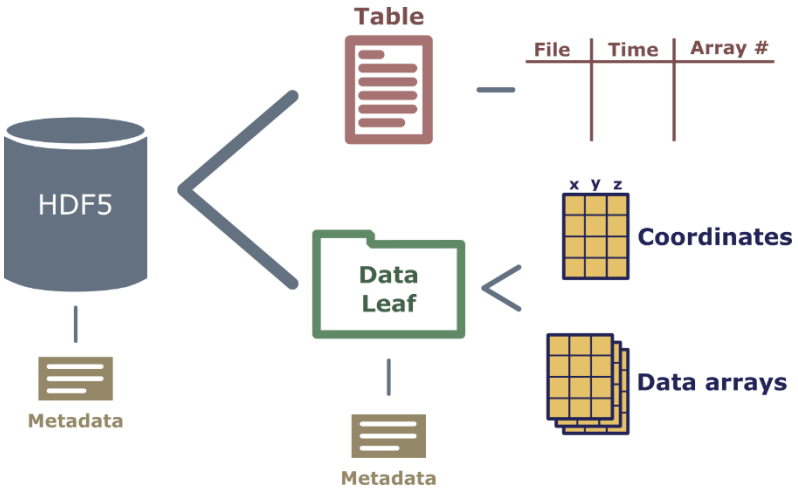

Figure 17 Schematic organization of a typical HDF5 file

Another important feature of the HDF5 files is that data can be partially read and load on memory. It is one of the reasons why the cells coordinates are stored in their own array, see Figure 17. Coordinates can be loaded and a desired slice can be selected i.e., a mask is generated. As data are sorted prior to be included in the HDF5, the mask can then be applied on each data array to easily and efficiently extract the desired sub-data. Therefore, the data manipulation is fast as unwanted data are not loaded in memory and can be performed on a standard computer which usually has less RAM than an HPC.

The development and use of this python module are not visible in the following description of this Ph.D. However, its development was crucial to achieve the final state of this work. In its current form the PyCMC module contains over 70 files and 15 000 lines of code (9000 with no blank or comment). The use of this module already went beyond the scope of this Ph.D. as it was also used to handle PICMC/DSMC data generated for the following collaborations or articles: [77–79].

5 The role of neutral particles

This chapter intends to discuss the combination of the pieces of software (1) and (3) of the *Virtual Coater* flowchart in Figure 15. It has the purpose to answer the following questions: *what is the role of neutral particles during the growth of TiO_x thin films by reactive dual-magnetron sputtering? Is it possible to make predictions on film properties based only on their modelling (i.e., neglecting charged particles)?*

The findings have been published in 2018 in Journal of Physics D: Applied Physics [80]. The article is organized in a way that first describes both the DSMC and kMC algorithms used (version 4.7 of Nascam). The hysteresis curve of the Ar/O_2 dual-magnetrons discharge is investigated with the DSMC algorithm, which includes a reactive wall model in order to take into account the reactive process description. Three species are included: Ar, O_2 and Ti. Ar is introduced with a constant inlet over the various simulations while the O_2 inlet varies from one simulation to another. Both targets are defined as source of Ti and O_2, the number of sputtered particles depending on the local chemical surface state, either Ti or TiO_2. Nascam simulations, i.e., kMC model, are started based on flux, angular and energy distribution of the species. The main findings are the followings:

1. The DSMC algorithm enables to reproduce and predict the O_2 partial pressure along with the hysteresis curve.
2. The kMC algorithm (Nascam) accurately predicts, based on the DSMC results, the composition and morphology of the deposited coatings.
3. Molecular oxygen is identified as responsible of the column tilting angles reduction of the coatings, while the metallic species (Ti) acts as a backbone for the growing film.

This study does not include the possible effects of ion bombardment during the film growth. As shown in chapter 7, the concomitant bombardment of energetic particles induces energy transfer to the growing film and generates adatom mobility. This in turn may affect the morphology and the crystallinity of the coating. The simulation of charged particles in a plasma discharge and their impact on the film growth was

undertaken by first checking how to include the PICMC algorithm within the *Virtual Coater* loop. This is the topic of the next chapter.

IOP Publishing Journal of Physics D: Applied Physics
J. Phys. D: Appl. Phys. **51** (2018) 195202 (17pp) https://doi.org/10.1088/1361-6463/aabb72

TiO_x deposited by magnetron sputtering: a joint modelling and experimental study

R Tonneau[1], P Moskovkin[1], A Pflug[2] and S Lucas[1]

[1] Laboratoire d'Analyse par Réactions Nucléaires (LARN), Namur Institute of Structured Matter (NISM), University of Namur (UNamur), 61 rue de Bruxelles, B-5000 Namur, Belgium
[2] Fraunhofer Institute for Surface Engineering and Thin Films IST, Bienroder Weg 54e, 38108 Braunschweig, Germany

E-mail: romain.tonneau@unamur.be, pavel.moskovkim@unamur.be, andreas.pflug@ist.fraunhofer.de and stephane.lucas@unamur.be

Received 15 December 2017, revised 26 March 2018
Accepted for publication 4 April 2018
Published 20 April 2018

Abstract

This paper presents a 3D multiscale simulation approach to model magnetron reactive sputter deposition of $TiO_{x\leqslant 2}$ at various O_2 inlets and its validation against experimental results. The simulation first involves the transport of sputtered material in a vacuum chamber by means of a three-dimensional direct simulation Monte Carlo (DSMC) technique. Second, the film growth at different positions on a 3D substrate is simulated using a kinetic Monte Carlo (kMC) method. When simulating the transport of species in the chamber, wall chemistry reactions are taken into account in order to get the proper content of the reactive species in the volume. Angular and energy distributions of particles are extracted from DSMC and used for film growth modelling by kMC.

Along with the simulation, experimental deposition of TiO_x coatings on silicon samples placed at different positions on a curved sample holder was performed. The experimental results are in agreement with the simulated ones. For a given coater, the plasma phase hysteresis behaviour, film composition and film morphology are predicted. The used methodology can be applied to any coater and any films. This paves the way to the elaboration of a virtual coater allowing a user to predict composition and morphology of films deposited in silico.

Keywords: plasma modelling, Monte Carlo simulation, reactive magnetron sputtering, film growth, titanium oxide, thin film

(Some figures may appear in colour only in the online journal)

1. Introduction

Reactive magnetron sputtering is a widely used method for the deposition of various compound layers both in laboratory and in industry. Its understanding is of great importance to master the quality and the properties of the products. The involved physical processes are complex and non-linear, and require the use of a wide range of simulation techniques and models. Several approaches can be used to model the physics of plasmas. The most complete method is the full kinetic theory [1, 2], which has the unfortunate drawback of being extremely complicated. Kinetic theory essentially considers in turn the interaction between each particle and every other particle in the system, with the electric and magnetic fields self-consistently calculated during the simulation. Other techniques model the plasma as a pressureless fluid, i.e. fully electromagnetic but not thermodynamic. Another commonly-used model is magnetohydrodynamics (MHD) [3]; MHD compromises on the electromagnetism but provides a framework for modelling in the fluid limit with full thermodynamics. This kind of model usually cannot be applied to magnetron sputtering as sputtering aims to use low pressure plasma which is out of the fluid limit range [4]. Amongst models dedicated to reactive magnetron sputtering, there are several 2D simulation models [5–7] and also analytical theories [8–12]. Both use different variations of the Berg model [10, 13]. Models

implementing real 3D geometry and time dependent algorithms are not common mainly because of either the availability of such codes or the high computational resources required. But today, with the evolution of high performance computing resources, one can think of not only gas flow simulations of complex systems but also plasma modelling. Whereas the gas flow simulation can be applied at a full scale system as it will be describe here, full 3D plasma simulation is not yet possible with the todays computer performances and therefore specific strategies have to be developed to run simulations in a reasonable time scale [14]. This paper suggests a plasma process simulation scheme by separating neutral particles from charged particles. Indeed the ionisation degree of the sputtered metal in a low-pressure plasma is weak and the transport may be described by neutral interactions only. In this case, the specie's motion is not affected by electric and/or magnetic fields and the transport of particles involves 'only' background gas collisions and diffusion in addition to the transport of sputtered material from the target to the sample. Direct simulation Monte Carlo method (DSMC) accurately simulates the time evolution of a real 3D system over several seconds in an acceptable computational time. DSMC features spatial resolution and can be coupled with RSD models [12, 15] to describe the reactive gas implantation dynamics of the target material or reaction wall surfaces. In a subsequent step, a full plasma simulation can then complete DSMC simulations in order to take into account the ionized and metastable species using for example the particle-in-cell Monte-Carlo (PICMC) algorithm.

To make a combined plasma simulation and film growth modelling, both multiple time-scale and space-scale simulation techniques have to be introduced. Indeed a whole plasma deposition process in real 3D geometry is at the meter scale, while in silico thin film growth simulation and evaluation of the final film properties is performed at the atomic level i.e. nanometre scale. Most of theoretical models dealing with thin film growth simulation and the underlying formation mechanisms are based on classical atomistic techniques, e.g. molecular dynamic (MD) [16–18] or kinetic Monte-Carlo (kMC) [19–21]. Both techniques differ especially in the procedure to calculate the particle movement within the atomistic system as well as in the applied structure size and simulation time. The fundamental basis for MD and kMC is a classical interaction potential describing the forces between the atoms in the investigated system. Therefore, the selected potentials are in fact one of the most critical parts in the classical atomistic simulation techniques determining the accuracy of the performed studies.

In MD simulation, the force field is applied to calculate the particle movement according to Newton's equation of motion. The force acting on atoms is determined at each simulation time step. The time evolution of the atomistic system is performed by applying specific methods for the numerical integration of the equations of motion, e.g. Velocity-Verlet algorithm [22]. The continuous motion of the particles within the defined simulation volume is one of the strengths of the growth models based on MD. This allows investigating the amorphous layer formation, which is a common case in thin film technology. Another advantage of the MD technique is the possibility to model the deposition of high energetic particles with good accuracy. Since the kinetic energy of the coating material in modern sputter coating techniques is up to several tenth of eV [23], the consideration of Newton's mechanics enables the physically correct description of the deposition event. By applying classical MD, one can investigate systems of millions of atoms, but for comparatively short simulation times in the range of few ns. Therefore, several approximations in the system size and simulation time have to be applied to model a film of reasonable layer thickness with MD based growth models.

To perform simulations at larger time and length scale, the kMC method is generally used [19–23]. This method allows the modelling of systems constituted of up to millions of atoms and for time ranges up to several hours. There are several approaches in implementing this method. One can classify events 'on the fly' to create a complete table of the events which happen during the simulations. This is the most accurate approach to create a table of all possible events. The table or database can then be stored and re-used, decreasing the computational time [24]. In the case of bond-counting kMC [19], one calculates the event rates taking into account the number of nearest neighbours. In specific event kMC, a predefined set of events is only allowed to occur, and the rates of these events are used as an input. In the kMC approach, a fixed predetermined lattice is usually used. Atoms may occupy only the lattice nodes. In case of compounds, a unit cell consists of two or more atoms. In this case, a predefined lattice with a given crystallographic orientation is used. The growth of compounds like TiO_2 [25], $BaTiO3_3$ [19], perovskites [23] were simulated by this technique. Another variant is adaptive kMC models [21, 24] where atoms can occupy interstitial positions. In the paper [26] a method for the modelling of simultaneous film growth with different orientation of polycrystalline is also proposed. The paper [27] presents a kMC model where atoms are not assumed to sit on lattice sites. For each state of the system, characterized by a local minimum of the potential energy surface, multiple searches for saddle points are carried out using random initial directions. Then the relevant transitions are found on the fly during the simulation. Thus, there is no limitation of fixed positions for the particles during the simulations.

By selecting the appropriate simulation method for the gas phase and film growth, one can set up a virtual coater that will predict films composition and morphology in a reasonable amount of time and for any coater geometry. In addition, virtual coater is a very useful tool to investigate, over a wide range of deposition conditions, the physics of film nucleation, film growth and to identify the responsible mechanisms of particular properties like roughness, porosity, density, etc. In this work, we propose to use a multiscale approach combining DSMC and MD/kMC like the one already published in [28] for optical thin films. This work firstly proposes a general multiscale approach applied to $TiO_{x\leqslant 2}$ films which involves DSMC simulations for the transport of sputtered particles in a dual magnetron chamber filled with a variable mixture of Ar and O_2. Secondly, it presents a kinetic Monte Carlo

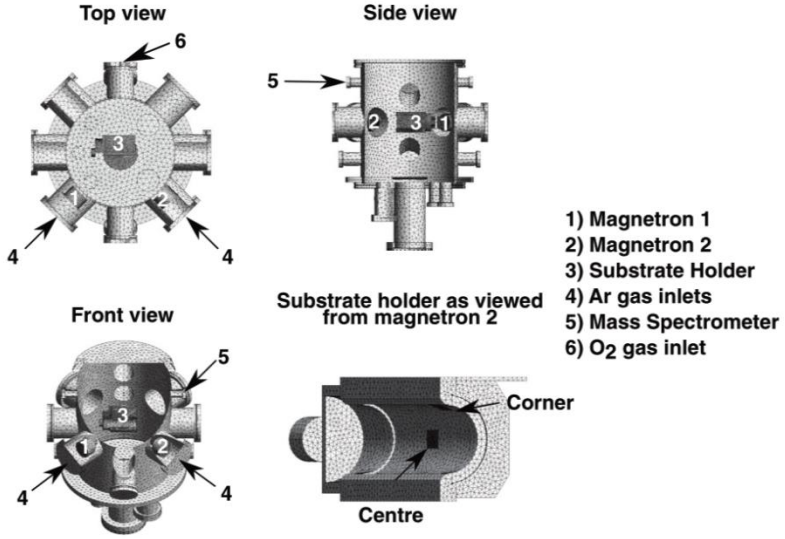

Figure 1. Coater and substrate holder geometry.

(kMC) code to simulate nucleation and film growth for thickness up to 500 nm. Simulations are benchmarked with experimental results. For this purpose, $Ti^{18}O_{x\leqslant 2}$ films are grown in the exactly same conditions as in silico. The use of $^{18}O_2$ was decided to underline the mechanisms involved in deposition and to get rid of possible perturbations coming from external pollution as it is often the case for high reactive metals like Ti.

2. Materials and methods

2.1. Geometrical coater description

Figure 1 presents a scheme of the coater used in this work. It is a double magnetron system in a cylindrical chamber (diameter, 0.32 m). The angle between axes of the two 2″ magnetrons is 90°. A turbo molecular pump with a capacity of 260 l s^{-1} is located underneath the chamber. A stainless steel plate is placed at the top of the tube pump to protect the pump, thereby reducing the effective pumping speed to $\cong$ 70 ls^{-1}. Ar is injected near the surface of each cathode while reactive O_2 is injected directly in the chamber.

A curved substrate holder is used and samples are placed at two locations on the holder as shown on figure 1. The centre position is parallel to the cathode surface and the corner location is inclined at 70° and is 25 mm away from the centre and 18 mm away from the median plane.

2.2. Gas phase simulations

The code used to perform the simulations of the particle transport in the deposition chamber had been developed at the Fraunhofer IST [29–31]. It implements a direct simulation Monte Carlo (DSMC) algorithm: particles move through a discretized computational space-time domain as described in figure 2.

After each time step, particles are paired up with the other particles located in the same computational vicinity and collision probability (according to collision cross section) is computed for these pairs. Collisions of these pairs are handled in a way that conserves energy and momentum. Each simulated particle is considered to represent a large number of real gas particles since using the real number of particles would by far exceed usual computational resources. One of the fundamental assumptions of the DSMC method is that particle movement can be decoupled from collisional behaviour and that particles move along straight-line paths with discrete changes in their velocity and energy caused by collisions. The simulation is divided into time steps that have to be small enough compared to the average time between collisions. Moreover, the volume wherein collisions take place (the cell) should be defined so that the collision probability is less than 1 at each time step. Therefore, its dimensions should be less than the mean free path. In the present case, the simulation box is divided in two regions: (i) a high resolution region, with cells dimension of $2 \times 2 \times 2\,mm^3$ and (ii) a low resolution region, $10 \times 10 \times 10\,mm^3$ for the rest of the simulation box. Cell sizes in these two regions are smaller than the typical mean free path of ~10–13 mm of the species at 0.5 Pa.

Figure 3 shows surface meshing and volume decomposition of the reactor used in this work.

The purpose of the high-resolution region is to accurately compute particles transport and particle-surface interactions in the substrate-targets region. Surface meshing is required to handle gas/surface interactions on the chamber walls or substrate. The Cartesian volume mesh is used to handle gas collisions described in table 1.

TiO and TiO_2 molecules are not included in the model. Hence, sputtered species are assumed to be Ti and O_2. Moreover, this model only takes into account molecular oxygen. According to previous work modelling Ar/O_2 discharges by mean of PICMC algorithms [7], the O_2 flux to substrate is several orders of magnitude higher than atomic oxygen.

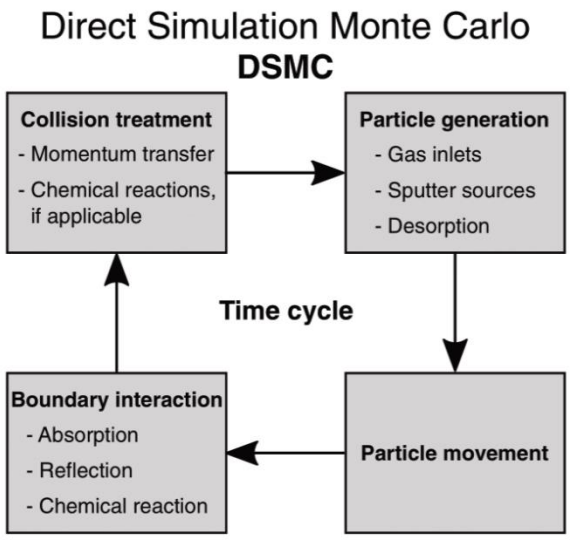

Figure 2. DSMC algorithm functional diagram.

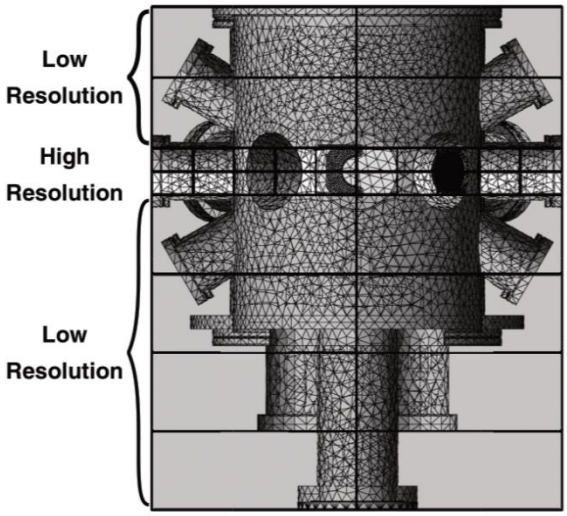

Figure 3. Meshed view of the reactor describing the low and high-resolution regiions.

Table 1. Gas phase collisions used in this work.

Momentum transfer collisions		
$Ar + Ar$	$O_2 + O_2$	$Ti + Ti$
$Ar + O_2$	$O_2 + Ti$	
$Ar + Ti$		

For gas phase collisions, the variable soft sphere (VSS) model [32, 33] is used to handle collisions between the process gases Ar and O_2. For sputtered monoatomic Ti, a simpler approximation is used. In [33] the VSS model based on the Lennard Jones interatomic potential is derived and the variation of the cross section and the deflection angle exponent is given for an energy range of 5 orders of magnitude. It is worth noting that for molecules, energy limits in the VSS model may arise by computing collision processes such as dissociation, excitation of internal vibrational or electronic states or even collisional ionization. However, those processes are not considered in this DSMC study. For the scattering between sputtered Ti and Ar the so-called Born-Mayer approximations is used for the interatomic potentials. They are defined for monoatomic species in [34] and are used for defining cross sections as shown in [35]. For Ti collision with O_2, an average of the Ti–Ti and O_2–O_2 cross sections is taken due to the non-availability of more accurate data.

The model also includes wall and target chemistry reactions to tackle the reactive process description. Indeed, in reactive magnetron sputtering (RMS) deposition, wall and target coverage have a time dependent evolution responsible of the well-known hysteresis behaviour.

The DSMC code uses a Cartesian cell structure for discretizing the volume, while the chamber wall, substrate and other geometric obstacles are represented by a triangular surface mesh. The latter is created prior to the simulation run with the free modelling and postprocessing software GMSH [36]. For cells intersecting with the surface mesh, their remaining cut-size volumes as well as the surface areas contained in the volume cell are pre-computed during initialization of the simulation run.

For the reactive wall model, it is assumed that the gas phase can interact with the top atomic layer of the wall surfaces and that there are two wall material phases, namely metallic Ti and TiO_2. For simplicity, the surface bond density n_s is assumed to be equal for both materials (9.3×10^{18} m^{-2}), i.e. n_s denotes the number of possible sites for Ti as well as for TiO_2 per unit area. Each intersecting cell i gets the intersecting mesh area A_i and the relative coverage fractions θ_{Ti}, $\theta_{TiO_2} = 1 - \theta_{Ti}$ respectively for metallic Ti and TiO_2 as additional variables. Additionally, the number n_{Ti}, n_{TiO_2} of 'deposited' Ti or TiO_2 sites below the first atomic layer is stored for each intersecting cell. By collision of an O_2 molecule with a wall within a cell i, it is possible to convert a fraction of the metallic Ti coverage into TiO_2. First, the probability p_{ox} of this oxidation reaction is obtained via

$$p_{ox} = \alpha_{O_2}\theta_{Ti} \tag{1}$$

with the oxygen sticking coefficient α_{O_2} (equal to 1 in the present study). Afterwards, a random number R between 0 and 1 is generated, and the reaction is actually executed if $R < p_{ox}$, otherwise the O_2 molecule is reflected from the surface with a Maxwellian wall velocity distribution based on the wall temperature. For the surface reaction with an O_2 molecule, the difference Δ_{ox} in surface fraction θ_{Ti} is computed via

$$\Delta_{ox} = \frac{w_{O_2}}{y n_s A_i} \tag{2}$$

with w_{O_2} as statistical weight of O_2 super particles and y being the required number of molecules to form one TiO_2 site ($y = 1$ in this study). For the used simulation parameters of $w_{O_2} = 5.0 \times 10^{11}$ and an intersecting cell area of around 4 mm^2 in the high-resolution region, Δ_{ox} is in the order of 1%–2%, which is sufficiently small to ensure a continuous

transition of the surface oxidation. Subsequently, Δ_{ox} is added to θ_{TiO_2} and subtracted from θ_{Ti}. It is enforced that $\theta_{TiO_2} \leqslant 1$ by cutting off the excess of Δ_{ox}, if required.

The opposite reaction is metal deposition with incoming Ti atoms. Since Ti can be deposited on both metallic Ti or TiO_2 sites, the probability for this reaction is just identical with the Ti sticking coefficient α_{Ti}. Again, a differential surface fraction is computed via

$$\Delta_{met} = \frac{w_{Ti}}{x n_s A_i} \tag{3}$$

with x being the required number of metal atoms to form one metal site. Whether the Ti is deposited onto Ti or TiO_2 is initially decided by a random experiment according to the actual surface fractions θ_{Ti}, θ_{TiO_2}. If it is deposited onto Ti, the surface fractions remain unchanged, however the amount n_{Ti} of deposited Ti is increased by Δ_{met}. When performing deposition onto TiO_2, Δ_{met} is substracted from θ_{TiO_2} and added to θ_{Ti} and n_{TiO_2}. Again, it is enforced that θ_{Ti}, θ_{TiO_2} are kept within [0,1].

For the target surface, the sputtering yield is computed as a linear combination from the oxide and metal sputtering yield according to the surface fractions θ_{Ti}, θ_{TiO_2} at the target cells, while the ion current is given as input parameter in accordance with experimental conditions. We implicitly assume that during sputtering the oxidized target surface is decomposed into Ti and O_2 molecules. The dissociation of O_2 into monoatomic O may be further considered, however it turned out that the oxygen flux at the substrate originating from the target is negligible compared to the oxygen flux from the gas phase. If a Ti or TiO_2 site is removed from the target's top atomic layer, it is replaced by material from below. In case of redeposition present at the target cell, the replacement material is randomly selected according to the deposited fractions n_{Ti}, n_{TiO_2}, otherwise Ti is chosen from the target bulk material.

This way, the DSMC model behaves in a similar way as the Berg model of reactive sputtering [13]. The difference is that there are individual surface oxidation fractions for each cell intersecting with the target or chamber surface and that the transport of sputtered particles between target and substrate is treated within the DSMC transport code.

2.3. Sputtered material definition

Targets are defined as sources of particles, which are transported into the gas phase. For proper calculation of the source's parameters, one must know (1) the racetrack geometry; (2) particle fluxes (3) angular and energy distribution of those particles.

(1) In order to take into account the non-uniform emission of atoms from the target, the geometrical description of the racetrack or the parallel components of $\vec{B}$ can be used to spatially weight the particle source emission:
(2) By knowing the experimental discharge current (or by selecting a possible one), it is possible to evaluate the amount of particles emitted from the metallic target due to sputtering events [37] according to:

Table 2. Values of Ti sputtering yield are issued from SRIM (Ar^+ of 380 eV). Total sputtering yield of TiO_2 is from [38]. Secondary electron emission yields used for the present simulations are issued from [3].

Target material	$\gamma_{Tot,sput}$	γ_e
Ti	0.56	0.114
TiO_2	0.205	0.080

$$N_{sput} = \frac{I_{power\ supply}}{e.\ (1\ +\gamma_e)} .\ \gamma_{sput}\ (\text{particle s}^{-1}), \tag{4}$$

where $I_{power\ Supply}$, γ_{sput}, γ_e and e are respectively: power supply current (A), sputtering yield (particle/ion), secondary emission electron yield (SEEY) (electron/ion) and elementary charge.

In order to model sputtering of the compound material and re-deposition of sputtered particles on targets, wall chemistry is applied to targets as well. An incoming ion could both sputter metallic titanium or oxidized titanium and give rise to the emission of several species considered as being atomic titanium or molecular oxygen. As the target is supposed to be a mixture of metallic Ti and TiO_2, equation (4) must be modified to take into account both species:

$$N_{sput} = \frac{I_{power\ Supply}}{e \cdot\ (1\ +\gamma_{e,compound})} \cdot\ (\theta_{met} \cdot\ \gamma_{sput,\,Ti} + \theta_{ox} \cdot \gamma_{sput,\,TiO_2}\ )\ \left(\text{particle s}^{-1}\right). \tag{5}$$

Here θ_{met} and θ_{ox} are respectively the fractions of metallic Ti and oxidized Ti of the target surface, so that:

$$\theta_{met} + \ \theta_{ox} = 1. \tag{6}$$

Unfortunately, the SEEY ($\gamma_{e,compound}$) value of the compound material is unknown. However, SEEY values of both metallic titanium and titanium dioxide had been previously measured and discussed in literature [3, 38]. Then, the simplest approach is to assume separation of metallic and oxidized titanium and to define the number of sputtered particles as a linear combination of the sputtered particles number of the two materials:

$$N_{sput} = \theta_{met} \cdot \frac{I_{power\ Supply}}{e \cdot\ (1\ +\gamma_{e,\ Ti})} \cdot\ \gamma_{sput,\ Ti} + \theta_{ox} \cdot \frac{I_{power\ Supply}}{e \cdot \left(1\ +\gamma_{e,\ TiO_2}\right)} \cdot \gamma_{sput,\ TiO_2}\ (\text{particle s}^{-1}). \tag{7}$$

Values of total sputtering yield and SEEY used are listed in table 2.

In order to obtain partial sputtering yields of Ti and O_2 out of total sputtering yield of TiO_2, SRIM calculations are used. Sputtering of argon ions of 450 eV onto TiO_2 is simulated. The relative sputtering is used to split the total sputtering yield from table 2. The results are partial sputtering yields for Ti and O of respectively 0.041 and 0.164 (i.e. 0.082 for O_2).

According to [39], SEEY values must be reduced by 54% because of magnetic fields inducing a significant recapture of the electrons by the target for a pressure of 0.5 Pa. Using corrected SEEYs and equation (7), the number of Ti and O_2 molecules which are emitted from targets are evaluated and presented at figure 4.

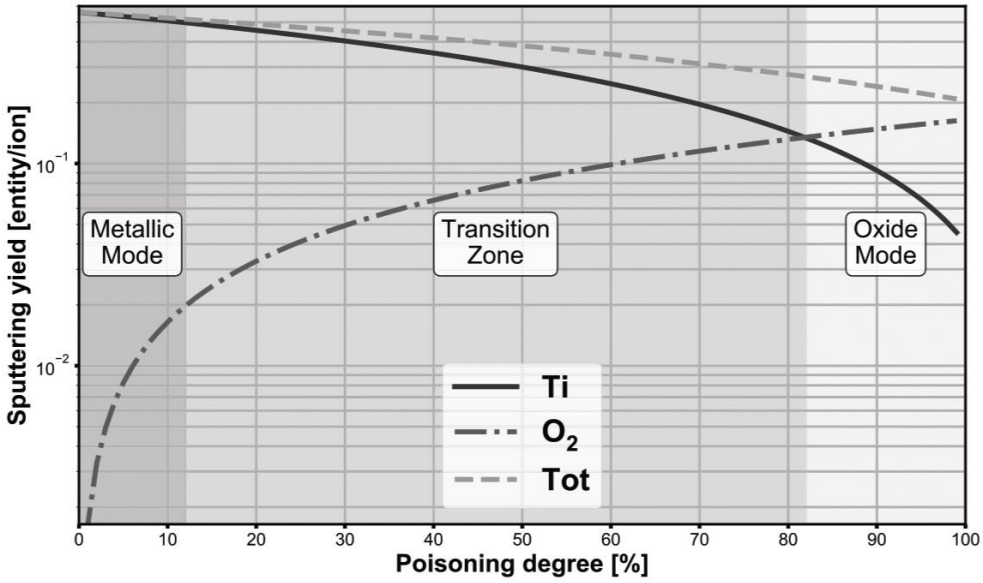

Figure 4. Evolution of target sputtering yield with target poisoning degree. Partial sputtering yield of Ti & O_2 for poisoned target are evaluated with both SRIM and value of total sputtering yield from table 2. The three operation modes are defined according to OES measurements shown on figure 6(a).

This plot can be related to [10] where the authors present an upgrade of the Berg model for reactive sputtering process and compute the sputter erosion rate versus reactive gas flow. Reactive gas flow is directly related to target poisoning degree, which is spatially non-uniform. While outside the racetrack, the target quickly falls into oxide mode, inside the racetrack the oxidation process is much slower.

(3) Regarding the angular distribution of all sputtered particles, probability of emission is assumed to be proportional to $\cos^n\theta$ with n = 1.5 [37]. Their energy distributions are evaluated by the Thompson formula [37]:

$$F(E) \propto \frac{E}{(E+U)^3}, \tag{8}$$

where U is the surface binding energy (used values are listed in table 3).

2.4. Pump definition

The pumping system is defined by adding particles absorption probability to a specific surface of the model. In this case, wall chemistry is not applied on this surface. The probability, f_i, to absorb a given species is calculated with the following.

First, the classical equation of gas kinetic theory defining the number of collisions per second onto a surface of area A is used:

$$\frac{\#\text{ of collisions}}{\text{time}} = \frac{1}{4}\frac{N}{V}A\langle v\rangle, \tag{9}$$

with $\frac{N}{V}$ corresponding to gas density and $\langle v\rangle$ the average gas velocity. The averaged gas velocity is obtained from the Maxwellian distribution by:

Table 3. Simulation parameters used in this study.

Parameter	Value
Time step	1 μs
Total physical time	3 s $\rightarrow$ 3.0 $\times$ 10^6 iterations
Surface binding energy for Ti	4.89 eV
Surface binding energy for TiO_2	6 eV
Ti and O_2 cosine exponent	1.5
Ti wall absorption coefficient	1
Wall temperature	300 K
Gas temperature	300 K
Pumping efficiency	260 l s^{-1}
Particles weighting factors	Ar: 1.0 $\times$ 10^{13} Ti: 1.0 $\times$ 10^{10} O_2: 5.0 $\times$ 10^{11}
Target-substrate distance	160 mm
Working base pressure (Ar)	0.5 Pa

$$\langle v\rangle = \sqrt{\frac{8kT}{\pi m}}. \tag{10}$$

Then, switching the density to the left-hand side of equation (9) gives the equation of the pumping speed, S_p. Indeed, it is usually defined as the volume of pumped gas per time unit:

$$S_p = \frac{A\cdot\langle v\rangle}{4}. \tag{11}$$

Equation (11) defines the maximal pumping speed of a given area, A. However, the pumping speed of a real pump is usually well below this value. To take it into account, the absorption probability, f_i, of a gas entity, with average velocity of $\langle \boldsymbol{v}\rangle$, by a surface area A is finally defined by equation (12):

$$f_i = \frac{4\cdot S_p}{A\cdot\langle v\rangle}, \tag{12}$$

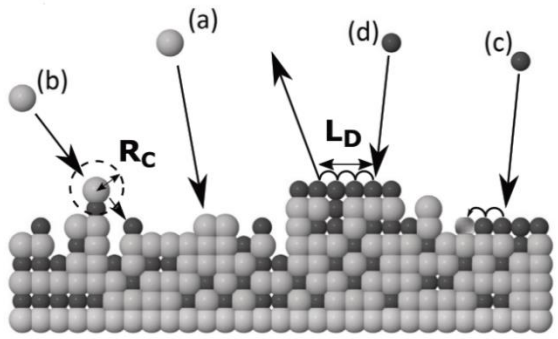

Figure 5. Schematic representation of the reactive growth model used in this study. Ti atoms are in light grey, O atoms are in dark grey. Ti atoms may be attached to the film (a) or/and induce displacement of other atoms (b). Oxygen atom can be attached (c) or reflected from the film (d) after a diffusion length of R_D.

where S_p stands for the pumping speed of the real pump i.e. 260 l s^{-1} in this study.

Table 3 summarizes the gas phase simulation conditions.

2.5. Film growth simulations

In order to simulate the growth of TiO_2, a kinetic Monte Carlo (kMC) approach on a 3D lattice is used. The model is based on a kinetic Monte Carlo code NASCAM [40]. The present work proposes a hit-and-stick model with variable sticking coefficients and with energy and momentum transfer from the deposited atoms to the film. The volume of discharge chamber is the source of fluxes of particle towards the substrate. Generally speaking, NASCAM includes five different possible fluxes of atomic species in the model:

– Metallic neutral particles,
– Metallic ions,
– Reactive neutral particles,
– Reactive ions,
– Neutral gas atoms.

Each flux is characterized by its own energy distribution and its own angular distribution. Neutral atoms are supposed to be low energy particles with broad angular distribution due to collisions with background gas. On the contrary, ions may have high energy and sometimes may come to the substrate at almost normal incident angles.

The critical point of the model is how reactive particles interact with the film. In this work, the following model is proposed (figure 5):

(1) Particles are considered to be randomly thrown towards the substrate with velocities according to energy and incident angular distribution functions computed by DSMC.
(2) Ti or O atoms may occupy predefined atomic position in a lattice. A simple cubic lattice is used. Such a lattice may be used as a model for amorphous state of TiO_2 since no difference on the crystallographic configuration is made in this work.
(3) When a Ti atom hits the surface of the growing film, it is attached with the sticking probability equals to 1.
(4) When an O atom hits the film surface, it is allowed to diffuse at the surface for a maximum distance L_D. If no free Ti bound is found, oxygen is then reflected. L_D parameter was introduced to mimic diffusion of oxygen atoms along the surface as it was shown in [41]. $L_D = 40$ Å is used to get the proper stoichiometry of titania in poison mode of the film growth. For the lower values of L_D, the stoichiometry of the titania film is noticeably different from 2. It is well known that the reactive flux is much higher than the flux of metal atoms (see later in this work). If all reactive atoms would stick to the surface, the resulting film would be over stoichiometric or only composed of reactive atoms. As this is not the case, most of the reactive atoms are reflected from the film. At the same time, the longer reactive atom can diffuse searching for a non-oxidized spot on the film, the higher will be the oxidation degree of the film for the same ratio of reactive flux to metallic flux. The shorter diffusion length of a reactive atom on the surface means the higher probability of reflection.
Opposite to DSMC simulations, oxygen attachment is not a probabilistic event in the kMC model. Whether an oxygen atom is attached to or reflected from the film is determined by the local composition of the film. However, on a long simulation run one can introduce an efficient sticking coefficient i.e. probability of oxidation reaction which is equal to the ratio of the oxygen incident flow to the oxygen content in the film. This point is discussed in more details in section 3.4 below.
(5) As during the film growth one may expect that fluxes of particles with non-thermal energies would influence the process of film growth, a model of interaction of energetic particles with the film is introduced. According to the model, an incident particle with energy E_0 transfer energy to a group of atoms of the film, which is located within the sphere with radius R_C centred on collision site of the particle with the film. All the atoms inside the sphere get energy equals to $\frac{E_0}{N_c}$, where N_c is the number of atoms inside the sphere. If the energy of the recoil is larger than displacement energy and there is an unoccupied lattice site nearby, the recoil is displaced to this site. The model assumes that only primary recoil and its nearest neighbours can move i.e. R_C is equal to a lattice parameter (≈3 Å). According to our knowledge, the displacement threshold energy is not known. However, this value should be less than the surface binding energy, which is the required energy to remove an atom from the surface. Moreover, the displacement energy for each given collision depends on the number of neighbours of the recoil. Therefore, the displacement energy for each elementary collision might be different. For all these reasons, a value of 3 eV is used for the displacement energy in the simulation.

Table 4. NASCAM simulation parameters used for this study.

Parameter	Value
Substrate size (nm)	300×3
Number of deposited atoms	3×10^6
Ti sticking coefficient	1
O sticking coefficient	From 0 to 1, depending on local film's surface composition
Displacement energy (eV)	3
Oxygen diffusion range, L_D (nm)	20

(6) As the simulations are performed at room temperature and the diffusion barriers are rather high ~1 eV, the diffusion of deposited atoms are neglected.
(7) The substrate dimensions are 1000×10 unit cells, which correspond to an actual size of approximately 300 nm $\times$ 3 nm, and the total number of deposited atoms, both titanium and oxygen is 3×10^6.
(8) Only Ti and O atoms were taken into account for the simulation of the film growth in accordance to gas phase simulations.

Although the model gives the possibility to have five different fluxes of depositing species, in the present work we use only fluxes of neutral titanium and atomic oxygen as they have been calculated by DSMC simulations i.e. molecular oxygen from DSMC is converted into atomic oxygen. In other words, we assume the dissociation of molecular oxygen during deposition event. If one wants to take into account ion fluxes towards the substrate then it can be done within the framework of this model. However, such simulations are out of the scope of the present study. Parameters of the simulations are summarized in table 4.

One may argue that it is possible to directly compute the stoichiometry from the DSMC simulation. However, due to computational resources, it is not possible to run tens of DSMC calculations. On the opposite, NASCAM is a very fast simulation tool. By only running a few DSMC's with different oxygen inlets and extract the particles fluxes towards substrate, it is possible to link O_2/Ti fluxes on substrate with oxygen inlet and then run as many NASCAM simulations as required to simulate the complete hysteresis curve.

2.6. Experimental measurements

Titanium dioxide and metallic titanium films are deposited at room temperature on a water-cooled substrate holder on silicon wafers and glassy carbon by dual DC magnetron reactive sputtering as described in figure 1. The used targets are 2 inches in diameter, 0.25 inch in thickness and made of pure Ti (99.995%) provided by the Kurt J. Lesker Company. The power supplies used are TDK Lambda Genesys, one for each magnetron. For deposition on glassy carbon, $^{18}O_2$ is used as reactive gas with the aim to differentiate oxygen from gas inlet and residual oxygen for compositional and gas phase analysis. Depositions on a silicon wafer with natural oxygen were performed to investigate the film morphology. Each magnetron is powered in constant current mode. The sample holder is grounded. The magnetrons configuration is set to close field for all the study. The purpose of such a configuration is to limit the flux of charged species impinging the substrate. Indeed, in close field, magnetic lines from one magnetron are closed on the other one. On the contrary, open field configuration has magnetic lines oriented towards the substrate favouring plasma expansion towards the substrate [42]. For this study, it was important to work in closed field to limit the flux of charged species onto the substrate as only neutral particles transport is simulated. The oxygen mass flow is controlled by a Nova Fabrica Ltd regulation system (FloTron™) allowing feedback regulation control with optical emission signal.

Three experimental parameters were measured during deposition: (i) oxygen partial pressure, (ii) deposition rate, (iii) targets voltage and (iv) optical emission of Ti. Devices used for those measurements are the following:

(i) Hiden Analytical HAL 301 mass spectrometer
(ii) Inficon Quartz Crystal Microbalance. The device is located at centre substrate location.
(iii) Data provided directly by TDK Lambda Genesys power supply.
(iv) FloTron (Ti: 363 nm)

200 nm to 500 nm thick coatings were deposited to compare the experimental stoichiometry with the one predicted by simulations. Glassy carbon samples stoichiometry is measured by Rutherford backscattering spectroscopy (RBS) with alpha particles of 2.0 MeV impinging the sample at normal incidence; the backscattered particles were collected at 135°, 165° and 175° and spectra were analysed with DataFurnace [43]. RBS is used instead of classical XPS analysis to avoid bias from preferential sputtering and get proper values of stoichiometry. Moreover, glassy carbon samples had been decided to avoid channelling in the substrate and overlapping signals of species during analysis.

3. Results

3.1. Plasma measurements

To measure the discharge parameters, plasma in pure argon with a flow of 18 sccm (one inlet of 9 sccm at each magnetron) is ignited with a current of 0.5 A for each magnetron. With an effective pumping speed of about 70 l s^{-1}, the resulting pressure is 0.5 Pa and will be the base pressure for all experiments/depositions. Then oxygen is added, oxygen inlet varies from 0 to 9 sccm with steps of 0.5 sccm. Each step is sustained for 2 min and total pressure, deposition rate and target voltages

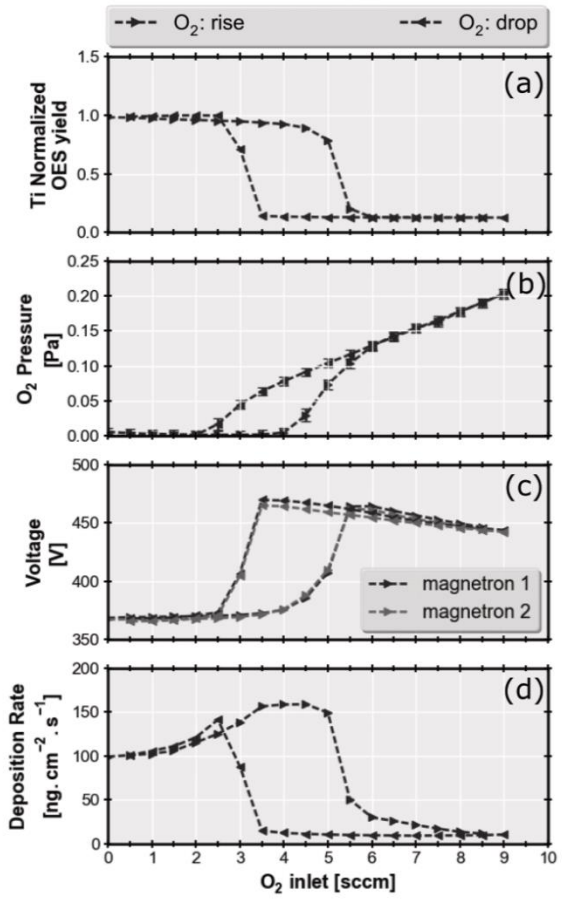

Figure 6. Experimental hysteresis curves. (a) Normalized optical emission yield of Ti. (b) Oxygen partial pressure (Pa). (c) Discharge voltage (V). (d) Deposition rate (ng/cm^2/s) as measured by QCM. For each parameter, the increasing oxygen inlet case is represented with right-hand oriented triangle and the decreasing oxygen inlet case with left-hand oriented triangle. For the discharge voltage (c), both magnetron voltages were recorded.

are recorded. Time integration is then performed to present data depending on oxygen inlet in figure 6.

3.2. Film deposition and characterization

To study the effect of oxygen concentration in the plasma on coating properties, several depositions with different oxygen content in the chamber are performed. These depositions correspond to different location on the hysteresis curve (i.e. Ti OES plasma intensity). Four different deposition conditions, as listed in table 5, are chosen: one in metallic mode, two in the transition zone and finally one in oxide mode.

In the following, references to 2 sccm, 4 sccm, 6 sccm and 8 sccm will be done. It corresponds to the oxygen inlet used for the corresponding DSMC simulations. The recorded deposition rate is the averaged value over the deposition. It is calculated by measuring the deposition time and sample's final thickness. This last measurement is performed with Dektak equipment.

Table 5. Experimental conditions of the depositions. The deposition rates in this table are calculated thanks to deposition time and final thickness. Data in brackets reflect the flow variation to keep the OES Ti yield constant.

		Metallic	Transition zone		Oxide
Parameters		#1	#2	#3	#4
OES Ti normalized intensity		0.88	0.70	0.45	0.10
Corresponding O_2 inlet (sccm)		2	[3–4]	[5–6]	8
Deposition rate (Å s^{-1})		2.1	3.3	2.4	0.24
Deposition time (s)		1736	1389	1263	8224
Initial vacuum (Pa)			$\leqslant 1.3 \times 10^{-3}$		
Films composition	Ti (%)	64.1	36.6	33.4	33.3
	O (%)	35.9	63.4	66.6	66.6

Table 6. Experiment-simulation comparison of gas partial pressure in steady state regime. Arrows next to O_2 inlet depict whether the simulation starts from metallic mode (↗) or oxide mode (↘).

	Ar (Pa)		O_2 (Pa)		
O_2 inlet	Exp.	Sim.	Exp. $^{16}O_2$	Exp. $^{18}O_2$	Sim.
2 sccm ↗	0.50	0.48	0.3×10^{-3}	2.9×10^{-3}	1.6×10^{-3}
4 sccm ↗	0.50	0.48	1.2×10^{-3}	4.8×10^{-3}	5.6×10^{-3}
5 sccm ↗	0.50	0.48	0.014	0.072	0.054
6 sccm ↗	0.50	0.47	0.017	0.128	0.131
8 sccm ↗	0.50	0.47	0.016	0.177	0.172
4 sccm ↘	0.50	0.48	0.010	0.078	0.077
3 sccm ↘	0.50	0.48	7.9×10^{-3}	0.044	0.034

3.3. DSMC simulations

Transport simulations by DSMC are performed in several steps. First, the partial pressure of Ar and O_2 is computed assuming no sputtering. Results are presented in table 6 and compared with the experimental data. One can observe a near perfect agreement except for very low partial pressure where pressure is below mass spectrometer sensitivity.

Second, simulations including sputtering and surface chemistry as described above are performed. All simulations start without oxygen and with an initial surface oxidation of 90% i.e. initially targets are also 90% oxidized. Figure 7 presents the sample holder absorption of oxygen and titanium over time.

Final oxygen partial pressure of both experiments and simulations are plotted in figure 8 for the same experimental values as in figure 6.

Computational time for each point was about 160 h on 96 CPUs. Angular and energy distributions of particles arriving at the substrate are sampled at different locations as depicted in figure 1. As the total pressure variation for the deposition with different oxygen content in the chamber is only of 30%, particles distributions have the same shape. For this reason

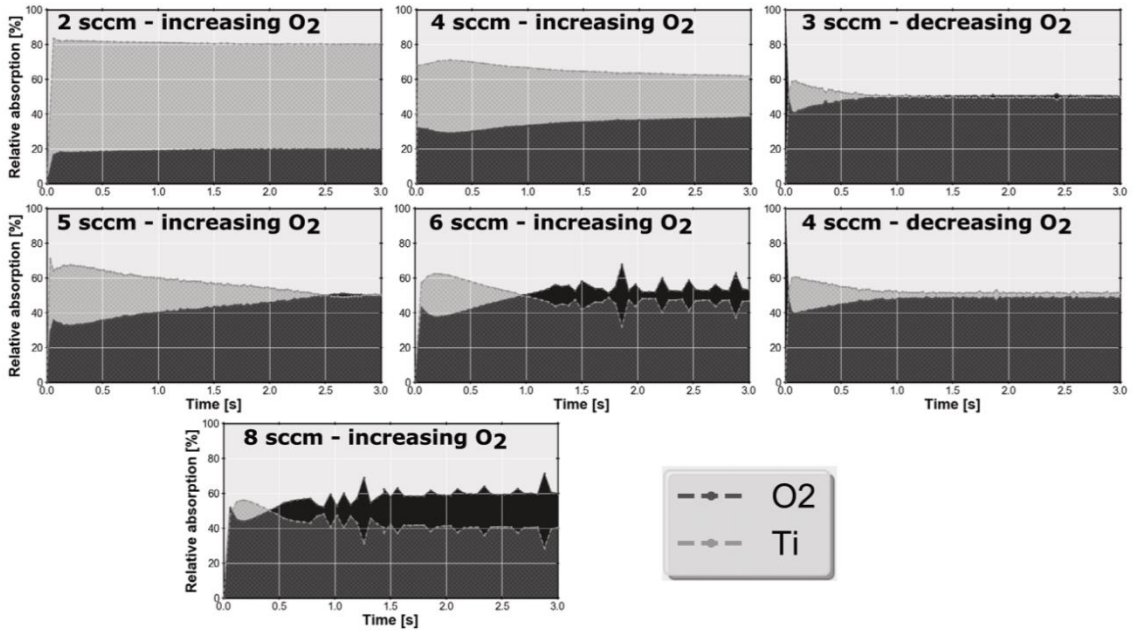

Figure 7. Time evolution (0–3 s) of titanium (grey) and oxygen (black) relative absorption (0%–100%) on the substrate holder.

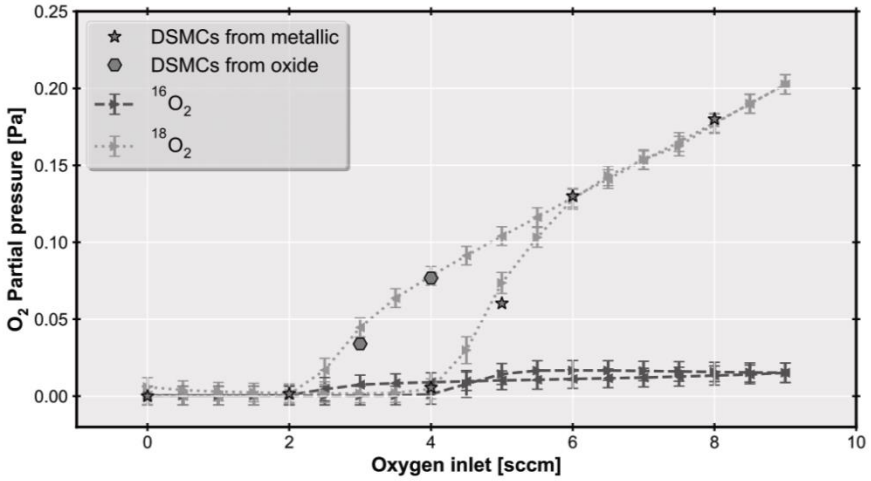

Figure 8. Comparison of oxygen partial pressure from DSMC (stars and octogons) and mass spectroscopy measurements (dashed curve). Stars stand for simulations starting with an initial O_2 partial pressure of 0 Pa and octogons for simulations starting from the 8 sccm star point i.e. O_2 partial pressure of 0.18 Pa.

only the 8 sccm O_2 inlet is presented. Figures 9 and 10 respectively corresponds to centre and corner substrate location.

Finally, figure 11 shows the fluxes expressed in SCCM toward the substrate as computed by DSMC. Ar is the major flow, O_2 and Ti flows evolved according to the O_2 inlet.

3.4. Film growth simulation and related properties

The final simulation step is to use particle fluxes, their angular and energy distributions and simulate film growth with NASCAM. In total, 15 simulations were performed; 4 directly with the data from DSMC and 11 by modifying the O_2/Ti incident flow ratio to extrapolate film stoichiometry for other oxygen inlets. The results are presented in figure 12 as well as film stoichiometry measured by RBS. Stoichiometry derived from DSMC's via the substrate final deposition rate at the desired location on the sample holder is also plotted for comparison. A classical S shape curved is obtained for the computed and measured concentrations versus the O/Ti incident flow. Stoichiometric films are obtained for O/Ti flow larger than ~80. Along with the results of the stoichiometry, the percentage of the reflected oxygen is presented on the same plot. As one can see, the model of film growth gives the proper behaviour of this parameter. The reflected oxygen also

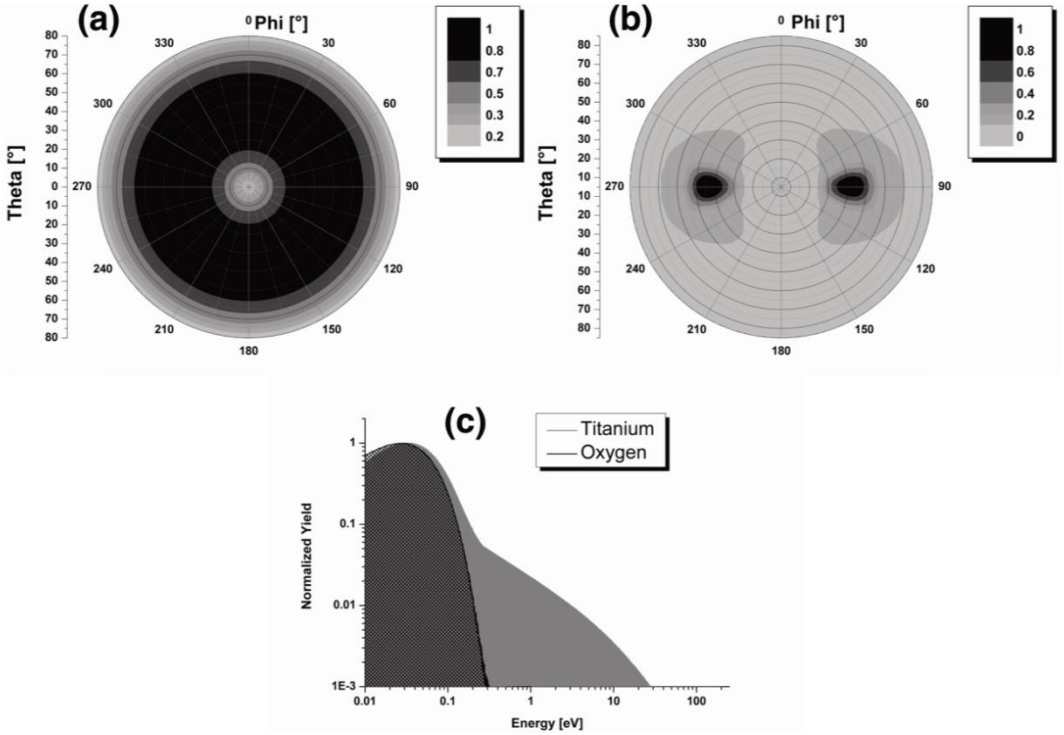

Figure 9. Angular and energy distributions in a steady state regime at central substrate location extracted from DSMC (8 sccm). Normalized angular distribution of oxygen (a); normalized angular distribution of titanium (b); normalized energy distribution of both species (c).

exhibits an S shaped curve, to reach almost 100% in poisoned mode when oxygen is in excess in gas phase by several order of magnitude compared to titanium. One can easily get the relationship between O/Ti incident number of atoms (x), the stoichiometry (s) and the relative amount of reflected oxygen (r). Let us define $f(\mathrm{O})$ and $f(\mathrm{Ti})$, respectively the flux of oxygen and titanium toward the substrate. Let us also define $N(\mathrm{O})$ and $N(\mathrm{Ti})$, respectively, as the amount of oxygen and titanium into the film.

$$x = \frac{f(\mathrm{O})}{f(\mathrm{Ti})} \tag{13}$$

$$s = \frac{N(\mathrm{O})}{N(\mathrm{Ti})}. \tag{14}$$

Then, the relative amount of oxygen reflected on the film is:

$$\begin{aligned} r &= 1 - \frac{N(\mathrm{O})}{f(\mathrm{O})} \\ &= 1 - \frac{s\,N(\mathrm{Ti})}{f(\mathrm{O})}. \end{aligned} \tag{15}$$

As the sticking coefficient of Ti is 1, all the incident titanium atoms are attached to the film

$$N(\mathrm{Ti}) = f(\mathrm{Ti}). \tag{16}$$

Finally,

$$r = 1 - \frac{s}{x}. \tag{17}$$

When the oxygen fraction of the incident flow is low, $x < 1$, the amount of reflected oxygen grows linearly with x. At $x \gg 1$ most of the oxygen is reflected, as the surface tends to be fully oxidized.

Generally speaking, one could define $\frac{s}{x}$ as the effective sticking coefficient of O for high reactive metal film. Partial Ti and TiO_2 fractions of the film, θ_{Ti} and $\theta_{\mathrm{TiO_2}}$ are introduced to allow comparison of the computed effective sticking coefficient with sticking coefficient used in DSMC simulations:

$$\theta_{\mathrm{TiO_2}} = \frac{s}{2} \tag{18}$$

$$\theta_{\mathrm{Ti}} = 1 - \theta_{\mathrm{TiO_2}}. \tag{19}$$

The effective sticking coefficient of oxygen as calculated from NASCAM simulations is plotted on figure 13 along with the sticking coefficient used for DSMCs.

Figure 14 shows a side-by-side comparison of TiO_2 morphology as measured by X-SEM and simulated by NASCAM (3 million atoms each simulation). One can see the development of columns for the corner sample, while at the centre location, the sample is more dense and with no tilted columns.

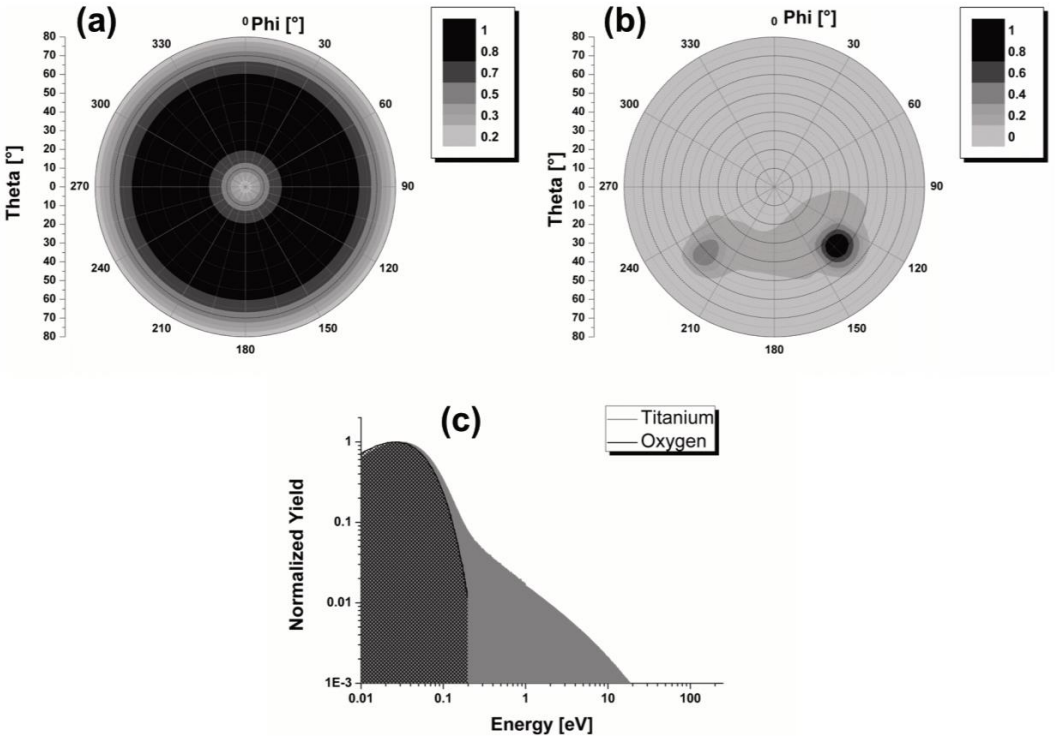

Figure 10. Angular and energy distributions in a steady state regime at corner substrate location extracted from DSMC (8 sccm). Normalized angular distribution of oxygen (a); normalized angular distribution of titanium (b); normalized energy distribution of both species (c).

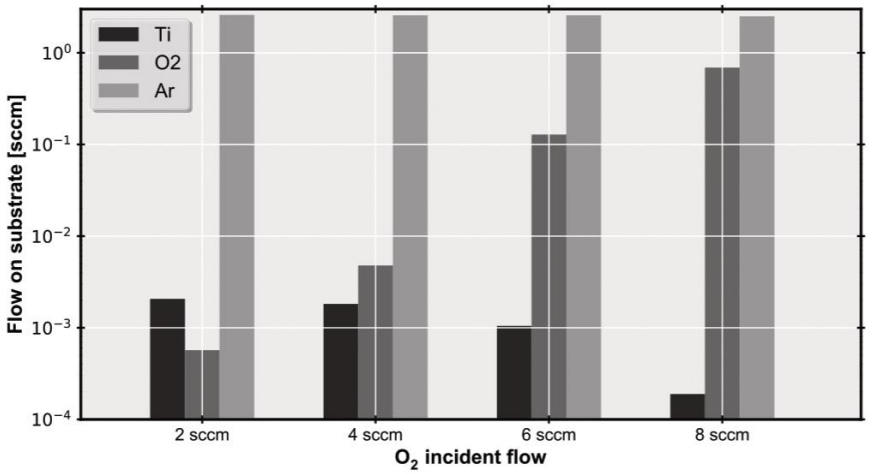

Figure 11. Neutral particles flow on substrate at central location (1 cm^2) as a function of O_2 inlet.

Figure 15 presents the comparison of the column angles (β) and column width of corner samples for each deposition condition obtained by SEM pictures and by NASCAM simulations.

4. Discussion

The mass deposition rate is decreasing by a factor of 10 with the increase of oxygen inlet from 2 to 8 sccm (figure 6). This is in agreement with the calculated titanium flow to the substrate (by DSMC), which also shows a drop by a factor of 10 (see figure 11). The reason of this drop can be found on figure 4, partial sputtering yield of titanium decreases from 0.56 to 0.048 when switching to poisoned mode. Hence it is not probable to grow over-stoichiometric titanium oxide (i.e. TiO_x $x > 2$), it is the titanium flow which rules the film growth. For the 2 sccm and 4 sccm cases, by comparing figures 6 and 7 one can see that the mass deposition rate increases while Ti flow

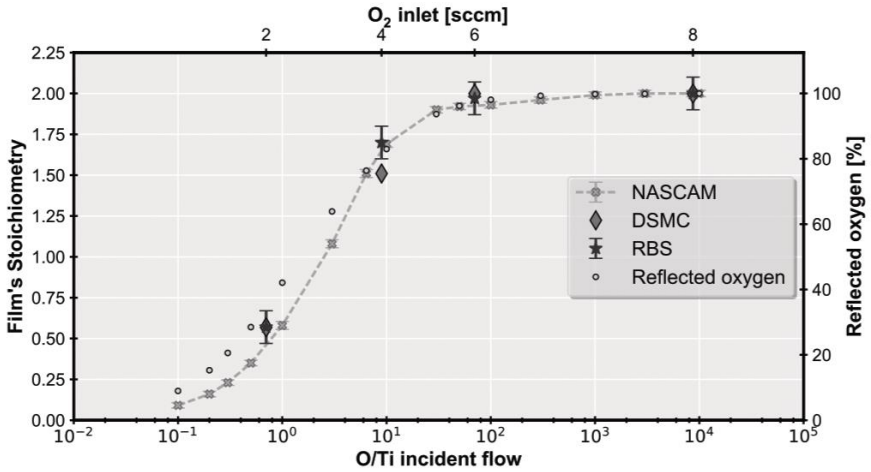

Figure 12. Comparison of film stoichiometry from (i) NASCAM simulation, (ii) DSMC and (iii) RBS measurements. This value is plotted either as a function of oxygen inlet in the chamber (upper axis) or the corresponding ratio O/Ti incident flow on the sample. The percentage of the reflected oxygen estimated by NASCAM simulation is also plotted.

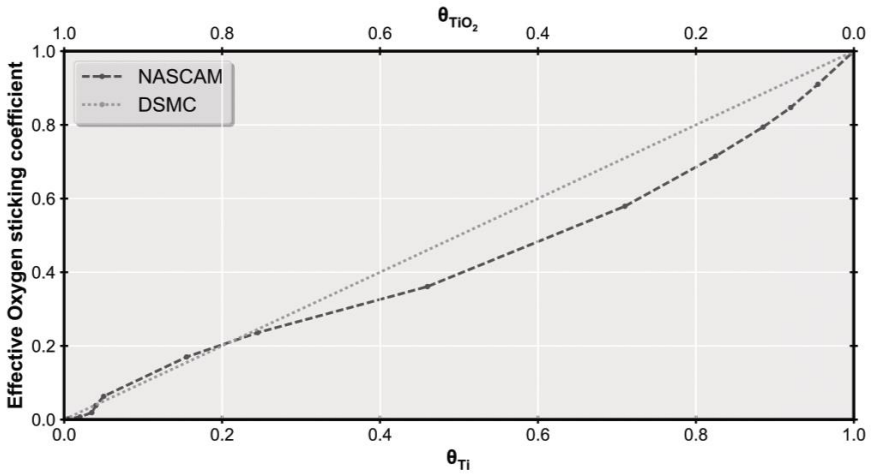

Figure 13. Effective oxygen sticking coefficient as calculated by NASCAM (dashed line) and oxygen sticking coefficient used for DSMC simulations (dotted line). Both are function of the metallic Ti fraction and TiO_2 fraction of film's surface.

remains almost constant. This is simply due to the formation of TiO_2 whose mass is larger than Ti.

Figure 7 presents the relative fluxes of titanium and oxygen on the sample holder. It shows that at 2 sccm oxygen inlet, the process operates in metallic mode. A stable value of about 80% of incoming species is titanium. The 4 sccm case is close to steady state behaviour after 3 s of real time simulation. Indeed, after 3 s of simulation, the titanium flow onto the substrate has decreases of about 15% which corresponds to the experimental decrease of OES Ti yield used for the feedback control loop. The 6 sccm case has the same behaviour as the 4 sccm case with a switch to oxide mode after 1.8 seconds. As it can be expected, the 8 sccm case exhibits a fast drop into oxide mode after only 0.35 s.

Oxygen partial pressures as calculated by DSMC are compared to experimental values in figure 8. The comparison of simulated oxygen partial pressure and experimental values shows a very good agreement. Since DSMC calculations compute O_2 partial pressure in the whole chamber volume, it is possible to extract values at the mass spectrometer location. It is very important to pay attention to this aspect. Indeed, for low O_2 inlet, the O_2 partial pressure in the chamber is highly non-uniform. It strongly depends on gas inlet location, reactive gas flow, chamber design and magnetron current. Other simulation tools may be used to predict the hysteresis of such common reactive magnetron sputtering (usually implementing Berg model [8, 9, 44]) such as RSD [15], however they do not compute the transport of reactive gas over chamber volume and therefore do not allow calculation of particle fluxes onto the substrate. Another advantage of a DSMC approach is the possibility to obtain energy and angular distributions of each species simulated as well as their absolute flows. Knowing those data is essential if one wants to think about evaluating film growth by using other simulation tools.

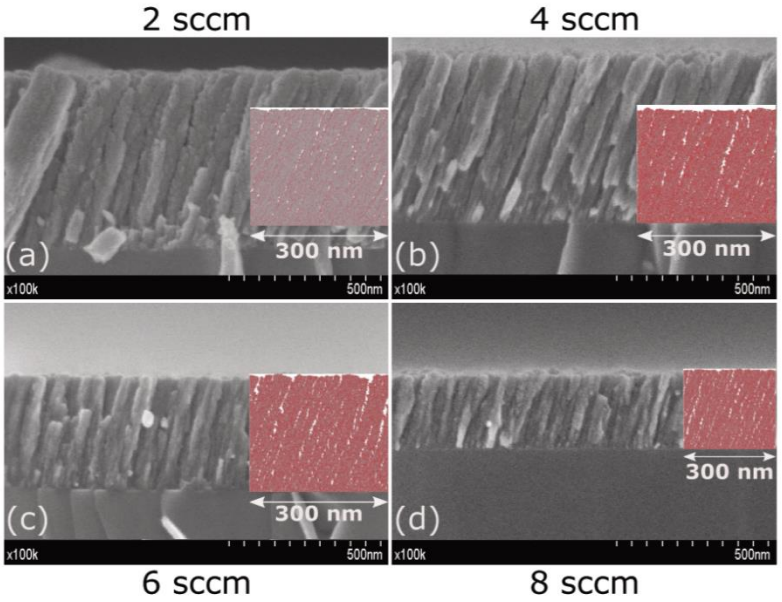

Figure 14. Comparison of the film's structure between SEM analyses and NASCAM simulations for the corner sample located along the hysteresis curve.

Figures 9 and 10 present the angular and energy distributions at the different substrate locations of titanium and oxygen. The oxygen angular distributions (figures 9(a) and 10(a)) are broad and have no preferential direction because it is part of the background pressure, and therefore the energy distribution is thermalized-Maxwellian like. The titanium case is very different as it only originates from sputtered cathodes. The angular distribution (figures 9(b) and 10(b)) is narrower and two hot spots are observed, one at $\theta = 45°$ and the other one at $\theta = -45°$. It corresponds to the directions of magnetrons from the sample point of view.

The energy distribution of titanium (figures 9(c) and 10(c)) exhibits two components. The first one, at low energy is very similar to the oxygen one and corresponds to thermalized titanium. The second one, at energies higher than 0.3 eV is the tail of the initial Thomson distribution slightly shifted to the lower energies as atoms collide in gas phase. DSMC time dependent simulations also reveal that Ti angular distribution at the sample surface does not evolve during all the deposition process on the contrary to oxygen. At the early stage of the discharge (~10 ms), the sputtered oxygen corresponds to initial oxygen on targets surface as all surfaces started 90% oxidized. As time went on, all chambers' surfaces oxidized and the overall partial pressure of oxygen increased, i.e. sputtered oxygen will spend more time in gas phase before to be absorbed by Ti on surface or pumped out. For this reason, the angular distribution of sputtered oxygen exhibits no more preferential direction after several seconds. At this time, almost all sputtered oxygen reaching the substrate is thermalized.

Figure 12 shows the comparison of computed DSMC and NASCAM film stoichiometry and the experimental ones. One can see that transition from metal to oxide mode occurs between 2 and 4 sccm. This is in relation with the inversion of the Ti and O_2 flow as demonstrated on figure 11. On the one hand, titanium flow decreases due to target poisoning and walls oxidation. On the other hand, oxygen partial pressure increases so does oxygen flow toward the substrate. For the same oxygen and titanium flow, the surface is more likely metallic. Indeed a titanium atom has a probability of 1 to stick on the surface. It is not the case for molecular oxygen. If such a molecule hits the substrate on an oxidized site, the molecule is not absorbed and is reflected instead. The more the surface is oxidized, the less the probability for an oxygen molecule to find a metallic titanium. Therefore, most of the oxygen species are reflected as shown in the same figure. It is worth to emphasize that in DSMC simulation, oxidation events are probabilistic as stated by equation (1). It only depends on the metallic fraction of titanium on surface (θ_{Ti}). In NASCAM simulations oxidation events i.e. atoms of oxygen sticking to the surface, are purely deterministic, no random number is involved. It only depends on the local surface composition of the film. Although it is close to the probability of the oxidation as it is introduced in the DSMC model, there are some differences between the effective sticking coefficient obtained from film growth simulations and the DSMC model (figure 13). These discrepancies can be attributed to the fact that splitting the content of the film into pure Ti and TiO_2 is not quite correct. Also, one can distinguish partial fractions of the surface as in DSMC and in the film as they are discussed here, it can be different. These differences between the two models explain the discrepancies of figure 12 regarding stoichiometry.

Finally, figure 14 compares evolution of the corner location film cross section along the hysteresis curve as measured experimentally by SEM with those obtained by simulation. One can see the presence of columns which are reproduced by simulations. Reported column's tilting angle (β) values averaged over six columns are plotted on figure 15. In addition, for the purpose of discussion, the simulated values for

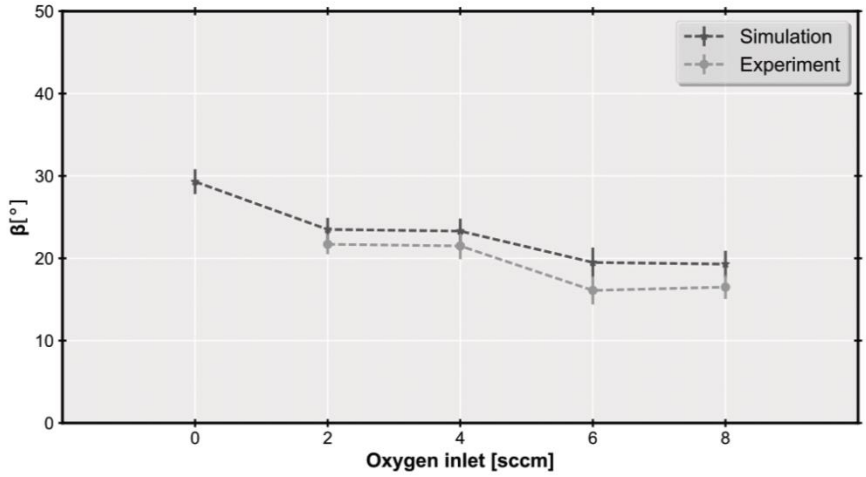

Figure 15. Comparison of column angles (β) of corner sample for NASCAM simulation and experimental coatings.

pure metallic deposition (no oxygen) are presented. An almost linear decrease with the oxygen flow is observed. In the metallic mode, film growth is mainly ruled by the flow of titanium atoms which come from targets i.e. with a preferential incoming direction. Directional atoms land on the substrate and according to the hit and stick film growth model, give rise to columns which are the result of shadowing effect as described in [45]. In the oxide mode, film growth is ruled both by titanium and oxygen flow, with high partial oxygen pressure. As oxygen comes uniformly from the whole space of the vacuum chamber, there is no preferential direction for incoming O_2 (see figures 9 and 10) and so no related shadowing effect for oxygen. The fluxes combination of these two species may explain the smaller value of column tilting angle in simulations for the oxide mode. It has to be noted that the decrease of column angle is temperature dependent. Indeed, for non-cooled substrate previous work demonstrated an increase of β while switching from metallic to oxide mode [46, 47]. It is explained by atoms diffusion. When oxygen atoms are added, they reduce the diffusion of Ti atoms by fixing it. The net result is an increase of β as mobility of deposited atoms is reduced. It is also worth pointing out that only neutral species were taken into account in simulations, though ions usually have much higher mean energies than neutral species. So a fraction of the energy brought to the substrate is neglected, which could result in slightly different film morphology. Indeed, as energetic particles arrive to the film mostly from one side, they force the deposited atoms to move in the same direction than the impact. Thus, the effect of energetic flow is to straighten out the columns. This may be the reason why the experimental tilting angles of the columns are smaller than those obtained in the simulations. In addition to ions, radiations may also impact the film growth. In [48], the authors tried to make a distinction between the energy flux brought by plasma species and infrared (IR) radiation emanating from the heated target. In a balanced magnetron discharge of 400 W they conclude that 36% of the energy flux towards the target is from IR radiation. The effect of radiation is to heat up the substrate. This energetic contribution is not taken into account in the used NASCAM simulations, given the substrate is water-cooled.

Also, it is not possible to infer anything regarding film crystallinity as the main parameter influencing it is energy brought to the substrate [48]. Moreover it is now well admitted [49–51] that in oxide mode, O^- ions are generated at target surface and can then reach substrate location with very high energy (a few hundreds of eV). Even in very limited quantity, those ions influence film growth and are worth a dedicated study. This is why there is on-going work on taking ions into account, both in plasma phase simulations and in film growth modelling.

5. Conclusion

A multi-scale plasma deposition process simulation chain was demonstrated. The current model allows transport modelling of sputtered material in gas phase with a DSMC algorithm dedicated to neutral species. A Berg-like wall chemistry was setup to model reactive absorption on all surfaces. Angular and energy distributions were extracted at desired locations and were used to model film growth by kMC. This modelling strategy was successfully applied on the study of $TiO_{x\leqslant 2}$ film growth from metal to oxide regime and in a geometry involving two magnetrons and low ion bombardment of water-cooled substrate. The model accurately reproduced the composition and morphology of deposited.

The growth of amorphous TiO_x film is explained by means of a so-called hit-and-stick model extended by the attachment rules for reactive species. Deposited atoms of Ti are attached to the film at the same place where they hit it. The sticking coefficient of the oxygen depends of the local oxidation degree of the deposited film. Indeed, oxygen can only be attached to non-fully oxidized Ti atoms in the vicinity of the hitting place. Ti flow rules the final morphology. Non-directional oxygen flow reduces by a small amount the column angle. Simulations can very accurately reproduce the films composition and offer a way to compute the effective sticking coefficient of reactive species on sub-stoichiometric films. In this work, it was also

shown both by experiment and by simulation that in reactive magnetron sputtering, metallic species are acting as a backbone for the film morphology, the role of oxygen and ions (Ti^+, O^-, …) being mostly related to crystalline phase selection, crystallinity and density. Therefore as a perspective, the next step is to include charged species into the simulation process. It requires calculation of both the electric and magnetic fields during the transport modelling of particles.

Acknowledgments

The authors are grateful to the European Commission for the financial support of the CORNET ERA-NET project CAPRICe (Computer Aided Process Refinement for Intelligent Coatings) under contract number IGF 101 EN. For all simulations, computational resources have been provided by the Consortium des Équipements de Calcul Intensif (CÉCI), funded by the Fonds de la Recherche Scientifique de Belgique (F.R.S.-FNRS) under Grant No. 2.5020.11. More specifically the Tier-1 super-computer of CENAERO was mainly used (http://tier1.cenaero.be/fr/zenobe). The authors would also like to thank the simulation team of the Fraunhofer institute of Braunschweig for their development work and advice.

ORCID iDs

R Tonneau https://orcid.org/0000-0002-3246-8420

References

[1] Sommerer T J, Hitchon W N G and Lawler J E 1989 Self-consistent kinetic model of the cathode fall of a glow discharge *Phys. Rev.* A **39** 6356–66
[2] Fixel D A and Hitchon W N G 2007 Convective scheme solution of the Boltzmann transport equation for nanoscale semiconductor devices *J. Comput. Phys.* **227** 1387–410
[3] Dendy R O 1990 *Plasma Dynamics* (Wotton-under-Edge: Clarendon)
[4] Bukowski J D, Graves D B and Vitello P 1996 Two-dimensional fluid model of an inductively coupled plasma with comparison to experimental spatial profiles *J. Appl. Phys.* **80** 2614–23
[5] Kwon U H and Lee W J 2006 Multiscale Monte Carlo simulation of circular DC magnetron sputtering: influence of magnetron design on target erosion and film deposition *Japan. J. Appl. Phys.* 1 **45** 8629–38
[6] Shidoji E, Nakano N and Makabe T 1999 Numerical simulation of the discharge in d.c. magnetron sputtering *Thin Solid Films* **351** 37–41
[7] Bultinck E and Bogaerts A 2009 Particle-in-cell/monte carlo collisions treatment of an Ar/O_2 magnetron discharge used for the reactive sputter deposition of TiO_x films *New J. Phys.* **11** 103010
[8] Kusano E 1993 Modeling of time-dependent process changes and hysteresis in Ti-O 2 reactive sputtering *J. Appl. Phys.* **73** 8565–74
[9] Knizikevičius R 2010 Simulation of reactive sputter deposition of TiO_2 films *Mater. Sci.* **16** 202–4
[10] Berg S, Särhammar E and Nyberg T 2014 Upgrading the 'Berg-model' for reactive sputtering processes *Thin Solid Films* **565** 186–92
[11] Särhammar E, Nyberg T and Berg S 2015 Applying 'the upgraded Berg model' to predict hysteresis free reactive sputtering *Surf. Coat. Technol.* **279** 39–43
[12] Depla D, Heirwegh S, Mahieu S and De Gryse R 2007 Towards a more complete model for reactive magnetron sputtering *J. Phys. D: Appl. Phys.* **40** 1957–65
[13] Berg S and Nyberg T 2005 Fundamental understanding and modeling of reactive sputtering processes *Thin Solid Films* **476** 215–30
[14] Bogaerts A, Bultinck E, Kolev I, Schwaederlé L, Van Aeken K, Buyle G and Depla D 2009 Computer modelling of magnetron discharges *J. Phys. D: Appl. Phys.* **42** 194018
[15] Strijckmans K and Depla D 2014 A time-dependent model for reactive sputter deposition *J. Phys. D: Appl. Phys.* **47** 235302
[16] Baguer N, Georgieva V, Calderin L, Todorov I T, Van Gils S and Bogaerts A 2009 Study of the nucleation and growth of TiO_2 and ZnO thin films by means of molecular dynamics simulations *J. Cryst. Growth* **311** 4034–43
[17] Taguchi M and Hamaguchi S 2007 MD simulations of amorphous SiO_2 thin film formation in reactive sputtering deposition processes *Thin Solid Films* **515** 4879–82
[18] Georgieva V, Saraiva M, Jehanathan N, Lebelev O I, Depla D and Bogaerts A 2009 Sputter-deposited Mg–Al–O thin films: linking molecular dynamics simulations to experiments *J. Phys. D: Appl. Phys.* **42** 65107
[19] Zheng X, Yang B, Zhu Z, Wu B and Mao Y 2007 Kinetic Monte Carlo simulation of growth of $BaTiO_3$ thin film via pulsed laser deposition *Trans. Nonferr. Met. Soc. China* **17** 1441–6
[20] Elsholz F, Schöll E and Rosenfeld A 2007 Kinetic Monte Carlo simulations of amorphous thin-film growth *Phys. Status Solidi* **244** 3639–46
[21] Gunn D S D, Allan N L and Purton J A 2014 Adaptive kinetic Monte Carlo simulation of solid oxide fuel cell components *J. Mater. Chem.* A **2** 13407–14
[22] Tahan C, Suewattana M, Larsen P, Zhang S and Krakauer H Kinetic Monte Carlo simulations of crystal growth in ferroelectric alloys *Phys. Rev.* B 71 224101
[23] Petrov P and Miller W 2009 A new kinetic Monte Carlo method for the thin film growth of perovskites *Surf. Rev. Lett.* **16** 909–16
[24] Kara A, Trushin O, Yildirim H and Rahman T S 2009 Off-lattice self-learning kinetic Monte Carlo: application to 2D cluster diffusion on the fcc(1 1 1) surface *J. Phys.: Condens. Matter* **21** 84213
[25] Vernon L, Kenny S D, Smith R and Sanville E 2011 Growth mechanisms for TiO 2 at its rutile (1 1 0) surface *Phys. Rev.* B **83** 75412
[26] Rubio J E, Jaraiz M, Martin-Bragado I, Hernandez-Mangas J M, Barbolla J and Gilmer G H 2003 Atomistic Monte Carlo simulations of three-dimensional polycrystalline thin films *J. Appl. Phys.* **94** 163–8
[27] Henkelman G and Jónsson H 2001 Long time scale kinetic Monte Carlo simulations without lattice approximation and predefined event table *J. Chem. Phys.* **115** 9657–66
[28] Turowski M, Jupé M, Melzig T, Moskovkin P, Daniel A, Pflug A, Lucas S and Ristau D 2015 Practice-oriented optical thin film growth simulation via multiple scale approach *Thin Solid Films* **592** 240–7
[29] Pflug A, Siemers M, Schwanke C and Szyszka B 2010 Simulation von plasma-beschichtungsprozessen *Vak. Forsch. Prax.* **22** 31–4
[30] Melzig T, Siemers M, Pflug A and Rank R 2014 3D PIC-MC simulation of anode effects in dual magnetron discharges *Surf. Coat. Technol.* **241** 30–2
[31] Schwanke C, Pflug A, Siemers M and Szyszka B 2012 *Applied Parallel and Scientific Computing* vol 7133 ed K Jónasson (Berlin: Springer)

[32] Bird G A 1994 *Molecular Gas Dynamics and the Direct Simulation of Gas Flows* (Oxford: Clarendon)
[33] Koura K and Matsumoto H 1991 Variable soft sphere molecular model for inverse-power-law or Lennard-Jones potential *Phys. Fluids* A **3** 2459–65
[34] Abrahamson A A 1969 Born–Mayer-type interatomic potential for neutral ground-state atoms with Z = 2 to Z = 105 *Phys. Rev.* **178** 76–9
[35] Nathan S S, Rao G M and Mohan S 1998 Transport of sputtered atoms in facing targets sputtering geometry: a numerical simulation study *J. Appl. Phys.* **84** 564
[36] Geuzaine C and Remacle J-F 2009 Gmsh: a 3-D finite element mesh generator with built-in pre- and post-processing facilities *Int. J. Numer. Methods Eng.* **79** 1309–31
[37] Depla D 2013 *Magnetrons, Reactive Gases and Sputtering* (Ghent: Diederik Depla)
[38] Depla D, Heirwegh S, Mahieu S, Haemers J and De Gryse R 2007 Understanding the discharge voltage behavior during reactive sputtering of oxides *J. Appl. Phys.* **101** 013301
[39] Buyle G, De Bosscher W, Depla D, Eufinger K, Haemers J and De Gryse R 2003 Recapture of secondary electrons by the target in a DC planar magnetron discharge *User Model. User-Adapt. Interact.* **70** 29–35
[40] Lucas S and Moskovkin P 2010 Simulation at high temperature of atomic deposition, islands coalescence, Ostwald and inverse Ostwald ripening with a general simple kinetic Monte Carlo code *Thin Solid Films* **518** 5355–61
[41] Blackwell S, Smith R, Kenny S D and Walls J M 2012 Atomistic modelling of titania grown using PVD methods 3–8
[42] Kelly P J and Arnell R D 2000 Magnetron sputtering: a review of recent developments and applications *Vacuum* **56** 159–72
[43] Barradas N P, Jeynes C and Webb R P 1998 Simulated annealing analysis of Rutherford backscattering data *R. Soc. Chem.*
[44] Martin N and Rousselot C 1998 Use of a theoretical model to investigate RF and DC reactive sputtering of titanium and chromium oxide coatings *Surf. Coat. Technol.* **110** 158–67
[45] Barranco A, Borras A, Gonzalez-Elipe A R and Palmero A 2016 Perspectives on oblique angle deposition of thin films: from fundamentals to devices *Prog. Mater. Sci.* **76** 59–153
[46] Dervaux J, Cormier P-A, Konstantinidis S, Di Ciuccio R, Coulembier O, Dubois P and Snyders R 2015 Deposition of porous titanium oxide thin films as anode material for dye sensitized solar cells *Vacuum* **114** 213–20
[47] Dervaux J, Cormier P-A, Moskovkin P, Douheret O, Konstantinidis S, Lazzaroni R, Lucas S and Snyders R 2017 Synthesis of nanostructured Ti thin films by combining glancing angle deposition and magnetron sputtering: a joint experimental and modeling study *Thin Solid Films* **636** 644–57
[48] Cormier P-A, Balhamri A, Thomann A-L, Dussart R, Semmar N, Lecas T, Snyders R and Konstantinidis S 2014 Titanium oxide thin film growth by magnetron sputtering: total energy flux and its relationship with the phase constitution *Surf. Coat. Technol.* **254** 291–7
[49] Tominaga K, Ito D and Miyamoto Y 2006 Energetic negative ions in titanium oxide deposition by reactive sputtering in Ar/O_2 *Vacuum* **80** 654–7
[50] Yamagishi M, Kuriki S, Song P K and Shigesato Y 2003 Thin film TiO_2 photocatalyst deposited by reactive magnetron sputtering *Thin Solid Films* **442** 227–31
[51] Amin A, Köhl D and Wuttig M 2010 The role of energetic ion bombardment during growth of TiO_2 thin films by reactive sputtering *J. Phys. D: Appl. Phys.* **43** 405303

6 The challenge of modelling charged particles

The previous chapter laid the foundations of *Virtual Coater* by successfully combining DMSC and k-MC algorithms to model the neutral particles involved in the deposition of TiO_x by reactive magnetron sputtering. The next step is the addition of charged particles within the simulation framework i.e., the point **(c)** of the *VC* flowchart in Figure 15. However, the task is not straightforward as the simulation of charged particles requires a new type of simulation algorithm with new constraints on the cell size and time step, considerably reducing the accessible physical time of the simulation.

These constraints are explained and discussed in the following dedicated article published in 2020 in *Plasma Sources Science and Technology* [81]. A solution to overcome these limitations is proposed and applied to the case of a pure Ar discharge with a Ti target. As PICMC simulations are more resource consuming than DSMC ones, the study is performed on a smaller scale model involving only one magnetron. The model includes the following species: Ar, Ar^+, Ti, Ti^+ and electrons. All cross sections included are also presented in the article. The simulation results are compared to experimental Langmuir probe characterization of the discharge. The application domain over the discharge current density of the PICMC simulations is evaluated. Even though the approach does not enable to simulate plasma with high ionization degree, it is proven suitable for the DC case. The major findings reported in the article are the followings:

1. A scaling strategy of the PICMC simulations is validated using Langmuir probe measurements.
2. The various species are to be scaled up according to their creation mechanism e.g., sputtered species scale with the discharge power while electron scales with the discharge current.
3. The PICMC algorithm does capture the complex physics of magnetized discharges. $\vec{E} \times \vec{B}$ inherent instabilities of the electrons are predicted and match the proposed scaling strategy.

These published results indicated that it is possible to scale up the computed quantities of PICMC simulations i.e., densities, fluxes and reaction rate of collisions up

to realistic values used in real depositions. Therefore, all the tools to perform full scale simulations are ready, and the final article presented in the next chapter (chapter 7) of this thesis is related to the addition of the PICMC algorithm to the *Virtual Coater* concept and to elucidate the role of energetic particles during film growth.

IOP Publishing Plasma Sources Science and Technology
Plasma Sources Sci. Technol. 29 (2020) 115007 (17pp) https://doi.org/10.1088/1361-6595/abb3a0

Magnetron sputtering: determining scaling relations towards real power discharges using 3D particle-in-cell Monte Carlo models

R Tonneau[1], A Pflug[2] and S Lucas[1,*]

[1] Namur Institute of Structured Matter (NISM), Laboratoire d'Analyse par Réactions Nucléaires (LARN), University of Namur (UNamur), 61 rue de Bruxelles, B-5000 Namur, Belgium
[2] Fraunhofer Institute for Surface Engineering and Thin Films IST; Bienroder Weg 54e, 38108 Braunschweig, Germany

E-mail: romain.tonneau@unamur.be, andreas.pf ug@ist.fraunhofer.de and stephane.lucas@unamur.be

Received 17 February 2020, revised 19 August 2020
Accepted for publication 28 August 2020
Published 11 November 2020

Abstract

Plasma simulation of glow-magnetized discharges with the particle-in-cell Monte Carlo (PICMC) method is constraint to low current densities because of otherwise huge computational requirements. The present work aims to show, how it is nevertheless possible to extrapolate information for higher current densities similar to realistic lab or industrial conditions by applying a scaling strategy on the simulation. This is demonstrated for a DC magnetron sputtering (DCMS) case study involving the following species: Ar, Ar^+, Ti, Ti^+ and electrons. The evolution of the electron density is extracted from the simulation and compared with experimental values obtained with a Langmuir probe. A linear relationship between the electron density and the discharge current is highlighted and explained by studying the reaction rates of both ionization and excitation collisions. This allows to scale the reaction rates with the discharge parameters: the Ar-electron impact ionization and excitation rates scale linearly with the discharge current, while the electron impact ionization rate of sputtered species scales quadratically with the discharge current. The simulations also feature propagating plasma instabilities, so-called spokes, but in average, the above-mentioned scaling laws hold. Consequently, the f ux of particles at the substrate during a plasma deposition process at realistic power density can be extrapolated from a 3D PICMC simulation at lower power density. Finally, the validity domain of the scaling strategy is discussed in the light of the model constraints.

Keywords: plasma simulation, particle-in-cell Monte-Carlo, magnetron sputtering, plasma dynamic, spoke, Langmuir probe

(Some f gures may appear in colour only in the online journal)

*Author to whom any correspondence should be addressed.

*Address for correspondence: Prof. Stéphane Lucas, University of Namur (UNamur), 61 rue de Bruxelles, B-5000 Namur, Belgium, Tel: +32 (0)81 725 481, Fax: +32 (0)81 725 474

1. Introduction

Magnetron sputtering is a highly successful plasma deposition technique supporting a large variety of applications. Understanding the magnetron discharge physics is still of prime importance for the optimisation of the film properties. The electron kinetics plays a major role for the plasma species (electrons, ions and neutrals) production, and the determination of electron density, temperature and distribution function are mandatory. In this respect, the plasma modelling is a valuable tool to estimate these physical quantities when experimental investigations are limited.

Fluid models as simulation algorithm are not suitable because of the magnetron sputtering low pressure operation range [1, 2]. When the electron mean free path largely exceeds the characteristic length of the discharge, the kinetic and self-consistent PICMC modelling method is the most appropriate [3, 4]. It simulates a reduced number of particles (called super-particles) in the discharge, whose fate is computed by solving the Newton–Lorentz equation, coupled with Maxwell equations for electric and magnetic fields self-consistent computation. Monte-Carlo methods, which compute the particles scattering and final velocities, usually handle the collisions. Surfaces and particle interactions are modelled by considering reflection, absorption and emission at such boundaries. When fully implemented and mastered, the PICMC approach is very powerful and helps to understand the plasma discharge. In combination with additional subsequent simulation methods like kinetic Monte-Carlo also insights about the film growth can be gained [5].

Unfortunately, the main drawback of this method is the enormous computational resources needed to perform a full-scale simulation. To ease the required computational effort, most of the available codes use 1D or 2D geometries [6–10] but discrepancies between 2D and 3D simulations of the same magnetron discharge have been reported [7] because 2D models principally cannot account for plasma instabilities occurring in electron drift direction. Therefore, 3D simulation is mandatory to capture the proper physics of the discharge. Unfortunately, comparison with real power used in reactors is not direct because simulations can be performed only at low current densities. Indeed, the PICMC method requires discretizing the 3D geometry in small cells, which have to match some physical constraints. One of those is the resolution of the electric potential for which the cell size has to be of the same order of magnitude than the Debye length. According to [11], a constraint of cell size lower than 3.4 Debye length is sufficient. Assuming an electron temperature of 3 eV and applying the previous considerations, a typical electron density achievable by PICMC algorithms is 2×10^{15} (m^{-3}). The corresponding Debye length for such density is 288×10^{-6} (m) leading to a possible cell size of 1 mm. However, typically experimental magnetron discharges exhibit electron densities as high as 1×10^{17} (m^{-3}). This would require a cell size lower than $\approx 138 \times 10^{-6}$(m), leading to a cell number of larger than1×10^{10} for a coater of 0.1 m^3. This clearly exceeds the numerical resources of today's high-performance computer facilities as further explained in section 2. In order to work around this limitation, the electron density has to be reduced to increase the Debye length and therefore allow larger cell size. Consequently, 3D simulations are performed at low current densities, i.e. few 10 μA cm^{-2}. For simulations at such low current densities, the question arises if they are suitable to explain the discharge behaviour at more realistic current densities and what should be the rule of thumb to apply if one wants to extrapolate the calculations to real discharge current conditions. This paper aims to answer these questions by using 3D PICMC simulations for a typical Ti magnetron discharge in pure Ar.

Literature already contains hints regarding the scalability of sputtered species (neutrals). In magnetron sputtering processes, it is admitted that the amount of sputtered species is proportional to the discharge power. Indeed, the analytical model of the sputtering yield γ_{sput} introduced by Sigmund [12] can be approximated by:

$$\gamma_{sput} = \frac{6}{4\pi^2}\alpha\frac{\gamma E}{U_s} \tag{1}$$

with E the ions energy, γ the energy transfer factor for an elastic collision, $U_s$the surface binding energy and α a dimensionless function of the incoming particle and target atom mass ratio. This equation shows that the sputter yield increases linearly with the incoming ion energy. Moreover, assuming the ions hitting the target gained kinetic energy crossing the plasma sheath and if the discharge potential (V_{disch}) is equal to the potential drop through the plasma sheath, one can rewrite equation (1):

$$\gamma_{sput} = \frac{6}{4\pi^2}\alpha\frac{\gamma e V_{disch}}{U_s}(s^{-1}) \tag{2}$$

with e the electron charge.

The number of atoms sputtered per second, N, can be expressed by:

$$N = \frac{I_{disch}}{e\left(1+\gamma_{e,eff}\right)}\gamma_{sput}(s^{-1}) \tag{3}$$

with I_{disch}, the discharge current and $\gamma_{e,eff}$ the effective secondary emission electron yield [13]. Combining equations (2) and (3):

$$N = \frac{6}{4\pi^2}\frac{\gamma\alpha}{U_s(1+\gamma_e)}I_{disch}V_{disch} \propto P_{disch}(s^{-1}) \tag{4}$$

The number of sputtered atoms is then proportional to the discharge power as also confirmed by experimental studies e.g. reported in [14]. Nowadays however, literature does not contain any information regarding the evolution of ionized sputtered species with the discharge parameters. The reason is twofold: (i) it is hard to collect quantitative data on ion species in DC magnetron sputtering (DCMS) and (ii) the density of the ionized sputtered species is very low as the ionization degree is also very low in DCMS. Therefore, a possible way to overcome these limitations is to use computer modelling to get more insight on the plasma dynamics operating in DC mode.

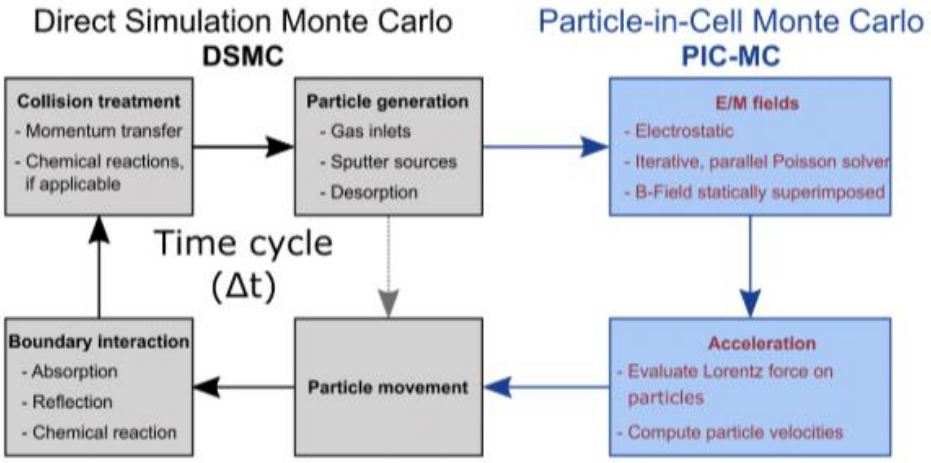

Figure 1. PICMC algorithm functional diagram.

Table 1. Physical and numerical values for typical low-pressure magnetron discharge condition.

Parameters	Value
p	0.5 (Pa)
σ	$10^{-19}(m^2)$
e	$1.6021 \times 10^{-19}(C)$
m_e	$9.1091 \times 10^{-31}(kg)$
ε_0	$8.8542 \times 10^{-12}(F\,m^{-1})$
T_e	3(eV)
N	$1.207 \times 10^{20}(particle/m^3)$
n_e	$1 \times 10^{17}(m^{-3})$
ν_e	$1.399 \times 10^{7}(Hz)$
ω_{pe}	$1.784 \times 10^{10}(Hz)$
λ_D	$40.7 \times 10^{-6}(m)$

2. PIC-MC and model description

The classical PIC-MC method is to use a 2D or 3D geometry and divide it into smaller cells forming the simulation grid. Super-particles are added into the simulation grid. Then, motion and Maxwell equations are resolved inside each cell for a Δt step time. The simulation principle is summarized in figure 1.

For a magnetron discharge, the magnetic field is precomputed from the magnet geometry and material, and is superimposed to the simulation grid.

The magnetic field is assumed constant throughout the simulation. In contrast, the electric field is computed at each time step as it evolves with the charged particles motion. After each time step, particles are paired up with the other particles located in the same computational cell and the collision probability (according to cross sections) is computed for these pairs. Because the computational time step has to be small compared to the average time between collisions, and the collision probability of a given particle in a cell should be less than one, the time step and cell dimension have to be defined accordingly for the most important species: the electrons. For that purpose, the method published by [11] was used. First, the cell size has to be small enough to resolve the electric potential distribution i.e. the same order of magnitude as the Debye length: $\Delta x \leqslant 3.4\lambda_D$. The Debye length can be computed according to the following formula:

$$\lambda_D = \left(\frac{\varepsilon_0 T_e}{e n_e}\right)^{1/2} (m) \tag{5}$$

with e the electron charge, n_e the electron density and ε_0 the dielectric permittivity.

Second, the time step has to be small enough so that the resulting step frequency is lower than both the electron collision frequency (equation (6)) and the electron plasma frequency (equation (7)). Those quantities are respectively computed by the following equations:

$$\nu_e = N\sigma\sqrt{\frac{8eT_e}{m_e\pi}} (Hz) \tag{6}$$

$$\omega_{pe} = \left(\frac{e^2 n_e}{\varepsilon_0 m_e}\right)^{1/2} (Hz) \tag{7}$$

Table 2. Cross sections implemented in PICMC model.

Momentum	Transfer	Charge Transfer	Electron Impact Ionization	Excitation
Ar + Ar Ar^+ + Ar e + Ar Ti + Ar	Ti^+ + Ar Ti + Ti Ti + Ti^+	Ar^+ + Ar [20]	Ar + e [21] Ti + e [22]	Ar + e [11.5 eV] [21]

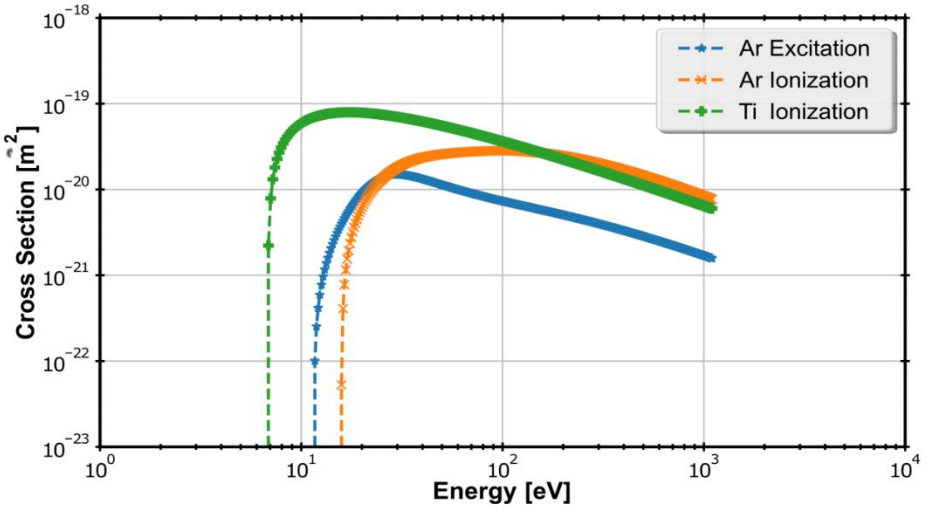

Figure 2. Electron impact ionization, and total excitation cross sections. Total excitation cross sections are obtained by summing up all partial excitation cross sections.

where N is the neutral species density, σ the electron-neutral collision cross section, T_e the electron temperature given in eV and m_e the electron mass.

Those three quantities and the related parameters value are calculated and listed in table 1 for typical experimental discharge conditions [15].

On the one hand, the proper resolution of the electron motion within the magnetic field restricts the time step to $\Delta t \leqslant 5 \times 10^{-11}$(s). On the other hand, the cell size limitation leads to a cell volume of 2.63×10^{-12}(m^3) i.e. 3.8×10^{10} cells for a 0.1 (m^3) simulation volume (cylinder 20 cm radius and 80 mm length around the magnetron). This number of cells would by far exceed the numerical resources of any High-Performance Computer (HPC) installation. In order to ensure proper collision statistics and to have a reasonable number of charged super particles per Debye sphere [2, 16], we assume that each cell contains at least 50 super particles in average. One super particle has at least 7 double-precision variables for velocity and position vectors as well as residual time, this sums up to an overall memory allocation of 100 TB for the particle data only.

In order to work around this cell size constraint, the electron density has to be reduced by diminishing the discharge current density to increase the Debye length and therefore allow greater cell size. Reducing electron density to 10^{15} (m^{-3}) decreases the number of cells to 3.8×10^7 i.e. 100 GB of particle data, which is still a large amount but doable with today's HPC resources.

In this work, the PICMC code developed at the Fraunhofer IST [17–19] is used with a discharge current ranging from 3 mA to 16 mA. The plasma chemical reactions used in the model are summarized in table 2.

All other momentum transfer collision cross sections are implemented from the Born–Mayer Potentials as already discussed in [23]. Electron impact ionization, Ar–e transfer momentum and total excitation cross sections of species of interest are presented in figure 2. For all the simulation cases, electron-electron collisions are neglected.

2.1. Geometrical coater description and simulation parameters

A magnetron chamber equipped with a 2 inch magnetron with a 99.9995% pure Ti target was used for this work [23]. It was powered by a TDK Lambda Genesys PSU and operated in constant current mode. The chamber was pumped with a 260 l s^{-1} turbomolecular pump and the base pressure was better than 1.3×10^{-4} Pa. The working pressure was 0.5 Pa for all experiments. A reduced 3D geometry with the volume of 6.53 l (see figure 3) is used for the simulations.

The magnetron is composed of a yoke with 14 attached cylindrical and identical magnets, 1 central and 13 evenly

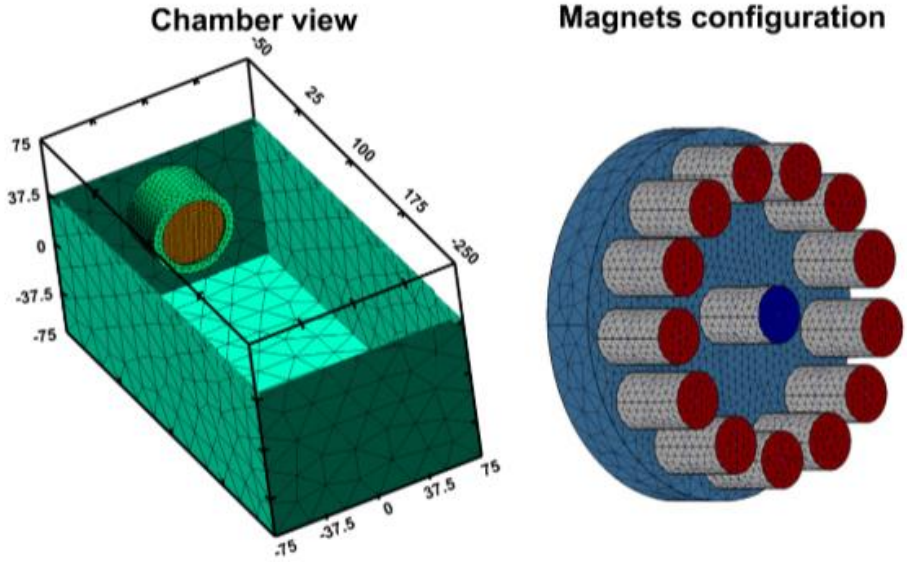

Figure 3. Single magnetron model definition (unit: mm).

Table 3. Simulation parameters of the Ti–Ar magnetron discharge computed in this work.

Parameter	Value
Time step	2.0×10^{-11}(s)
Total physical time	150 μs $\rightarrow$ 7.5×10^6 iterations
Initial gas temperature	300(K)
Surface binding energy for Ti	4.89(eV)
Ti cosine exponent	1.5
Wall temperature	300(K)
Neutral particles weighting factors	Ar: 2.5×10^{10} Ti: 3.5×10^6
Charged particles weighting factors	e^-, Ar^+ : 1.0×10^5 Ti^+ : 2.0×10^2
Working base pressure (Ar)	0.5(Pa)
Initial charged density (m^{-3})	e^-, Ar^+: 1.0×10^{13} Ti^+: 0
Secondary electron emission yield (SEEY)	0.114 [24]
Ar^+ (300 eV) sputter yield on Ti	0.54
Ti^+ (300 eV) sputter yield on Ti	0.35
Ti and Ti^+ sticking coefficient	1

separated as outer magnet ring. The magnets have a 10.2 (mm) diameter, a 15.0 (mm) length and are made of NdFeB. Prior to plasma simulation, the magnetic field is computed on the simulation grid. As in front of the target a higher electron density is expected than elsewhere in the simulation box, the cell size is fine-tuned within the geometry. The simulation box is divided into several segments. While the current simulation code does not support hanging nodes, the cell spacing perpendicular to the target—i.e. the direction where the highest gradients in electric potential occur—can be adjusted from one segment to another. The resulting number of cells is 1001 250 for low current simulations ($J_{\text{disch}} < 40\ \mu\text{A.cm}^{-2}$, $n_e < 5 \times 10^{15}\ \text{m}^{-3}$) and 6525 000 for higher current simulations ($J_{\text{disch}} < 75\ \mu\text{A.cm}^{-2}$, $n_e < 1 \times 10^{16}\ \text{m}^{-3}$). Simulation parameters are summarized in table 3.

The base pressure of Ar is identical for each simulation. No gas inlet is defined, as the neutral distribution is assumed to not evolve on such a short time scale (150 μs) for standard DCMS. For very high current densities, as found in high-power impulse magnetron sputtering, the present assumption would be no more valid due to the sputter wind [25]. Walls are defined such as Ar ions are neutralized while hitting a surface, resulting in the emission of one Ar and one possible electron with a probability of 0.114. Sputtering events are implemented using the sputtering yields listed in table 3. Sputtering yield is assumed constant over the simulation. Sputtered Ti atoms are emitted according to a Thompson like distribution for energy distribution and a cosine exponent for angular distribution. The surface binding energy and the cosine exponent are also listed in the related table. Secondary electrons are emitted from the

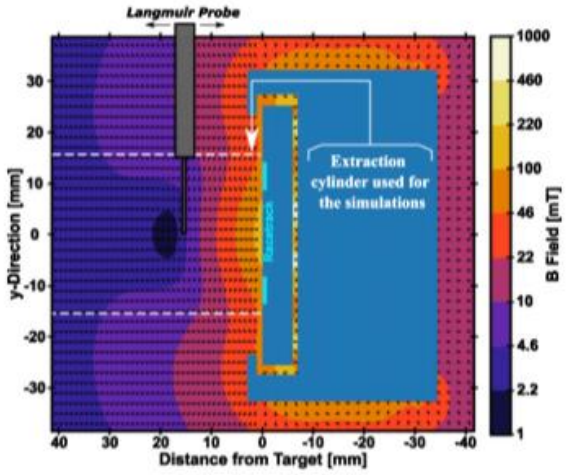

Figure 4. 2D absolute $\vec{B}$ field strength map in the vicinity of the magnetron. The langmuir probe location, the racetrack location and the cylinder involved in data mining are also indicated on the plot.

cathode with a uniform energy distribution within the range 0–10 (eV).

2.2. Langmuir probe measurements and calculations

Plasma characterization is performed using a Langmuir probe ESPION from Hiden Analytical. A tungsten tip with a length of 12 mm and a radius of 300 μm is used. It is located inside the plasma and biased positively or negatively to draw electron or ion current. The probe tip is placed parallel to the target surface i.e. perpendicular to the magnetic field at two distances from the cathode surface: 10 and 15 mm. According to simulation results, the magnetic field intensity quickly drops below 19 mT in front of the target.

Previous works [26, 27] have demonstrated that the magnetic field does not influence the I–V characteristic of a cylindrical Langmuir probe if the probe radius is lower than the electrons Larmor radius and if the probe is perpendicular to the magnetic field. The Larmor radius of an electron is calculated by:

$$L_R = \frac{\sqrt{2m_e T_e}}{eB} \ (m) \tag{8}$$

For a 3 eV electron, the calculated L_R in a 19 mT $\vec{B}$ field is 305 μm. Thus, the magnetic field influence is neglected for the low energy range.

The simulations are mainly focused on the electron characteristics, since these particles are the ones driving the discharges. The electron density is extracted from a cylinder of 15 mm (probe physical dimension) radius perpendicularly aligned with the target surface as depicted in figure 4. The obtained values are the mean electron densities extracted from within the 2 mm thick cylindrical slices of the simulation volume. For each simulation, two slices centred at 10 mm and 15 mm away from the target are used.

3. Results

First, the discharge behaviour is experimentally characterized by recording the power, current and voltage triplet over a wide range of values, see figure 5.

Current values are divided by the surface of the 2 inches target to display current density values instead. The amount of sputtered Ti is calculated using Equation (3) by assuming a constant secondary electron emission yield (table 3) and using the sputtering yield fit of Ti bombard by Ar^+ ions [28]. Ar^+ ion energy is evaluated assuming the plasma sheath potential drop is equal to the discharge voltage. A linear relationship with the discharge power is observed.

In total, 13 simulations at various discharge powers/currents were performed (table 4).

All simulations exhibit the same general spatial distributions of particles. The 1.26 mA.cm^{-2} case is used as an example. The particle densities and electric potential are time average over the last 50 μs of physical simulation time and 2D maps of the median plane are presented on figure 6.

The background gas is Ar and therefore exhibits a homogeneous spatial distribution (figure 6(A)). Electron and Ar^+ have the same spatial distribution as it can be seen on figures 6(C) and (D). Their densities are maximal in front of the target. The Ti^+ (figure 6(F)) shows the same behaviour but with about two or three orders of magnitude lower absolute values. Regarding Ti, two hot spots can be observed on figure 6(E), which correspond to the intersection of the 2D cut plane with the circular sputter erosion track, close to the regions of maximum density for electron and Ar^+ ions. The density of Ti is decreasing with the distance from the target surface. Finally, the electric potential is plotted on figure 6(B). The potential has positive homogeneous values all over the simulation volume except in front of the target. At y-positions 10 and −10 mm, the potential gradient in front of the target surface is higher than any other location. These two locations match with the two hot spots observed for the Ti density and those of the electron and Ar^+ densities.

Electron densities, at vertical distances to the target of 10 and 15 mm, as measured by the Langmuir probe and computed by simulation are plotted together as a function of the discharge current on figure 7. The curves are fitted with linear functions and presented in a log-log scale, in order to easily display the evolution over several decades, both on electron densities and discharge currents.

Figure 8 plots the simulated evolution of the reaction rates of electron impact ionisation for both Ar and Ti and electron impact excitation for Ar, averaged over the whole simulation volume as a function of the discharge current density.

One can see that the evolution of the Ar ion curve (figure 8(A)) is different to the Ti ions one (figure 8(B)). Indeed, data of the Ar related collisions can be fitted with a linear function, while Ti ionization requires a quadratic function to be fitted versus the discharge current density. In addition, the reaction rate of Ti ionization is 10^3–10^4 lower than the Ar ionization, in agreement with a typical ionization rates of DC magnetron sputtering ($\leqslant$1%).

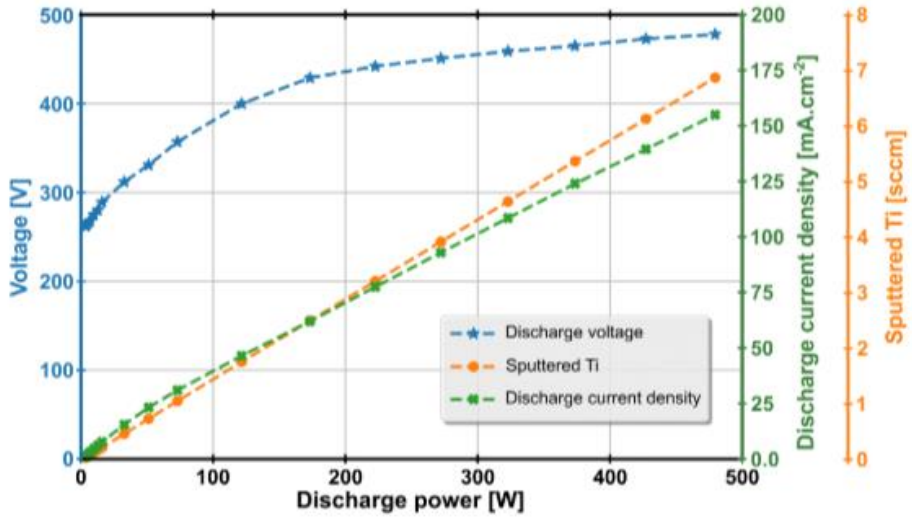

Figure 5. Experimental discharge power parameters. Sputtered Ti is calculated using discharge voltage and current values along with sputtering yield of Ti, secondary electron emission yield is assumed constant. Calculated values are expressed in sccm ($1\mathbf{sccm} \cong 4.478 \times 10^{17}\text{particles} \cdot \text{s}^{-1}$).

Table 4. Discharge parameters of the simulations.

Discharge power (W)	Discharge current density (mA.cm^{-2})	Discharge voltage (V)
1.0	0.61	249.4
1.1	0.67	247.8
1.2	0.73	248.1
1.3	0.80	247.6
1.4	0.86	246.3
1.5	0.92	246.7
1.6	0.99	247.3
1.7	1.06	244.2
1.8	1.12	243.6
1.9	1.19	242.1
2.0	1.26	242.5
3.0	1.74	267.6
4.0	2.37	270.6

Simulations also enables to compute the fluxes of particles along the target axis. Fluxes of Ar^+, Ti, Ti^+ and electrons were extracted in the same fashion as the electron density. The computed fluxes averaged for each slice are plotted in figure 9. Fluxes oriented towards the target are negative, while fluxes moving away from the target are positive values. In order to better show the variations, different scales were used for each sub-figure.

Below 3.3 mm, the net electron flux is close to zero and becomes positive further away with first a quick increase. A maximum is reached for all cases at 9.5 mm and afterward the fluxes stabilize and slowly decrease. The flux of the main ion species, Ar^+, is plotted in figure 9(C). The global behaviour is similar to electrons except that the magnitude of the negative flux is 40 to 50 times greater than the positive flux. Moreover, the sign changes within a 15–20 mm range which corresponds to the slope of the electric potential. Figure 9(B) shows the flux of the sputtered species, Ti. Values are positives, throughout the whole simulation domain and decrease with higher distance from target. Finally, the Ti^+ flux is plotted in figure 9(C). The general behaviour is similar to the other ion species, Ar^+, but in this case, the negative magnitude is only 10 times higher than the positive one.

In order to study the possible scalability of the simulations with the discharge current, the data from figure 9 were compared at several distances from the target in figure 10.

The respective fluxes of all species are extracted at vertical distances from the target of 30, 45, 60, and 75 mm. They are normalized with the lowest discharge current case, and plotted as a function of different variables. Those variables are selected based on the scaling trends highlighted by figure 8, so that each data set has a linear behaviour. X-axis variables will be explained and discussed later in this paper. All plots

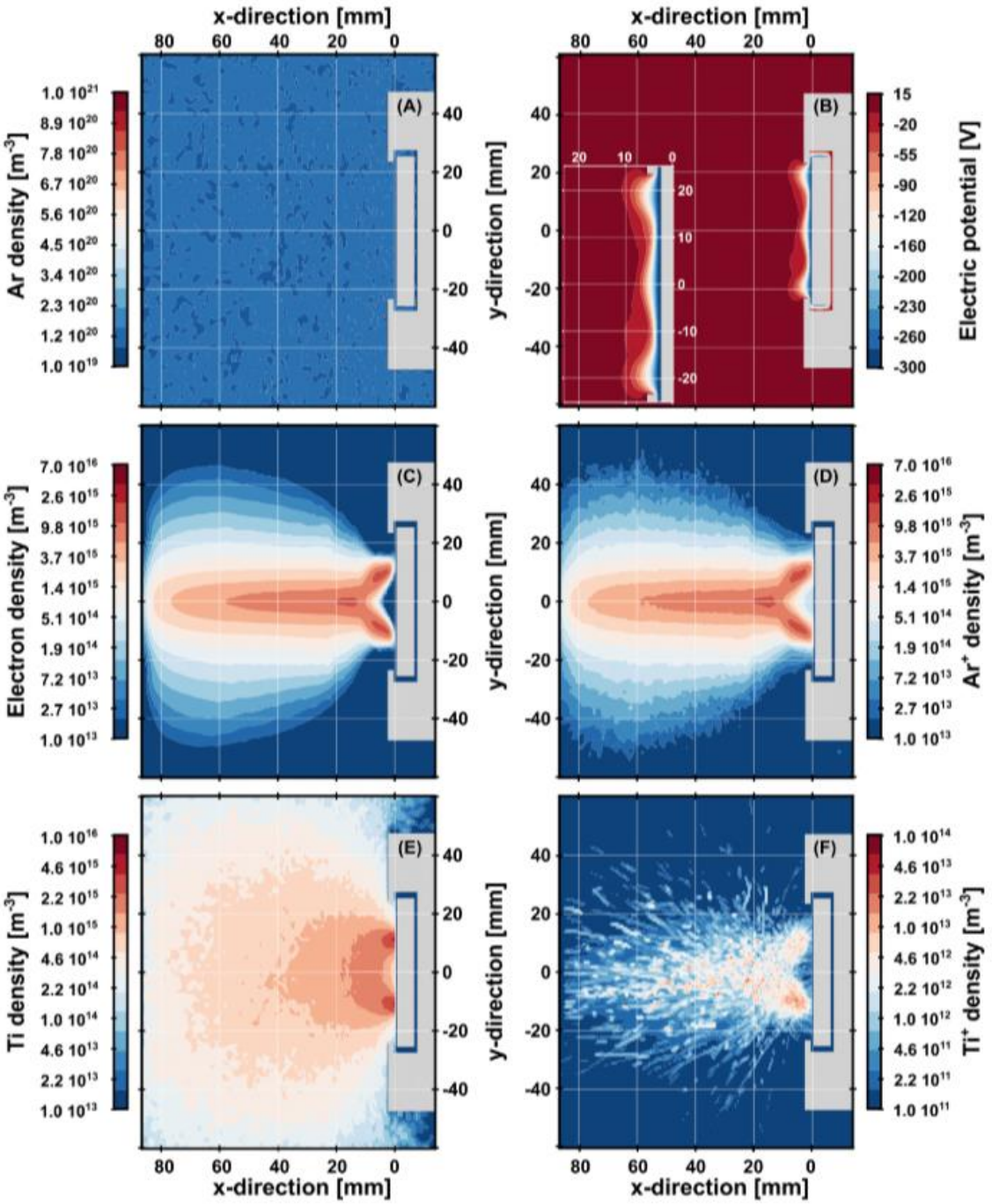

Figure 6. 2D maps of the median plane from the 1.26 mA.cm^{-2} case. All maps are time averaged over the last 50 μs of simulation. (A)-(C)-(D)-(E)-(F) Spatial distribution of particle densities. (B) Spatial distribution of the electric potential (plasma potential). A zoom over the plasma sheath with the target surface is incrusted.

exhibit a perfect linear relationship with their respective x-variable. The same normalization procedure applies for the experimentally calculated Ti flux emitted by the target added on figure 10(B).

4. Discussion

Modelling a plasma discharge with a PICMC method requires great computer resources and must be performed within

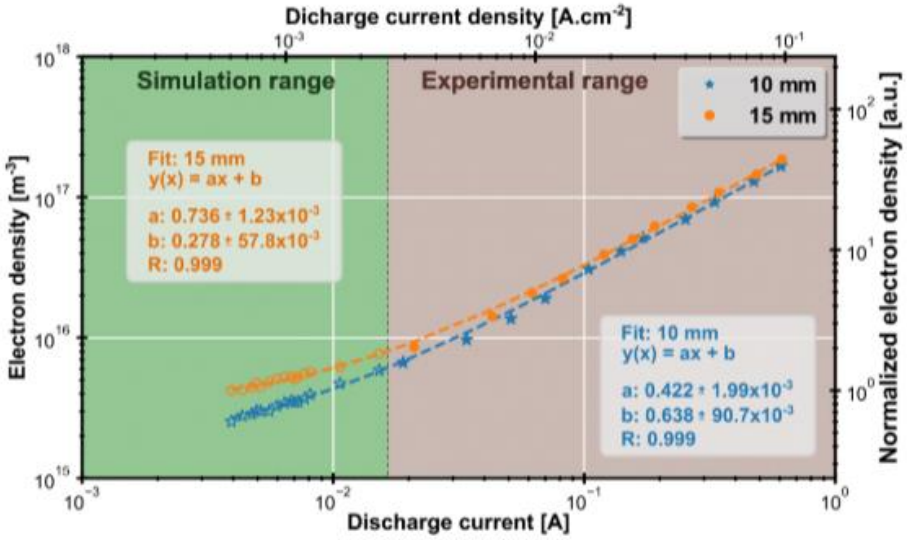

Figure 7. Electron density as a function of discharge current for two different vertical distances to the target. Unfilled markers correspond to simulation results and the filled one to experimental results. Normalized values are computed with the lowest discharge current case. The fit parameters of each normalized reactions rates are shown, as well as the Pearson correlation coefficient R.

numerical constraints. One of those is the limitation is the electron density, which implies a limited discharge power. In order to scale up the simulations to real power/current discharge, it is necessary to analyse the plasma ionization region because, first, it is the source of particles, and second, the discharge has to operate in a similar mode than the experimental one. The simulation model can be applied to low discharge current densities (these results are not presented in this paper)leading to dark discharge instead of a glow discharge [29]. Typically, for current densities below $10^{-7} A \cdot \mathrm{cm}^{-2}$, the discharge is in the self-sustained Townsend mode. In this case, very few ionization events take place and a thick sheath is observed, as the cathode potential is screened by the few charged species generated. The Debye length is large and in the magnetic confinement region (MCR), the electric potential is low ($\leqslant -100$V) and electrons are not energetic. Only those escaping the MCR can cross the whole cathode potential trough the large sheath and generate some ionization events. Consequently, two separate regions with two different electron density are observed. One in front of the cathode, due to the $\vec{E} \times \vec{B}$ field and the other one a few centimetres away, where electrons have crossed the whole cathode potential.

Increasing the current induces an increase of both the secondary electrons (SE) emission from the cathode and the electron density. When the electron density is high enough, ionization events are most likely to occur in the MCR and the cathode sheath decreases, so that SE can gain a large fraction of the cathode voltage. With such a geometry, and for discharge current densities higher than $10^{-6} A \cdot \mathrm{cm}^{-2}$, only one 'high' electron density region is observed near the cathode, with a steady decrease of the density while escaping the MCR when moving away from the cathode. This can be easily understood as a large fraction of ionization events (i.e. charged particles generation) take place in the MCR, and when flying away from the MCR, electrons are not trapped by the magnetic field anymore, and can diffuse. The behaviour of the electron density was already reported by previous works in similar pressure and power conditions with Langmuir probes [30, 31].

Therefore, when comparing simulation and experimental data, best is to probe the ionization region where most of the ionization occurs. For this reason, both the experimental and simulated Langmuir probes were placed in the ionization zone i.e. 10 and 15 mm away from the cathode (figure 4). At such a distance, the probe is also far enough from the MCR, so that the effect of the magnetic field is negligible. The measured and simulated electron densities are presented in figure 7, where both of them exhibit a linear dependence with the discharge current. Simulated electron densities were averaged within a cylinder whose radius has similar length than the Langmuir probe filament and is 2 mm thick. Simulated and experimental data fit together on a straight line in both the 10 and 15 mm cases. The 15 mm case has higher density values due to the magnetic field. Indeed, one can see the distribution of the electron density on figure 6, at 10 mm from the target the density is lower than at 15 mm which is closer to the magnetic null region (darker region in figure 4). The fitted normalized curves slopes both exhibit positive values lower than 1. The origin of the linear trend observed in figure 7 is twofold: (i) the ion induced secondary electron (SE) emission from the cathode and (ii) electron creation in the gas by impact ionization. The SE emission can be related to the discharge current by the following relationship:

$$I_{\mathrm{disch}} = I_{\mathrm{ions}}(1 + \gamma_{\mathrm{e,eff}})\ (A) \tag{9}$$

With I_{ions} the ion current onto the target and $\gamma_{\mathrm{e,eff}}$ the effective ion induced secondary emission electron yield (SEEY). $\gamma_{\mathrm{e,eff}}$,

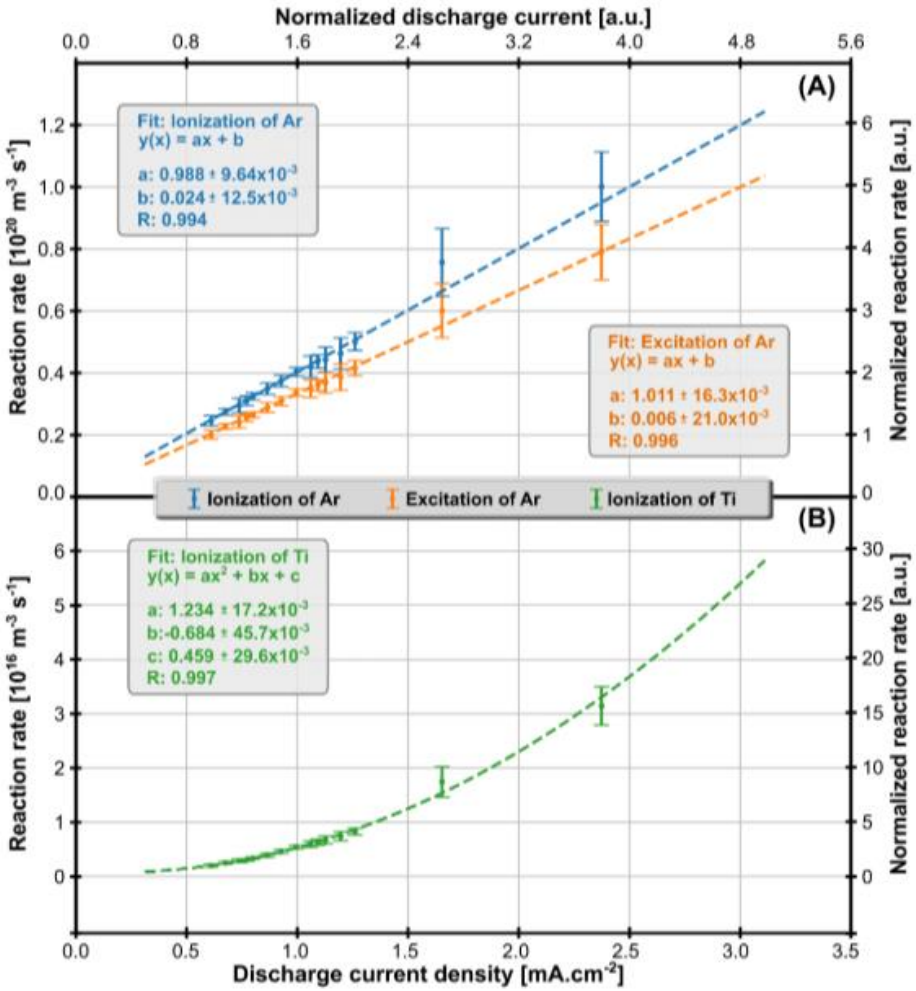

Figure 8. Simulated evolution of the reaction rates of ionization related collisions with the discharge current density. In figure (A), the electron impact ionization and the electron impact excitation of Ar is plotted. Normalized values are computed with the lowest discharge current density case of electron impact excitation. Both reaction rates are fitted with a linear function. In figure (B), the reaction rate of the electron impact ionization of Ti is plotted and fitted with a quadratic function. Normalized values are computed in the same manner as for the Ar case in figure (A). The fit parameters of each normalized reactions rates are shown, as well as the Pearson correlation coefficient R.

differs from γ_e by including the probability of ionization in the sheath and the probability of SE recapture at the target.

Over the typical DCMS working conditions (200–500 V), SEEY for a clean metallic target can be considered constant [24]. Therefore, the number of SE is directly proportional to the discharge current. Regarding the electron creation in the gas phase by electron impact ionization, this number depend on the initial number of SE emitted by the target, the fraction of the SE that causes ionization before they are lost from the system and the average number of new bulk electrons created through ionization cascade caused by SE. The average number of bulk electrons created by SE is mainly related to the electron energy distribution function (EEDF) of the bulk electron population and the nature of the background gas. In the present study, the nature of the background gas is always Ar, therefore there is no change of collision cross section. The fraction of SE that causes ionization before they are lost can be assumed as coater dependant (geometry, magnetic arrangement, pressure,...) and is thus also constant. Finally, assuming a constant EEDF of the bulk electron population over the discharge conditions, which is the largest electron population, leads to an electron density linearly dependent of the discharge current i.e. the number of electrons generated in the plasma bulk is driven by the SE and each SE produces, on average, the same number of bulk electrons.

The gas phase electron generation originates from collisions cascades of energetic electrons. Interestingly, their creation through argon ionization also exhibits a linear dependence with the discharge current density, as shown in figure 8(A). The same applies for Ar excitation and their slopes are close to one. To understand these observations, one has to consider the reaction rates formalism, which, for the collision

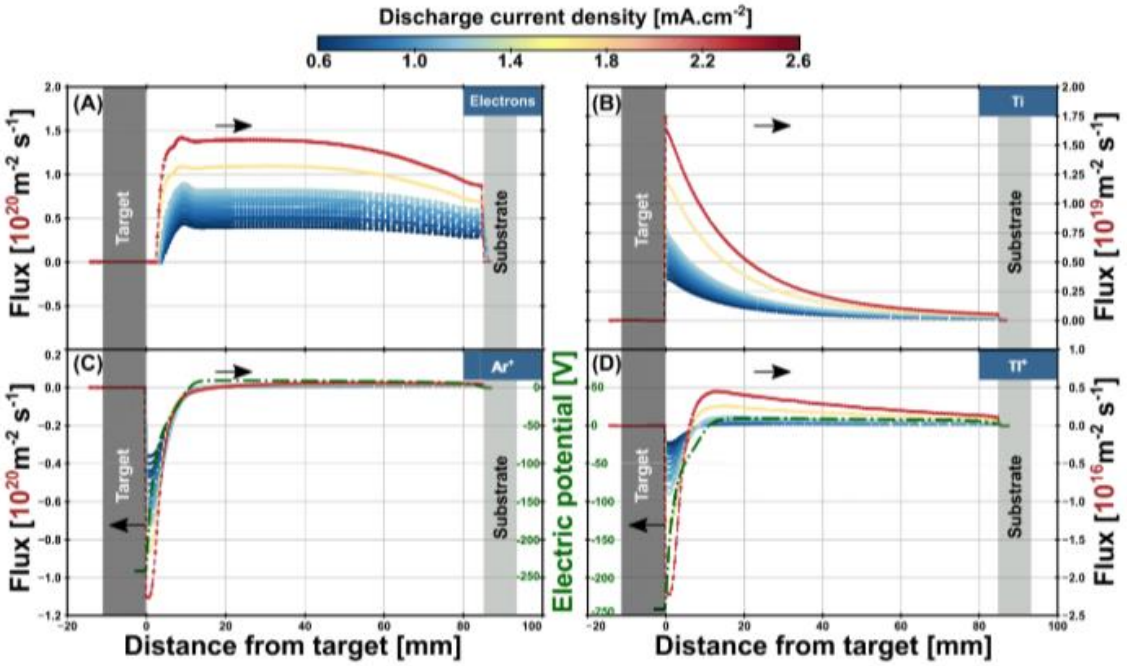

Figure 9. Simulated evolution of the parallel component (with the target surface normal vector) of each species flux as a function of the target distance. Fluxes oriented towards the target are negative, while fluxes escaping from the target are positive. Four species are plotted, electrons (figure A), sputtered titanium (figure B), Ar ions (figure C) and Ti^+ ions (figure D). On figures (C) and (D), time average electric potential for a discharge current density of 1.26 mA cm^{-2} and along an axis-centred line is added for illustration (green lines).

of two species A and B in a zero-dimensional volume can be expressed as [32].

$$R_{AB} = n_A n_B \iint \left[v_{rel} \sigma_{AB}(v_{rel}) f_A(\vec{v}_A) f_B(\vec{v}_B) \right] \times d^3 v_A d^3 v_B \ (m^{-3} s^{-1}) \quad (10)$$

With $\sigma_{AB}$the collision cross-section of the two involved species, $\vec{v}_{rel}$their relative velocity and f_A, f_B their respective velocity distribution functions.

For electron-impact ionization, the velocity of the atom/molecule is negligible as electrons are much lighter. In this case, equation (10) becomes:

$$R_{Ae} = n_A n_e \int v_e \sigma_{Ae}(v_e) f_e(\vec{v}_e) d^3 v_e \ (m^{-3} s^{-1}) \quad (11)$$

Finally, using spherical coordinates and changing electron velocity, v_e, to electron energy, E:

$$R_{Ae} = n_A n_e \sqrt{\frac{2}{m_e}} \int \sigma_{Ae}(E) f_E(E) E dE \ (m^{-3} s^{-1}) \quad (12)$$

With $\int f_E(E) \sqrt{E} dE = 1$.

If the EEDF is assumed to be constant over the discharge condition range, then the production rate R_{Ae} will also scale linearly with the electron density as $\int E \sigma_{Ae}(E) f_E(E) dE =$ constant., as observed in figure 8(A). The electron impact excitation average reaction yield is slightly below the electron impact ionization yield. It was an expected result, as excitation by electron has a similar cross section as excitation by electron but with a higher maximal yield.

For Ti, the situation is slightly different. In figure 8(B), the reaction rate of the Ti ionization collisions is plotted and fitted against the discharge current. In this case, the relationship is quadratic instead of linear. This can be explained as followed: the production of Ti ions depends on the production of two other species, sputtered Ti and electrons. Rewriting equation (12) in the case of Ti ionization gives:

$$R_{Ti-e} = n_{Ti} n_e \sqrt{\frac{2}{m_e}} \int \sigma_{Tie}(E) f_E(E) E dE \ (m^{-3} s^{-1}) \quad (13)$$

As previously discussed, in the ionization region n_e is proportional to the discharge current:

$$n_e \propto I_{disch} \quad (14)$$

According to equation (3), the production of sputtered species (N_{Ti}) can be expressed as:

$$N_{Ti}(I, E) = \frac{I_{disch}}{e(1 + \gamma_e)} \gamma_{sput}(E) \ (s^{-1}) \quad (15)$$

With $\gamma_{sput}(E)$, the sputtering yield of Ti.

Using, equation (1) and rewriting equation (15) :

$$N_{Ti}(I, E) \propto I_{disch} \cdot \gamma_{sput}(E) \approx I_{disch} \cdot V_{disch} = P_{disch} \quad (16)$$

Therefore, the production of sputtered titanium is proportional to the discharge power.

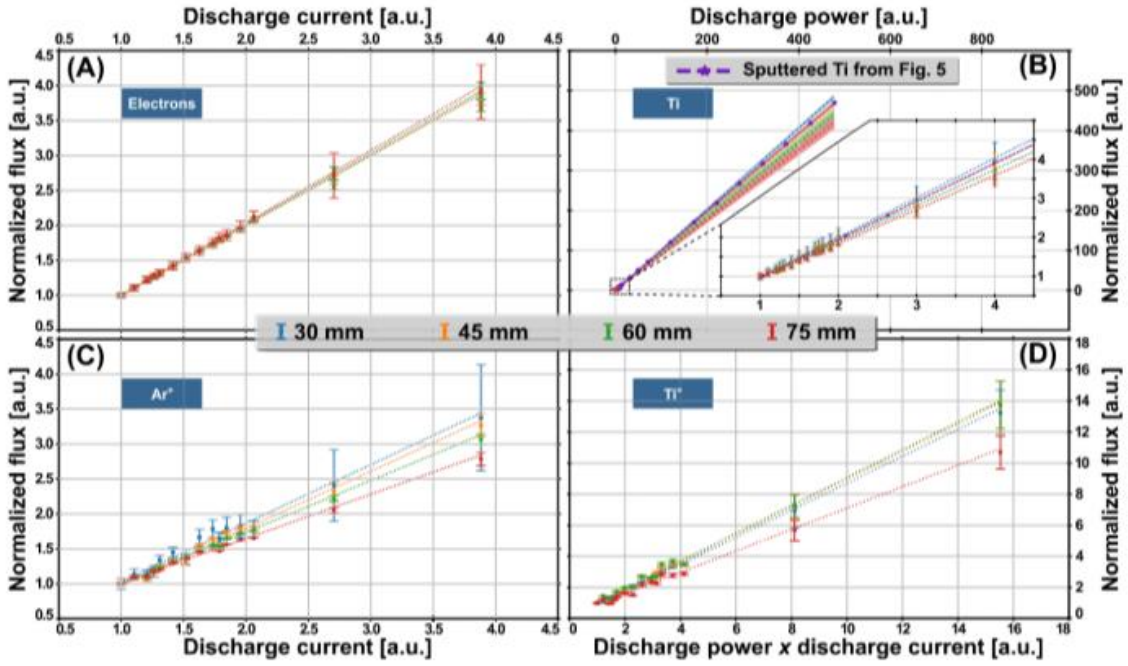

Figure 10. Simulated evolution of the species flux for 4 different vertical distances to the target. Figure (A): evolution of the normalized electron flux with the normalized discharge current. Figure (B): evolution of the normalized Ti flux as a function of the normalized discharge power. The measured flux of Ti emitted by the target, as calculated on figure 5, is added for comparison. The same normalization parameters are applied. Figure (C): normalized flux of Ar ions with the normalized discharge current. Figure (D): evolution of the normalized Ti ions flux as a function of the normalized product of the discharge power with the discharge current.

Finally, combining equation (13), equation (14) and equation (16) gives:

$$R_{\mathrm{Ti}-e} \propto I_{\mathrm{disch}}^{2} V_{\mathrm{disch}} \tag{17}$$

The quadratic dependence is the one observed in figure 8(B).

Up to now, the PICMC simulation method is demonstrated to be a valuable tool to predict the electron density and the production rate of ionization products. One additional particular feature of using this plasma simulation method is the possibility to get a better insight of the plasma dynamic and electrons. Neutrals and ions fluxes can also be derived. This is of particular interest if one wants to understand the origin of the species, which give rise to the film growth and infer on how to scale up the simulated fluxes to derive a realistic full current density situation of an experimental magnetron deposition process. Figure 9 plots the species flux components alongside the x-direction, normal to the target surface. The most obvious behaviour is the one of sputtered Ti in figure 9(B). The target being the sole source of Ti via sputtering events, the flux is high close to the target and then continuously drops while escaping the target due to diffusion in the background gas (see figure 6(E)). According to the simulations, the ionization degree is about 10^{-3}. Therefore, loss of Ti neutrals by ionization is negligible and the Ti^{+} concentration is very low as shown in figure 6(F). Ti^{+} exhibits two behaviours with the target distance: at the target, the net flux is oriented towards the cathode while 10 mm away, the net flux is oriented towards the substrate. If a titanium atom is ionized close enough to the target, it will be back attracted to the target and will participate to sputtering (self-sputtering). Due to the very low ionization degree, the self-sputtering is 10^{4} lower than sputtering by Ar^{+} (figure 9(C)). The Ar ions exhibit the same global behaviour as the Ti ions, except their flux switches from a negative to a positive sign at a larger distance from the cathode. This phenomenon can be related to the kinetic energy of the initial neutral atoms. For Ar, the kinetic energy is thermally distributed (39 meV), while for Ti atoms, the initial energy distribution has a Thompson-like shape, with a maximum around 2.4 eV and an energy tail leading to several 10 eV. Moreover, the initial angular distribution of sputtered species is oriented towards the substrate. Combined, these initial parameters confer the sputtered atoms a substrate oriented initial momentum, allowing them to overcome a small negative potential barrier once ionized, which is not the case of Ar ions. The electric potential evolution supports the explanation as it switches from negative to positive values at a distance to target of 11.2 mm and stabilize at 8–9 V, 15 mm from the target.

Electron flux is plotted in figure 9(A). At first, the electron flux increases, reaches a maximum at 9.5 mm and then slowly decreases down to the substrate. However, in front of the target, the electron net flux is close to zero i.e. electrons seem to not move towards the target neither

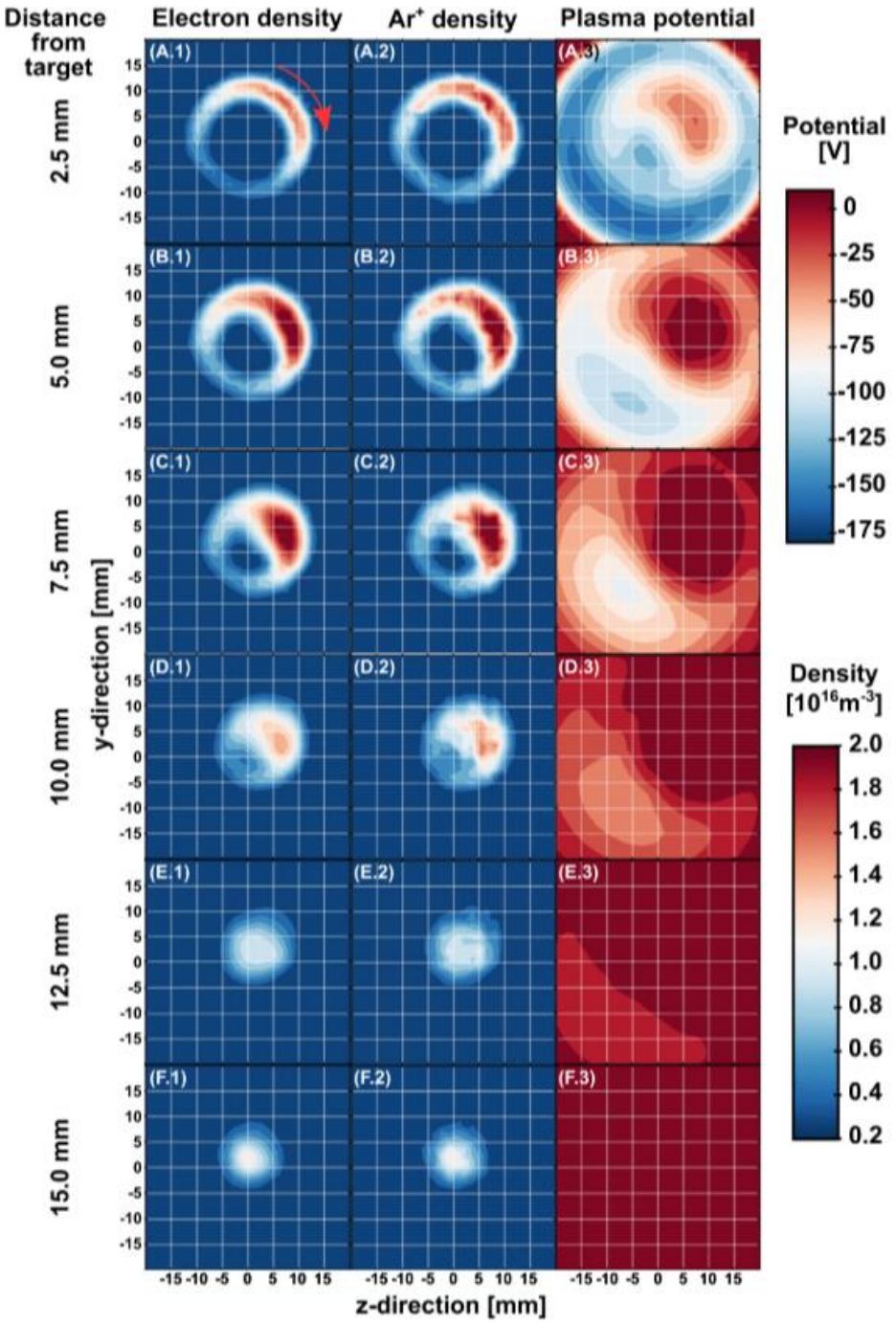

Figure 11. 2D maps of the electron density (∗.1 column), the Ar ion density (∗.2 column) and the plasma potential (∗.3 column) for various distances from the target. The simulated current density is 1.26 mA cm^{-2}. The arrow on the top left map indicates the direction of the spoke rotation.

towards the plasma bulk. The reason is because not all secondary electrons emitted from the cathode are interacting with the gas phase. A large fraction of them can reach back the target due the magnetic field shape in this region [13]. Therefore, the net flux tends to zero close to the target surface.

In the same fashion as the electron density and the reaction rates, figure 10 shows the scaling laws of species fluxes with the discharge parameters at various distances from the target. The electron flux, in figure 10(A), exhibits a linear dependence with the discharge current. Indeed, the more the discharge current increases, the more the electron density increases and the more electrons escape the MCR via the magnetic null region. At this location, the plasma potential is steady regarding the discharge current as sheath effects and $\vec{E} \times \vec{B}$ instabilities happen closer from the target. The flux of electrons is directional; as electrons are not magnetized anymore, they can travel a large distance without interacting with other species. Therefore, as the plasma potential is uniform, the flux remains directional, even several centimetres away from the target. Regarding all the other species, they behave differently to electrons, as they diffuse inside the background gas and interact with it more frequently. At 0.5 Pa and room temperature, the typical mean free path is about 1.3 cm. The flux of Ar ions, in figure 10(C), scales linearly with the discharge current. However, the longer distance from the target, the more the diffusion occurs and the less the slope of the fluxes fits over the distance. The sputtered Ti flux and the Ti ions fluxes exhibit the same behaviour as the Ar ions, except they scale linearly with other parameters. The Ti flux (figure 10(B)) linearly scales with the discharge power, as previously explained, while the Ti ions flux linearly scales with the product of the discharge power by the discharge current. Those scaling laws are the same as the ones demonstrated for the reaction rates evolution. Along with the Ti flux computed by the simulations, the amount of Ti sputtered by the target, calculated from the experimental *IV* curve (figure 5), is added on figure 10(B). The same normalization procedure is applied on those data to demonstrate their fit with the simulation results.

As previously stated, one of the major improvements of 3D PICMC simulations is that it accounts for the inherent instabilities of $\vec{E} \times \vec{B}$ plasma discharges called spokes. Many studies have been formulated several explanations to describe the behaviour of these self-organizing structures [33–36]. The interested reader is encouraged to rely on the literature for the explanation regarding the origin of the spokes. This paper is focused on their impact on the discharge behaviour and their potential implications on the upscaling laws of the PICMC simulations. Previously another team using the same software had already reported the formation of spokes in their simulations [7]. All simulations performed for this study exhibits spokes creation. For each case, only one spoke is observed and rotate in the $-\vec{E} \times \vec{B}$ direction, the same observation had already been experimentally reported by Anders *et al* in [21] for the DCMS regime. They had also measured the velocity of the ionization zones in the range 3–10 km s^{-1}. In the present study, all velocities are in the range 2.7–3 km s^{-1}. No relationship with the discharge current is observed. The 1.26 mA cm^{-2} case is used to display the structure of the rotating spoke, see figure 11.

The arrow of the top left map indicates the rotating direction of the spoke. From this figure, it is clear that the Ar^+ density follows the electron density as it was already noticed on figure 6. The negative potential of the target is more efficiently screened in the spoke region due to the increased number of charge carriers. Therefore, a higher plasma potential is observed in this region, see right column ∗.3 of figure 11. When increasing the target distance, the charged particles density decreases and the high-density zone is moved towards the target central axis i.e. towards the magnetic null region. In the MCR the charged particles density can be seen as a rotating high-density region forming a dome like structure whose apex is at the magnetic null point and whose base is parallel to the target surface.

The data from the simulations are used to track the spoke locations and compute their mean electron density i.e. the average density value within the volume in which the electron density is greater or equal to 75% of the maximal density value. The spoke motion is tracked down each microseconds of simulation time and the average density is time averaged over the last 50 μs of simulation. The results are plotted on figure 12.

A remarkable correlation between the discharge current density and the average spoke density is obtained. The found relationship between the average electron density of the spokes and the discharge current density is linear as it was also observed on figure 7 for the electron density outside the MCR.

The spoke being the space region with the highest charged density and being located in the close vicinity of the target, it is the region where the plasma sheath will be the smallest. Therefore, one could consider the spoke density as one of the main limiting factors within the simulations. As previously explained the simulation cell size is related to the Debye length, the less the Debye length, the greater the total number of cells and with it, the simulation time and the amount of required memory.

Finally, knowing how the electron density, the reactions rates and the species fluxes scale with the discharge parameters, one can specify the various plasma discharge conditions, which can be simulated and scaled up with the assumptions of this work: (i) the electrons originate either from the homogeneous reactions happening in the gas phase or from secondary emission, and (ii) the electron energy distribution is constant over the DCMS standard range conditions. Figure 13 illustrates the different electric discharge regimes and indicates the simulation range along with the up-scalable domain.

This well-known graph was originally dedicated to the classical DC electrical discharge between parallel-plane electrodes. Therefore, the discharge current density values have been adapted from [37] to fit with the typical magnetron discharge values. Except for the normal/abnormal glow transition the qualitative behaviour of the magnetron discharge is identical. Indeed, the abnormal glow transition occurs when the discharge covers the whole cathode. The voltage then begins to increase significantly in order to compensate the lack of new surface to cover. In the case of magnetically enhanced plasma discharges, the plasma is inherently confined and cannot expands over the whole cathode surface. The magnetron discharges can be considerate as operating mostly in abnormal glow mode.

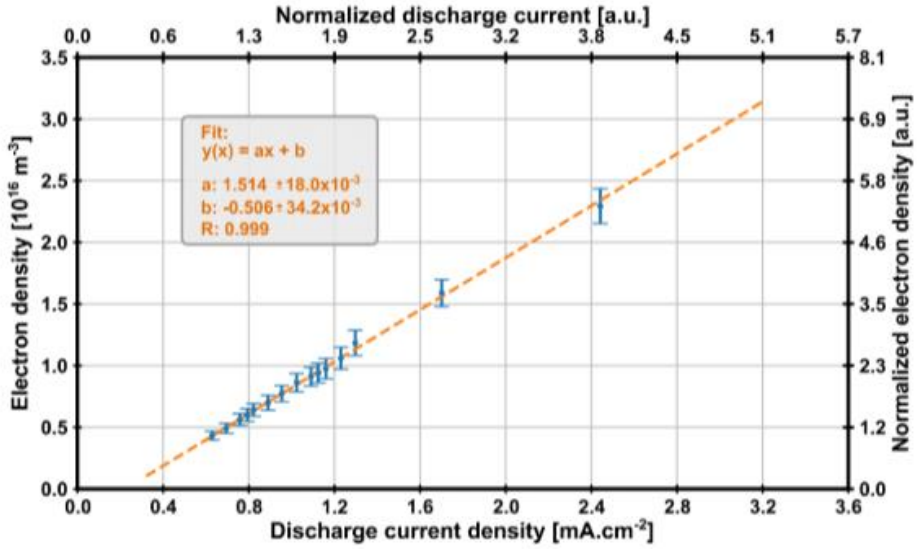

Figure 12. Evolution of the average electron density within spokes as a function of the discharge current density. Normalized values are computed according to the lowest discharge current case.The fit parameters correspond to the linear fit of the normalized data.The Pearson correlation coefficient, R, is also reported in the fit parameters.

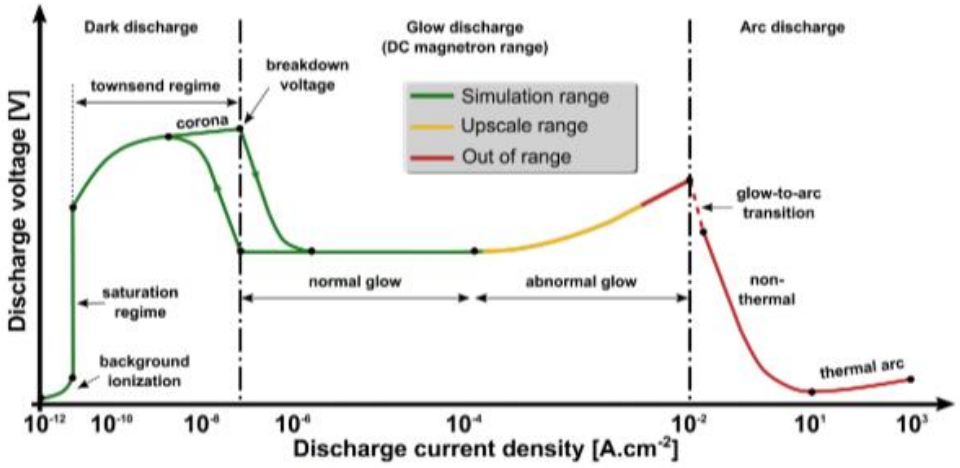

Figure 13. Basic glow discharge (adapted from [37]) structure indicating what is the accessible range for the simulation (green), the upscalable range (yellow) and the out of range domain (red) i.e. unaccessible with the considered simulation model.

As simulations are mainly constraint by electron density, simulations can be performed overall the dark discharge mode and up to the normal glow discharge. Simulation data can be up-scaled beyond this domain. However, the up-scaled laws are only valid as long as the discharge is governed by background gas ionization. When the discharge current density is increased, the electron density increases. This leads to several new phenomena: (a) an increase of the ionization degree of the discharge, i.e. the increase of sputtered atom ions, which can affect the scaling law of the sputtered atoms, the electron density and the sputtering itself, as self-sputtering is less efficient, (b) the heating up of the target, with possible thermionic electron emission and (c) an increase in electron-electron interactions, which are not included in the present simulation model. Electron–electron collisions would also have the side effect of drastically modifying the EEDF, while a constant EEDF is one of the base assumptions to apply the scaling strategy. Therefore, the scale-up laws described in this work are valid up to abnormal glow regimes. Regimes close to arc discharge and arc discharges cannot be reached with the presented strategy. However, those discharge modes are unlikely to be reached by a DC magnetron device as it would certainly permanently damage the target and/or the magnets due to overheating. For the magnetron configuration used in this study, this experimental limit is reach for current densities higher than 50 mA cm^2.

Table 5. Scaling parameters highlighted by the present study.

Species	Scaling parameter
Ar	Constant
Electron	I_{disch}
Ar^+	I_{disch}
Sputtered metal	P_{disch}
Ionized sputtered metal	I_{disch} P_{disch}

5. Conclusions

A single magnetron 3D model was set up and a Particle-in-Cell Monte-Carlo code was used to model a magnetron discharge for various discharge current densities. Due to numerical constraints, it is not possible to simulate at real discharge power. Therefore, a scaling strategy was studied and validated by Langmuir probe measurements. This was done in order to be able to scale-up simulation results to real discharge current densities, assuming the following assumptions: (i) the electrons originate either from the reactions happening in the gas phase or from secondary emission and (ii) the electron energy distribution is constant. The species fluxes towards the substrate were also investigated with the simulations, and upscaling laws were derived. The results are presented in table 5.

It was established that the presented 3D model accounts for the inherent instabilities of $\vec{E} \times \vec{B}$ plasma discharges called spokes. The spokes were tracked over the time and it was demonstrated that their evolution with the discharge parameters follows the same law as the global electron density i.e. linear scale with the discharge current.

Finally, the validity domain of both the simulation model and the scaling laws were highlighted for the glow discharge case. The simulation model can be applied as such in the dark discharge and the normal glow discharge cases. The upscaling strategy can then be used to infer particle densities/fluxes for the abnormal glow discharge mode. For late abnormal glow discharge and arc discharge modes, the present simulation model cannot be used. In addition, the spoke instabilities have been identified as one the main limiting factor for the simulation as they are the space region with the highest electron density.

Acknowledgments

This work was carried out in the framework of the industrial collective research project VICIA (Virtual Coater for Industrial Application) under contract number IGF/CORNET no. 199 EN. It was supported by the German Federal Ministry for Economic Affairs and Energy (BMWi) through the AiF (German Federation of Industrial Research Associations eV) and by the Belgian Direction Générale Opérationelle de l'Economie, de l'Emploi et de la Recherche (DGO6). The present research benefited from computational resources made available on the Tier-1 supercomputer of the Fédération Wallonie-Bruxelles, infrastructure funded by the Walloon Region under the grant agreement no 1117545. The authors would also like to thank the simulation team of the Fraunhofer Institute of Braunschweig for their development work and advice.

ORCID iDs

R Tonneau https://orcid.org/0000-0002-3246-8420
S Lucas https://orcid.org/0000-0003-3229-9855

References

[1] Derzsi A, Hartmann P, Korolov I, Karcsony J, Bnó G and Donkó Z 2009 *J. Phys. D. Appl. Phys.* **42** 100701
[2] Donkó Z, Hartmann P and Kutasi K 2006 *Plasma Sources Sci. Technol.* **15** 178–86
[3] Verboncoeur J P 2005 *Plasma Phys. Control. Fusion* **47** A231–60
[4] Siemers M, Pflug A, Melzig T, Gehrke K, Weimar A and Szyszka B 2014 *Surf. Coatings Technol.* **241** 50–3
[5] Mathioudaki S, Vandenabeele C, Tonneau R, Pflug A and Lucas S 2019 *J. Vac. Sci. Technol.* A **37** 031301
[6] Zhao H Y and Mu Z X 2008 *Phys.* B **17** 1475–9
[7] Pflug A, Siemers M, Melzig T, Schäfer L and Bräuer G 2014 *Surf. Coatings Technol* **260** 411–6
[8] Van Der Straaten T A, Cramer N F, Falconer I S and James B W 2006 *Particle-in-cell Simulat.* **31** 177–90
[9] Kim H C, Iza F, Yang S S, Radmilović-Radjenović M and Lee J K 2005 *J. Phys. D. Appl. Phys.* **38**
[10] Shon C H, Lee J K, Lee H J, Yang Y and Chung T H 1998 *IEEE Trans. Plasma Sci.* **26** 1635–44
[11] Tskhakaya D, Matyash K, Schneider R and Taccogna F 2007 *Contrib. Plasma Phys.* **47** 563–94
[12] Sigmund P 1969 *Phys. Rev.* **184** 383–416
[13] Buyle G, De Bosscher W, Depla D, Eufinger K, Haemers J and De Gryse R 2003 *User Model. User-adapt. Interact.* **70** 29–35
[14] Musil J, Satava V and Baroch P 2010 *Thin Solid Films* **519** 775–7
[15] Sigurjonsson P and Gudmundsson J T 2008 *J. Phys. Conf. Ser.* **100**
[16] Turner M M 2006 *Phys. Plasmas* **13**
[17] Pflug A, Siemers M, Schwanke C and Szyszka B 2010 *Vak. Forsch. Prax.* **22** 31–4
[18] Melzig T, Siemers M, Pflug A and Rank R 2014 *Surf. Coatings Technol.* **241** 30–2
[19] Schwanke C, Pflug A, Siemers M and Szyszka B 2012 *Applied Parallel and Scientific Computing* vol 7133 ed K Jónasson (Berlin: Springer)
[20] Phelps A V 1994 *J. Appl. Phys.* **76** 747–53
[21] Pancheshnyi S, Biagi S, Bordage M C, Hagelaar G J M, Morgan W L, Phelps A V and Pitchford L C 2012 *Chem. Phys.* **398** 148–53
[22] Lennon M A, Bell K L, Gilbody H B, Hughes J G, Kingston A E, Murray M J and Smith F J 1988 *J. Phys. Chem. Ref. Data* **17** 1285–363
[23] Tonneau R, Moskovkin P, Pflug A and Lucas S 2018 *J. Phys. D. Appl. Phys.* **51** 195202
[24] Depla D, Mahieu S and De Gryse R 2009 *Thin Solid Films* **517** 2825–39
[25] Jimenez F, Ekpe S D and Dew S K 2006 *J. Vac. Sci. Technol.* A **24** 1530–4
[26] Godyak V, Piejak R and Alexandrovich B 1992 *Plasma Sources Sci. Technol.* **1** 36–58
[27] Kagan Y M and Perel' V I 1964 *Sov. Phys. Usp.* **6** 767–93

[28] Rainer B and Wolfgang E 2007 *Sputtering by Particle Bombardment Experiments and Computer Calculations from Threshold to MeV Energies* (Berlin: Springer) (https://doi.org/10.1007/978-3-540-44502-9)
[29] Lieberman M A and Lichtenberg A J 2005 *Principles of Plasma Discharges and Materials Processing* 2nd edn (Hoboken, NJ: Wiley)
[30] Seo S-H and Chang H-Y 2004 *J. Appl. Phys.* **96** 1310–7
[31] Field D J, Dew S K and Burrell R E 2002 *J. Vac. Sci. Technol.* A **20** 2032
[32] Benedikt J 2010 *J. Phys. D. Appl. Phys.* **43** 043001
[33] Revel A, Minea T and Tsikata S 2016 *Phys. Plasmas* **23** 100701
[34] Hecimovic A, Maszl C, Schulz-Von Der Gathen V, Böke M and Von Keudell A 2016 *Plasma Sources Sci. Technol.* **25** 035001
[35] Brenning N, Lundin D, Minea T, Costin C and Vitelaru C 2013 *J. Phys. D. Appl. Phys.* **46** 084005
[36] Panjan M and Anders A 2017 *J. Appl. Phys.* **121** 063302
[37] Roth J R, Rahel J, Dai X and Sherman D M 2005 *J. Phys. D. Appl. Phys.* **38** 555–67

7 The role of charged particles

With Chapter 6, the last necessary piece of tool required for the design of the *Virtual Coater* was introduced and validated.

The present chapter aims to close the loop of the *VC* concept as presented in chapter 4, by putting together the three software packages of the *VC* flowchart from Figure 15. Its goal is to answer the following questions: *what are the effects of charged particles on the final film properties? Overall, can Virtual Coater predict these properties?*

For this purpose, DSMC simulations are restarted in order to include atomic oxygen as new neutral particle. The results are used as input to new PICMC simulation in order to capture information about charged particles within the dual magnetron coater. The particle fluxes are then scaled up according to the laws described in chapter 6 and extended to the case of reactive magnetron sputtering. O_2^+ ions are assumed to follow the same laws as Ar^+ ions, as O_2 is also part of the background gas. O^+ ions are assumed to follow the same law as Ti^+ ions, as being produced at first by sputtering. Finally, the flux of O^- ions is assumed proportional to the discharge current density as most of the negative ions hitting the substrate are produced at the target surface.

Angular and energy distributions of the particles are inputs for thin film growth by Nascam simulations. The addition of energetic particles in Nascam simulations enables to efficiently predict the tilting column angles of the coating subject to a higher flux of O^- ions.

It has to be mentioned that a new version of Nascam was used for this part of the thesis. Indeed, in version 4.7, energetic particles were transferring their energy only in a very local area i.e., only to their first neighbours; the subsequent collision cascade was therefore not accounted for. The new Nascam version (V5) implements a binary collision approximation (BCA) algorithm, which enables a more accurate description of the collision cascades and therefore a better description of the energy transfer to the growing film. More details can be found in Annex 1 .1.

The main findings of this part can be resumed as follow:

1. The computed densities and fluxes of the charged and neutral species enable to predict the final coating morphology. Indeed, Nascam simulations accurately reproduce the column tilting angles of the inclined samples.
2. The growth of an amorphous TiO_2 thin film in the transition region is explained by the inhibition of the Ti diffusion occurring on the surface of the growing film.

The O^- ions flux is demonstrated to be highly directional and responsible for the crystallization of the coatings by drastically increasing the Normalized Energy Flux (NEF) towards the substrate location.

Understanding the role of energetic particles during the growth of TiO_2 thin films by reactive magnetron sputtering through multi-scale Monte Carlo simulations and experimental deposition

R. Tonneau[1], P. Moskovkin[1], J. Muller[1], T. Melzig[2], E. Haye[1], S. Konstantinidis[3], A. Pflug[2], S. Lucas[1]

[1]Namur Institute of Structured Matter (NISM), Laboratoire d'Analyse par Réactions Nucléaires (LARN), University of Namur (UNamur), 61 rue de Bruxelles, B-5000 Namur, Belgium

[2] Fraunhofer Institute for Surface Engineering and Thin Films IST; Bienroder Weg 54e, 38108 Braunschweig, Germany

[3] University of Mons, Plasma-Surface Interaction Chemistry, 23place du Parc, 7000 Mons Belgium

Email addresses: romain.tonneau@unamur.be; pavel.moskovkim@unamur.be; jerome.muller@unamur.be; thomas.melzig@ist.fraunhofer.de, emile.haye@unamur.be; stephanos.konstantinidis@umons.ac.be; andreas.pflug@ist.fraunhofer.de; stephane.lucas@unamur.be

Corresponding author: Prof. Stéphane Lucas, University of Namur (UNamur), 61 rue de Bruxelles, B-5000 Namur, Belgium, Tel : +32 (0)81 725 479, Fax: +32 (0)81 725 474, email: lucas.stephane@unamur.be

Abstract

In this paper, a previously established 3D multi-scale simulation chain of plasma deposition process, based on a combination of a Direct Simulation Monte Carlo (gas phase) algorithm and a kinetic Monte Carlo (film growth) code, is improved by the addition of a Particle-in-Cell Monte Carlo Collision algorithm in order to take into account and clarify the role of charged particles. The kinetic Monte Carlo code is also extended with a binary collision approximation algorithm to handle charged particles. This modelling strategy is successfully applied to the growth of TiO_2 thin films by means of reactive magnetron sputtering. In order to highlight the effects of negative oxygen ions, two substrate locations are selected: one in the median plane of the targets and another one off-median plane. The model efficiently predicts the densities and fluxes of both charged and neutral particles towards the substrate. Typical results such as particle densities, the discharge current density and ion flux onto the target and the various substrate locations are calculated. The angular distribution and energy distribution of all involved particles are sampled at these very same substrate locations and the NAnoSCAle Modelling (NASCAM) code implementing the kinetic Monte Carlo approach, uses these results to explain the morphology of the experimentally deposited coatings. The changes throughout the transition from metallic deposition to stoichiometric TiO_2, of the columnar structure of the deposited films is explained by the suppression of the atom diffusion, on the growing film, due to Ti oxidation. Moreover, the high energy negative atomic oxygen ions originating from the targets are identified as origin of the abnormally low inclination of the columnar structure experimentally observed for the oxide mode coatings. Measurements of the normalized energy flux (energy per deposited atom) is experimentally investigated to support and highlight the important role of energetic particles during film growth.

1. Introduction

Nowadays, reactive magnetron sputtering (RMS) is a well-mastered process used for the production of various thin films whose properties can widely differ from their bulk equivalent because of ultra-fast condensation of species coming from the plasma. The plasma/surface interactions during the film growth are the driving forces for those peculiar properties [1] and linking those interactions with the characteristics of the materials at a nanoscale level is of great scientific interest. This is especially true when the film growth takes place by condensation of neutral species but also energetic particles (ions and atoms).

The influence and the generation of charged species in the RMS gas phase has been thoroughly studied in the last decades, and some computer models have been proposed [2–4]. Unfortunately, most of them involve computational modelling of separated phenomena taking place either at the target, on the substrate, or in the gas phase. The present study aims to use today's numerical capabilities in order to simulate a complete chain of mechanisms occurring in RMS deposition processes; i.e., from plasma ignition at the target, transport in the gas phase to film growth at desired substrate location. For that purpose, particle-in-cell Monte Carlo modelling of the plasma phase, and kinetic Monte-Carlo (kMC) modelling of film growth are combined together into a Virtual Coater to simulate the RMS deposition of titanium dioxide. Indeed, TiO_2 thin films are nowadays involved in a large range of applications [5–9], making it an interesting system to study. The deposition of thin TiO_2 thin films by RMS generally results in coatings which can be either fully amorphous or comprise two different crystalline phases, namely anatase and rutile [10]. Those phases exhibit different physical properties. On the one hand, the rutile phase has a higher mass density and a high refractive index making it suitable for applications like anti-reflective coatings [11,12]. On the other hand, the anatase phase is hydrophilic and exhibits a high photocatalytic activity, making it suitable for self-cleaning [13],

antibacterial and antimicrobial surfaces [14–16] as well as anti-fogging applications for optical coatings [17,18].

In a previous work [19], the role of the neutral species in the growth of TiO_2 was investigated with Direct Simulation Monte Carlo (DSMC) modelling combined with kMC modelling. One of the key features was the addition of a wall chemistry similar to Berg's model [20] to model reactive absorption on surfaces. Angular and energy distributions of film forming species are extracted at substrate locations and used to model film growth via the kinetic Monte Carlo method using the NASCAM implementation [21]. This modelling strategy accurately reproduces the composition and morphology of deposited columnar coatings, but when compared with experimental results, the angles of the columns are overestimated by the simulations and the deviation increases with the oxygen content in the discharge. This first model approach is characterised by the absence of any charged particles and therefore atom relocation due to energy transfer is not considered. The present study aims to improve the simulation model. For that purpose, plasma modelling via the particle-in-cell Monte Carlo (PICMC) method is first added to the simulation chain in order to get insights about the creation and transport of charged particles and their role on the growth of TiO_2 as deposited by RMS. Second, experimental deposition of Ti in either metallic, transition or full oxide mode is performed on flat substrate oriented either perpendicularly or tilted with respect to the mean sputter flux direction facing the targets or placed in a location that prevents energetic ions like O^- to participate to the film growth. Indeed, negative oxygen ions in RMS is a well-documented topic, and most of the related articles are focussed on experiments to reveal their existence [44–47] and to elaborate on their impacts on the film growth [48–50]. Unfortunately, the literature is not as extensive regarding the modelling of their production yield. One of the best approach was performed by Mahieu *et al* [51] who included negative oxygen ion emission from an Al_2O_3 target in the SiMTRA [39] model. Simulation results were compared to experimental

measurements obtained from energy resolved mass spectrometry. They demonstrated that the energy and spatial distributions of the high-energy O^- ions can be reproduced by creating those ions at the target surface and computing their transport through the neutral gas. In the same study, they also showed that the amount of high-energy negative ions steeply increases when the target switches from metallic to oxide mode and exhibits a plateau when in the oxide mode. Therefore, the amount of high energy O^- depends on the target condition and not on the O_2 partial pressure.

In the present study, extensive characterization of the film morphology as a function of process dynamics are provided by scanning electron microscopy (SEM), atomic force spectroscopy (AFM), optical emission spectroscopy (OES) and active thermal probe (ATP). The experimental results are compared with simulations to gather a full picture of the physical phenomena happening during the growth of the thin films.

2. *Materials and methods*

2.1. Gas phase model description

The kinetic and self-consistent PICMC method is the most appropriate for the low-pressure RMS processes [4,5]. This technique simulates a reduced number of representative particles (called super-particles) in the discharge and computes their trajectory by solving the Newton-Lorentz equation coupled with the Poisson equation for self-consistent computation of the charge and electric potential distribution in electrostatic approximation. The collisions are managed by a Monte-Carlo method that computes the scattering and final velocities of particles. The PICMC simulations performed in the current study involve ten species: Ar, O_2, O, Ti, Ar^+, O_2^+, O^+, O^-, Ti^+ and electrons. All PICMC simulations start with an initial background gas distribution as obtained from previous DSMC simulation runs, including a dynamic wall chemistry model as described in [19]. The subsequent PICMC simulations are running for a physical time interval of 150 µs, long enough to reach steady state from the charged particles point of view.

The code used to perform both, the DSMC and PICMC simulations has been developed at the Fraunhofer IST [22–24]. In DSMC mode, the code handles only neutral particles and wall chemistry while the PICMC mode enables computation of charged particle's trajectories in a self-consistent electric field plus a previously computed constant magnetic field. Both simulation methods are alternatingly iterated to reach steady-state solution for both neutral and charged particles. Indeed, when dealing with charged species, the inherent numerical constraints of the PICMC method [25] impose strict limitation on the upper values for cell spacing and time step, and therefore only a physical time interval of a few hundreds of microseconds can be simulated with feasible computational effort. While that may be already sufficient to get steady-state regarding charged particles, it is not the case for neutral particles which usually require several milliseconds or even seconds depending on the geometry and

reaction chemistry. To solve this, a time-scale splitting method is applied to achieve steady-state for both, charged and neutral species. It assumes a constant neutral particle distribution during plasma time scale and constant plasma properties during the time scale of neutral transport. The absence of charged particles in the DSMC method allows to use larger cell spacing and time step. Combining DSMC and PICMC methods is therefore the strategy to put in place to simulate a complete plasma deposition process. It is important to note that the DSMC algorithm always uses the real 3D geometry of the coater while a volume reduced geometry is used with the PICMC algorithm. For the PICMC algorithm being most resource consuming, the smallest geometry as possible is used with this method to improve the overall simulation speed. The chart of Figure 1 illustrates the iterative workflow used to perform the present study.

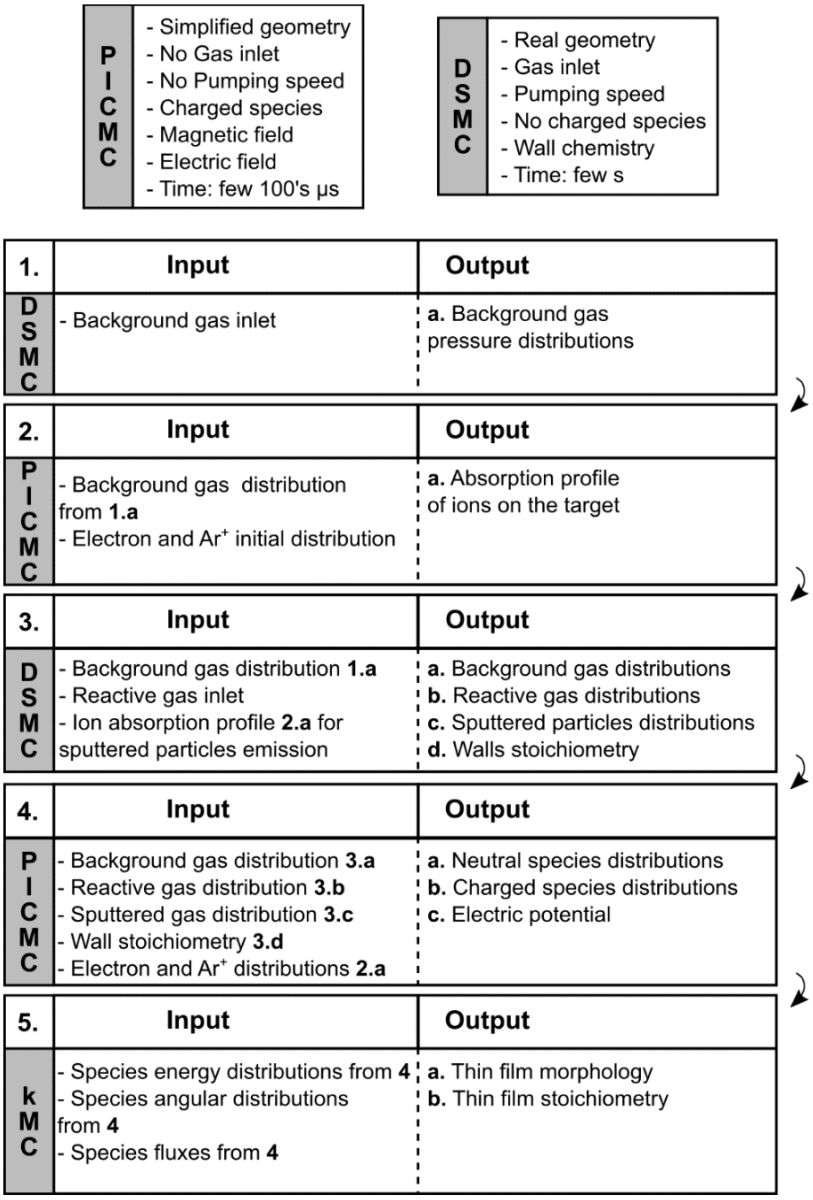

Figure 1 Simulation workflow chart

First, the DSMC algorithm is used with Ar only within the real 3D geometry to simulate the sputter gas distribution in the chamber. Second, the PICMC algorithm is used to compute the absorption profile of ions onto the target in order to obtain the racetrack profile. Third, a reactive gas inlet, wall chemistry and sputtered particles are included in the DSMC simulation model. The racetrack profile taken from the second simulation enables to use a realistic emission profile of particles sputtered from the target. The combination of these three

simulations steps has been already successfully used in our previous work to predict the well know hysteresis behaviour of reactive deposition of TiO_2 by RMS [19]. The fourth step uses the neutral particle distributions as simulated at step three in order to compute the distributions of charged particles in a simplified 3D geometry (Figure 2.A). That ensures the model treatment of all the species, namely Ar, O_2, O, Ti, Ar^+, O_2^+, O^+, O^-, Ti^+, condensing on the substrate. Finally, a kinetic Monte Carlo (kMC) algorithm as described in [19] is used to perform film growth simulations based on the outputs of step 4.

A detailed description of the Ti / TiO_2 wall reaction chemistry used within the DSMC method and relevant model parameters used can be found in [19]. In this previous study, for the sake of simplicity and due to the lack of plasma simulation, oxygen dissociation and hence, atomic oxygen was not included in the model. This simplification is no more valid for the present study as its very purpose is to study the effect of charged particles. Thus, the model is extended with the following:

- Atomic oxygen is included as additional species.
- The material sputtered by the target is either Ti or O.
- The reactive wall model includes formation of TiO_2 and TiO from metallic Ti. The sticking coefficient of O is assumed to be the same as O_2 (value of 1). The sticking coefficients of O and O_2 onto TiO sites are assumed to be 1 and 0. For TiO_2 sites all oxygen sticking coefficients are set to 0.

The Variable Soft Sphere Model [26,27] is used to handle collisions between the process gases Ar, O_2 and O. The same assumption as in [19] is made for collisions between Ti and O: an average of the Ti-Ti and O-O cross sections is taken due to the non-availability of more accurate data. The same conclusions regarding film growth are obtained with this updated model i.e. the Ti flux rules the final morphology of the coatings and the deposited Ti acts as a backbone for

the growing films. Moreover, the addition of atomic oxygen does not change the columnar orientation of the films.

Besides the neutral species related cross-sections, the PICMC algorithm implements 36 more cross sections involving charged species. All the cross-sections used along with their references are gathered in Table 1.

#	Reaction	Type	Ref
	Momentum transfer collisions		
(1)	$Ar + Ar \rightarrow Ar + Ar$	VSS	[26]
(2)	$Ar + Ar^+ \rightarrow Ar + Ar^+$	$Q_W(\epsilon_i)$	[28]
(3)	$Ar + Ti \rightarrow Ar + Ti$	BM	[29,30]
(4)	$Ar + Ti^+ \rightarrow Ar + Ti^+$	BM	Same as (3)
(5)	$Ti + Ti \rightarrow Ti + Ti$	BM	[29,30]
(6)	$Ar + O \rightarrow Ar + O$	BM	[29,30]
(7)	$Ar^+ + Ti \rightarrow Ar^+ + Ti$	BM	Same as (3)
(8)	$O_2 + O_2 \rightarrow O_2 + O_2$	VSS	[26]
(9)	$Ti + Ti^+ \rightarrow Ti + Ti^+$	BM	Same as (5)
(10)	$Ar + O_2 \rightarrow Ar + O_2$	VSS	[26,27]
(11)	$e + Ar \rightarrow e + Ar$	$Q_W(\epsilon_i)$	[28]
(12)	$O_2 + O \rightarrow O_2 + O$	BM	[29,30]
(13)	$Ti + O_2 \rightarrow Ti + O_2$	BM	Average of (5) & (8)
(14)	$O + O_2^+ \rightarrow O + O_2^+$	BM	[29,30]
(15)	$Ti + O \rightarrow Ti + O$	BM	[29,30]
(16)	$O + O \rightarrow O + O$	BM	[29,30]
(17)	$Ar + O^- \rightarrow Ar + O^-$	BM	Same as (6)

(18)	$Ar^+ + O \rightarrow Ar^+ + O$	BM	Same as (6)
(19)	$Ti + O^- \rightarrow Ti + O^-$	BM	Same as (15)
(20)	$Ti^+ + O \rightarrow Ti^+ + O$	BM	Same as (15)
(21)	$O + O^- \rightarrow O + O^-$	BM	Same as (16)
(22)	$O_2 + O^- \rightarrow O_2 + O^-$	BM	Average of (16) & (8)
(23)	$Ti^+ + O_2 \rightarrow Ti^+ + O_2$	BM	Same as (13)
(24)	$Ti + O_2^+ \rightarrow Ti + O_2^+$	BM	Same as (13)
(25)	$e + O_2 \rightarrow e + O_2$	$\sigma(\epsilon)$	[31]
	Charge transfer collisions		
(26)	$Ar + Ar^+ \rightarrow Ar^+ + Ar$	$Q_W(\epsilon_i)$	[28]
(27)	$Ar + {O_2}^+ \rightarrow Ar^+ + O_2$	$\sigma(\epsilon)$	[32]
(28)	$O_2 + O_2^+ \rightarrow O_2^+ + O_2$	$\sigma(\epsilon)$	[33]
(29)	$Ar^+ + O_2 \rightarrow Ar + {O_2}^+$	$\sigma(\epsilon)$	[34]
	Excitation collisions		
(30)	$e + Ar \rightarrow e + Ar^*$	$Q_W(\epsilon_i)$	[28]
(31)	$e + O_2 \rightarrow e + O_2(a^1\Delta_g)$	$\sigma(\epsilon)$	[31]
(32)	$e + O_2 \rightarrow e + O_2(A^3\Sigma_u^-)$	$\sigma(\epsilon)$	[31]
(33)	$e + O_2 \rightarrow e + O_2(B^3\Sigma_u^-)$	$\sigma(\epsilon)$	[31]
(34)	$e + O_2 \rightarrow e + O_2(c^1\Sigma_g^+)$	$\sigma(\epsilon)$	[31]
(35)	$e + O_2 \rightarrow e + O_2(B^3\Sigma_u^- + {}^1\Delta_u)$	$\sigma(\epsilon)$	[31]
(36)	$e + O_2 \rightarrow e + O_2(b^1\Sigma_g^+)$	$\sigma(\epsilon)$	[31]
(37)	$e + O_2 \rightarrow e + O_2(v = 1)$	$\sigma(\epsilon)$	[31]
(38)	$e + O_2 \rightarrow e + O_2(v = 2)$	$\sigma(\epsilon)$	[31]

(39)	$e + O_2 \rightarrow e + O_2(v = 3)$	$\sigma(\epsilon)$	[31]
	Ionization collisions		
(40)	$e + Ar \rightarrow 2e + Ar^+$	$\sigma(\epsilon)$	[28]
(41)	$e + O_2 \rightarrow 2e + {O_2}^+$	$\sigma(\epsilon)$	[31]
(42)	$e + Ti \rightarrow 2e + Ti^+$	$\sigma(\epsilon)$	[35]
(43)	$e + O \rightarrow 2e + O^+$	$\sigma(\epsilon)$	[36]
(44)	$e + O_2 \rightarrow O + O^-$	$\sigma(\epsilon)$	[37]

Table 1 *List of the cross sections implemented in the PICMC model. The references of the cross sections* ($\boldsymbol{\sigma(\epsilon)}$)*, the Born-Mayer-Type interatomic potential parameters (BM) or the various integrated transport cross sections* $\boldsymbol{Q_W(\epsilon_i)}$*, are listed in the last column. Due to lack of data un the literature some reaction cross sections are assumed as identical as other known ones. In this case, the reference column indicates to which other collision the reaction relates to.*

Plasma-Wall interactions

In addition to interactions in the plasma, charged particles also interact with the walls through reflection, neutralization, adsorption or creation of new particles. All included positive ions in the present study are assumed to neutralize after reflection at the walls (sticking coefficient of 0). For negative charge species (electrons and O^-), their sticking coefficient is set to 1 for all surfaces.

Positive ions near the target can bombard the target surface. While the sputtering behaviour of metallic targets is well documented in the literature [38–41], this is not the case with oxidized targets sputtered by ions with energy lower than 500 eV. For reactive processes, O_2^+ is assumed to be dissociated at target surface (as the ion kinetic energy is much larger than the binding energy of the molecular ion), and each fragment keeps half of the initial kinetic energy of the molecular ion. TRIDYN simulations [42,43] are used to evaluate the sputter yield for both metallic (pure Ti) and fully oxidized targets (TiO_2). For the transition case, the target is assumed to consist of both metallic Ti or TiO_2 sites emitting particles independently from their neighbours. In the present model, sputtered TiO_2 molecules are decomposed into Ti and O_2, and the overall sputter flux consists of a linear combination of the sputtered particles from either Ti or TiO_2. Secondary electron emission yield values are listed in Table 2. The backscattering of positive ions hitting the target at high energy is not included in the model. Indeed, this phenomenon is significant only for high atomic mass target materials.

Additionally, negative atomic oxygen ions are included in the model by assigning a negative ion emission yield (γ_{O^-}) to the TiO_2 material, where γ_{O^-} is the probability for an incoming ion to generate a negative oxygen ion. Unfortunately, to the best of our knowledge, no predictive model exists to estimate the amount of created O^- at the target. Moreover, as the O^- ions are accelerated in the cathode sheath, their angular distribution is very narrow, leading to significant sensitivity on the placement of mass spectrometry measurements. Recently Moens *et al.* [52]

demonstrated the non-negligible effect of space-charge to the O^- transport through the gas phase and compared their results with experimental measurements leading to the determination of a $\gamma_{O^-} = 1.49\ \%$ for the reactive deposition of CeO_2. In addition to their modelling approach, Mahieu *et al.* [51] established an experimental relationship between the effective secondary emission yield of an oxide with the number of O^- emitted. However, by the time it was not possible to give quantitative values for the O^- emission from TiO_2. Using their experimental relationship and taking $\gamma_{O^-} = 1.49\ \%$ for CeO_2lead to $\gamma_{O^-} = 0.10\ \%$ for TiO_2 i.e. 0.10% of the oxygen sputtered from the target is emitted as negative oxygen ion. This constant value will be used for all the simulation of the current study. Finally, Mahieu *et al.* [51] also showed that the energy distribution of O^- ions is divided in 3 main contributions: (i) low energy ions ($E < 50\ eV$) (ii) high energy ions ($E = eV_{disch}$) related to the discharge voltage and (iii) mid-energy range ions ($50\ eV \leq E \leq eV_{disch}$). The low energy contribution (i) corresponds to negative oxygen ions created in the plasma bulk via dissociative electron attachment to O_2. The high-energy range are O^- ions created at target surface and accelerated through the entire cathode sheath. The mid-energy range O^- corresponds to target emission of negative molecular ions such as O_2^-, MO^- and MO_2^-. This mid-energy range, was demonstrated to be at least one order of magnitude less important than the contribution (ii). In the present model, only the contribution of (i) and (ii) are implemented due to the non-availability of collision cross-sections for TiO and TiO_2 molecules.

Film growth modelling

The simulation of TiO_2 film growth is based on a 3D kinetic Monte-Carlo approach using the software NASCAM [21]. The operating mode of NASCAM has been described in detail in a previous paper dedicated to TiO_2 deposited by magnetron sputtering [19] and is mainly based on a "hit-and-stick" model with variable sticking coefficients and with energy and momentum

transfer from the deposited atoms to the film. However, this previous work was limited to the deposition of low energy neutral particles, and a simplified energy transfer algorithm was used, where the energy of incident particle is supposed to be not higher than 100 eV. Then, the modelling of adatom displacement due to ion bombardment was rather limited.

In this present study, an advanced model has been integrated to NASCAM in order to include high energy ions deposition. It is based on a Monte-Carlo binary collision approximation (BCA) model [53,54], where the collisions of an incoming ion are considered as a sequence of independent collisions. More precisely, a linear collision cascade BCA model [53,55,56] is used where all the recoils produced in the film are treated as a sequence of recoil generations, and where the path of a moving atom between two collisions is supposed to be linear.

2.2. Description of the experimental coater configuration

The coater comprises two circular magnetron sputtering sources by Kurt J. Lesker company with a diameter of 5.1 cm and a target thickness of 6.4 mm. The target material is Ti (99.995%). As shown in Figure 2 (A), they are inclined against each other by 90° and point towards a substrate holder located in the centre of the coater at a distance of 150 mm. The magnets of both magnetrons are polarized in closed field configuration. The system is pumped with a 260 $l.s^{-1}$ capacity turbo molecular pump. The DC generators are TDK Lambda Genesys, one for each magnetron. During deposition, both power supplies operate in constant current mode at a fixed value of 0.5 A. The same procedure is followed for all experimental depositions. First, the chamber is loaded with clean samples. Second, the chamber is pumped to a base pressure below $1.3x10^{-4}$ Pa. Third, the chamber is filled with Ar at a constant pressure of 0.5 Pa. Fourth, oxygen is injected into the chamber. The oxygen mass flow is controlled by a Nova Fabrica Ltd regulation system (FloTron^{TM}) allowing feedback regulation control based on optical emission signal. Devices used for in-situ measurements are the following:

(i) Inficon Quartz Crystal Microbalance. The device is located at central substrate location.

(ii) Data provided directly by TDK Lambda Genesys power supply.

(iii) FloTron (Ti: 363 nm)

(iv) Active Thermal Probe from Neoplas Control and located at central substrate location in order to evaluate the energy influx toward the substrate.

350 nm to 500 nm tick coatings were deposited to compare their properties with the one predicted by simulations.

Silicon samples were analysed by AFM, X-ray Diffraction (PANalytical X'Pert PRO diffractometer, Cu Kα 1.5406 Å, θ/θ configuration), and SEM (Jeol 7500F). AFM images were recorded in air, in tapping mode with a Nanoscope III from Veeco Instruments (Santa Barbara, CA, USA). The cantilevers (Tap300Al-G from Budget Sensors) were silicon cantilevers with a resonance frequency around 300 kHz and a typical spring constant of around 40 N/m, and an integrated silicon tip with a nominal apex radius of curvature <10 nm. So-called soft-tapping conditions were used, that is the ratio between the set-point amplitude and the free amplitude of the cantilever vibration was always kept above 0.8. Images were recorded at 5×5 µm², 3×3 µm², and 1×1 µm² sizes with 512×512 lines per image.

In order to study the influence of the ion fluxes on the coating properties, samples are loaded in a way that two of them are positioned directly in the median plane of the machine. Two others are located 40 mm above the median plane, not directly in the axis of the targets. A sketch of the sample holder positions is drawn on Figure 2.B

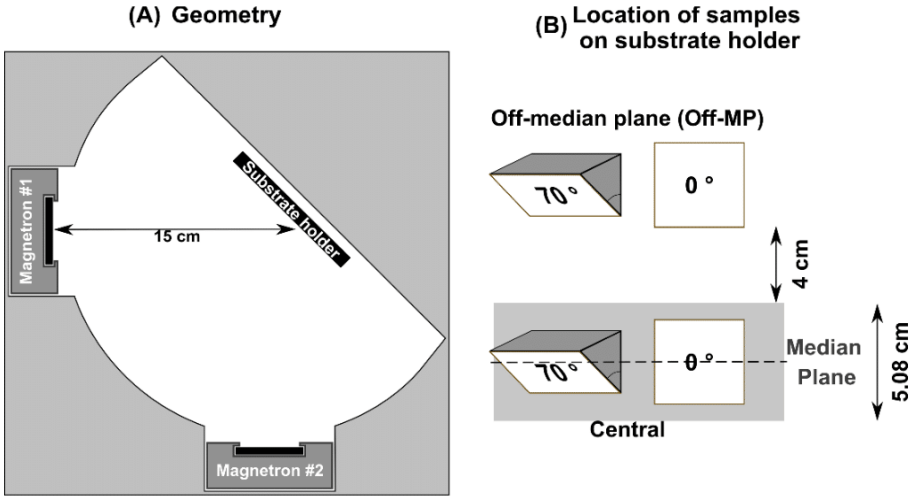

Figure 2 *(A) Simplified geometry used for PICMC simulations (B) sketch of the sample holder with the positions of the various samples.*

For each deposition the coater was loaded with 4 samples at different locations:

- 2 samples in the median plane: 1 tilted at 70° and one straight.
- 2 samples off the median plane (off-MP): 1 titled at 70° and one straight.

The purpose of the inclined samples is to study the impact on the columnar orientation of the coatings of energetic particles (ions). Indeed, it has been previously demonstrated that at an angle of 70°, the film growth of TiO_2 is expected to be columnar [19].

The TiO_2 deposition parameters as a function of oxygen flow show a pronounced hysteresis behaviour as shown in Figure 3. The coated samples are produced at three selected working points, one in metal mode at an oxygen flow of 2 sccm, one in oxide mode at 8 sccm and a third one in transition mode. The latter requires a feedback loop control provided by the FloTron with a set point of 50% of the OES Ti intensity in metal mode, which results in an oxygen flow in the range of 3-5 sccm.

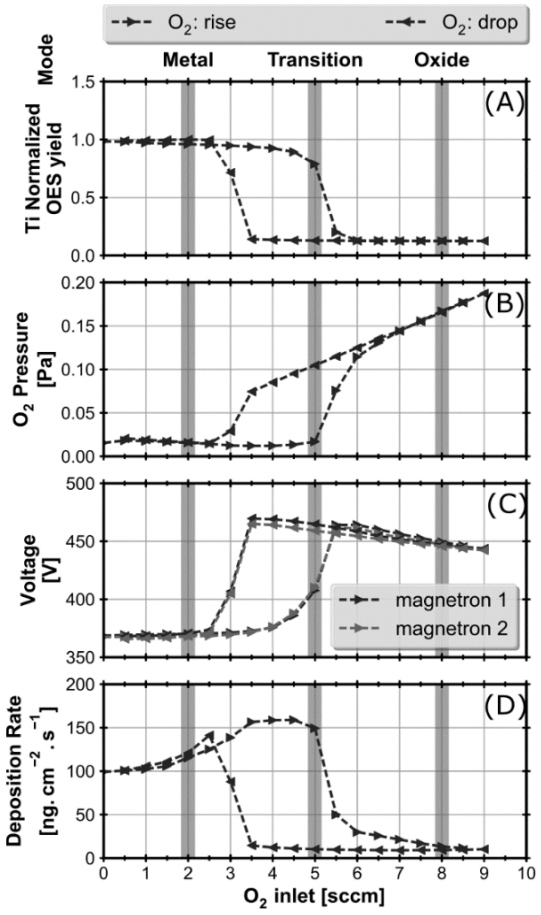

Figure 3 *Experimental hysteresis curves adapted from* [19] *(A) Normalized Optical Emission yield of Ti (B) Oxygen partial pressure [Pa] (C) Discharge voltage [V] (D) Deposition rate [ng/cm²/s] as measured by QCM. For each parameter, the increasing oxygen inlet case is represented with right-hand oriented triangle and the decreasing oxygen inlet case with left-hand oriented triangles. The discharge voltages (C) are shown for, both magnetron sources, separately. The three greyed regions indicate the conditions selected for the experimental deposition: metal mode (left), transition mode (middle) and oxide mode (right).*

3. Results

This section summarizes the results from the simulations as well as from the experiments. A detailed comparison and discussion follow in the next section. Simulations are performed using the iterative procedure shown in Figure 1 and described in section 2.1 with parameters as summarized in Table 2.

Simulation Parameters		Value		
Time step [PICMC]		2.0 x 10^{-11} $[s]$		
Total physical time [PICMC]		150 µs ➔ 7.5 x 10^6 iterations		
Time step [DSMC]		1.0 x 10^{-6} $[s]$		
Total physical time [DSMC]		3 s ➔ 3.0 x 10^6 iterations		
Cell size		1.5 x 1.5 x 1.5 mm³		
Initial gas temperature		300 $[K]$		
Wall temperature		300 $[K]$		
Surface binding energy for Ti		4.89 $[eV]$		
Surface binding energy for TiO_2		6 [eV]		
Ti and O cosine exponent		1.5		
Negative ion yield γ_{O^-}		0.1 %		
Initial charged density [m^{-3}]		Ar^+: 1.0 x 10^{13} Electron: 1.0 x 10^{13}		
Secondary Electron Emission Yield [SEEY]		Metal: 0.114 [41] Oxide: 0.080 [57]		
Ti and Ti^+ sticking coefficient		1		
Charged particles weighting factor		7.5 x 10^4		
		Metal	**Transition**	**Oxide**
Neutral particles weighting factor	**Ar**	4.5 x 10^{10}	4.5 x 10^{10}	4.5 x 10^{10}
	O_2	8.1 x 10^8	1.5 x 10^{10}	2.0 x 10^{10}
	O	1.0 x 10^7	1.0 x 10^7	6.0 x 10^8
	Ti	8.0 x 10^7	4.0 x 10^7	1.0 x 10^7

Table 2*: Simulation parameters of the PICMC Ar/O_2 magnetron discharges performed in this work*

First, 2D maps of the density distributions of neutral particles obtained at the end of step 4 by time-averaging over the last 50 µs are plotted in Figure 4.

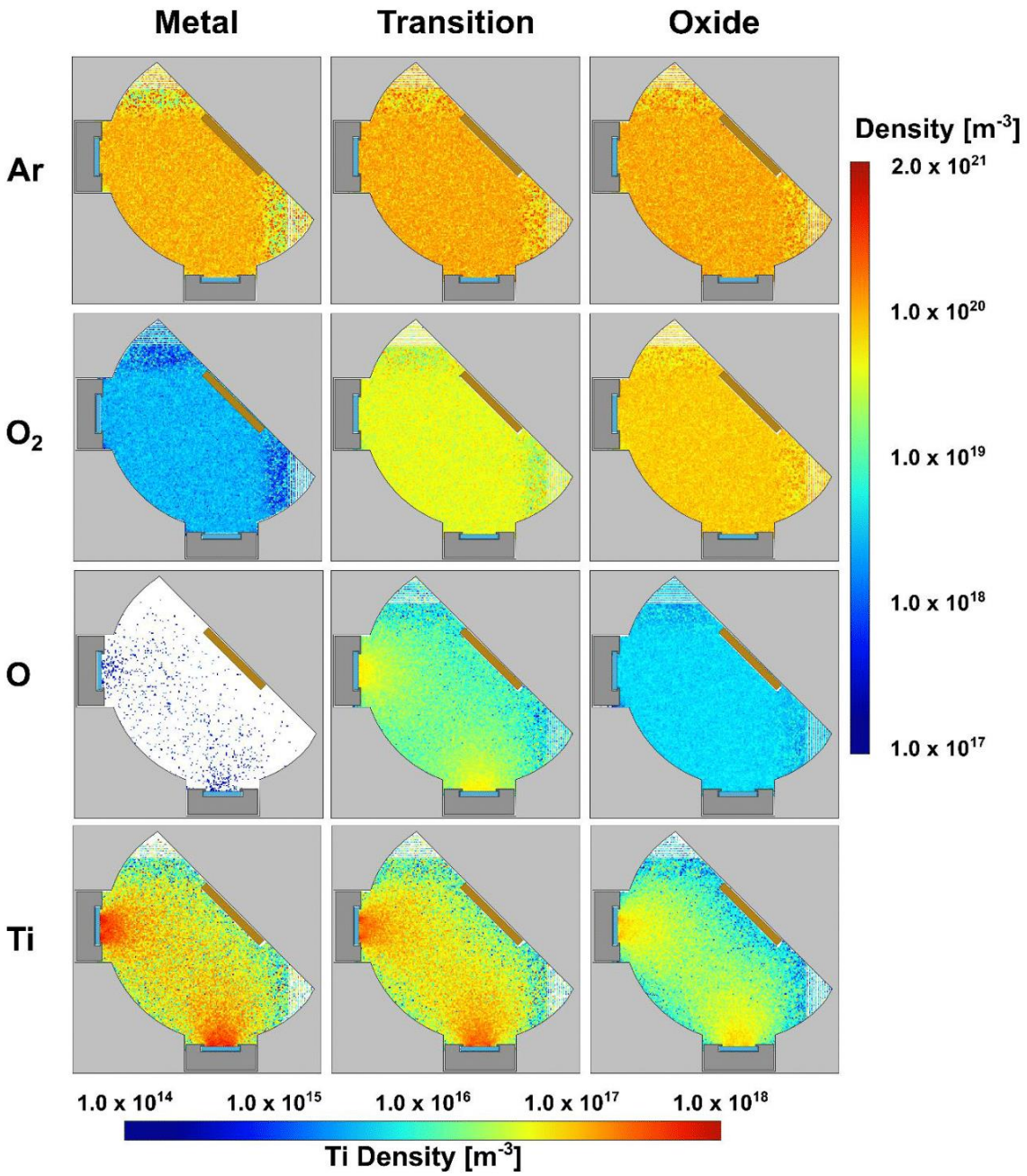

Figure 4 *2D maps densities of the neutral species for the reactive sputtering operation modes. The plots for Ar, O2 and O use the right-hand side colormap. The bottom colormap corresponds only to the titanium.*

In all three work modes, the same Ar partial pressure (0.5 Pa) is used which results in the same Ar density. The O_2 density increases from $2\,x\,10^{18}\,m^{-3}$ for the metal mode up to

$6\ x\ 10^{19}\ m^{-3}$for the oxide mode. The O density also drastically increases while switching from metallic mode to oxide mode but in a very different fashion than molecular oxygen. At first, the density is very low and spatially inhomogeneous for both metal and transition mode. In oxide mode, the distribution tends to be evenly distributed in the simulation volume. Finally, the titanium is plotted at the bottom of the figure. A different scale is used in order to correctly highlight the decreasing density evolution from metallic mode to oxide mode. In metal and transition mode, the spatial distribution of Ti is similar as for atomic oxygen. The same plot procedure is used to present the evolution of the charged particle density distributions on Figure 5 by time-averaging over the last 50 µs of the final PICMC simulation step

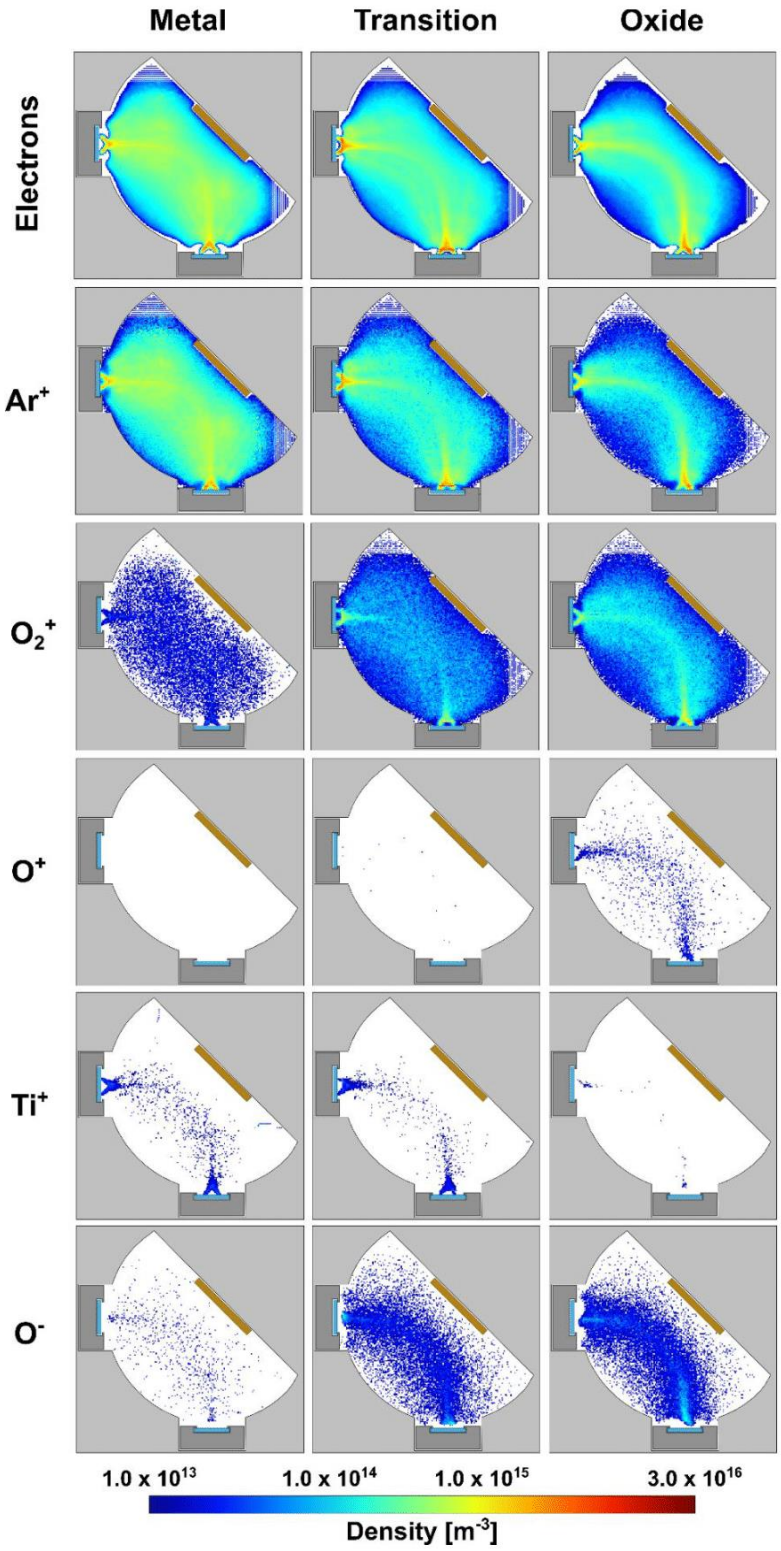

Figure 5 *2D maps densities of the charged species for the three cases. All maps use the same colormap to ease the comparison.*

While the electron density distribution exhibits a similar shape in all the three cases, with increasing oxygen inlet it is being more focussed to the magnetic field lines according to the closed field magnetic configuration. In accordance to the quasi-neutrality requirement, the same behaviour is observed for the Ar^+ density evolution. In all cases, the maximal density is located near the targets. The closed field magnetic configuration of the dual magnetron system can be observed on these maps. Indeed, the high-density tails originating from both targets bend to join together in front of the substrate holder which corresponds to the magnetic field topology. The absolute molecular ion O_2^+ density increases with the increasing oxygen inlet. It has a similar shape as Ar^+ but is very low in absolute value in both metal and transition mode. In oxide mode, the O^+ density increases but is still very low in comparison to Ar^+ or O_2^+. The Ti^+ density exhibits a behaviour similar to the neutral Ti but with very low densities. Finally, the O^- density is very low in metal mode and increases in transition and oxide mode. Even though the global intensity is small across the three cases, in oxide mode the high-density tail of this ion is more pronounced than for the other cases.

To have an overview of the discharge, it is useful to visualize the particle densities. However, if one wants to simulate film growth, it is also needed to compute the particle fluxes at the substrate location. To do so, the various fluxes are averaged in two different cylindrical regions of 15 mm radius and 10 mm length around the central and the off-median plane locations of the substrate. The obtained fluxes are plotted in Figure 6 for non-tilted samples; except for O^- ions tilted samples would exhibit lower flux intensities but the same ratios.

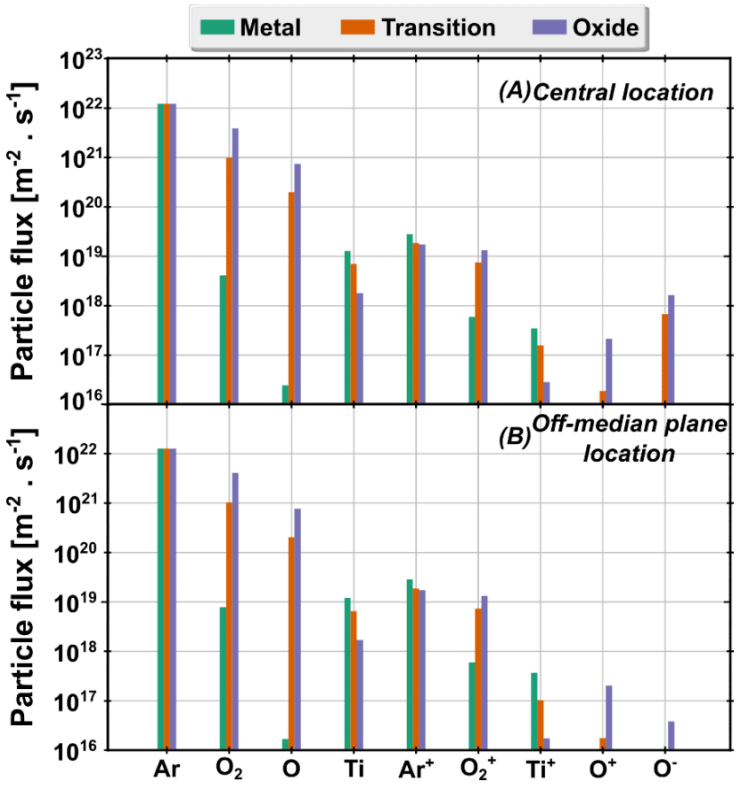

Figure 6 *Fluxes of particles towards the substrate holder. Both central and off-median plane locations, as defined on Figure 2.B, are separately plotted.*

First, the general trends of relative fluxes from one location to another are very similar. The Ar flux is independent from operation mode and substrate position. Its values are close to 1.2×10^{22}/m²s, which results from a partial pressure of 0.5 Pa and a temperature of 300 K. For O_2, the flux increases from 4.1×10^{18} to $3.6 \times 10^{21}\ m^{-2}s^{-1}$ when switching from metal to oxide mode, which corresponds to the trend of O_2 density. The same applies for atomic oxygen although its variation from metal to transition mode is much higher than for O_2. Both the titanium and Ti^+ fluxes are decreasing by one order of magnitude when switching to oxide mode. Because it is the background gas, Ar^+ has always the highest intensity amongst the ions. From metal to oxide mode, its flux is reduced from 2.6×10^{19} to $1.7 \times 10^{19}\ m^{-2}s^{-1}$, since with increasing O_2 inlet, an increasing fraction of the generated ions consists of O_2^+. The same

observation applies for both O^+ and O^- ions, with the exception that for the metallic case fluxes are well below $1.0\ x\ 10^{16}\ m^{-2}s^{-1}$ and can be considered negligible. Finally, it is possible to compare fluxes of particles hitting the central location and the off-median planes location. Ar and O_2 fluxes are similar for both locations as the respective partial pressures are identical for both positions. Atomic oxygen fluxes for transition and oxide modes are very similar but in metal mode, the O flux at off-median plane is only 50% compared to the central location. The titanium flux is reduced by 10% at off-median plane location compared to central location. A short reduction (~5%) of the fluxes is also observed for all the ions except for the negative oxygen ion. For this last one, the flux drops by two orders of magnitude when moving away from the centre toward the off-median plane location.

To be able to use the data gathered from simulations of step 1 to step 4 (Figure 1) and proceed with step 5, i.e. the kMC method to simulate the film growth, it is necessary to feed the latter with the detailed growth conditions resulting from the process. For this purpose, the energy and the angular distributions of the particles are sampled within virtual planes sized 20×20 mm² located at the four different substrate positions indicated in Figure 2 B. Figure 7 shows the typical angular distributions of the particles at the various substrate locations. This figure is to be linked with the Table 3 in order to attribute an angular distribution to a specific particle at a given substrate location for the three discharge modes.

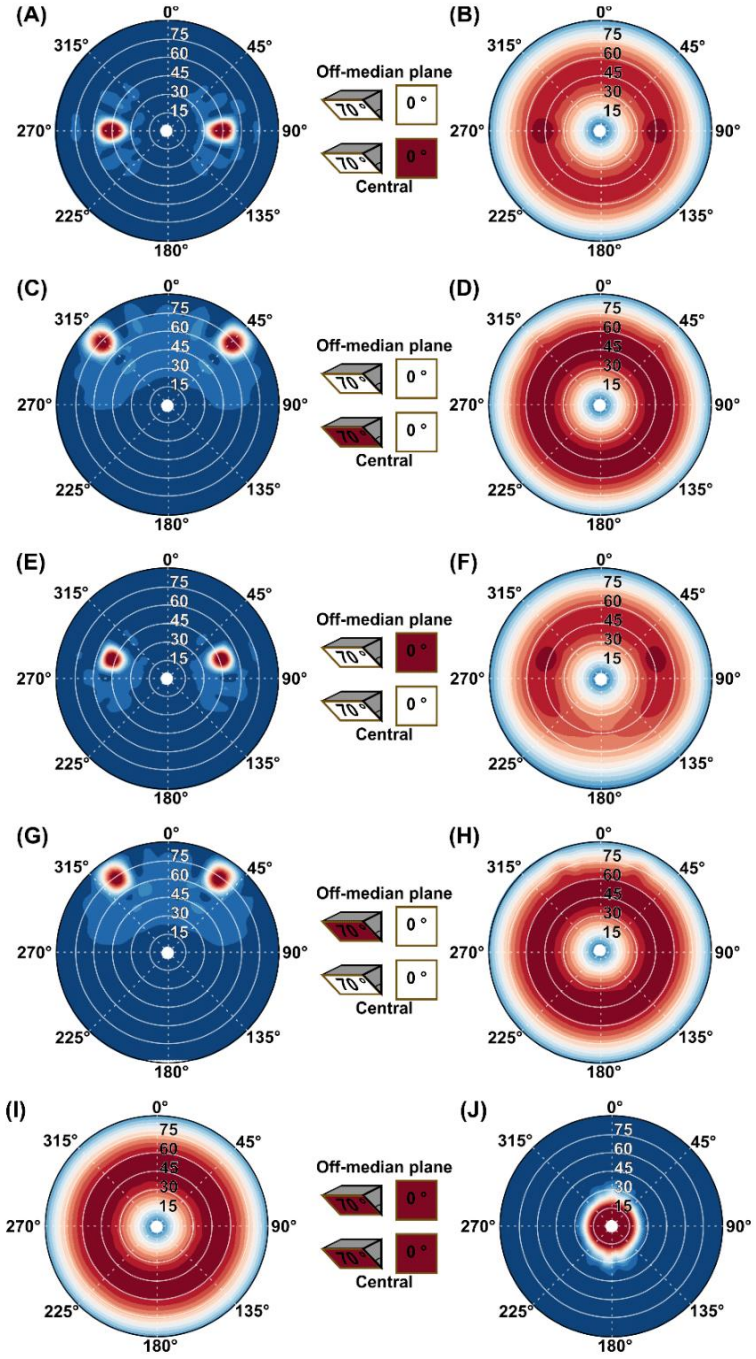

Figure 7 *Typical angular distributions of the various species at substrate locations. See Table 3 for the attribution of an angular distribution to each species. A small sketch the substrate holder is drawn at the bottom left corner of each distributions to indicate to which substrate location the distribution may apply to.*

		Central	Central 70	Off-MP	Off-MP 70
Metal	**Ar, O_2**	I	I	I	I
	Ti, O, O^-	A	C	E	G
	Ar^+, O_2^+	J	J	J	J
	O^+, Ti^+				
Transition	**Ar, O_2**	I	I	I	I
	Ti, O^-	A	C	E	G
	O	B	D	F	H
	Ar^+, O_2^+	J	J	J	J
	O^+, Ti^+				
Oxide	**Ar, O_2, O**	I	I	I	I
	Ti, O^-	A	C	E	G
	Ar^+, O_2^+	J	J	J	J
	O^+, Ti^+				

Table 3 *Angular distributions of each species and locations for metal, transition and oxide mode. The letters correspond to an angular distribution of Figure 7*

Ar and O_2 background species exhibit no preferential direction when bombarding the substrates. Therefore, those distributions correspond to Figure 7.I. Figure 7.A is the typical angular distribution at central location of a sputtered species. Two hot spots are observed at 45° each, corresponding to the target's directions. Figure 7.C, Figure 7.E and Figure 7.G are also attributed to the sputtered species but respectively for the central 70, off MP and off MP 70 locations. The Figure 7.B, Figure 7.D, Figure 7.F and Figure 7.H are attributed to the atomic oxygen of the transition mode only. Indeed, those distributions can be seen as a combination of the corresponding sputtered angular distribution (A, C, E or G) with the angular distribution of

a background neutral species (I). While in oxide mode, the partial pressure of atomic oxygen is high enough to fit with Figure 7.I, in the transition it is not yet the case. It can also be observed that for D and H, the background contribution is more pronounced than for B and F. All of the O^- angular distributions are attributed to the "sputtered species distributions" A, C, E and G. All other ions are related to the distribution J, corresponding, to a perpendicular direction. It is the case for all the locations as the substrate holder is always grounded. To complete the analysis of the particle's properties flowing towards the substrate holder, Figure 8 plots the typical energy distributions of the various species.

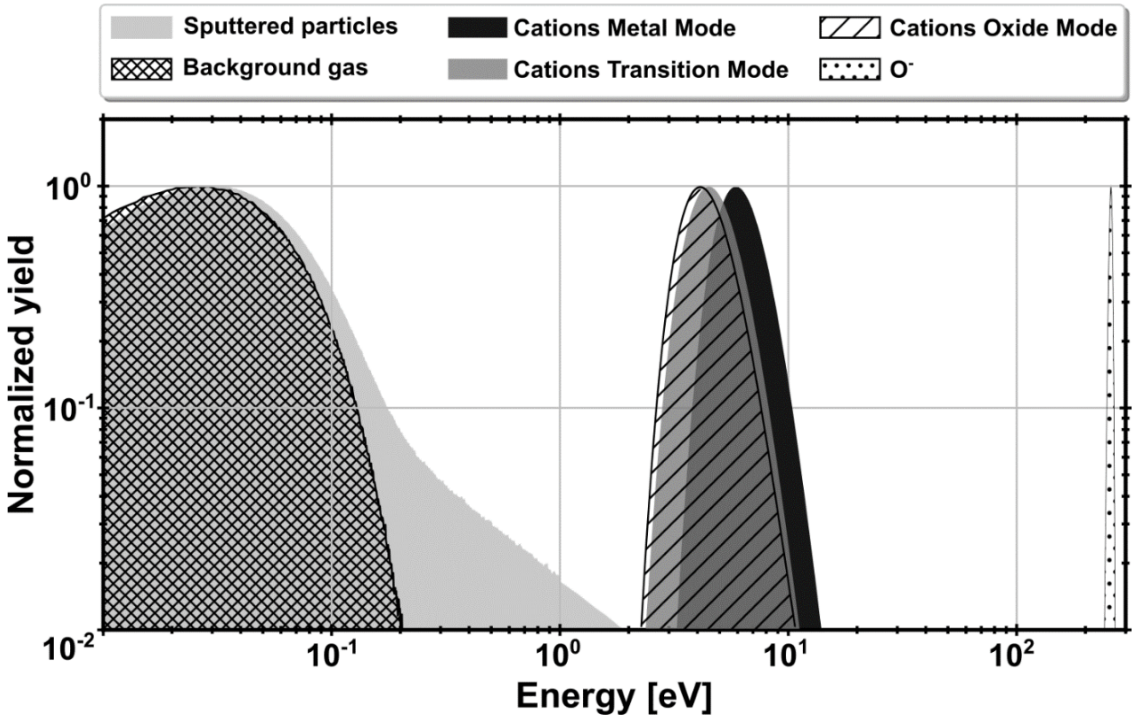

Figure 8 *Typical energy distribution functions of the involved species.*

Background gas energy distributions exhibit a Maxwellian distribution at room temperature. The distribution related to sputtered particles is a well-known Thomson -like distribution. The cations have a peak-like distribution whose energy depends on the operation mode. The position of the maximum is shifted towards lower energies when sweeping from metal mode to oxide

mode. The energy distribution of negative oxygen is centred at the discharge voltage and is very narrow.

Finally, those data are used to perform film growth simulations by using NASCAM as the final simulation step. The model used for this study allows the use of 5 different species: metal mode includes Ti, Ti^+, O_2 and Ar^+ and both transition and oxide modes include Ti, Ti^+, O_2, O, Ar^+ and O^-. For those last simulations the species O_2 and O are merged together in order to account for both. The simulation parameters are listed in Table 4:

Parameter	Value
Substrate size (nm)	300 x 3
Number of deposited atoms	3 x 10^6
Ti sticking coefficient	1
O sticking coefficient	From 0 to 1, depending on local film's surface composition.
Displacement energy (eV)	3
Oxygen diffusion range, L_D (nm)	20

Table 4: NASCAM simulation parameters used for this study

Simulation were performed at room temperature, without thermal diffusion. The simulated morphology of the coatings is compared to SEM cross section views in Figure 10 and the columnar orientation of both are compared in Table 6.

Table 5 shows data collected during the experimental deposition. The films composition has been analysed by Rutherford Backscattering Spectroscopy (RBS) as reported in [19].

Parameters		*Metal*	*Transition*	*Oxide*
Discharge current [A]		0.500	0.500	0.500
Discharge Voltage [V]		365	462	448
O_2 inlet [sccm]		2	[3-5]	8
Deposition Rate [Å/s]		2.1	3.3	0.24
OES Ti normalized intensity		0.88	0.50	0.10
Initial vacuum [Pa]			$\leq 1.3 \times 10^{-3}$	
Films composition	**Ti [%]**	64.1	36.6	33.3
	O [%]	35.9	63.4	66.6

Table 5: *experimental conditions of the depositions. The deposition rates in this table are calculated thanks to deposition time and final thickness. Data in brackets reflect the flow variation to keep the OES Ti yield constant.*

Figure 9 presents the comparison between SEM top views and 1x1 µm AFM maps. The same scale is use for both SEM and AFM pictures. For all cases, AFM maps are very much alike SEM top views. The coating roughness as calculated with AFM maps are presented in Table 6. Coatings from the transition mode exhibit the lowest roughness. Indeed, their respective roughness is always lower than 4.2 ± 1.5 nm while oxide mode coating roughness are in the range [6.3 - 11] and [8.4 – 14.4] for metal mode. When selecting a mode, the tilted samples always have a higher roughness than the non-tilted ones.

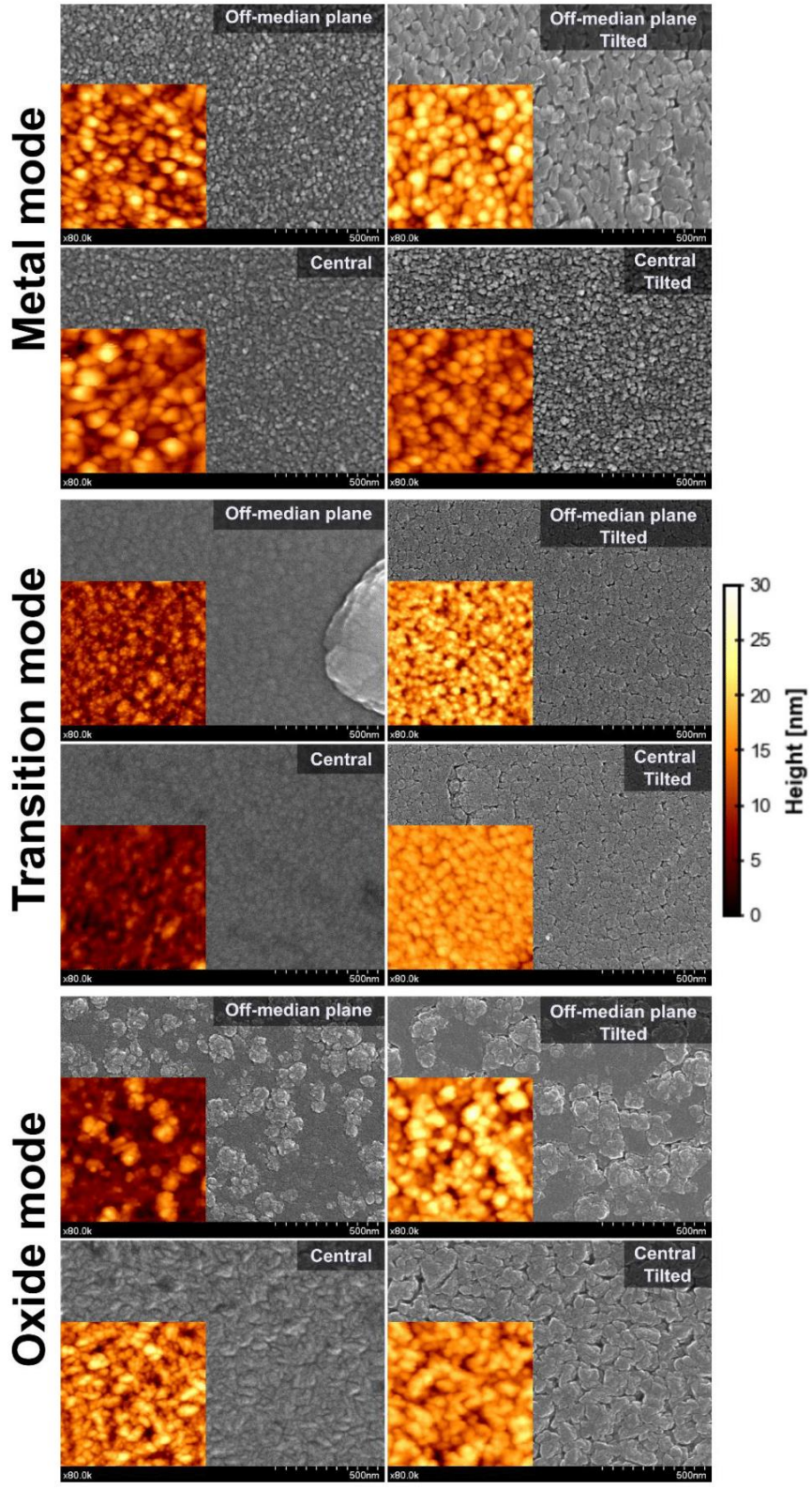

Figure 9 *SEM top view pictures along with 1x1 µm AFM maps of deposited coatings*

Figure 10 compare the SEM cross section views along with the simulated coating obtained by NASCAM. As reported in [19], the 70° tilted samples all exhibit columnar structure growth with various columnar orientation. Those are measured and compared in Table 6. One can observe a good agreement.

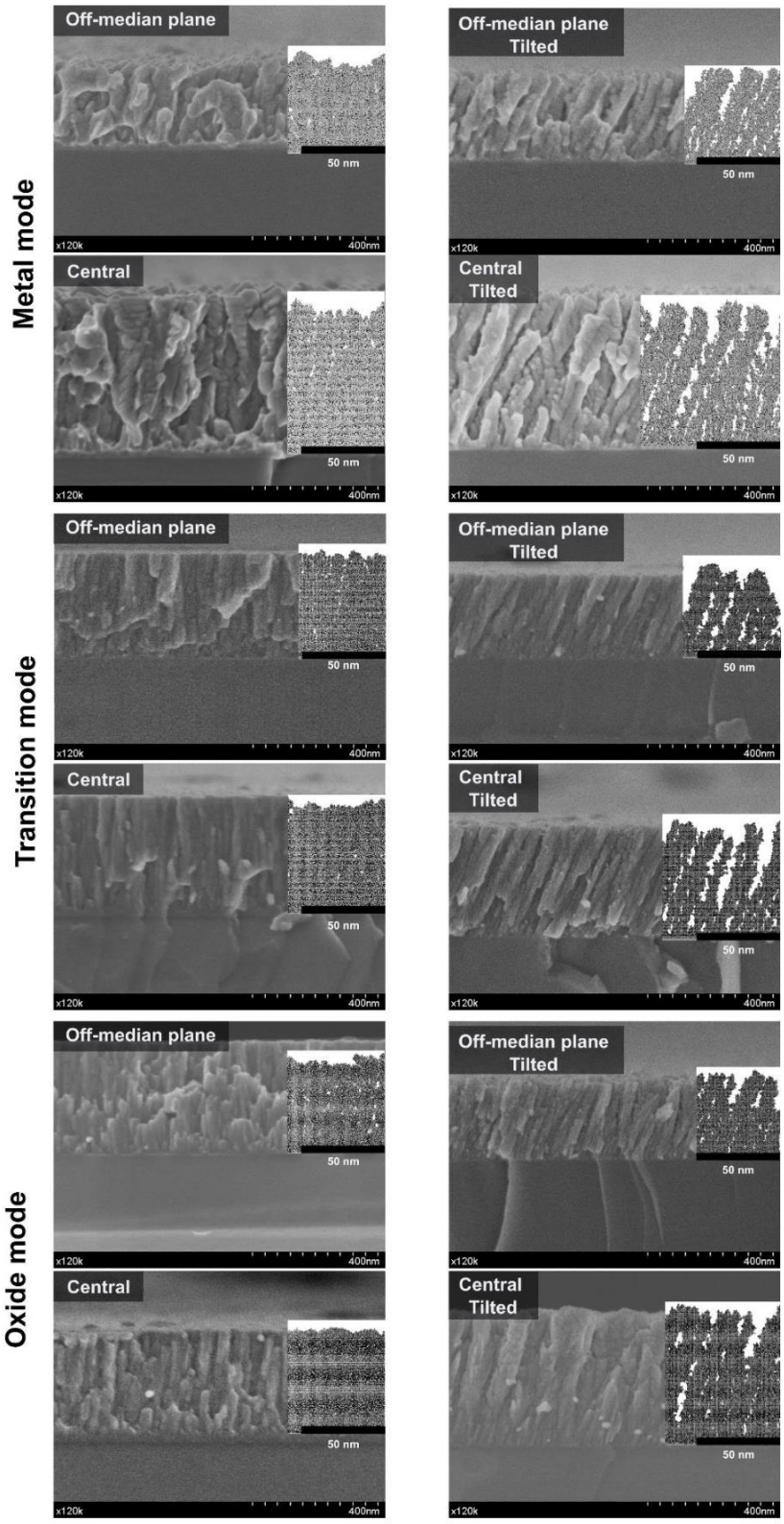

Figure 10 *SEM cross sections views along with NASCAM simulations of the film growth*

For each tilted sample locations, NASCAM simulations were ran using two different configurations. The first one neglect all ion fluxes during the film growth. The second one corresponds to previously described simulations including ions. The obtained values are compared to the column titling angles (β) as measured with SEM pictures on Figure 11.

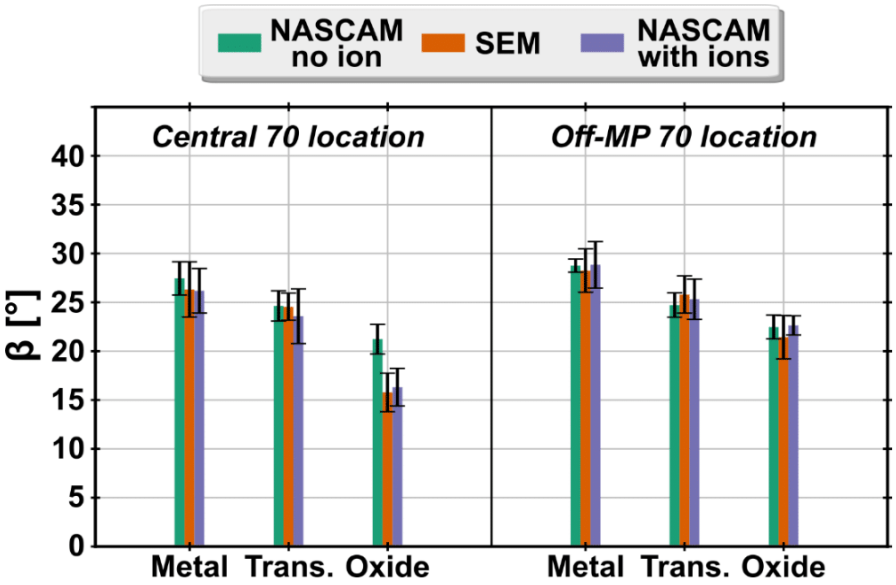

Figure 11 *Comparison of column tilting angles (β) of 70° inclined samples. Values from SEM cross-section pictures (*Figure 10*) and simulated values using NASCAM that either include or neglect ions. Left side sand for central location samples; right side is dedicated to off-MP samples.*

Both metal cases exhibit the highest β values. At off-median plane 70 location a steadily decreases of β with the increasing oxygen inlet is observed. At this location there is no difference between simulation including ions or neglecting ions. Those are anyway in agreement with SEM measurements. At central 70 location, metal and transition cases have similar evolution to the ones of off-MP 70 location. A good agreement is observed amongst all measured values. A pronounced drop of β is observed for the SEM oxide mode. This drop is also noticeable with the simulated β values including ions, while simulated values neglecting ions exhibit a similar behaviour than off-MP 70 location.

Finally, samples were analysed by XRD. The results are showed on Figure 12:

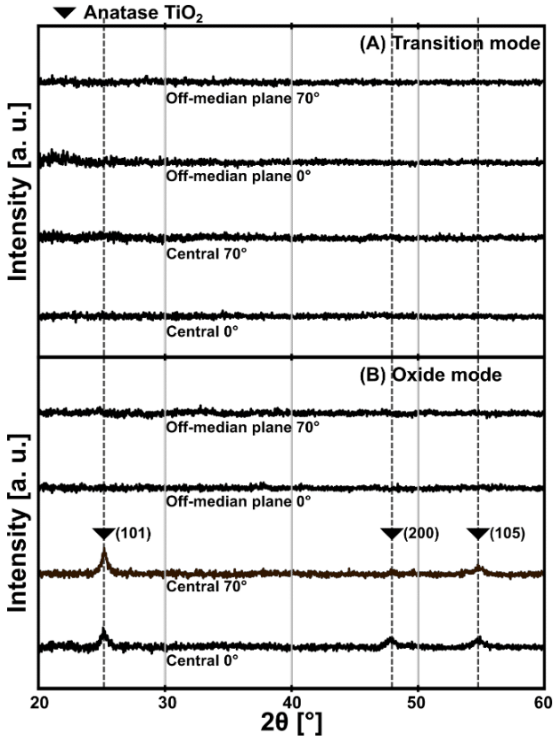

Figure 12 *XRD patterns of TiO2 coatings: samples related to the transition mode are plotted on (A) while oxide mode samples are on (B).*

No diffraction peaks are observed for coatings produced in transition mode (Figure 12.A), the 4 sample locations are amorphous. Oxide mode samples (Figure 12.B), exhibit two different diffractograms: off-median plane locations are amorphous while central location samples have both peaks corresponding to anatase phase with three distinctive peaks located at 25.3°, 48.1° and 53.9° corresponding to anatase (101) (200) and (105) crystal planes (JCPDF 21–1272).. A (101) preferential orientation is observed, complying with the results of [58,59].

All experimental measurements are summarized in Table 6. In addition, the total energy influx at the central and off-median plane sample positions have been measured by an active thermal

probe (ATP)[60]. The power delivered to a 7x7 mm probe set at 200 °C was measured. This power originates from thermal radiation, surface chemical reactions and/or from particle flux toward the probe. It was not possible to differentiate the various components of the energy influx.

		Metallic	Transition	Oxide
Thickness [nm]	Central	518	381	355
	Central 70	484	362	428
	Off-MP	271	347	360
	Off-MP 70	267	270	252
RMS Roughness [nm]	Central	13.9 ± 2.9	1.6 ± 0.2	7.5 ± 0.8
	Central 70	14.4 ± 0.8	4.2 ± 1.5	11.0 ± 0.5
	Off-MP	8.0 ± 1.6	2.3 ± 1.1	6.3 ± 1.5
	Off-MP 70	10.1 ± 3.3	2.7 ± 1.2	8.8 ± 1.3
Experimental Column Angles [°]	Central 70	28.3 ± 0.6	23.2 ± 1.2	13.4 ± 2.3
	Off-MP 70	25.1 ± 1.2	24.7 ± 1.6	21.5 ± 2.3
Simulated Column Angles [°]	Central 70	25.3 ± 1.8	23.0 ± 1.1	8.8 ± 2.2
	Off-MP 70	27.9 ± 1.2	24.1 ± 1.6	23.9 ± 2.9
Active Thermal probe [mW/cm²]	Central	26.9 ± 1.6	27.1 ± 1.4	26.7 ± 1.3
	Off-MP	18.2 ± 1.3	17.6 ± 1.1	17.1 ± 1.5
Normalized Energy Flux [eV/at.]	Central	324	242	2231
	Off-MP	223	163	1744

Table 6 *List of measurement values performed on samples. The results of the active thermal probe analysis are added to ease the comparison.*

4. Discussion

The discussion of the results is presented as a comparison with the discussion of [19] where the growth of TiO_2 in the same experimental conditions was studied by considering only neutral particles. First of all, as previously explained in section 2.1, the numerical model handling neutral particles is improved by the addition of atomic oxygen species. Therefore, Figure 4 and Figure 5 present the final density distributions of all both neutral and charged species in the gas phase. As also observed in [19] and in Figure 3.D, the Ti density is reduced by one order of magnitude with the increase of oxygen flow. The second frequently sputtered particle is atomic oxygen. Its density distribution evolves in an opposite way than Ti. With increasing oxygen flow, a larger fraction of the target material is oxidized and therefore, a larger part of the sputtering flux originates from TiO_2 sites, which are assumed to be decomposed during sputtering. When the molecular oxygen flow is increased, target surfaces are poisoned and turned to TiO_2 thereby preventing the sticking of both atomic and molecular oxygen. The consequence is a less efficient gettering of oxygen atoms by the walls and an increase of their residual time and overall density. This is the reason why in oxide mode, the density of atomic oxygen appears to be homogenous in opposition to transition and metal modes. A direct consequence is a change on the angular and energy distributions of O. While in metal and transition mode, the energy distribution of O at substrate location is a Thompson-like distribution (Figure 8), it becomes pure Maxwellian in oxide mode. The same is true for the angular distributions. In metal mode, the angular distribution of O has features of a sputtered species such as Ti. However, in oxide mode, the longer O residual time leads to thermalization resulting in a more isotropic angular distribution similar as for Ar and O_2. For Ti, the density reduction is a consequence of the drop of the sputtering yield due to target poisoning and an increased contribution of the O_2^+ ions in the sputtering current, which is less efficient than

sputtering by Ar^+ ions. The density never gets homogeneous because Ti is always deposited on walls with 100% sticking coefficient irrespective of their oxidation state.

The density distributions of charged species are very different from the neutral ones. In plasma sputtering processes, the most important species for the discharge is by far the electron. Due to their low scattering rate with other species, they usually have a much higher temperature than all other species in the discharge. Consequently, the grounded chamber walls absorb them more quickly than ions. This results in a positive space charge in the plasma bulk, which causes acceleration of positive ions towards the walls and negative ions to reside in the positive plasma bulk. When a magnetic field is present, the field is confining electrons as it is shown in Figure 5. The electrons ionize neutral species Ar, O, O_2 and Ti via electron impact collisions thereby creating additional electrons and ions along their path. Ar^+ is the main ion produced in the discharge, followed by O_2^+. The threshold energy of the O_2 ionization is lower than for Ar, but this is overcompensated by the higher partial pressure of Ar compared to O_2. Therefore, charged particles distribution in the plasma is mainly driven by the concentration of neutral gas species and their specific cross sections. When the partial pressure of O_2 is increased, the absolute density of Ar^+ decreases as more and more energy of the electrons is transferred to the oxygen. Indeed, the electron impact excitation of the molecular oxygen plays an important role in the discharge: it is much more likely to excite O_2 at low energy excitation states than to perform ionization. Therefore, O_2 tends to decrease the available electron energy, which reduces the production of Ar^+ ions. The stated argument: “charged particles composition driven by neutral particles composition”, also explains why the densities of the three other ions (O^+, Ti^+ and O^-) is much smaller than the ones of O_2^+ or Ar^+.

Negative O^- ions are created by two mechanisms: the first one is dissociative attachment of electrons on O_2 gas molecules (reaction 44) and the second one is the generation at the target surface due to sputtering. When the partial pressure of O_2 is increased, O^- ions are created in

the plasma bulk. Because the electrons are confined by the magnetic field near the targets, the O^- ions are created in the same area. In contrast to electrons, O^- are heavy particles, hence they are not efficiently trapped by the magnetic field but pushed away from the targets due to the pre-sheath related electric field in that area. It is the reason of the large gap observed between the targets and the higher density region of the negative oxygen ion, see Figure 5. This also explains the flare like shape of the density distribution at the symmetry axis of the magnetrons. The ions created at the targets are accelerated straight away by the sheath leaving a very low-density region. These observations are supported by another study implementing a 2D PICMC algorithm for the Ar/O_2 magnetron discharge of TiO_2 [2,3].

The analysis of the particle fluxes towards the various sample locations (Figure 6) unsurprisingly reveals the same flux of Ar for all operational modes and sample locations. The same argument applies for atomic oxygen in transition or oxide modes. As previously explained the reason is that these species constitute the background gas. The novelty of this study is the addition of the charged particles in the simulation treatment at the substrate locations. Their relevance is due their high kinetic energy caused by the sheath in between the grounded substrate and the plasma bulk at a positive potential of around 5-10 V. This sheath acceleration is always perpendicular to the substrate surface, which explains the shape of the corresponding angular distribution (Figure 7.J). The simulated energy distributions for the positive ions presented in Figure 8 can be related to the work of Mišina *et al.* [61]. They use energy resolved mass spectrometry to measure ion energy distributions at substrate location for a WTi target at 0.5 Pa. They have found similar shape for the distributions except for the high-energy tail extended to higher energies. They have attributed it to reflected Ar on the target during the sputtering. The yield of this high-energy tail is found to be four orders of magnitude lower than the maximal peak intensity. This process is not included in the PICMC model and no high-

energy tail is observed. In the present case, there is no heavy element such as W in the target, which should also contribute to reduce the backscattering of Ar^+.

The O^- ions behave exceptionally in comparison to all other ions in the simulation. Indeed, those, which are created in the plasma bulk by reaction (44) have a very low kinetic energy that does not allow them to overcome the substrate-plasma sheath. Therefore, only high-energy ions created at the target surface are capable to reach the substrate. Their energy is so high that the substrate sheath does not modify significantly neither their energy nor their angular distributions. In [52] Moens *et al.* demonstrated the importance of the space-charge for the O^- ion transport through the gas phase. The PICMC approach allows to inherently account for it. It is very important for this study as one goal is to compare the growth of TiO_2 with samples located in the O^- flux and other samples located off-median plane (off-MP) in order to strongly reduce this flux. The flux comparison of Figure 6, highlights that at the off-MP location, the flux of O^- ions is not completely deleted but is at least reduced by 97,8 %. This result agrees with the experimental investigation of the deposited coating by XRD (Figure 12). The only coatings not totally amorphous are the ones bombarded by O^- ions in the median place in oxide mode. Those at off-MP locations are amorphous as well as all of the samples deposited in the transition mode. According to Figure 6, the flux of O^- in transition mode is only 2.5 times lower than the corresponding one in oxide mode. However, the deposition rate is 13.8 times higher in the transition; resulting in a strongly reduced energy flux by O^- ions per deposited atom. The experimentally calculated values of normalized energy flux (NEF), see Table 6, confirm this statement. The values for the NEF in oxide mode are one order of magnitude higher than those for the metal mode or transition mode. The energy fluxes to the substrate as measured by the probe do not show significant variations from one discharge mode to another. It is not possible to sort out the components of the energy flux as it accounts for all energy components: radiations, surface chemical reactions, electric contribution (charged particles) and sputtered

particles fluxes. In [60] using the same kind of probes, Gauter *et al.* have highlighted that for the Ti sputter deposition the dominant component is the radiation. This observation could explain why no evident modification of the energy flux is measured while the deposition rate, and therefore the sputtered particles component of the energy flux, decreases significantly.

The evolution of the coating's roughness based on AFM measurements (Figure 9) and reported in Table 6 indicates smoother coatings in transition mode. The final roughness of coatings can be explained on the basis of two main competing phenomena occurring at atomic scale, the shadowing effect and the surface diffusion. The shadowing leads to preferred growth in the vertical direction while surface diffusion tends to smooth growing surfaces or promote crystallographic growth. The competition between these two factors drives the morphology of the coatings [62,63]. Therefore, both the angular distributions of the deposited particles and their mobility on the surface play an important role during the film growth. The shadowing effect is easily identified as responsible for the higher roughness of the coatings on 70° tilted substrate positions. When increasing the oxygen inlet, the coatings becomes smoother at first (transition mode) and then the roughness increases (oxide mode). In transition mode, the mobility of the metallic atoms is not sufficient to ensure crystalline growth of TiO_2. The low mobility of the Ti is attributed to the increasing partial pressure of O_2 i.e. oxygen atoms and molecules act as a barrier to the diffusing Ti inducing amorphization of the films. When the partial pressure of O_2 is high enough, the discharge switches to oxide mode, the targets oxidize and the sputtering yield of Ti severely drops. However, the computed charged particle fluxes (Figure 6) and the measured energy fluxes (Table 6) do not significantly change i.e. the available energy per deposited atom increases even without considering O^- ions bombardment. In other words, the effective surface temperature of the growing film is increased. It was already reported that the surface temperature plays an important role during the film growth by magnetron sputtering [64] and has an impact on the surface roughness.

Finally, the columnar orientations (β) measured by SEM and obtained by NASCAM simulations are compared, see Figure 11. In order to highlight the effect of the charged particles on the columnar orientation, NASCAM simulations are performed with and without accounting for charged particles. A general good agreement is observed between the experiment and simulation values. The decrease of the β values with the increasing oxygen inlet is explained by the non-directionality of the oxygen flow in comparison to sputtered Ti [19]. The best match is obtained for the transition mode. As previously discussed, in transition mode, the relative high deposition rate combined with an increased oxygen flux disabled the surface diffusion of deposited metallic atoms. It explains the good morphology prediction obtained by the simulations for this operation mode as atom diffusion is not activated in the NASCAM simulations. Oxide mode related simulations exhibit much higher β values for the central location than the ones measured on SEM pictures when using the "no-ion" mode of NASCAM. The reason can be attributed to the higher NEF values which can be related to an increase of the infrared contribution or an increase of high energy particles condensing on the growing film. As it was discussed above, the energy of O^- ions is rather high, and these ions cause a strong local rearrangement of surface atoms by means of atomic displacement cascades thus changing the morphology of the sample. Although a good agreement between β values is also observed when switching off charged particles contribution, simulation values over-estimate the columnar orientation. According to the previous study [19], the over-estimation may be explained by high energy charged particles which can affect film growth as highlighted in the study of Van Steenberge *et al.* [65]. As energetic particles arrive to the film mostly from one side, they tend to force the deposited atoms to move in the same direction than the impact due to momentum transfer. By using NASCAM with the BCA mode, i.e. with ions included, the modelling of adatom displacement due to ion bombardment seems to be well described,

showing a good agreement between column tilting angle from experimental SEM pictures and simulation results (Figure 11).

Linking this comparative study of β values with total energy flux values of Table 6 indicates that below 2000 eV/atom, neglecting charged particles still lead to good prediction of coating morphology. The central location 70 in oxide mode highlights the paramount role of high-energetic particles on the film growth and therefore those should always be accounted for to predict film properties. However, when the total energy flux jumps from 200-400 eV/atom to 1700-2000 eV/atom, it hardly affects the film morphology. It is to be expected to have a threshold above which it should have a significant impact on the coating properties. Indeed, TiO_2 coatings are well known to exhibit anatase and rutile phase when the temperature is increased. One way to increase the temperature of the growing film is to increase the energy brought by incident particles i.e. increase the total energy flux. According to the present study, the total energy flux threshold for the transition from amorphous to anatase TiO_2 is located in the range 2000-2500 eV/atom. The current data does not allow to speculate furthermore about the threshold for the phase transition from anatase to rutile TiO_2. However, Cormier *et al.* [66] have highlighted the transition from anatase to rutile phase for NEF values higher than 10 keV/at. Several other studies have obtained NEF values in line with the current study and with another measurement methods (mostly thermopile-based probe) [66,67].

5. Conclusions

A previously established 3D multi-scale simulation model of a reactive magnetron sputtering process is improved by the addition of plasma modelling via the PICMC method in order to take into account and clarify the role of charged particles. Moreover, an algorithm implementing the binary collision approximation (BCA) extends the previously used kinetic Monte Carlo code for atomistic film growth simulation, in order to properly handle the momentum of the impact of energetic charged particles. This extended multi-scale model is successfully applied to study the growth of TiO_2 thin films by reactive magnetron sputtering. The coater geometry involves a dual magnetron system in a closed field magnetic configuration with water-cooled substrates. In order to highlight the effects of negative oxygen ions, two substrate locations were selected: one in the median plane of the targets and another one in the off-median plane. The model predicts the densities and fluxes of both charged and neutral particles towards the substrate and uses them to explain the morphology of the deposited coatings.

Amorphous growth of TiO_2 films in the transition mode is explained by the suppression of the diffusion process by the oxygen acting as trapping site for Ti. The presented simulations were able to explain the experimentally observed difference in crystallographic structure between the coatings grown in front of the targets and at off-median plane location. It was shown that negative oxygen ions flux is very directional and it is dramatically reduced when moving from the median plane of the targets to off-median plane, therefore explaining the difference in crystallography of the samples. Indeed, it was also experimentally shown that the normalized energy flux (NEF), i.e. the total energy per deposited atom, drastically increased when the discharge switches from metal to oxide mode. An increase of the NEF values from off-MP location to central location is also reported, which support the paramount impact of the negative oxygen ions during film growth.

Finally, the simulations accurately predicted the column tilting angles of 70° tilted samples and highlighted the important role of charged particles on the final morphology of TiO_2 coatings even for DC-reactive magnetron sputtering processes. The developed 3D multi-scale model for reactive magnetron sputtering allows thus an accurate prediction of the coating morphology and properties, and its fine tuning for a specific application, avoiding the time and energy consuming "trials and tests" procedure.

6. Acknowledgments

This work was carried out in the framework of the industrial collective research project VICIA (Virtual Coater for Industrial Application) under contract number IGF/CORNET no. 199 EN. It was supported by the German Federal Ministry for Economic Affairs and Energy (BMWi) through the AiF (German Federation of Industrial Research Associations eV) and by the Belgian Direction Générale Opérationelle de l'Economie, de l'Emploi et de la Recherche (DGO6).

For all simulations, computational resources have been provided by the Consortium des Équipements de Calcul Intensif (CÉCI), funded by the Fonds de la Recherche Scientifique de Belgique (F.R.S.-FNRS) under Grant No. 2.5020.11. More specifically the Tier-1 super-computer of CENAERO was mainly used (http://tier1.cenaero.be/fr/zenobe). The authors would also like to thank the simulation team of the Fraunhofer institute of Braunschweig for their development work and advice. The PC² and SIAM platforms of UNamur are acknowledged for XRD and RBS measurements respectively. SK is Senior Research Associate of the Fund for Scientific Research (FRS - FNRS, Belgium). SK and SL would like to thank the Walloon Region of Belgium and the European Regional Development Fund for financial support through the Diag&Growth project.

7. *References*

[1] Pflug, A.; Siemers, M.; Melzig, T.; Keunecke, M.; Schäfer, L. & Bräuer G 2016 *Handbook of Software Solutions for ICME*

[2] Bultinck E and Bogaerts A 2011 Characterization of an Ar/O $_2$ magnetron plasma by a multi-species Monte Carlo model *Plasma Sources Sci. Technol.* **20** 045013

[3] Bultinck E and Bogaerts A 2009 Particle-in-cell/monte carlo collisions treatment of an Ar/O2 magnetron discharge used for the reactive sputter deposition of TiOx films *New J. Phys.* **11**

[4] Depla D, Heirwegh S, Mahieu S and Gryse R De 2007 Towards a more complete model for reactive magnetron sputtering *J. Phys. D. Appl. Phys.* **40** 1957–65

[5] Glöß D, Frach P, Zywitzki O, Modes T, Klinkenberg S and Gottfried C 2005 Photocatalytic titanium dioxide thin films prepared by reactive pulse magnetron sputtering at low temperature *Surf. Coatings Technol.* **200** 967–71

[6] Nadel S J and Greene P 2001 Strategies for high rate reactive sputtering *Thin Solid Films* **392** 174–83

[7] Mohamed S H, Kappertz O, Leervad Pedersen T P, Drese R and Wuttig M 2003 Properties of TiOx coatings prepared by dc magnetron sputtering *Phys. status solidi* **198** 224–37

[8] Hitosugi T, Ueda A, Nakao S, Yamada N, Furubayashi Y, Hirose Y, Shimada T and Hasegawa T 2007 Fabrication of highly conductive Ti1-x Nbx O2 polycrystalline films on glass substrates via crystallization of amorphous phase grown by pulsed laser deposition *Appl. Phys. Lett.* **90** 20–3

[9] Alami J, Sarakinos K, Uslu F, Klever C, Dukwen J and Wuttig M 2009 On the phase formation of titanium oxide films grown by reactive high power pulsed magnetron sputtering *J. Phys. D. Appl. Phys.* **42**

[10] Löbl P, Huppertz M and Mergel D 1994 Nucleation and growth in TiO< sub> 2</sub> films prepared by sputtering and evaporation *Thin Solid Films* **251** 72–9

[11] Sanz R, Romano L, Zimbone M, Buccheri M A, Scuderi V, Impellizzeri G, Scuderi M, Nicotra G, Jensen J and Privitera V 2015 UV-black rutile TiO2: An antireflective photocatalytic nanostructure *J. Appl. Phys.* **117**

[12] Cai J, Ye J, Chen S, Zhao X, Zhang D, Chen S, Ma Y, Jin S and Qi L 2012 Self-cleaning, broadband and quasi-omnidirectional antireflective structures based on mesocrystalline rutile TiO2 nanorod arrays *Energy Environ. Sci.* **5** 7575–81

[13] Worasukhkhung S, Pudwat S, Eiamchai P, Horprathum M, Dumrongrattana S and Aiempanakit K 2012 Hydrophilic property of TiO2 films sputtered on glass/ITO for self cleaning glass and heat mirror application *Procedia Eng.* **32** 780–6

[14] Liu Y, Wang X, Yang F and Yang X 2008 Excellent antimicrobial properties of mesoporous anatase TiO2 and Ag/TiO2 composite films *Microporous Mesoporous Mater.* **114** 431–9

[15] Joost U, Juganson K, Visnapuu M, Mortimer M, Kahru A, Nõmmiste E, Joost U, Kisand V and Ivask A 2015 Photocatalytic antibacterial activity of nano-TiO2 (anatase)-based thin films: Effects on Escherichia coli cells and fatty acids *J. Photochem. Photobiol. B Biol.* **142** 178–85

[16] Fu G, Vary P S and Lin C T 2005 Anatase TiO 2 nanocomposites for antimicrobial coatings *J. Phys. Chem. B* **109** 8889–98

[17] Watanabe T, Nakajima A, Wang R, Minabe M, Koizumi S, Fujishima A and Hashimoto K 1999 Photocatalytic activity and photoinduced hydrophilicity of titanium dioxide coated glass *Thin Solid Films* **351** 260–3

[18] Lai Y, Tang Y, Gong J, Gong D, Chi L, Lin C and Chen Z 2012 Transparent superhydrophobic/superhydrophilic TiO 2-based coatings for self-cleaning and anti-

fogging *J. Mater. Chem.* **22** 7420–6

[19] Tonneau R, Moskovkin P, Pflug A and Lucas S 2018 TiO $_x$ deposited by magnetron sputtering: a joint modelling and experimental study *J. Phys. D. Appl. Phys.* **51** 195202

[20] Berg S and Nyberg T 2005 Fundamental understanding and modeling of reactive sputtering processes *Thin Solid Films* **476** 215–30

[21] Lucas S and Moskovkin P 2010 Simulation at high temperature of atomic deposition, islands coalescence, Ostwald and inverse Ostwald ripening with a general simple kinetic Monte Carlo code *Thin Solid Films* **518** 5355–61

[22] Pflug A, Siemers M, Schwanke C and Szyszka B 2010 Simulation von Plasma-Beschichtungsprozessen *Vak. Forsch. und Prax.* **22** 31–4

[23] Melzig T, Siemers M, Pflug A and Rank R 2014 3D PIC-MC simulation of anode effects in dual magnetron discharges *Surf. Coatings Technol.* **241** 30–2

[24] Schwanke C, Pflug A, Siemers M and Szyszka B 2012 *Applied Parallel and Scientific Computing* vol 7133, ed K Jónasson (Berlin, Heidelberg: Springer Berlin Heidelberg)

[25] Tonneau R, Pflug A and Lucas S 2020 Magnetron sputtering: determining scaling relations towards real power discharges using 3D Particle-In-Cell Monte Carlo models *Plasma Sources Sci. Technol.*

[26] Bird G A 1994 *Molecular gas dynamics and the direct simulation of gas flows* (Clarendon Press)

[27] Koura K and Matsumoto H 1991 Variable soft sphere molecular model for inverse-power-law or Lennard-Jones potential *Phys. Fluids A Fluid Dyn.* **3** 2459–65

[28] Phelps A V. 1994 The application of scattering cross sections to ion flux models in discharge sheaths *J. Appl. Phys.* **76** 747–53

[29] Nathan S S, Rao G M and Mohan S 1998 Transport of sputtered atoms in facing targets sputtering geometry: A numerical simulation study *J. Appl. Phys.* **84** 564

[30] Abrahamson A A 1969 Born-Mayer-Type Interatomic Potential for Neutral Ground-State Atoms with Z = 2 to Z = 105 *Phys. Rev.* **178** 76–9

[31] Hagelaar G J M and Pitchford L C 2005 Solving the Boltzmann equation to obtain electron transport coefficients and rate coefficients for fluid models *Plasma Sources Sci. Technol.* **14** 722–33

[32] Dressler R A, Chiu Y H, Levandier D J and Ng C Y 2000 Collision-induced dissociation dynamics in O2++Ne(Ar) collisions: The role of electronic excitation *J. Chem. Phys.* **113** 8561–6

[33] Squires L and Baer T 1976 Cross sections for symmetric charge transfer reactions of Xe+ and NO+ in selected internal and translational energy states *J. Chem. Phys.* **65** 4001–6

[34] Flesch G D, Nourbakhsh S and Ng C Y 1990 Absolute state-selected and state-to-state total cross sections for the reaction Ar+(2P3/2,1/2)+O2 *J. Chem. Phys.* **92** 3590–604

[35] Lennon M A, Bell K L, Gilbody H B, Hughes J G, Kingston A E, Murray M J and Smith F J 1988 Recommended Data on the Electron Impact Ionization of Atoms and Ions: Fluorine to Nickel *J. Phys. Chem. Ref. Data* **17** 1285–363

[36] Kim Y K and Desclaux J P 2002 Ionization of carbon, nitrogen, and oxygen by electron impact *Phys. Rev. A - At. Mol. Opt. Phys.* **66** 127081–1270812

[37] Lawton S A and Phelps A V. 1978 Excitation of the b 1Σg+ state of O2 by low energy electrons *J. Chem. Phys.* **69** 1007–9

[38] Alvarez R, Garcia-Martin J M, Garcia-Valenzuela A, Macias-Montero M, Ferrer F J, Santiso J, Rico V, Cotrino J, Gonzalez-Elipe A R and Palmero A 2015 Nanostructured Ti thin films by magnetron sputtering at oblique angles *J. Phys. D. Appl. Phys.* **49** 45303

[39] Van Aeken K, Mahieu S and Depla D 2008 The metal flux from a rotating cylindrical magnetron: A Monte Carlo simulation *J. Phys. D. Appl. Phys.* **41**

[40] Bogaerts A, Bultinck E, Eckert M, Georgieva V, Mao M, Neyts E and Schwaederle L Computer Modeling of Plasmas and Plasma- Surface Interactions 295–307

[41] Depla D, Mahieu S and De Gryse R 2009 Magnetron sputter deposition: Linking discharge voltage with target properties *Thin Solid Films* **517** 2825–39

[42] Moller W, Eckstein W and Biersack J P 1988 TRIDYN BINARY COLLISION SIMULATION OF ATOMIC COLLISIONS OO1O-4655 / 88 / $ 03 . 50 © Elsevier Science Publishers WV . (North-Holland Physics Publishing Division) LONG WRITE-UP I . Introduction Computer simulations of atomic collisions based on the binar *Physics (College. Park. Md).* **51** 355–68

[43] Gudmundsson J T, Lundin D, Brenning N, Raadu M A, Huo C and Minea T M 2016 An ionization region model of the reactive Ar/O2 high power impulse magnetron sputtering discharge *Plasma Sources Sci. Technol.* **25**

[44] Tominaga K, Ito D and Miyamoto Y 2006 Energetic negative ions in titanium oxide deposition by reactive sputtering in Ar/O2 *Vacuum* **80** 654–7

[45] Mahieu S and Depla D 2007 Correlation between electron and negative O- ion emission during reactive sputtering of oxides *Appl. Phys. Lett.* **90** 2–4

[46] Kluth O, Schöpe G, Rech B, Menner R, Oertel M, Orgassa K and Schock H W 2006 Comparative material study on RF and DC magnetron sputtered ZnO:Al films *Thin Solid Films* vol 502 pp 311–6

[47] Welzel T and Ellmer K 2012 Negative oxygen ion formation in reactive magnetron sputtering processes for transparent conductive oxides *J. Vac. Sci. Technol. A Vacuum, Surfaces, Film.*

[48] Amin A, Köhl D and Wuttig M 2010 The role of energetic ion bombardment during growth of TiO2 thin films by reactive sputtering *J. Phys. D. Appl. Phys.* **43**

[49] Thomann A L, Cormier P A, Dolique V, Semmar N, Dussart R, Lecas T, Courtois B and

Brault P 2013 Energy transferred to the substrate surface during reactive magnetron sputtering of aluminum in Ar/O2 atmosphere *Thin Solid Films* **539** 88–95

[50] Ellmer K and Welzel T 2012 Reactive magnetron sputtering of transparent conductive oxide thin films: Role of energetic particle (ion) bombardment *J. Mater. Res.* **27** 765–79

[51] Mahieu S, Leroy W P, Van Aeken K and Depla D 2009 Modeling the flux of high energy negative ions during reactive magnetron sputtering *J. Appl. Phys.* **106** 6–13

[52] Moens F, Kalvas T, Van Steenberge S and Depla D 2017 Effect of space charge on the negative oxygen flux during reactive sputtering *J. Phys. D. Appl. Phys.* **50**

[53] Robinson M T and Torrens I M 1974 Computer simulation of atomic-displacement cascades in solids in the binary-collision approximation *Phys. Rev. B* **9** 5008–24

[54] Biersack J P and Haggmark L G 1980 A Monte Carlo computer program for the transport of energetic ions in amorphous targets *Nucl. Instruments Methods* **174** 257–69

[55] Santos I, Marqués L A, Pelaz L and López P 2009 Improved atomistic damage generation model for binary collision simulations *J. Appl. Phys.* **105** 83530

[56] Ghoniem N M and Chou S P 1988 Binary collision Monte Carlo simulations of cascades in polyatomic ceramics *J. Nucl. Mater.* **155**–**157** 1263–7

[57] Dendy R O 1990 *Plasma Dynamics*

[58] Bait L, Azzouz L, Madaoui N and Saoula N 2017 Influence of substrate bias voltage on the properties of TiO 2 deposited by radio-frequency magnetron sputtering on 304L for biomaterials applications *Appl. Surf. Sci.* **395** 72–7

[59] Wang B, Wei S, Guo L, Wang Y, Liang Y, Xu B, Pan F, Tang A and Chen X 2017 Effect of deposition parameters on properties of TiO2 films deposited by reactive magnetron sputtering *Ceram. Int.* **43** 10991–8

[60] Gauter S, Haase F and Kersten H 2019 Experimentally unraveling the energy flux originating from a DC magnetron sputtering source *Thin Solid Films* **669** 8–18

[61] Mišina M, Shaginyan L R, Maček M and Panjan P 2001 Energy resolved ion mass spectroscopy of the plasma during reactive magnetron sputtering *Surf. Coatings Technol.* **142–144** 348–54

[62] Jiang N, Shen Y G, Mai Y W, Chan T and Tung S C 2004 Nanocomposite Ti-Si-N films deposited by reactive unbalanced magnetron sputtering at room temperature *Mater. Sci. Eng. B Solid-State Mater. Adv. Technol.* **106** 163–71

[63] Shen Y G, Mai Y W, McKenzie D R, Zhang Q C, McFall W D and McBride W E 2000 Composition, residual stress, and structural properties of thin tungsten nitride films deposited by reactive magnetron sputtering *J. Appl. Phys.* **88** 1380–8

[64] Rode D L, Gaddam V R and Yi J H 2007 Subnanometer surface roughness of dc magnetron sputtered Al films *J. Appl. Phys.* **102**

[65] Van Steenberge S, Leroy W P, Hubin A and Depla D 2014 Momentum transfer driven textural changes of CeO2thin films *Appl. Phys. Lett.* **105**

[66] Cormier P -a., Balhamri a., Thomann a.-L, Dussart R, Semmar N, Lecas T, Snyders R and Konstantinidis S 2014 Titanium oxide thin film growth by magnetron sputtering: Total energy flux and its relationship with the phase constitution *Surf. Coatings Technol.* **254** 291–7

[67] Thomann A L, Caillard A, Raza M, El Mokh M, Cormier P A and Konstantinidis S 2019 Energy flux measurements during magnetron sputter deposition processes *Surf. Coatings Technol.* **377** 124887

8 Conclusion

This thesis describes the scientific basis, the construction principles, and the operational parameters of a *Virtual Coater* system to study the deposition of thin films by means of physical vapor deposition techniques. It was applied to the case of TiO_x thin films deposited with a reactive dual magnetron system. Because a magnetron sputtering system is an extremely complex system, this research aimed to provide modelling tools enabling the simulation of a complete plasma deposition process and a better understanding of the specific mechanisms occurring during film growth.

To take the challenge, a multiscale approach was required. Three sorts of algorithms were put together and to compose the core of *Virtual Coater*: *(i)* a **Direct Simulation Monte Carlo** algorithm handling the gas diffusion of neutral species in the complete 3D geometry over long time scale (several seconds); *(ii)* a **Particle-in-Cell Monte Carlo** algorithm enabling the addition of charged particles within the gas phase. However, due to the large computational resources required, it was necessary to interface the algorithm with the first one i.e., working with a simplified 3D geometry and over shorter time scale (several hundreds of micro-seconds); *(iii)* a **kinetic Monte Carlo** algorithm modelling the film growth on the atomic scale.

All these algorithms were required to be interfaced together in order to build *Virtual Coater*. This interfacing work, along with the validation of the simulation results, was performed in three steps through the present PhD thesis. A full chapter is dedicated to each and the work is crystallized in two published articles and one submitted:

The role of neutral particles (chapter 5)

In this section, the DSMC algorithm was successfully used to simulate the hysteresis behaviour of the discharge by using the real 3D geometry of the coater. The partial pressure of oxygen as experimentally measured by mass spectroscopy and computed by the DSMC algorithm were in perfect agreement. The validation of the DSMC algorithm enables its results to be used as an input for subsequent k-MC film growth Nascam simulations. For that purpose, fluxes of Ar, Ti and O_2 as well as their respective angular and energy distributions at substrate locations were computed from

the DSMC results. This method enabled to reproduce the film stoichiometry successfully, as well as its morphology. Although a good agreement between tilting columns angles of the 70° inclined samples was observed, the experimental measurements show smaller values than the ones predicted in the oxide mode. This deviation is attributed to energetic particles bombardment during the film growth, which was not included in the model at that time, as only neutral species were involved. The effective sticking coefficient of oxygen molecules onto metallic Ti was also derived from this work.

The challenge of modelling charged particles (chapter 6)

To bring the *VC* concept to the next step, we had to expand it with a Particle-in-Cell Monte Carlo algorithm in order to include charged particles modelling. To meet the resource requirement of the PICMC approach it was necessary to simplify the 3D model and to operate the plasma at a very low discharge current. Thirteen simulations using a simplified single magnetron configuration with discharge current densities from 0.6 to 2.4 $mA.cm^{-2}$ were performed for 150 µs each. At first, the computed electron densities were compared to experimental measurements (at higher discharge current densities) and a linear relationship of the electron density versus the discharge current density was reported. As a second step, the production of Ar and Ti ions was analysed through the ionization by electron impact collision rate data. On the one hand, Ar ionization rate was shown to exhibit the same linear relationship with the discharge current because electron and Ar^+ densities are the main charged species in the discharge and it is necessary to keep their proportional relative abundance in order to preserve the global neutral electrical charge of the plasma. The Ti^+ ions production rate exhibits a linear relationship with the product of the discharge power density by the discharge current density. Indeed, the number of Ti atoms in the gas phase depends on (i) the number of ions responsible for the target sputtering and (ii) the sputtering yield for a given specie scales with the energy of the incoming ions (assuming a normal incident direction with respect to the target surface). Therefore, the number of sputtered Ti atoms is proportional to the product of the discharge current density by the discharge current voltage (assuming the incoming ions hit the target with an energy eV_{disch}), which is by definition the discharge power density. Finally, the Ti^+ will be produced by electron impact and the production rate is proportional to the electron density, which is also proportional to the discharge current density. The

previously explained scaling laws were then successfully applied to the flux of particles flowing towards the substrate location enabling the scaling of PICMC simulations to real discharge power. It was also shown that the method based on the PICMC algorithm properly captures the physics of the magnetron sputtering process, as it also predicts the formation of propagating ionization zones, called spokes. These are due to the $\vec{E}x\vec{B}$ field in front of the target. The average electron density of the spokes was demonstrated to follow the same scaling law as the global electron density of the discharge, i.e., linear relationship with the discharge current density. Finally, the validity domain of the scaling laws was discussed. According to the author, the PICMC simulation of a DC discharge can be upscaled as long as the electron-electron collision rate remains negligible and the ionization rate of the sputtered species remains low, i.e., as long as the ion current towards the target is mainly carried by background gas ions.

The role of charged particles (chapter 7)

To complete the *Virtual Coater* construction, the validated PICMC algorithm was added to the loop to bring the *VC* to its final configuration, as showed in Figure 15. DCMS simulations were restarted including atomic oxygen as sputtered species instead of molecular oxygen. The computed final densities of these neutral species i.e. Ar, Ti, O_2 and O, were then pipped into the simplified 3D geometry in order to simulate the plasma discharge. The simulations were focused on the three regimes of the hysteresis curve: metallic, transition and oxide modes. In addition to the 4 neutral species, 6 charged species were included: electrons, Ar^+, Ti^+, O_2^+, O^+ and O^-. While all these species can be produced in gas phase, only O^- is created at the target surface during a sputtering event. Scientific literature was used to evaluate the probability of such events, with the assumption that all ions participating to sputtering have the same probability to produce an O^- ions. These O^- are accelerated straight away by the plasma sheath and bombard all surfaces in front of the targets. This flux of highly energetic species was already reported in literature, as well as the possible effects on film properties, but the 3D modelling approach including self-consistent electric field calculation was still missing. The highlighted scaling laws of Chapter 6 were used to scale the fluxes of charged species towards the substrate up to real discharge power parameters. Subsequent film growth simulations based on the PICMC and DSMC

computed results were then started with an improved version of Nascam (version 5), which includes a binary collision approximation and collision cascades modelling. The simulated coating morphologies were in line with experimental cross section SEM analysis. In particular, Nascam efficiently predicted the tilting column angles in all three discharge modes. Indeed, the experimental results show a reduction in the tilting column angles while switching the discharge from metal to oxide mode. In Chapter 1 , the molecular oxygen was demonstrated to reduce the tilting column angles but it was also shown that it is not a sufficient explanation, as experimental measurements in oxide mode were still lower than the ones predicted by Nascam. By taking into account charged particles, and especially O^- ions, *Virtual Coater* was finally able to correctly predict the tilting column angles of the coatings and also the dependencies with the substrate location. The effect of highly energetic particles was also highlighted experimentally by measuring the Normalized Energy Flux and performing X-ray diffraction on the deposited coating. The ones in the flux of O^- i.e., with higher NEF values, exhibited anatase phase while the ones with lower NEF values (off median plane) were amorphous. In addition, the amorphous growth of the coating in transition mode was explained by the suppression of the diffusion process by the oxygen acting as trapping site for Ti. *Virtual Coater* was successfully setup and benchmarked with experimental measurements throughout the present PhD thesis. Many parameters are experimentally tunable during any PVD process. Experiments require time and money to understand the effects of these parameters, as well as their optimization to meet the specific coating properties. *Virtual Coater* enables to optimize these parameters without the need for real-life experiment, enabling a more precise and deeper understanding of the effects of different parameters on the resulting thin film growth.

9 Recommendations for future work

The present thesis also raised many new questions, the answers to some of which probably hold the key for interesting developments for PVD processes using *Virtual Coater*.

9.1. Magnetic configuration of the dual magnetron sputtering system

This PhD work was performed by keeping the same magnetic configuration of the dual magnetron system i.e., closed field configuration (see Figure 7). This configuration was originally chosen to support the early development of *Virtual Coater* because at that time, the simulation of charged species were not supported. It is well admitted that in a closed field configuration, the flux energetic species is reduced compared to a mirror field configuration. Now that *VC* supports the simulation of charged particles in both gas phase and film growth software packages, a differential study of the magnetic configuration could certainly enable a better understanding of dual magnetron systems. For example, Figure 18 aggregates the measurements obtained during this thesis with the ATP for the two magnetron configurations.

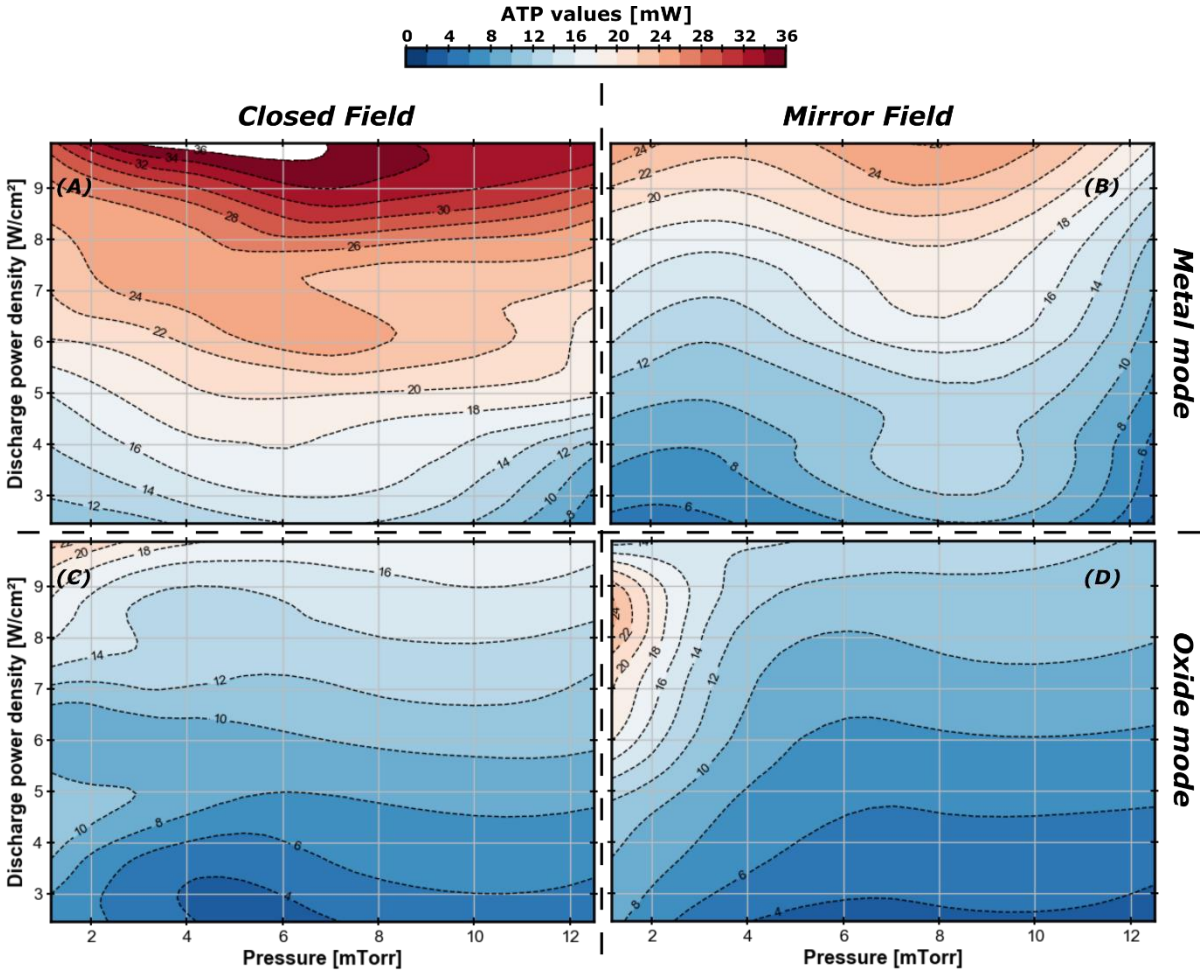

Figure 18 *Experimental Active Thermal Probe (ATP) measurements at substrate location for various configurations:* ***(A)*** *Closed field - Metal mode;* ***(B)*** *Mirror field – Metal mode;* ***(C)*** *Closed field – Oxide mode;* ***(D)*** *Mirror field – Oxide mode*

One can see that the ATP values increase with the discharge power density regardless of the pressure and the magnetic configuration. The metal mode maps (A & B) mostly exhibit higher ATP values for the corresponding values of oxide mode maps (C & D). In metal mode, the results also show a much higher measured energy flux when the magnets are configured in closed field. This observation is in agreement with the article of Kelly *et al.* [82]. They claim that in closed field configuration, the plasma expands towards the substrate region, increasing the energy brought to probe. These measurements demonstrate that some work should be performed on such comparative study in order to provide normalized energy flux values based on these measurements. Indeed, by taking into account the deposition rates in the various conditions, the maps in Figure 18 would drastically change. The deposition rate in oxide mode is generally at least 10 times lower than in metal mode, leading to a dramatic increase of the normalized energy flux. These measurements could be

compared with the results *Virtual Coater* could provide and the effect on the film growth could also be highlighted.

9.2. Electron energization mechanisms in magnetron sputtering

The simulation chain could also be used to support the study of more fundamental questions such as the understanding of the bi-Maxwellian distribution of the electron energy distribution function (EEDF). In [83], Bogaerts et al. analysed a glow discharge of Ar with a Langmuir probe. They reported that generally three electronic populations exist in a glow discharge: (i) a highly energetic primary population (SE) originating from the cathode and having not yet experienced many collisions; (ii) a second electronic population with less energy due to many collisions but not yet thermalized; and finally (iii) a thermalized electron group. The authors were able to measure the populations (ii) and (iii) with temperature of respectively 4.5 and 0.5 eV. However, the population (i) was not observed.

In order to try to give an explanation on the origin of the bi-Maxwellian EEDF, one may focus on the Ohmic heating of electrons. Recently, the role of Ohmic heating in magnetron sputtering was highlighted [84,85]. Brenning et al. [85] suggested that a non-negligible fraction of the discharge voltage drops within the plasma bulk enabling an efficient way to energize electrons outside the cathode sheath. Taking into account Ohmic heating, it is possible to rewrite the explanation of the multiple electron populations from Bogaert et al. to the case of magnetron sputtering: the first population (i) results from sheath energization of secondary electrons and form a high energy group of electrons. However, due to the magnetic field, the target recaptures a non-negligible fraction of those electrons. (ii) The second electron population is composed of electrons originating from ionization events in the ionization region (IR). Those electrons are accelerated by a fraction of the potential drop left in the IR, giving rise to a less highly energetic population of electrons. Finally (iii), thermalized electrons are the third electron population. This potential explanation may sound unlikely, as experimental works reported bi-Maxwellian distribution, not tri-Maxwellian. However, the third electron population implies a very efficient cooling down mechanism of electrons. As inelastic collisions (excitation and ionization) are threshold phenomena, they are not suitable to thermalize electrons with lower energy than this threshold. The

most effective thermalization processes for electrons are therefore elastic collisions. Moreover, the energy transfer by like particle collisions is very efficient. This means that electron-electron (e-e) collisions are an important process for the thermalization of the EEDF. As the fraction of charged species is very low (<< 1%) in DC magnetron sputtering process, the frequency of e-e collisions is negligible compared with e-Ar collisions.

A possible simulation strategy to unravel the bi-Maxwellian nature of electrons based on the single magnetron model of Chapter 6 is presented in Figure 19.

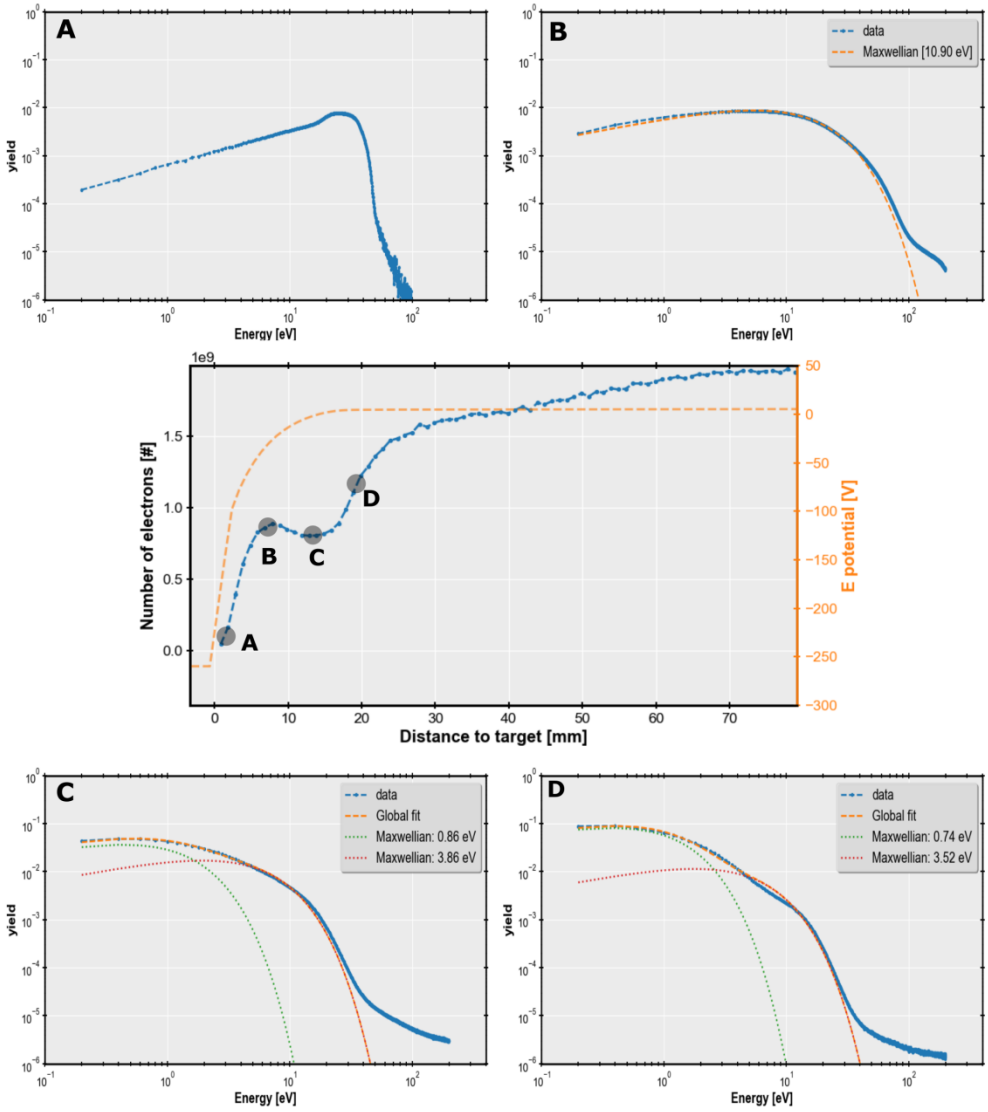

Figure 19 *The central figure plots the evolution of the number of simulated electrons with the evolution of target distance. The orange curve depicts the evolution of the electrical potential. 5 zones are used to sample the EEDF (A, B, C and D). Zone A is in the cathode sheath, zone B is within the magnetic confinement region, zone C and D are within the region where Ohmic heating take place.*

Four EEDFs' are extracted from the simulation. The EEDF of zone A is located right above the target; it presents electrons having travelled less than 1 mm in the cathode axial direction. The EEDF is not Maxwellian as the emission of SE by the target is not supposed to be Maxwellian. Those electrons are highly energetic as they are energized by the plasma sheath. In the magnetic confinement region (zone B), EEDF follow a single Maxwellian distribution with a corresponding energy of 10.9 eV. The origin of the Maxwellian distribution can probably be attributed to the spoke. As electrons are efficiently trapped in this region, they experience many inelastic collisions, which are efficient cooling mechanisms. This is the reason of the Maxwellian shape of the EEDF. In zone C, newly created electrons are accelerated by the fraction target potential expanding within the plasma, depending on where ionization events occurred. It is the reason why the EEDF is split in two populations. The new population has a lower temperature as it is the result of the low energy electrons heating. In zone D, the EEDF bifurcation is more pronounced because the newly formed electrons will not gain much energy, as the electrical potential has reached the saturation value (plasma potential).

9.3. Use of ceramic targets for compound deposition:

The hysteresis behaviour of the reactive magnetron sputtering is a problem for industrial applications. Indeed, the nature of the hysteresis is that, when there is a small variation in the deposition condition, it is not possible to reach back the previous conditions without looping around the complete hysteresis. Several approaches may be used to overcome this problem by eliminating or reducing the hysteresis. One of them is the use of a ceramic target instead of metallic ones, e.g., a sub-stoichiometric target of $TiO_{1.8}$ instead of Ti targets. The idea is to include as much oxygen as possible within the target bulk while keeping sufficient conductivity of the target to enable plasma ignition with DC power supply.

During this PhD work, Soleras Advanced Coatings[5] kindly provided such targets. Experimental work was performed with the targets, e.g., the hysteresis behaviour was tested, see Figure 20.

[5] https://www.soleras.com/

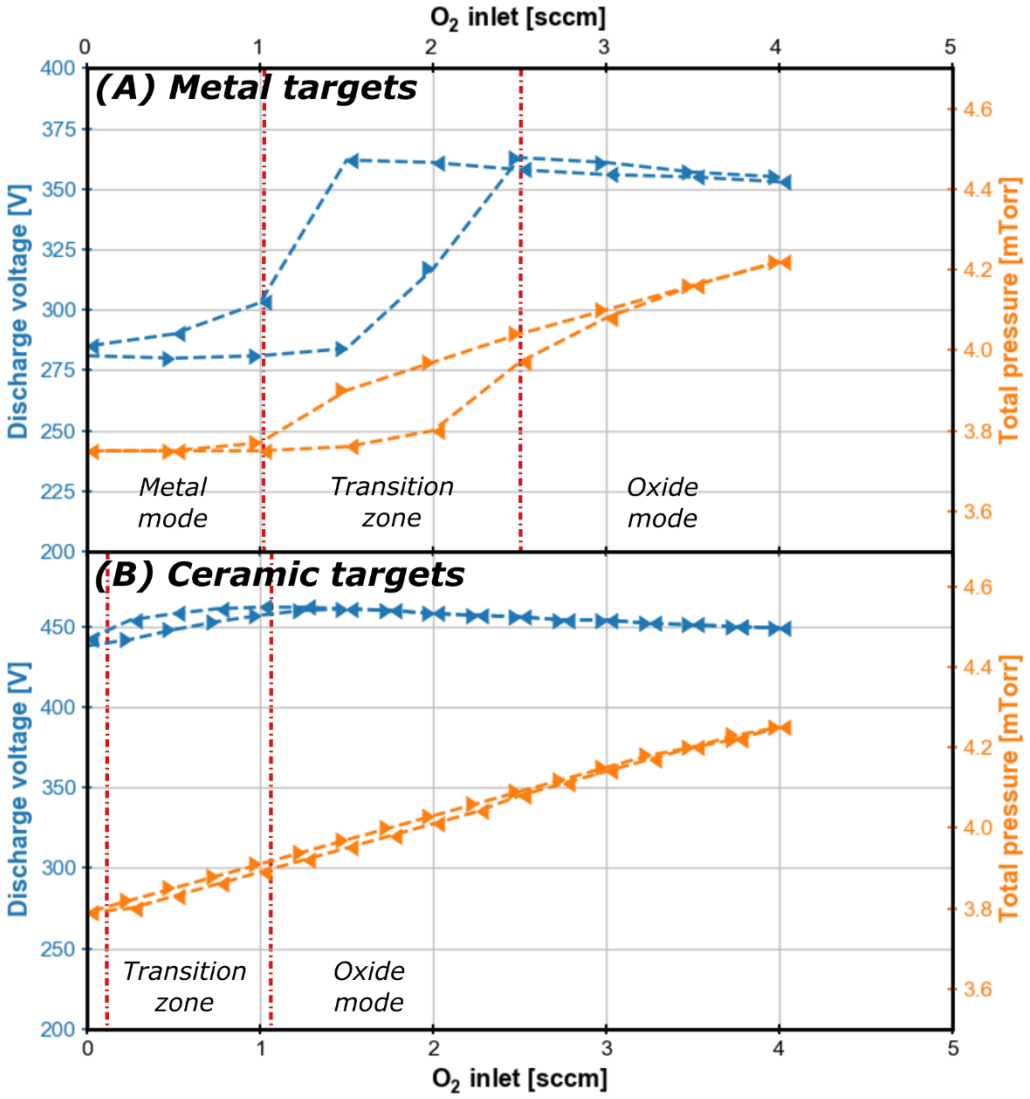

Figure 20 *Hysteresis experiments with the dual magnetron system at a discharge current of 200 mA.* ***(A)*** *using metal targets,* ***(B)*** *using ceramic targets. For both cases, A and B, the blue curve (upper one) is the discharge voltage evolution and the orange curve (lower one) is the evolution of the total pressure. Arrow markers also indicate whether the oxygen is increasing (right oriented) or decreasing (left oriented).*

The discharge voltage versus oxygen flow curves displayed almost no hysteresis behaviour for the ceramic targets. In addition to these measurements the active thermal probe combined with RBS analysis of deposited coatings enabled the calculation of the normalized energy flux toward the substrate located 15 cm away from the targets (same geometrical configuration as used during the PhD). The comparative study is presented in Figure 21.

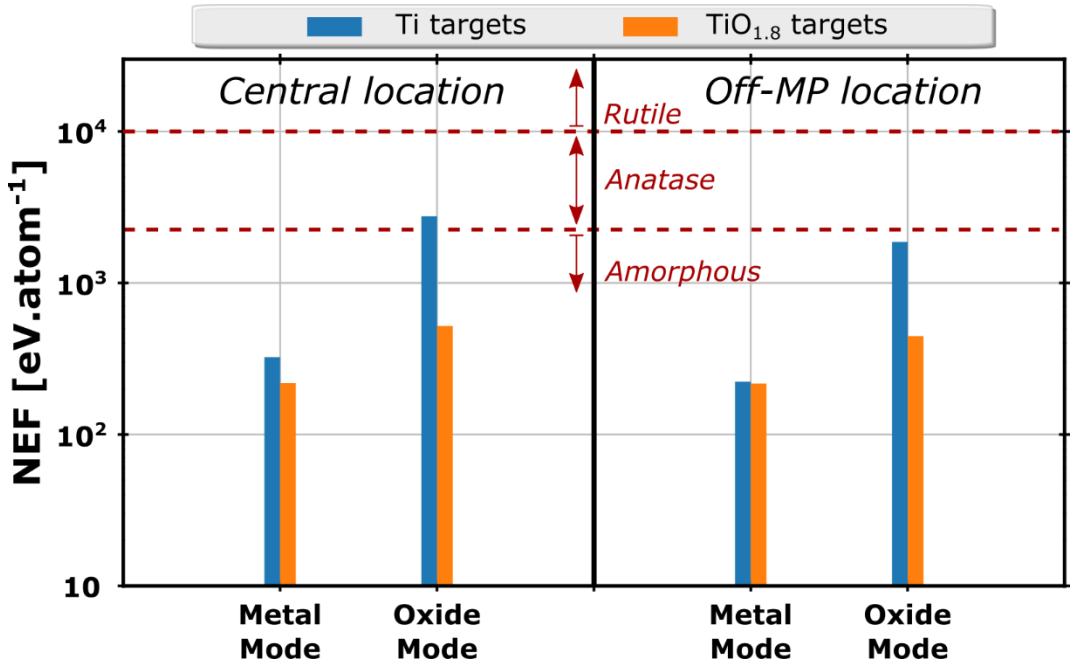

Figure 21 Experimental *Normalized Energy Flux (NEF) values measured at 2 locations: central and off-median plane (off-MP), for both metal and oxide mode and with either Ti targets or ceramic $TiO_{1.8}$ targets. The red dashed lines indicate the NEF thresholds for the formation of the three crystallographic phases of TiO_2. All discharges operate at a constant current of 250 mA.*

When no oxygen is added to the discharge (metal mode), all NEF measurements exhibit values within the range 200-400 eV. $atom^{-1}$ regardless of the location and the target type. Once in oxide mode, the NEF values observed for the Ti targets case drastically increases, as showed in chapter 7, due to the reduction of the deposition rate. Regarding the ceramic targets, the NEF values also increase when switching from metal to oxide mode but stay well below 1000 eV. $atom^{-1}$. The main reason explaining the lower NEF is better deposition rate when using ceramic targets. Therefore, the use of ceramic targets seems to enable the deposition of TiO_2 coatings at much lower NEF values, below a typical value of 2000 eV. In that case, the coating should be amorphous as we showed in chapter 7. *Virtual Coater* should be used to provide more insight about the use of ceramic targets in magnetron sputtering techniques.

9.4. Extension to other deposition processes

Of course, an easy thought is to extend the application of *VC* to other dry deposition processes as those presented in Figure 1 or Figure 2. VC cannot easily model all the techniques and modifications would probably be required. For instance, evaporation would certainly be the fastest process to model. Another technique suitable for *VC* is

ion beam sputtering. It was already studied with the presented simulation tools in [86,87] with the exception that the film modelling was handled by a Molecular Dynamic algorithm. It is the proof that *Virtual Coater* is a versatile tool which can be configured to meet scientific challenges. Regarding the HiPIMS processes, chapter 6 disable the potential use of the presented PICMC algorithm. Indeed, HiPIMS techniques produce very high electron density, which is not compatible with the developed scaling strategy. Therefore, either an alternative to the PICMC method should be studied or another PICMC approach could perhaps be involved, as it was proposed by Minea et al. [88] with a 2D model.

Plasma Enhanced Chemical Vapor Deposition (PECVD) should also be mentioned but this topic is related to the following point 9.6. Finally, another obvious extension of the *VC* application field is the frequency modification of the applied electric field powering the plasma discharge. For example, pulsed or RF magnetron sputtering could be studied without the need to modify the presented model if the same coater geometry is used.

9.5. Nascam for plasma-target interaction investigation

During this PhD, a new version of Nascam was introduced, which implements a BCA algorithm in order to better handle collision cascades induced by energetic particle bombardment. This approach could be used to study the effect of the sputtering onto the target. Of course, Nascam is dedicated to a small surface by comparison with a target surface, but certainly, the stoichiometric evolution of a composite or ceramic target still could be considered. This topic is scientifically relevant for today's technologies, which sometimes require many species to be co-deposited [89–91].

9.6. Improvement of the Virtual Coater for complex plasma chemistry

A final recommendation for future work is the improvement of the *Virtual Coater* configuration. Indeed, in its presented form, the major drawback is that it does not enable to model the gas diffusion of the neutral species created by charged species collisions. Even if the cross sections are included, the species can be created but the PICMC simulations cannot easily simulate long enough physical times to reach their steady state densities. That was demonstrated for two cases originating from the collaboration between A. Pflug and S. Lucas's groups. The first involved the plasma polymerization of cyclopropylamine in a pulsed discharge [77,78]. The second is about the case of DC-PECVD of an Ar/Acetylene discharge [79]. In both cases, the authors faced issues with long run of PICMC simulation in order to reach the steady state for radical species. One way to overcome this limitation would be to include charged species in the DSMC algorithm to take the simulation to another level. The team of A. Pflug at the Fraunhofer Institute of Braunschweig has already tested this solution. The idea is to load the charged species in the DSMC algorithm but in a frozen state, i.e. no motion allowed. If a state close to the steady state was reached for charged particles, they could still participate within the Monte Carlo collision routine for the creation of neutral species. They would then diffuse and could be loaded again in the PICMC simulations to check if the density state is steady or not. If not, the PICMC simulation can perform one more run and then be re-used in a new DSMC simulation. This DSMC-PICMC loop can go on as long as the final state is not reached, as it enables to model up to several seconds of discharge. The "improved" flow chart of this simulation chain is presented in Figure 22.

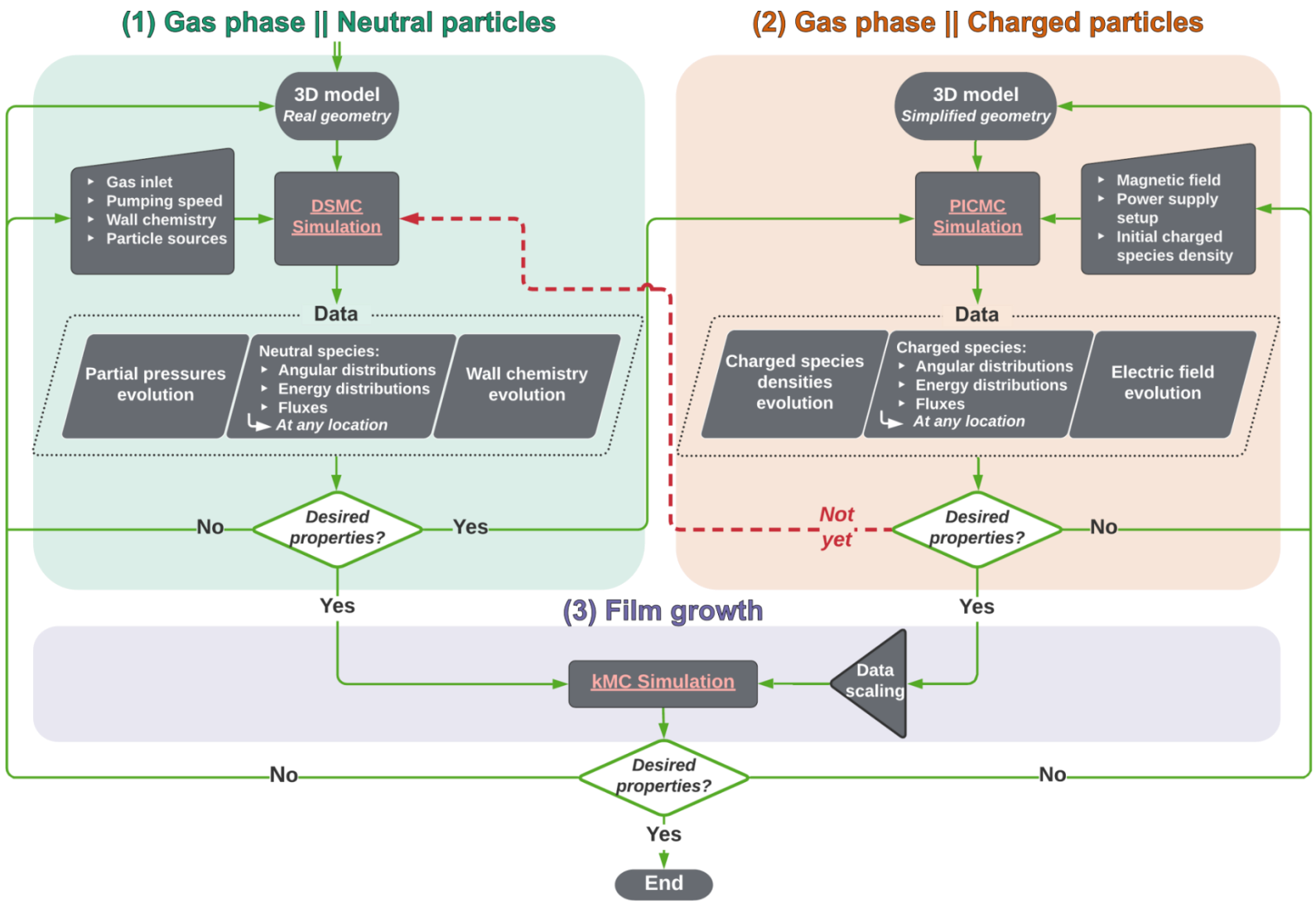

Figure 22 *Suggested flowchart for the Improved Virtual Coater concept*

10 References

[1] Choy K L 2003 *Chemical vapour deposition of coatings* vol 48 (Elsevier Ltd)

[2] Martin P M 2009 *Handbook of Deposition Technologies for Films and Coatings: Science, Applications and Technology* (Los Angeles, CA: William Andrew Publishing)

[3] Ohring M 2002 *Materials Science of Thin Films* (San Diego, CA: Academic Press)

[4] Mattox D M M 1998 *Handbook of physical vapor deposition (PVD) Processing Film Formation, Adhesition , Surface Preparation and Contamination Control*

[5] Mahan J E 2000 Physical Vapor Deposition of Thin Films *Phys. Vap. Depos. Thin Film. by John E. Mahan, pp. 336. ISBN 0-471-33001-9. Wiley-VCH , January 2000.*

[6] Rockett A 2008 *The materials science of semiconductors* (Springer US)

[7] Tudose I V, Suchea M P and Inter- F N 2019 Magnetron Sputtering Chemical and physical methods for multifunctional nanostructured inter- face fabrication Antimicrobial Coatings for Textiles

[8] Langmuir I 1928 Oscillations in ionized gases *Proc. Natl. Acad. Sci. U. S. A.* **14** 627–37

[9] Chapman B and Vossen J L 1981 Glow Discharge Processes: Sputtering and Plasma Etching *Phys. Today*

[10] Chen F F 1984 *Introduction to Plasma Physics and Controlled Fusion*

[11] Georgieva V, Saraiva M, Jehanathan N, Lebelev O I, Depla D and Bogaerts A 2009 Sputter-deposited Mg–Al–O thin films: linking molecular dynamics simulations to experiments *J. Phys. D. Appl. Phys.* **42** 065107

[12] Åstrand M, Selinder T I and Sjöstrand M E 2005 Deposition of Ti1-xAlxN using bipolar pulsed dual magnetron sputtering *Surf. Coatings Technol.*

[13] Trinh D H, Kubart T, Nyberg T, Ottosson M, Hultman L and Högberg H 2008 Direct current magnetron sputtering deposition of nanocomposite alumina - zirconia thin films *Thin Solid Films*

[14] Saraiva M, Georgieva V, Mahieu S, Van Aeken K, Bogaerts A and Depla D 2010 Compositional effects on the growth of Mg (M) O films *J. Appl. Phys.*

[15] Baroch P and Musil J 2008 Plasma drift in dual magnetron discharge *IEEE Trans. Plasma Sci.*

[16] Musil J and Baroch P 2005 Discharge in dual magnetron sputtering system *IEEE Trans. Plasma Sci.*

[17] Yusupov M, Bultinck E, Depla D and Bogaerts A 2011 Behavior of electrons in a dual-magnetron sputter deposition system: A Monte Carlo model *New J. Phys.* **13**

[18] Yusupov M, Bultinck E, Depla D and Bogaerts A 2011 Elucidating the asymmetric behavior of the discharge in a dual magnetron sputter deposition system *Appl. Phys. Lett.* **98** 2012–5

[19] Melzig T, Siemers M, Pflug A and Rank R 2014 3D PIC-MC simulation of anode effects in dual magnetron discharges *Surf. Coatings Technol.* **241** 30–2

[20] Depla D, Haemers J and De Gryse R 2006 Discharge voltage measurements during reactive sputtering of oxides *Thin Solid Films* **515** 468–71

[21] Bunshah R F and Deshpandey C V. 1985 Plasma assisted physical vapor deposition processes: A review *J. Vac. Sci. Technol. A Vacuum, Surfaces, Film.*

[22] Martin P M 2011 *Introduction to Surface Engineering and Functionally Engineered Materials*

[23] Thornton J A 1975 Influence of substrate temperature and deposition rate on structure of thick sputtered Cu coatings. *J Vac Sci Technol* **12** 830–5

[24] Ginley D S, H. Hosono and D.C. Paine 2011 *Handbook of Transparent Conductors* (New York: Springer US)

[25] Anders A 2010 A structure zone diagram including plasma-based deposition

and ion etching *Thin Solid Films* **518** 4087–90

[26] Pekker L and Krasheninnikov S I 2000 On the theory of low-pressure magnetron glow discharge *Phys. Plasmas*

[27] Gu L and Lieberman M A 1988 Axial distribution of optical emission in a planar magnetron discharge *J. Vac. Sci. Technol. A Vacuum, Surfaces, Film.*

[28] Bradley J W, Arnell R D and Armour D G 1997 Measurement and modelling of the bulk plasma in magnetron sputtering sources *Surf. Coatings Technol.*

[29] Bradley J W, Thompson S and Gonzalvo Y A 2001 Measurement of the plasma potential in a magnetron discharge and the prediction of the electron drift speeds *Plasma Sources Sci. Technol.* **10** 490–501

[30] Wendt A E and Lieberman M A 1990 Spatial structure of a planar magnetron discharge *J. Vac. Sci. Technol. A Vacuum, Surfaces, Film.*

[31] Kolev I and Bogaerts A 2004 Numerical models of the planar magnetron glow discharges *Contrib. to Plasma Phys.*

[32] Bogaerts A, Van Straaten M and Gijbels R 1995 Description of the thermalization process of the sputtered atoms in a glow discharge using a three-dimensional Monte Carlo method *J. Appl. Phys.*

[33] Birdsall C K 1991 Particle-in-cell charged-particle simulations, plus Monte Carlo collisions with neutral atoms, PIC-MCC *IEEE Trans. Plasma Sci.* **19** 65–85

[34] Kolev I and Bogaerts A 2006 PIC – MCC Numerical Simulation of a DC Planar Magnetron 127–34

[35] Pflug A, Siemers M, Melzig T, Schäfer L and Bräuer G 2014 Simulation of linear magnetron discharges in 2D and 3D *Surf. Coatings Technol.* **260** 411–6

[36] Markidis S, Henri P, Lapenta G, Rönnmark K, Hamrin M, Meliani Z and Laure E 2014 The Fluid-Kinetic Particle-in-Cell method for plasma simulations *J. Comput. Phys.* **271** 415–29

[37] Glish G L and Vachet R W 2003 The basics of mass spectrometry in the twenty-first century *Nat. Rev. Drug Discov.* **2** 140–50

[38] Chernushevich I V., Loboda A V. and Thomson B A 2001 An introduction to quadrupole-time-of-flight mass spectrometry *J. Mass Spectrom.* **36** 849–65

[39] Fantz U 2006 Basics of plasma spectroscopy *Plasma Sources Sci. Technol.* **15**

[40] Merlino R L 2007 Understanding Langmuir probe current-voltage characteristics *Am. J. Phys.* **75** 1078–85

[41] Allen J E 1992 Probe theory - the orbital motion approach *Phys. Scr.* **45** 497–503

[42] Magnus F and Gudmundsson J T 2008 Digital smoothing of the Langmuir probe I-V characteristic *Rev. Sci. Instrum.* **79**

[43] Harbauer K, Welzel T and Ellmer K 2012 A combined sensor for the diagnostics of plasma and film properties in magnetron sputtering processes *Thin Solid Films* **520** 6429–33

[44] Gauter S, Haase F and Kersten H 2019 Experimentally unraveling the energy flux originating from a DC magnetron sputtering source *Thin Solid Films* **669** 8–18

[45] Wiese R, Kersten H, Wiese G and Bartsch R 2015 Energy influx measurements with an active thermal probe in plasma-technological processes *EPJ Tech. Instrum.* **2** 2

[46] Yongqiang Wang and Michael Nastasi 2010 *Handbook modern ion beam materials analysis* vol 1 (Cambridge University Press)

[47] Zhou W, Apkarian R, Wang Z L and Joy D 2007 Fundamentals of scanning electron microscopy (SEM) *Scanning Microscopy for Nanotechnology: Techniques and Applications*

[48] Voigtländer B 2019 *Atomic Force Microscopy* (Cham: Springer International Publishing)

[49] Waseda Y, Matsubara E and Shinoda K 2011 *X-Ray Diffraction Crystallography*

[50] Kennedy B A 1990 *Surface Mining* ed B A Kennedy (Society for Mining, Metallurgy, and Exploration (SME))

[51] Ghosh T B, Dhabal S and Datta A K 2003 On crystallite size dependence of phase stability of nanocrystalline TiO2 *J. Appl. Phys.*

[52] Diebold U 2003 The surface science of titanium dioxide *Surf. Sci. Rep.* **48** 53–229

[53] Fujishima A and Zhang X 2006 Titanium dioxide photocatalysis: present situation and future approaches *Comptes Rendus Chim.* **9** 750–60

[54] Diebold U 2003 The surface science of titanium dioxide *Surf. Sci. Rep.* **48** 53–229

[55] Strijckmans K and Depla D 2014 A time-dependent model for reactive sputter deposition *J. Phys. D. Appl. Phys.* **47** 235302

[56] Berg S, Blom H, Larsson T and Nender C 1987 Modeling of reactive sputtering of compound materials *J. Vac. Sci. Technol. A Vacuum, Surfaces, Film.* **5** 202–7

[57] Depla D, Li X Y, Mahieu S, Van Aeken K, Leroy W P, Haemers J, De Gryse R and Bogaerts A 2010 Rotating cylindrical magnetron sputtering: Simulation of the reactive process *J. Appl. Phys.* **107**

[58] Chen Z Y, Bogaerts A, Depla D and Ignatova V 2003 Dynamic Monte Carlo simulation for reactive sputtering of aluminium *Nucl. Instruments Methods Phys. Res. Sect. B Beam Interact. with Mater. Atoms* **207** 415–23

[59] Güttler D, Abendroth B, Grötzschel R, Möller W and Depla D 2004 Mechanisms of target poisoning during magnetron sputtering as investigated by real-time in situ analysis and collisional computer simulation *Appl. Phys. Lett.* **85** 6134–6

[60] Van Aeken K, Mahieu S and Depla D 2008 The metal flux from a rotating cylindrical magnetron: A Monte Carlo simulation *J. Phys. D. Appl. Phys.* **41**

[61] Tominaga K, Ito D and Miyamoto Y 2006 Energetic negative ions in titanium oxide deposition by reactive sputtering in Ar/O2 *Vacuum* **80** 654–7

[62] Mahieu S and Depla D 2007 Correlation between electron and negative O- ion emission during reactive sputtering of oxides *Appl. Phys. Lett.* **90** 2–4

[63] Kluth O, Schöpe G, Rech B, Menner R, Oertel M, Orgassa K and Schock H W 2006 Comparative material study on RF and DC magnetron sputtered ZnO:Al films *Thin Solid Films* vol 502 pp 311–6

[64] Welzel T and Ellmer K 2012 Negative oxygen ion formation in reactive magnetron sputtering processes for transparent conductive oxides *J. Vac. Sci. Technol. A Vacuum, Surfaces, Film.*

[65] Amin A, Köhl D and Wuttig M 2010 The role of energetic ion bombardment during growth of TiO2 thin films by reactive sputtering *J. Phys. D. Appl. Phys.* **43**

[66] Thomann A L, Cormier P A, Dolique V, Semmar N, Dussart R, Lecas T, Courtois B and Brault P 2013 Energy transferred to the substrate surface during reactive magnetron sputtering of aluminum in Ar/O2 atmosphere *Thin Solid Films* **539** 88–95

[67] Ellmer K and Welzel T 2012 Reactive magnetron sputtering of transparent conductive oxide thin films: Role of energetic particle (ion) bombardment *J. Mater. Res.* **27** 765–79

[68] Mahieu S, Leroy W P, Van Aeken K and Depla D 2009 Modeling the flux of high energy negative ions during reactive magnetron sputtering *J. Appl. Phys.* **106** 6–13

[69] Vahedi V and Surendra M 1995 A Monte Carlo collision model for the particle-in-cell method: applications to argon and oxygen discharges *Comput. Phys. Commun.* **87** 179–98

[70] Kondo S and Nanbu K 1999 Self-consistent numerical analysis of a planar dc magnetron discharge by the particle-in-cell/Monte Carlo method *J. Phys. D. Appl. Phys.* **32** 1142–52

[71] Nanbu K and Kondo S 1997 Analysis of Three-Dimensional DC Magnetron Discharge by the Particle-in-Cell/Monte Carlo Method *Jpn. J. Appl. Phys.* **36** 4808–14

[72] Bultinck E and Bogaerts A 2009 Particle-in-cell/monte carlo collisions treatment

of an Ar/O2 magnetron discharge used for the reactive sputter deposition of TiOx films *New J. Phys.* **11**

[73] Bultinck E and Bogaerts A 2011 Characterization of an Ar/O2 magnetron plasma by a multi-species Monte Carlo model *Plasma Sources Sci. Technol.* **20** 045013

[74] Plasmatechnik V-, Pflug A, Siemers M, Schwanke C and Szyszka B 2010 Simulation von **22** 31–4

[75] Schwanke C, Pflug A, Siemers M and Szyszka B 2012 *Applied Parallel and Scientific Computing* vol 7133, ed K Jónasson (Berlin, Heidelberg: Springer Berlin Heidelberg)

[76] Lucas S and Moskovkin P 2010 Simulation at high temperature of atomic deposition, islands coalescence, Ostwald and inverse Ostwald ripening with a general simple kinetic Monte Carlo code *Thin Solid Films* **518** 5355–61

[77] Mathioudaki S, Vandenabeele C R, Tonneau R, Pflug A, Tennyson J and Lucas S 2020 Plasma polymerization of cyclopropylamine in a low-pressure cylindrical magnetron reactor: A PIC-MC study of the roles of ions and radicals *J. Vac. Sci. Technol. A* **38** 033003

[78] Mathioudaki S, Vandenabeele C, Tonneau R, Pflug A and Lucas S 2019 Characterization of a pulsed low pressure argon discharge in a cylindrical magnetron reactor by plasma diagnostic and 3D plasma modeling *J. Vac. Sci. Technol. A* **37** 031301

[79] Fauroux A, Vandenabeele C, Pflug A and Lucas S 2020 *Experimental and theoretical study of a magnetron DC-PECVD acetylene discharge: Determination of the main species and reactions taking place in the plasma* vol 400 (Elsevier B.V)

[80] Tonneau R, Moskovkin P, Pflug A and Lucas S 2018 TiO_x deposited by magnetron sputtering: a joint modelling and experimental study *J. Phys. D. Appl. Phys.* **51** 195202

[81] Tonneau R, Pflug A and Lucas S 2020 Magnetron sputtering: determining

scaling relations towards real power discharges using 3D Particle-In-Cell Monte Carlo models *Plasma Sources Sci. Technol.*

[82] Kelly P . and Arnell R . 2000 Magnetron sputtering: a review of recent developments and applications *Vacuum* **56** 159–72

[83] Bogaerts A, Quentmeier A, Jakubowski N and RenaatGijbels 1995 plasma diagnostics of an analytical grimm-type glow discharge in argon andin neon: Langmuir probe and opticat emission spectromery measurements *Spectrochim. Acta B* **50** 1337–49

[84] Huo C, Lundin D, Raadu M A, Anders A, Gudmundsson J T and Brenning N 2013 On sheath energization and Ohmic heating in sputtering magnetrons *Plasma Sources Sci. Technol.* **22**

[85] Brenning N, Gudmundsson J T, Lundin D, Minea T, Raadu M A and Helmersson U 2016 The role of Ohmic heating in dc magnetron sputtering *Plasma Sources Sci. Technol.* **25** 65024

[86] Turowski M, Jupé M, Melzig T, Moskovkin P, Daniel A, Pflug A, Lucas S and Ristau D 2015 Practice-oriented optical thin film growth simulation via multiple scale approach *Thin Solid Films* vol 592 pp 240–7

[87] Turowski M, Jupé M, Ehlers H, Melzig T, Pflug A and Ristau D 2015 Simulation in thin film technology *Opt. Syst. Des. 2015 Adv. Opt. Thin Film. V* **9627** 962707

[88] Minea T M, Costin C, Revel A, Lundin D and Caillault L 2014 Kinetics of plasma species and their ionization in short-HiPIMS by particle modeling *Surf. Coatings Technol.* **255** 52–61

[89] Feng Z, Ke P and Wang A 2015 Preparation of Ti2AlC MAX Phase Coating by DC Magnetron Sputtering Deposition and Vacuum Heat Treatment *J. Mater. Sci. Technol.* **31** 1193–7

[90] Frodelius J, Eklund P, Beckers M, Persson P O ., Högberg H and Hultman L 2010 Sputter deposition from a Ti2AlC target: Process characterization and conditions for growth of Ti2AlC *Thin Solid Films* **518** 1621–6

[91] Rauch J Y, Rousselot C and Martin N 2002 Structure and composition of TixAll-

xN thin films sputter deposited using a composite metallic target *Surf. Coatings Technol.* **157** 138–43

[92] Zunger A, Wei S-H, Ferreira L G and Bernard J E 1990 Special quasirandom structures *Phys. Rev. Lett.* **65** 353

[93] Robinson M T and Torrens I M 1974 Computer simulation of atomic-displacement cascades in solids in the binary-collision approximation *Phys. Rev. B* **9** 5008–24

[94] Biersack J P and Haggmark L G 1980 A Monte Carlo computer program for the transport of energetic ions in amorphous targets *Nucl. Instruments Methods* **174** 257–69

[95] Santos I, Marqús L A, Pelaz L and López P 2009 Improved atomistic damage generation model for binary collision simulations *J. Appl. Phys.* **105** 0–8

[96] Ghoniem N M and Chou S P 1988 Binary collision Monte Carlo simulations of cascades in polyatomic ceramics *J. Nucl. Mater.* **155**–**157** 1263–7

11 Annexes

11.1. Description of Nascam 5

A Nascam 5 project is built as a pack of modules containing a list of objects, created by the user, and dedicated to a well-defined task. It can be used to define one (or several) mesh, set the attachment rules of a given species or set the energy and angle distribution of an incident flow. These modules and their interactions are summarized in Figure 23. The mains modules are SLiMe (Simple & Light Mesher), NERD (Nascam Events and Reactions Definition) and MADS (Molecules and Atoms Deposition and Sputtering).

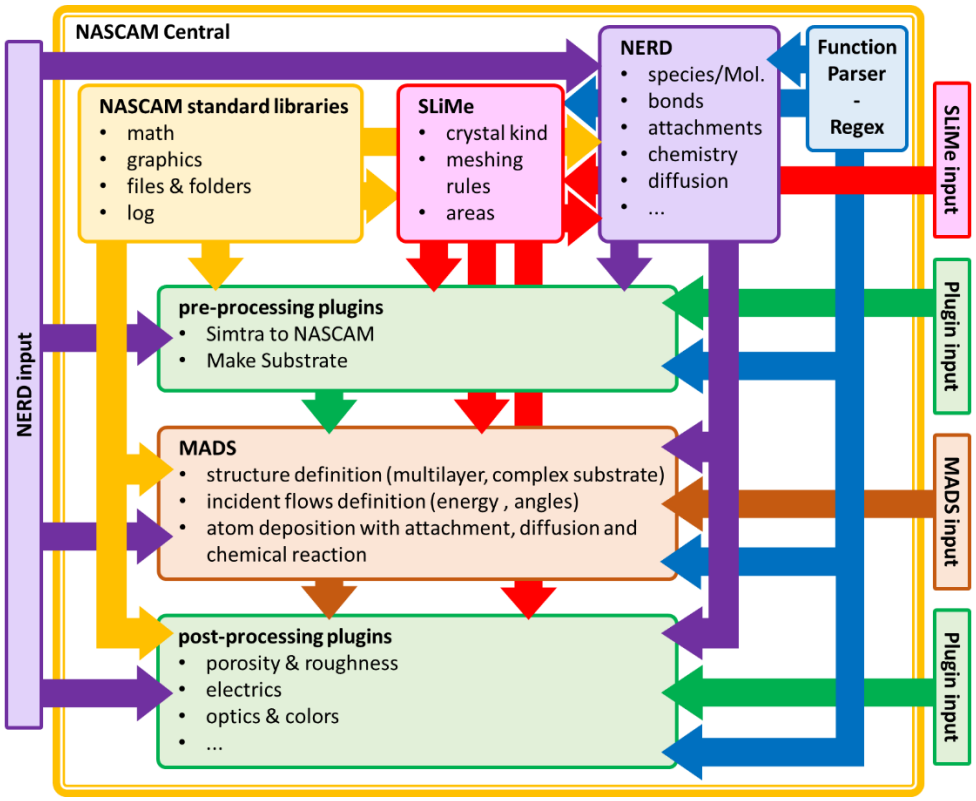

Figure 23 *Nascam 5 flowchart*

The module SLiMe is dedicated to the definition of the computational domain. It includes 3 kinds of objects: Computational Box, Grid and Area. The first one defines the computational box size and its boundary conditions. The second one is dedicated to the discretization of the computational domain in a set of cells which will be used as

predefined positions possibly occupied by a moving atom during the simulation process (one atom per cell). It allows to build structured meshes (e.g. for crystalline coatings, see Figure 24-left) or unstructured meshes (for amorphous materials, see Figure 24-middle) by means of the super-cell method [92]. By creating multiple Grid objects (see Figure 24-right), it is possible to model complex patterns like multi-grain or interfaces between two layers of different crystallographic structures.

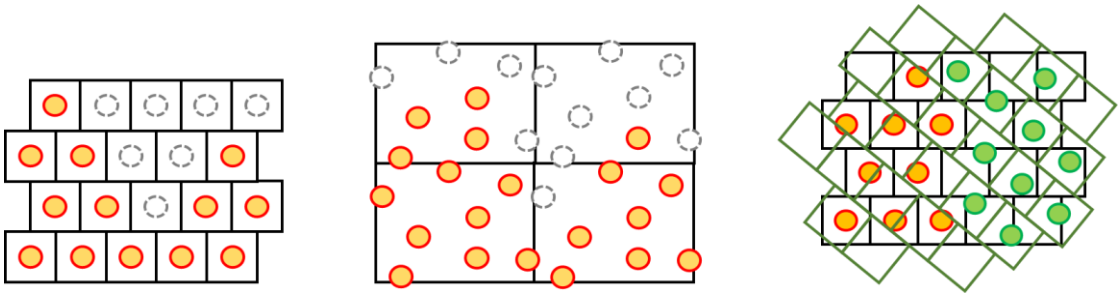

Figure 24 *Possible kinds of grid in Nascam 5. From left to right: structured grid, pseudo-random grid and multi-grids.*

Finally, the third object (Area) is a major tool allowing to define standard region of interest (ROI). It can be used by other objects for example to build the list of positions allowed during a diffusion or relaxation process, to study some characteristics like the binding energy or the stoichiometry, the density or the number of atoms in a given area.

The module NERD allows to set the physical rules for a specific simulation, form the definition of molecules to the description of attachment rules. Several objects are dedicated to the definition of particles from simple atoms and macro-atoms, to clusters and molecules, as shown in Figure 25.

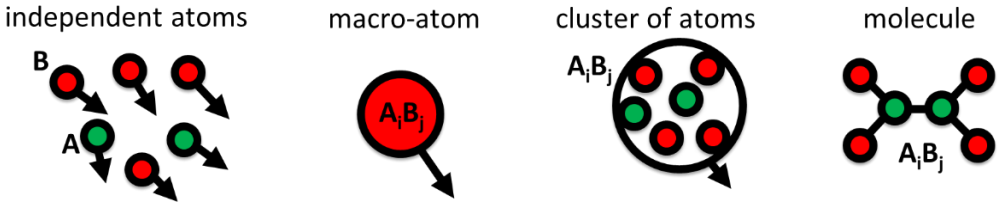

Figure 25 *possible kinds of particles deposited during a Nascam 5 process*

A particle object can be associated to physical properties like the mass, the surface binding energy, or to other object dedicated for example to the definition of attachment or chemical reaction rules. Another pack of objects is devoted to the events

description. In Nascam 5, an event can be an attachment or a detachment (by diffusion, energy transfer or chemical reaction) which will be associated to a particle (atom or macro-atom). An event can be associated to a probability obtained from literature or from experiment. Furthermore, if several events are allowed for a single particle, it is possible to weight each event. For example, Figure 26 shows the diagram of an Attachment object used to check if a particle is allowed to stick to the coating. In this case, the attachment is restricted by the stoichiometry in a given Area (stoichiometry area). If the stoichiometry is not respected, the algorithm will check at the positions defined by a second area (diffusion area) to mimic the diffusion of the particle along the coating surface. If the stoichiometry is still not respected after diffusion, the particle is supposed to be reflected from the film. This kind of object has been used in Chapter 7 to set the attachment rules of an oxygen particle to a TiO_2 coating.

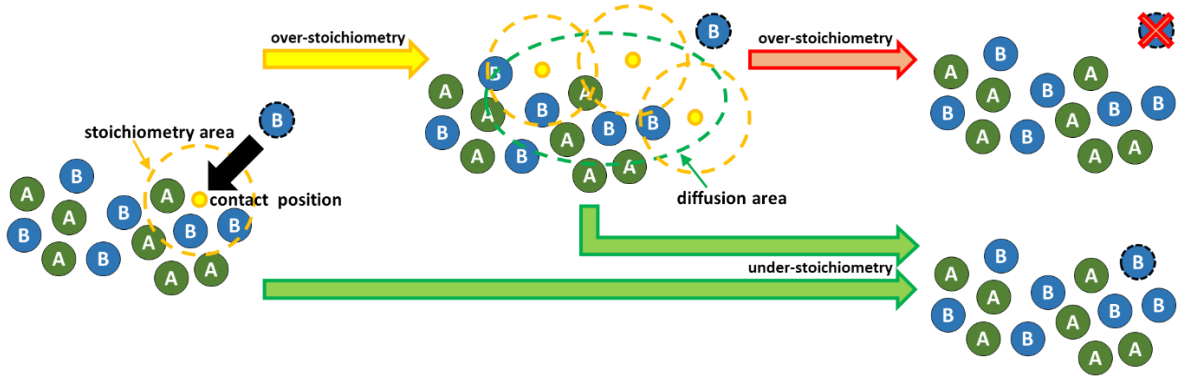

Figure 26 *Example of attachment rule defined by a maximal stoichiometry*

When a new particle is to be deposited on the growing film, the energy transfer is calculated according to Monte-Carlo binary elastic collision approximation (BCA) where the collisions of an incoming particle are considered as a sequence of independent collisions [93,94]. More precisely, a linear collision cascade BCA model [93,95,96] is used where all the recoils produced in the film are treated as a sequence of recoil generations, and where the path of a moving atom between two collisions is supposed to be linear, see Figure 27(A).

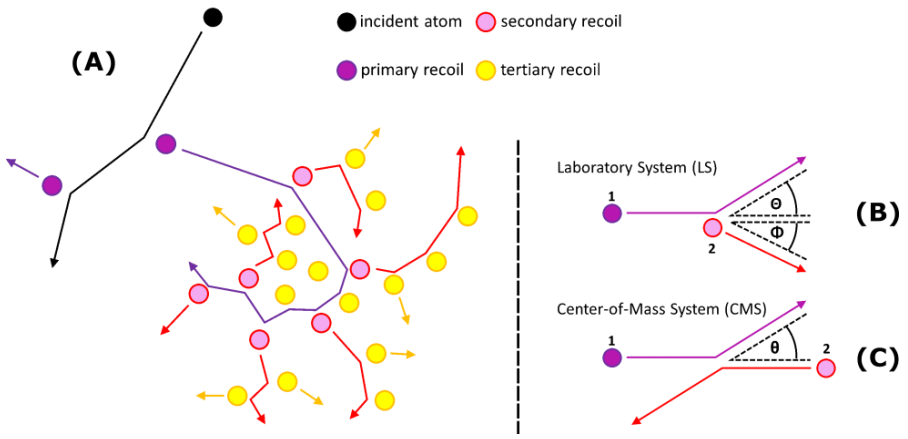

Figure 27 (A)*Schematic view of a full collision cascade with the binary collision approximation; Right: geometrical description of a collision process in BCA mode:* ***(B)*** *Φ and Θ - recoil and scattering angle in the Laboratory System,* ***(C)*** *θ - scattering angle in the Centre-of-Mass System*

The BCA algorithm is mainly based on the computation, for each collision, of the energy transferred from an incoming particle to a second particle belonging to the film (Figure 27(B)). This transferred energy, ΔE, is given by:

$$\Delta E = E\frac{4m_1m_2}{(m_1+m_2)^2}\sin^2\left(\frac{\theta}{2}\right)$$

where m_1 and m_2 are masses of projectile and recoil particles, E the projectile energy in the Laboratory System (LS) and θ is the scattering angle in the centre-of-mass system (CMS), see Figure 27(C):

$$\theta = \pi - 2b\int_0^{R_m}\frac{dR}{R^2\sqrt{1-\frac{U(R)}{E_c}-\frac{b^2}{R^2}}}$$

where b is an impact parameter, R_m is the minimum distance between the atoms, and E_c is the energy in the CMS:

$$E_c = E\frac{m_2}{m_1+m_2}$$

The recoil (Φ) and scattering (θ) angles in the LS, Figure 27(B), can be calculated as:

$$\Phi = \frac{\pi-\theta}{2}$$

$$\Theta = \tan^{-1}\left(\frac{\sin\theta}{\frac{m_1}{m_2}+\cos\theta}\right)$$

The last module MADS focuses on the description of the experiment to be modelled. This module gives access to several objects, like the one allowing to create (or import) a complex substrate, or the one which simply define the final stack (i.e., multi-layer). One really important MADS object is the flow object allowing to associate to a particle (atom, molecule...) some angular and energy distributions (e.g., obtained analytically, experimentally, or numerically by DSMC/PICMC) in order to mimic the deposition of such particles by PVD or PECVD. By associating several flows, it is possible to simulate the full process of a multi-species film growth.

11.2. Main parameters of Virtual Coater configuration

The main parameters of the final configuration of *Virtual Coater* are aggregate in the following table:

Parameters		DSMC	PICMC
3D Geometry		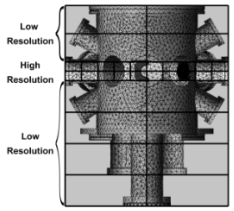	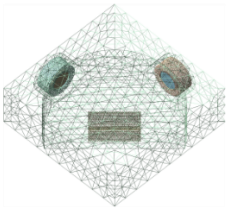
Involved species		Ar - O_2 - O - Ti	Ar - O_2 - O - Ti Ar^+ - O_2^+ - O^+- Ti^+ e^- - O^-
Time step [s]		$1x10^{-6}$	$2x10^{-11}$
Total physical time [s]		3 - 5	$150x10^{-6}$
# Iterations		$3x10^6$ - $5x10^6$	$7.5x10^6$
Cell size [mm³]		High res.: 1.5 x 1.5 x 1.5 Low res. : 10 x 10 x 10	1.5 x 1.5 x 1.5
Pumping efficiency [$L.s^{-1}$]		260	-
Dynamic wall chemistry		Yes	No
Sticking coefficients	**Ti**	1.0	1.0
	$O_{(2)}$	Variable	-
	Ti^+	-	1.0
Negative ion yield γ_{O^-}		-	0.1 %
Initial charge density [m^{-3}]		-	e^- & Ar^+: $1.0x10^{13}$
SEEY	**Ti**	0.114	
	TiO_2	0.080	
Ti & $O_{(2)}$ cosine exponant		1.5	
Initial gas T [K]		300	
Wall T [K]		300	
Ar base pressure [Pa]		0.5	
Target - substrate distance [mm]		160	
Surf. binding energy [eV]	**Ti**	4.89	
	TiO_2	6.0	
Particle weighting factors			
Charged species		-	$7.5x10^4$
Neutral species		***Metal*** / ***Trans.*** / ***Oxide***	
	Ar	$4.5x10^{10}$	
	O_2	$8.1x10^8$ / $1.5x10^{10}$ / $2.0x10^{10}$	
	O	$1.0x10^7$ / $1.0x10^7$ / $6.0x10^8$	
	Ti	$8.0x10^7$ / $4.0x10^7$ / $1.0x10^7$	